Experimental and Theoretical Aspects of Quantum Chaos in Rydberg Atoms in Strong Fields

by

Hong Jiao

B.S., University of California, Berkeley
(1987)
M.S., California Institute of Technology
(1989)

Submitted to the Department of Physics
in partial fulfillment of the requirements for the degree of

Doctor of Philosophy

at the

MASSACHUSETTS INSTITUTE OF TECHNOLOGY

February 1996

Signature of Author ____________________

Department of Physics
December 4, 1995

Certified by ____________________

Daniel Kleppner
Lester Wolfe Professor of Physics
Thesis Supervisor

Accepted by ____________________

George F. Koster
Professor of Physics
Chairman, Departmental Committee on Graduate Students

Experimental and Theoretical Aspects of Quantum Chaos in Rydberg Atoms in Strong Fields

by

Hong Jiao

Submitted to the Department of Physics
on December 4, 1995, in partial fulfillment of the
requirements for the degree of
Doctor of Philosophy

Abstract

We describe experimental and theoretical studies of the connection between quantum and classical dynamics centered on the Rydberg atom in strong fields, a disorderly system. Primary emphasis is on systems with three degrees of freedom and also the continuum behavior of systems with two degrees of freedom. Topics include theoretical studies of classical chaotic ionization, experimental observation of bifurcations of classical periodic orbits in Rydberg atoms in parallel electric and magnetic fields, analysis of classical ionization and semiclassical recurrence spectra of the diamagnetic Rydberg atom in the positive energy region, and a statistical analysis of quantum manifestation of electric field induced chaos in Rydberg atoms in crossed electric and magnetic fields.

Thesis Supervisor: Daniel Kleppner
Lester Wolfe Professor of Physics

Contents

APPENDICES

List of Figures

List of Tables

Chapter 1

Introduction

1.1 Preface

The time evolution of a classical system is locally well known, described by Hamilton equations of motion with given initial conditions. The solutions to the equations of motion are always possible for short time, at worst by numerical integration. However, simple nonlinear systems with as few as two degrees of freedom can display chaotic behavior, in which the motion is unpredictable for sufficiently long times. One characteristic of such chaotic motion is the instability of trajectories whose neighbors diverge expenentially. The evolution of these trajectories is thus highly sensitive to initial conditions. Our finite precision in measuring the initial conditions makes prediction of the long time behavior impossible. Such chaotic behavior has been found in numerous nonlinear systems (for reviews, see [Sch84] [Gle87]), most notably the Henon-Heiles system [HH64].

Quantum mechanics provides a more fundamental description of nature than classical mechanics. One must replace classical mechanics with quantum mechanics when studying phenomena at nuclear, atomic, and even molecular levels. Certain phenomena, such as superconductivity, manifest quantum mechanical behavior on a macroscopic scale. While the link between a classically regular system and its quantum counterpart is well established through semiclassical quantization, the connection between a classically chaotic system and its quantum counterpart is far less satisfactory. In particular, the quantum origin and signature of classical chaos in the semiclassical limit are not well understood. As a result, quantum chaos — the study of quantum behavior of a classically disorderly system — has attracted a great deal of interest in the last decade. There have been numerous theoretical investigations in nuclear, molecular, and atomic physics [SN87] [Cas85]. However, experiments capable of detailed interpretation are few. One set of studies involves microwave ionization of hydrogen atoms [BK74] [BK87] [KvL95]. More recently, the quantum kicked rotor has been realized expermentally [MRB$^+$95] [RBM$^+$95].

In this thesis, we study the Rydberg atom in strong static fields. This system offers a rich testing ground for quantum chaos. A review is presented in [HRW89].

1.1.1 Rydberg Atom in Strong Fields

The Rydberg atom in strong static fields has become a popular system for the study of quantum chaos. It is one of the simplest systems whose classical behavior displays a transition to chaos. In addition, Rydberg atoms can be readily studied experimentally, and the external fields can be carefully controlled. Consequently, the chaotic nature of such a system can be investigated experimentally with great clarity and detail. Finally, powerful numerical methods have been developed to perform accurate quantum computations in certain energy-field regimes.

1.1.2 Theories of Quantum Chaos

There are primarily two approaches to correlating spectral features with classical dynamics. The first attempts to discern classical chaos through a statistical analysis of the energy eigenvalues [BG84]. In particular, the energy-level statistics of a system with regular classical dynamics display a Poisson distribution [BT77], whereas the energy-level statistics of a system with chaotic classical dynamics obey the statistics of random matrix ensembles [BGS84]. This method emphasizes small scale spectral fluctuations, and the most often used statistical quantity is the nearest-neighbor-spacings distribution (NNS). While this statistical approach has enjoyed success in many systems (i.e. the diamagnetic hydrogen atom [DG86]), it sometime fails (i.e. the odd-parity diamagnetic lithium atom [Cou95]).

The second approach provides a more intuitive link between quantum spectra and classical dynamics through the semiclassical periodic-orbit theory developed by Gutzwiller [Gut90]. According to this theory, each classical periodic orbit modulates the quantum density of states with the period of the orbit. Delos and co-workers further developed the theory suitable for computing quantum spectra, the so-called closed-orbit theory. This theory asserts that a quantum spectrum is modulated by each classical closed orbit — a periodic orbit that is closed at the nucleus [DD87]. This approach relates large scale spectral structures to classical trajectories and gives recipes for computing quantum spectra by summing over closed classical orbits. This semiclassical theory has been successfully applied to many systems, including the hydrogen atom in a uniform magnetic field [HMW$^+$88], alkali atoms in a uniform electric field [ERWS88] [CJSK94], the helium atom in a uniform magnetic field [vdVVH93], and the rubidium atom in crossed electric and magnetic fields [RFW91].

1.1.3 The Goal of the Thesis

Previous studies have focused primarily on bound states for the following reasons: Quantum solutions are more tractable for bound states than for the continuum; classical motion can be conveniently portrayed by surface of section; and experimental studies are much easier to carry out and interpret for bound states than the continuum. Nevertheless, an understanding of an unbound system is essential for establishing the connection between quantum and classical descriptions of a general disorderly system. As a step toward this goal, this thesis presents detailed theoretical and experimental studies of a Rydberg atom in strong fields in the unbound regime. In particular, we relate experimental quantum spectra of a Rydberg atom in a magnetic field and in parallel electric and magnetic fields in the unbound regime with the classical dynamics through the semiclassical closed-orbit theory. We also investigate theoretically the Rydberg atom in crossed electric and magnetic fields, a system with three degrees of freedom.

1.2 Background of Atoms in Strong Fields

1.2.1 The Hamiltonian

The Hamiltonian of a hydrogen atom in uniform electric and magnetic fields (magnetic field along the z-axis) is

$$H = \frac{p^2}{2} - \frac{1}{r} + \frac{1}{2}BL_z + \frac{1}{8}B^2(x^2 + y^2) + F_z z + F_x x, \tag{1.1}$$

where F and B are the electric and magnetic fields, respectively, and $L_z = xp_y - yp_x$ is the z component of the angular momentum. Atomic units are used here and, with few exceptions, throughout this thesis. Some of the commonly used atomic units are given in Table 1.1. Relativistic effects, spin couplings between electron and the nucleus, and the effect due to finite mass of the nucleus [1] are ignored. These effects are too small to be observed experimentally. The mass of the electron is understood to be

---

[1] This effect for an atom in crossed fields is discussed in Chapter 8.

Physical Quantity	Unit	Size in cgs
Length	$\hbar^2/me^2 = a_0$	0.529177×10^{-8} cm
Energy	$me^4/\hbar^2$	2.1947464×10^5 cm^{-1}
Velocity	$e^2/\hbar = \alpha c$	2.18×10^8 cm/sec
Magnetic moment	$e\hbar/2mc$	1.4 MHz/gauss
Electric field	e/a_0^2	5.142×10^9 V/cm
Magnetic field	$\hbar/ea_0^2$	2.350518×10^9 gauss

Table 1.1: Some of the commonly used atomic units.

the reduced mass of the system. Finally, for precision studies, the $BL_z/2$ term should be multiplied by a factor $\beta = (m_n - m_e)/(m_n + m_e)$ to account for the motion of the nucleus [HRW81] (m_n and m_e are the nuclear and the electron masses, respectively).

The first two terms in the Hamiltonian are the unperturbed Hamiltonian for a Coulomb potential. The solutions are well known and can be found in any introductory quantum mechanics books. The third term is the paramagnetic interaction, giving rise to the usual Zeeman effect. If the system has rotational symmetry about z-axis, this term is constant and can be trivially transformed away. The fourth term is the diamagnetic interaction. Its cylindrical symmetry breaks the spherical symmetry of the Coulomb potential. As a result, the system becomes nonseparable and the classical system displays a transition to chaos in a certain energy-field regime. The fifth term is the contribution from the electric field parallel to the magnetic field. In the absence of the magnetic field, it gives rise to the familiar Stark effect. Finally, the last term represents the interaction of the system with an electric field perpendicular to the magnetic field. This interaction destroys the rotational symmetry about either field axis. The paramagnetic term is not conserved. Furthermore, the potential becomes velocity dependent.

1.2.2 Rydberg Atoms

Our goal is to investigate the behavior of an atom in strong external fields. This requires the external field strengths to be comparable to the unperturbed Coulomb potential. Table 1.1 shows that the atomic units for electric and magnetic fields are huge, exceeding the fields one can produce in a laboratory by many orders of magnitude. However, modest laboratory fields can perturb *Rydberg* atoms greatly. To see this, consider the interaction due to the magnetic field which consists of the paramagnetic interaction,

$$H_p = \frac{1}{2}Bm, \tag{1.2}$$

and the diamagnetic interaction,

$$H_d = \frac{1}{8}B^2(x^2+y^2) \approx \frac{1}{8}B^2n^4, \tag{1.3}$$

where n and m are the principal and the magnetic quantum numbers, respectively. The ratio of the diamagnetic to paramagnetic interactions,

$$\frac{H_d}{H_p} = \frac{1}{4}\frac{n^4}{m}B, \tag{1.4}$$

is small for low lying states (small n) at laboratory field strength. For example, $H_d/H_p \approx 10^{-4}$ for the 2P($m = 1$) state at $B = 6$ T. However, the situation is quite different for Rydberg states where the size of the atom can be enormous. For example, Eqn. 1.4 yields $H_d/H_p \approx 1$ for $n = 20$ ($B = 6$ T). In fact, for $n >> 1$, the diamagnetic effect is comparable to the unperturbed electronic binding energy

$$|H_0| = \frac{1}{2n^2}. \tag{1.5}$$

The ratio of diamagnetic interaction to the unperturbed binding energy scales as

$$\frac{H_d}{|H_0|} = \frac{1}{4}B^2 n^6, \tag{1.6}$$

and at $B = 6$ T and $n = 43$, $H_d/|H_0| \approx 1$. Similarly the electric field interaction [BS57],

$$H_F = Fz \approx \frac{3}{2}n^2 F, \tag{1.7}$$

is also comparable to the electronic binding energy of a Rydberg atom at laboratory field strength. This ratio scales as

$$\frac{H_F}{|H_0|} = 3n^4 F, \tag{1.8}$$

and $H_F/H_0 \approx 1$ at $F = 2000$ V/cm and $n = 32$. Both the electric field ($F = 2000$ V/cm) and the magnetic field ($B = 6$ T) strengths as well as the Rydberg atoms are readily accessible in the laboratory.

To summarize, the effects of laboratory electric and magnetic fields are not small compared to the unperturbed electronic binding energy of a Rydberg atom. The resulting system is in general not separable, and its classical counterpart may undergo a transition to chaos. Finding the connection between the quantum and classical behavior of such a disorderly system is the main goal of this thesis.

1.2.3 Symmetries

Symmetries are important in both classical mechanics and quantum mechanics because they correspond to constants of motion and allow separation or partial separation of the Hamiltonian, and thus simplify the problem. Constants of motion reduce the dimensionality of the system. If a time-independent system with N degrees of freedom has n constants of motion, then the dimensionality of the system is N-n+1.

System	Continuous Symmetry	Discrete Symmetry
No field	$E, \vec{L}, \vec{A}$	P
Electric field only	E, L_z, C_z	none
Magnet field only	E, L_z	P
Parallel fields	E, L_z	none
Crossed fields	E	P_z
Arbitrary fields	E	none

Table 1.2: Symmetries of various systems, where E is the total energy; $\vec{L}$ is the angular momentum; $\vec{A}$ is the Laplace-Runge-Lenz vector; $\vec{C}$ is the generalized Laplace-Runge-Lenz vector (see Sec. 4.1.2); P is parity; and P_z is z-parity.

For example, a hydrogen atom in an electric field, having three constants of motion (E, L_z, and C_z), becomes one-dimensional. E is the energy, and L_z and C_z are the angular momentum and the generalized Laplace-Runge-Lenz vector in the direction of the electric field, respectively. This system is completely separable, and the exact solutions can always be found. That is, the classical Hamilton equations of motion can be trivially integrated and the Schroedinger equation can be solved by separation of variables. The hydrogen atom in a magnetic field or parallel electric and magnetic fields has two constants of motion (E and L_z), and is thus reduced to two dimensions. This system is not completely separable and no general methods exist for finding exact quantum solutions. The mixed symmetries of the spherical Coulomb potential and the cylindrical magnetic field potential give rise to classical chaos. Finally, the hydrogen atom in crossed electric and magnetic fields has only one constant of motion (E), and thus remains three-dimensional. The symmetries of these systems are summarized in Table 1.2.

1.3 A Brief History

1.3.1 Early Progress in Diamagnetic Rydberg Atoms

The first experimental investigation of the diamagnetic effect on a Rydberg atom was performed by Jenkins and Segré in 1939 [JS39]. With a hydrogen lamp and a low resolution spectrograph, they studied $n = 10$ to 35 states of sodium and potassium at $B \approx 2.7$ T and observed a quadratic dependence of the energy levels on magnetic field. Schiff and Snyder explained the findings using perturbation theory [SS39]. Furthermore, they divided the energy spectrum into l and n mixing regimes.

An important discovery was made by Garton and Tomkins in 1969 [GT69]. They carried out absorption spectroscopy on barium at $B \approx 2.4$ T using a high resolution grating spectrograph. They made measurements through the zero field ionization limit, where they discovered unexpected oscillatory structures in the photoabsorption spectrum superimposed on a smooth background. The frequency of this modulation is very close to 1.5 times the cyclotron frequency, corresponding to the separation of the Landau states of free electrons in a magnetic field. Hence this modulation has been dubbed quasi-Landau oscillation. This important work stimulated modern interest both experimentally and theoretically in Rydberg atoms in strong fields.

An explanation of this phenomenon was first provided by Edmonds [Edm70] and later more quantitatively by Reinhardt [Rei83]. They showed that these oscillations are correlated with a periodic orbit of the electron moving in a plane perpendicular to the magnetic field. The period of the orbit turns out to be the same as the period of the quasi-Landau oscillations. This classical periodic orbit hence manifests itself as a sinusoidal oscillation in the quantum photoabsorption spectrum.

1.3.2 Closed-Orbit Theory and Scaled-Energy Spectroscopy

In the mid 1980's, Welge and co-workers carried out a series of experiments on hydrogen atoms in a magnetic field using pulsed VUV and UV lasers with resolution of 0.07 cm^{-1}. By Fourier transforming their spectrum, they observed a peak at the period of the quasi-Landau oscillation, and also peaks corresponding to the periodic orbits out of the plane [MWHW86][HWM+86]. In an attempt to make a quantitative connection between classical orbits and the quantum spectra, Delos and co-workers developed the closed-orbit theory [DD87]. In this theory, each classical closed orbit modulates the quantum spectrum with the period of the orbit. The strength of the modulation (the recurrence strength) is determined by the short-time stability of the given orbit.

To characterize such a recurrence more quantitatively, Welge and co-workers developed a novel experimental technique: scaled-energy spectroscopy. They exploited a classical scaling law of the system. The classical dynamics depends on $\epsilon = E/B^{2/3}$, not on E and B separately. By varying the experimental parameters to keep the classical scaled energy constant, they were able to observe recurrences associated with classical orbits with unprecedented precision and detail [HMW+88] [MWW+94].

1.3.3 Spectroscopy on Lithium

The first laser spectroscopy on Li in external fields was performed by Liberman and co-workers using a single UV laser [CLKP+86b]. Among other findings, they observed the core induced anticrossing in the energy levels [CLKP+86a]. In addition, they measured this anticrossing in Li in parallel electric and magnetic fields [CLLK+89].

The laser spectroscopy of Rydberg atoms in strong fields developed here at MIT was first carried out by Kleppner and co-workers. The first experiments employed a sodium atomic beam and a pulsed dye laser. Among other findings, this work provided evidence of an approximate symmetry [ZKK80] and led to its theoretical discovery by Herrick [Her82]. Kash, Welch and Iu, our predecessors on the experiment, replaced sodium with lithium and the pulsed dye laser with two CW dye lasers. They performed high resolution spectroscopy on lithium in a strong magnetic field. Among other important contributions, they observed unexpected behavior such as narrow resonances and orderly structures in the positive energy region [WKI$^+$89b][IWK$^+$89]. Some of the findings were eventually explained by Delande and Gay based on statistical ideas from random matrix theory [GDG93].

1.3.4 Numerical Advances

Advances in computing power and computational techniques have resulted in steady progress in accurate quantum computations.

Clark and Taylor were among the first to use the Sturmian basis, an efficient basis set for calculating highly excited states of hydrogen in a uniform magnetic field [CT82]. An oscillator basis in semi-parabolic coordinates was used by Wintgen and co-workers [WF86a]. Their result shows good agreement with the experimental spectra taken by Welge and co-workers far into the classically chaotic regime [WHW$^+$86]. Furthermore, Wintgen and Friedrich performed a nearest-neighbor-spacings study with their numerically computed quantum spectra. The result displays a transition to a Wigner-like distribution as the classical counterpart undergoes a transition to chaos [WF86b]. Large scale calculations have also been carried out by Wunner and co-workers. Their computations agree with experimental results up to 12 cm^{-1} below the ionization limit [WZW$^+$87]. O'Mahony and Taylor also performed similar calculations for nonhydrogenic atoms [OT86].

More recently, spurred by high precision spectra from our laboratory, Delande and Gay developed methods of complex rotation to achieve accurate quantum computations up to 30 cm^{-1} *above* the ionization limit [IWK+91]. This method has been extended to hydrogen in crossed electric and magnetic fields by Main and Wunner. They computed the quantum spectra above the classical ionization limit (the saddle point) in their investigation of Ericson fluctuations in the crossed fields system [MW92].

1.4 Overview of the Experiment

In this thesis, we report the result of an investigation of Rydberg atoms in strong static fields. Experimentally we have conducted high resolution spectroscopy on lithium. The CW lasers needed to perform high resolution spectroscopy on hydrogen Rydberg states are not readily available. On the other hand, a two-step excitation scheme for atomic lithium, the most hydrogen-like alkali atom, can be easily achieved as shown in Fig. 1-1. In the presence of a magnetic field, parity is conserved. Our excitation scheme excites the odd parity final states. Due to the relatively small quantum defect of the P states (≈ 0.05), the quantum spectra of odd parity states have been shown to be very hydrogenic [WKI+89a]. In the presence of an electric field, the final states are a superposition of both even and odd parities. Due to the large quantum defect of the S states (≈ 0.4), the quantum spectra of lithium and hydrogen are in general very different. In particular, lithium atoms in strong fields can exhibit core induced chaos [Cou95] [CSJK95]. In this thesis, we will primarily study the recurrence spectra — the Fourier transform of the scaled-energy spectra — of the short period orbits, which have been shown to be nearly identical to those of a hydrogen atom [ERWS88]. As we will show, the lithium spectra can be interpreted in terms of the classical dynamics of hydrogen.

Our experiment employs a lithium atomic beam that travels along the axis of a split-coil superconducting magnet to reduce the motional electric field effect. A pair

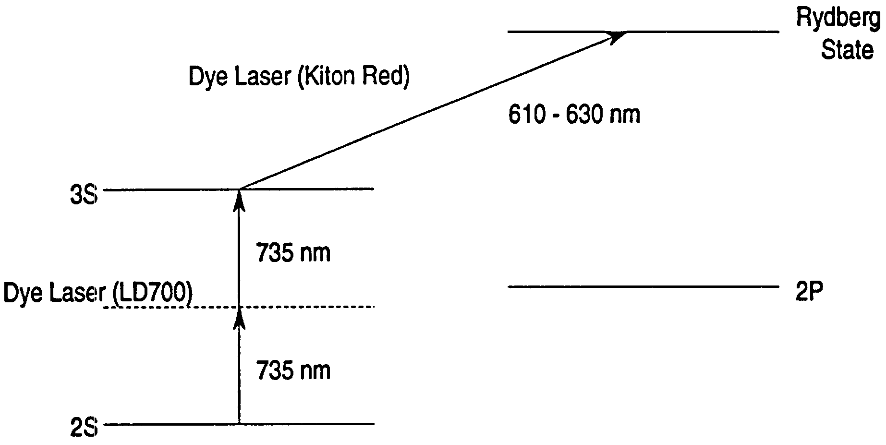

Figure 1-1: Excitation scheme. Lithium atoms are excited from 2S to 3S through a two-photon transition by a dye laser, and another dye laser makes the transition from 3S to the Rydberg state. (Dye names are enclosed in the parentheses.)

of field plates provides an electric field parallel to the atomic beam. Laser beams intersect the atomic beam at right angles to reduce Doppler broadening. One laser drives the 2S → 3S two-photon transition, and a second laser excites the Rydberg states that are field ionized. The resulting ions are detected by a microchannel plate (MCP). To generate conventional energy spectra, the laser frequency is varied at fixed electric and magnetic fields. To perform scaled-energy spectroscopy, the magnet is ramped, and the electric field and the laser frequency are varied accordingly in order to keep the classical parameters constant.

1.5 Outline of the Thesis

This thesis deals with experimental and theoretical aspects of quantum chaos in Rydberg atoms in strong external fields. Its content is divided into three parts:

- Experimental details (Ch2 and Ch3).
- Theoretical background (Ch4 and Ch5).
- Experimental and theoretical results (Ch6, Ch7, and Ch8).

Chapter 2 presents a detailed account of the experimental setup. Primary emphasis is on the magnet, the interaction region, the detector, and data taking procedures. Chapter 3 describes a new excitation scheme which we have recently implemented. It includes a discussion of the fine and hyperfine structure of lithium as well as such experimental details as lasers and optics. However, all data presented in this thesis were taken with the old excitation scheme.

Chapter 4 and chapter 5 serve as backgrounds for classical and quantum chaos, respectively. Chapter 4 addresses the issues related to integrable and nonintegrable classical systems, and the origin of classical chaos. Chapter 5 provides necessary background for a semiclassical approach to quantum chaos, the closed-orbit theory.

Chapter 6 deals with Rydberg atoms in parallel electric and magnetic fields in the continuum. The focus here is on the transition to chaos as the system evolves from an electric field to a magnetic field dominated region. The main results include the experimental observation of bifurcations of closed orbits, and the connection between recurrence spectroscopy and classical chaotic ionization.

Chapter 7 discusses diamagnetic Rydberg atoms in the positive energy regime. The main result is the transition to regular motion as the scaled energy increases positively. The semiclassical connection to quantum spectrum is established by the recurrence spectroscopy.

Chapter 8 deals with Rydberg atoms in crossed electric and magnetic fields. The techniques for characterizing classical chaos are presented. The quantum spectra are computed numerically. Finally, the signature of classical chaos in quantum spectra is revealed by a statistical analysis of eigenvalues. In particular, the nearest-neighbor-spacings distributions are shown to undergo a transition from Poisson-like behavior to Wigner-like behavior as the classical system displays a transition to chaos.

Finally, eight appendices provide additional experimental and numerical details.

Chapter 2

Experimental Techniques

The goal of the experiment is to measure the energy levels of lithium Rydberg atoms in strong electric and magnetic fields. The method is based on laser spectroscopy in which the atoms are excited by the scheme that was shown in Fig. 1-1. The excited atoms are detected by field ionization.

A simplified schematic diagram of our apparatus is shown in Fig. 2-1. The experiment employs a lithium atomic beam that travels along the axis of a split-coil superconducting magnet to reduce motional electric field effect. A pair of field plates provides an electric field parallel to the atomic beam. The laser beams intersect the atomic beam at right angles to reduce Doppler broadening. A fixed frequency dye laser drives the 2S → 3S two-photon transition, and a second tunable dye laser excites the Rydberg states. The excited atoms are field ionized, and the ions are detected by a microchannel plate (MCP). To generate a conventional spectrum, the laser frequency is varied at fixed electric and/or magnetic fields. To perform scaled-energy spectroscopy, the magnet is ramped and the electric field and the laser frequency are varied accordingly in order to keep the classical parameters constant. Finally, to calibrate the energy scale, the laser frequency is measured accurately with an iodine absorption cell and a high resolution calibrated Fabry-Perot etalon.

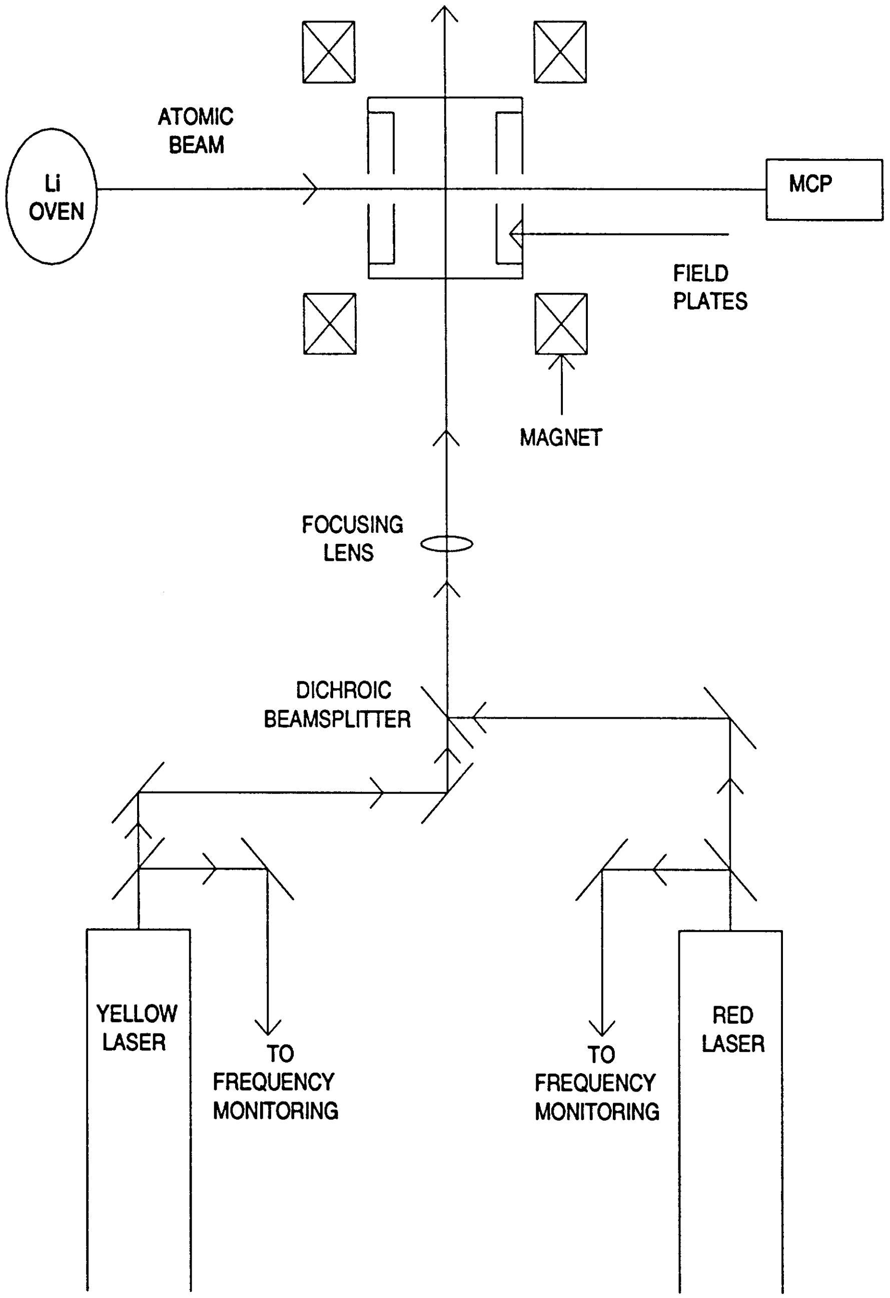

Figure 2-1: Schematic diagram of the apparatus.

Major features and various details of the apparatus have been described in a previous thesis [Kas88]. Here we describe in detail only the new aspects of the experiment, namely, the magnet, the interaction region, and the detector.

2.1 Atomic Beam

The atomic source produces a collimated beam of lithium atoms with sufficient flux to produce strong signals in the interaction region. Although the laser beams intersect the atomic beam at right angles, any divergence of the atomic beam can give rise to first-order Doppler broadening. Furthermore, the finite interaction time, which depends on the atomic beam velocity and laser beam size, gives rise to transit time broadening. Consequently, the properties of the atomic beam largely determine the experimental resolution. In this section, we discuss these issues and the atomic beam source itself.

2.1.1 Atomic Beam Source

The tube oven used by our predecessors is ill-suited to the current experiment because of the Lorentz force arising from the interaction between the large current that heats the tube oven and the huge fringing field of our magnet (see Sec. 2.3). A mu-metal shield is not useful because the magnetic field at the oven is too large (1 T).

We constructed a lithium oven following a design by Chun-Ho Iu at SUNY-Stonybrook [Cou95]. The essential feature is a 3/4″ diameter stainless rod bored out to hold lithium. The oven is sealed except for a 0.040″ aperture which allows the lithium atoms to escape, thus forming an atomic beam. Four 20 Ω heaters, connected in parallel, deliver up to 1400 W of heating. We control the current through the heaters with a variable transformer. We usually operate the oven at 650 °C, which requires about 320 W of power, corresponding to 2 A through each heater. The temperature at the oven is monitored with a chromel-alumel (type K) thermocouple. The time required to attain this equilibrium temperature is about 1 1/2 hours. At this operating temperature, 2 grams of lithium usually last several hundred hours.

The oven is surrounded by a water cooled cold shield which condenses most of the lithium except that which passes through a 1/2″ diameter hole. The oven assembly is mounted on a flange at the top of the oven manifold. A 6″ diameter bellows between this flange and the rest of the oven manifold allows adjustments of the oven position in order to maximize the flux through the interaction region. The oven and interaction region are about 40 cm apart. A 2 3/4″ conflat gate valve, installed between the oven manifold and the interaction region, acts as an on-off shutter for the atomic beam and allows independent vacuum operation on either side of the valve.

The vacuum of the oven manifold is maintained by a 2″ Varian M2 diffusion pump, backed by a Varian SD-90 vacuum pump. A Varian 322 water-cooled baffle reduces backstreaming into the oven manifold. The pressure in the foreline is measured with a Hasting DV-6M thermocouple gauge, while the pressure in the oven manifold is measured with a CVC GPH-320B Penning gauge. Overnight baking usually lowers the pressure to less than 10^{-7} Torr, below the lower limit of the Penning gauge. At one point, we were concerned that diffusion pump oil was contaminating our interaction region, leading to undesirable stray electric fields. A Varian V60 turbo pump was installed. However, we found no evidence that the turbo pump reduces the stray field. Moreover, the fringing magnetic field interferes seriously with the proper operation of the turbo pump. Consequently, we switched back to the diffusion pump. Future users should keep in mind that proper magnetic shielding must be provided before a turbo pump can be operated in the presence of the magnetic field.

Finally, the source of our lithium is a 1/8″ diameter lithium wire from LITHCO. Its natural abundance consists of 6% ^{6}Li and 94% ^{7}Li. Fortunately, our excitation scheme permits laser selection of either isotope. While lithium reacts vigorously with

Atomic beam flux	1.3×10^{14} atoms/cm^2/sec
Atomic beam current	1.6×10^{12} atoms/sec
Atomic density	4.2×10^{8} atoms/cm^3
Velocity, v	2×10^{5} cm/sec
Divergence, $\delta\theta$	3×10^{-3} radian
Diameter	2 mm

Table 2.1: Atomic beam properties in the interaction region.

water, we find that exposing lithium to air temporarily while loading the oven is relatively harmless, though this should not be done in a humid environment.

Table 2.1 describes the atomic beam properties for an assumed operating temperature (650 °C). These are based on elementary kinetic theory [Ram56].

2.1.2 Doppler Broadening and Transit Time Linewidth

The atomic beam and the laser beams intersect at right angles in the interaction region. To estimate the residual first-order Doppler broadening, we consider atoms with velocity v in a beam with divergence $\delta\theta$. These atoms experience a spread in resonance frequency

$$\delta\nu_{D1} = \left(\frac{v}{c}\right) \nu \, \delta\theta. \tag{2.1}$$

The transition wavelength is about 610 nm. Using the data in Table 2.1, the residual first-order Doppler broadening is $\delta\nu_{D1} = 10$ MHz.

Second-order Doppler broadening is

$$\delta\nu_{D2} = \frac{1}{2} \left(\frac{v^2}{c^2}\right) \nu. \tag{2.2}$$

We find $\delta\nu_{D2} = 11$ kHz, which is negligible compared with the residual first-order

Doppler broadening and other broadening mechanisms in this experiment.

Our spectral resolution is also limited by the finite interaction time of the atomic beam and the laser beam. For an atomic beam travelling at velocity v intersecting a laser beam at its waist w at a right angle, the linewidth due to finite interaction time is about

$$\delta\nu_{tof} = \frac{1}{2\pi}\frac{v}{2w}. \tag{2.3}$$

When the laser beam is focused to a beam waist of 50 μm, the transit time broadening becomes $\delta\nu_{tof} = 7$ MHz.

Finally the natural linewidth of 3S state is about 6 MHz while those of the Rydberg states are negligible. The laser linewidth is about 1 MHz. Our final experimental resolution, about 25 MHz, is given roughly by the sum of all the effects discussed.

2.2 Lasers and Optics

Two Coherent CR699-21 ring dye lasers are used to excite lithium atoms to Rydberg states in a two-step excitation scheme. Each laser is frequency stabilized to a reference cavity with a resulting linewidth of about 1 MHz. However, the cavity and hence the laser can drift as much as 100 MHz/hour depending on the stability of the air temperature and pressure. To achieve optimum output power, the optics must remain clean and well aligned. This involves substantial effort, much of which is described in a previous thesis [Kas88]. Finally to reduce dye instability, we cool the dye jet with a Neslab CFT-75 recirculating chiller.

The laser that drives the 2S → 3S two-photon transition (735 nm) (the red laser) uses LD700 dye and is pumped by a Coherent CR3000K krypton-ion laser. The output power of the ion laser is relatively stable, even though its power supply is highly unreliable. We operate the krypton-ion laser multiline at 676.4 nm and 647.1 nm. At full current (60 A), the output power is about 6 W. At this pumping power, we usually get about 1 W of single-mode output power from LD700 at 735 nm. Although the dye laser power increases as a function dye circulator pressure, the dye jet tends to be unstable at higher pressure. We operate the dye jet at 40 psi.

The laser that drives the 3S to Rydberg transition (610 nm to 630 nm) (the yellow laser) uses Kiton Red dye and is pumped by a Coherent Innova 100-10 argon-ion laser operating on the single line at 514.5 nm. At maximum current (50 A), its output power is about 20 W multiline and 10 W at 514.5 nm. However, the dye jet must be run at an unusually high pressure (80 psi) at this pumping power. The jet nozzle made by Coherent is not suitable for this operating pressure. It causes dye overheating and related instabilities [1]. Consequently, we pump Kiton Red with 7 W single line at 514.5 nm (37 A) at a jet pressure of 55 psi. The single-mode output power is 250 mW to 300 mW at 620 nm.

Both dye laser beams are expanded with telescopes and overlapped with a dichroic mirror (99% reflection at 735 nm and 70% transmission at 620 nm). They are then focused by a 40 cm focal length lens onto the atomic beam in the interaction region after passing through a broadband AR coated window. At the interaction region, the beam waist of the red laser is about 50 μm and that of the yellow laser is about 65 μm. The intersection between the red laser and atomic beam is optimized by maximizing the fluorescent signals (see Sec. 2.4.1). To achieve good overlap between the two laser beams, the beams are first temporarily deflected by a plane mirror before the window and then overlapped at their foci through a 50 μm diameter pinhole. After removing the temporary mirror, the beams usually overlap well enough to give detectable Rydberg signals. The final overlap is optimized by maximizing the Rydberg

---

[1] Recently, a German laser company, Radiant Dyes Laser Accessories GmbH, developed a new nozzle that is suitable for pressure up to 100 psi.

signals (see Sec. 2.5.1).

A small fraction of each laser beam is deflected from the main beam path for frequency monitoring. A 1.5 GHz free spectral range Fabry-Perot etalon is used to display the spectral characteristics of each laser. The resolution is rather low, but is adequate for qualitative purposes.

To set the laser frequency to within a few GHz of the desired transition frequency, we use a wavemeter consisting of a Michelson interferometer with a moving arm and a single-frequency temperature stabilized HeNe laser. The wavelength is found by comparing the number of interference fringes of the HeNe laser to the unknown laser produced by moving one of the interferometer arms. The HeNe frequency is known to within 2 GHz. The ratio of the number of fringes times the HeNe frequency thus gives the wavelength of the unknown laser. The precision is about 2×10^{-6}. This is sufficient to find the 2S → 3S two-photon transition frequency. However, this uncertainty is too large for a precise measurement of the yellow laser frequency used to determine the Rydberg energy levels accurately. The latter determination is accomplished by an iodine reference cell and a high resolution Fabry-Perot etalon.

Iodine absorption signals serve as our frequency reference. A temperature and pressure-stabilized Fabry-Perot etalon [Iu91] is used to transfer the known frequency of an iodine peak to a Rydberg transition. The etalon has a nominal FSR of 300 MHz and a finess of about 200 at 620 nm. The calibration of the FSR is achieved by using Rydberg levels of lithium as the frequency standard. The most recent calibration yields an FSR of 298.93779(3) MHz [Iu91]. The accuracy in assigning energies of Rydberg states is about 0.001 cm^{-1}, primarily limited by the uncertainty in the FSR calibration and the exact position of a given iodine peak. This is close to our experimental resolution mentioned in Sec. 2.1.2. During each scan of the yellow laser, the normalized iodine absorption signals and the Fabry-Perot output as well as Rydberg signals are recorded (see Fig. 2-6 for such a scan).

Rated central field	6 tesla
Rated magnet voltage	2.5 V
Homogeneity over 1 cm^3 volume	0.001
Inductance	112.8 henry
Inner (bore) diameter	5.25″
Outside diameter	13.25″
Length	7.5″

Table 2.2: Specifications of the magnet.

2.3 The Magnet

The magnet provides a strong and uniform magnetic field at the laser-atom interaction point. We use a 6 T split-coil superconducting magnet, made by American Magnetics in 1991. The windings consist of many filaments of superconductor, in our case, Nb_3Sn, embedded in a copper matrix. The magnet is impregnated with epoxies to prevent the movement due to the Lorentz force, the so-called "training" effect. Any microscopic motion can quench the magnet. Finally, the magnet is welded into a 50-liter liquid helium dewar which sits inside a liquid nitrogen dewar. The magnet can provide magnetic fields up to 6 T with a homogeneity of 0.001 over a 1 cm^3 volume. These and certain other specifications of the magnet are shown in Table 2.2.

The magnet is energized by an IPS 100A power supply made by Cryomagnetics. The basic operating components are a sweep generator, a high current power supply and a persistent switch heater power supply. The operational procedures are straightforward and are summarized in Appendix A. The vacuum jacket of the cryostat is evacuated by a Varian V-60 turbo pump. At room temperature, the pressure can go down to $1-2\times10^{-6}$ Torr (monitored by an ion gauge). When the dewar is filled with liquid helium, the pressure drops to 1×10^{-8} Torr. Detailed cryogenic considerations are provided in Appendix B.

2.3.1 Magnetic Field Profile

The magnet is a "high-field" type superconducting magnet. Apparatus such as a turbo pump or a multi-channel electron multiplier does not work well in high magnetic fields. For this reason, it is important to know the field in the vicinity of the magnet. We have calculated the field by methods described in Appendix C. Figure 2-2 shows the result of B_ρ and B_z for various z and ρ. All calculations are for 1 T at the center of the magnet. Figure 2-3 shows a comparison with measurements made with a gaussmeter. The agreement appears reasonable.

2.3.2 Field Monitoring

The most straightforward method for monitoring the magnetic field depends on the linearity between the field and the current. Our magnet is a type II superconductor. The Meissner effect, a phenomenon of the repulsion of magnetic field by a superconductor, is incomplete in such a superconductor. (Kittel provides an excellent introduction to this subject [Kit86].) An effect known as flux jumping, in which the field lines penetrate into the superconductor, generates a non-linearity between the magnetic field and the current. The filaments of our superconductors are twisted to reduce this effect. To calibrate the field to current ratio, the field is determined by using the atoms themselves (see Sec. 2.6.1). Currents up to 10 A are measured with a Keithley 197 DMM current meter. The calibration yields 1158.5(1.0) Gauss/A. To measure currents greater than 10 A, a shunt, whose resistance has been carefully calibrated, has been connected in series with the magnet. Hence the voltage reading across the shunt effectively translates into the magnetic field in the interaction region. Our scaled-energy spectroscopy (Sec. 2.6.3) relies on this proportionality. The overall uncertainty in the field determination, as described in Sec. 2.6.1, is about ±20 gauss.

We can also monitor the field in the interaction region using a Hall probe. We

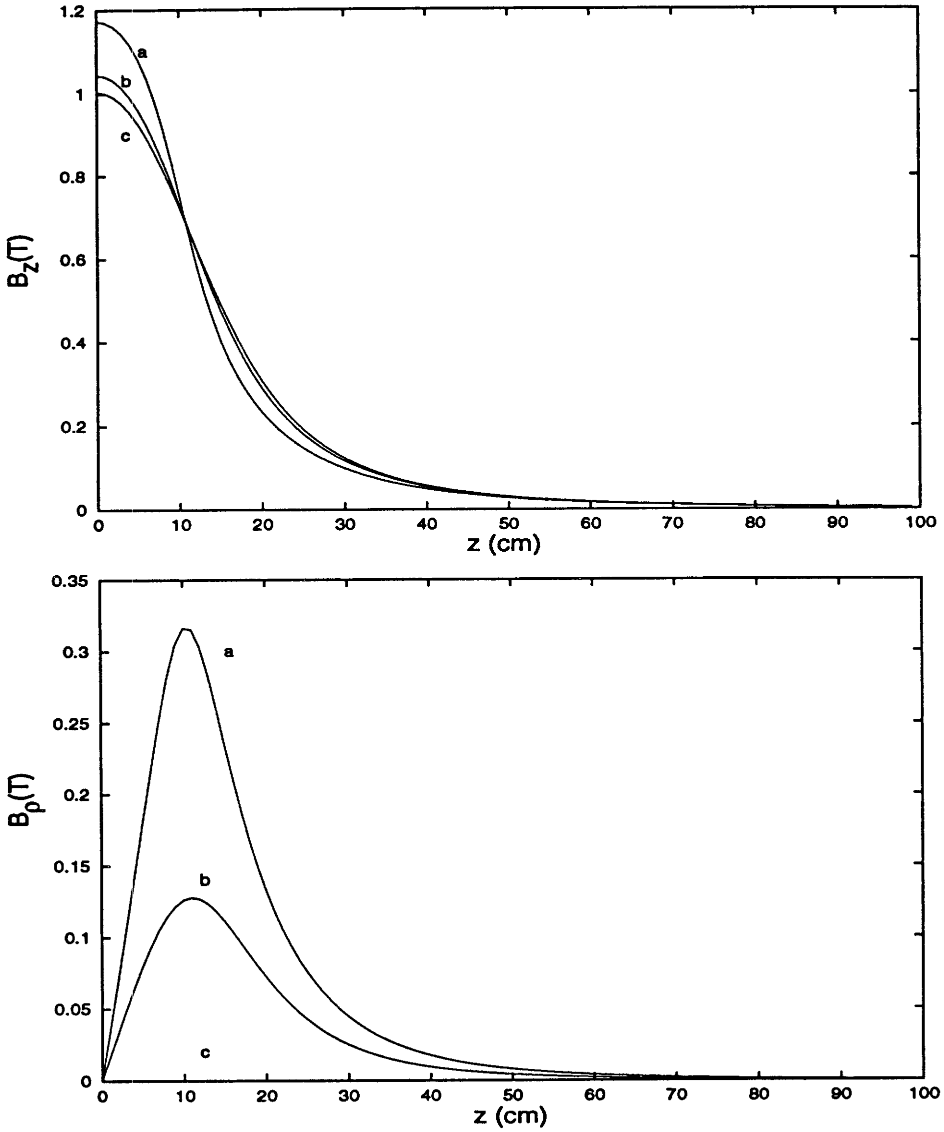

Figure 2-2: Numerical calculation of the field of a split-coil magnet. ρ is the radial distance from the center of the coil, and z is the distance along the axis of the coil. a)$\rho = 10$ cm, b) $\rho = 5$ cm, c) $\rho = 0$ cm. Top figure is the axial field, B_z. Bottom figure is the radial field, B_ρ.

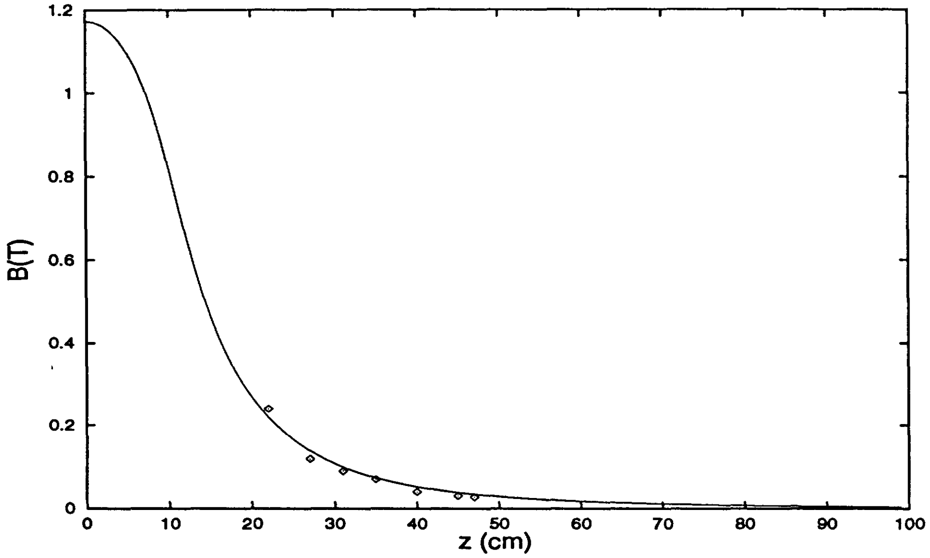

Figure 2-3: A comparison between calculations and actual measurements of the total field of the magnet. The diamonds are points measured with a gaussmeter.

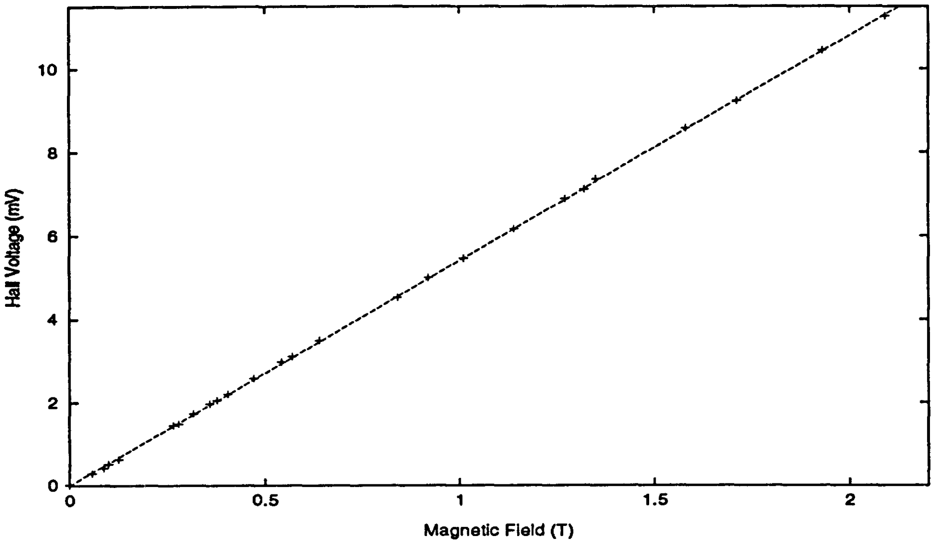

Figure 2-4: Calibration of Hall probe against magnetic field. The diamonds are the experimental measured values and the line is a linear fit.

employ an F.W. Bell BHA-921 cryogenic semiconductor probe because of its wide dynamic range (beween -15 T and +15 T) and its wide operating temperature range (between -269 °C and 100 °C). The Hall probe is driven by a constant temperature stabilized current supply. The electronic details are described in a previous thesis [Kas88]. We usually place the Hall probe about $1''$ away from the interaction point. Figure 2-4 shows the Hall probe voltage versus the magnetic field measured with the atoms (Sec. 2.6.1). The linear relationship suggests that we could calibrate the magnetic field to Hall voltage ratio in the same way as the field to current ratio. Since the Hall probe is not at the interaction point, this cannot provide a reliable absolute calibration. Nevertheless the Hall probe can be used differentially over small changes in field. We measure the absolute fields at the end points of a small field interval, and thus obtain $\Delta B/\Delta V_H$. By measuring the Hall voltage along the interval, the absolute magnetic field is deduced at every point.

2.4 Interaction Region

The interaction region provides the environment in which the atoms are excited by the lasers. The requirements of this interaction region are threefold. First, it must be equipped to collect the 2P → 2S cascade fluorescence in order to monitor the 3S population. Next, it must be capable of providing a uniform electric field at the laser-atom interaction point. Finally, it must provide an environment with very small stray electric fields.

A schematic diagram of the interaction region is shown in Fig. 2-5. It is constructed from an aluminum cylinder 2″ long and 2″ in diameter. Two mirrors and a 1/4″ diameter light pipe are used to collect the fluorescent light (see Sec. 2.4.1) . Two 1 mm diameter knife-edge baffles (not shown) are installed along the laser beams to minimize the scattered light. The inside surfaces of the interaction region are coated by Aqua-dag, a black material that further reduces the scattered light.

2.4.1 Fluorescence Detection

The 3S state population is monitored by observing the 2P → 2S cascade fluorescence at 670 nm. Two mirrors in the interaction region increase the collection efficiency as shown in Fig. 2-5. The hole in the lower mirror holds a plexiglass light pipe. The upper mirror focuses the light onto the light pipe which is then coupled into a glass fiber bundle with 1/4″ active diameter. The 12 foot long fiber bundle, made by General Fiber Optics, Inc, has an overall transmission of about 25%. Exiting the fiber bundle, the light passes through two Ealing narrow bandpass filters (about 10 nm bandwidth) at 670 nm before being focused onto a RCA Model C31034A photomultiplier tube (PMT). This PMT has the special features of a very low dark count rate and reasonable quantum efficiency at 670 nm. Its specifications are shown in Table 2.3. The PMT becomes inoperative in the presence of few thousand gauss

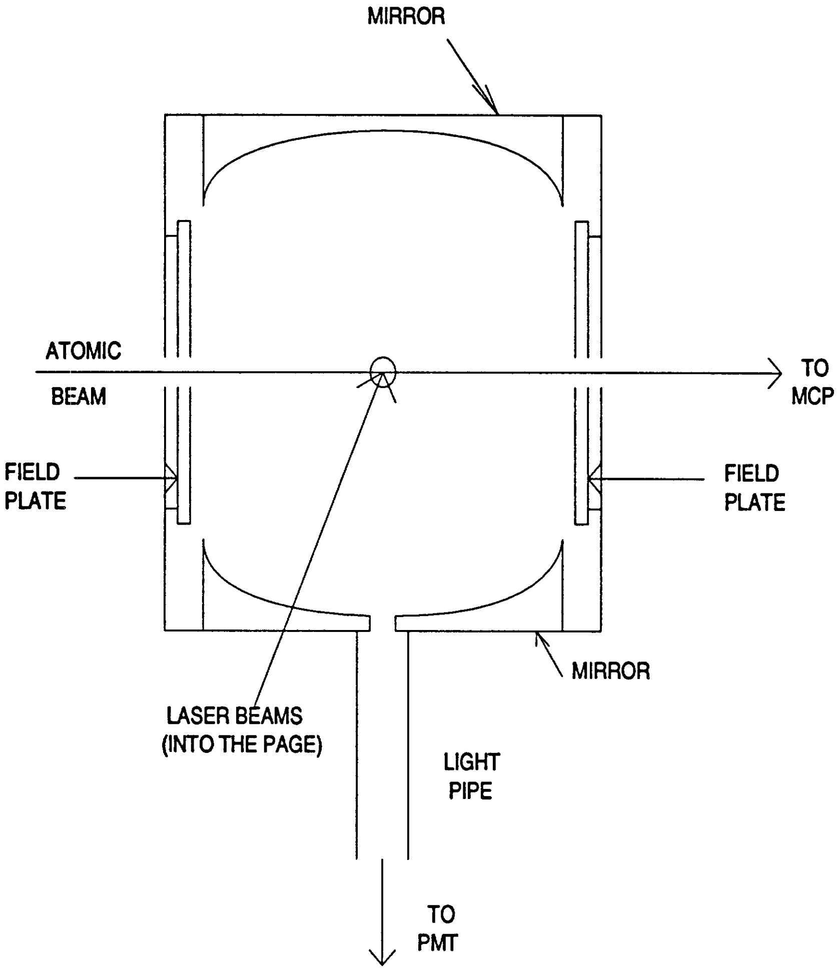

Figure 2-5: Schematic of the interaction region.

Photocathode material	GaAs
Bias on the cathode	1680 V
Quantum efficiency at 670 nm	12%
Quantum efficiency at 813 nm	10%
Gain	6×10^5
Dark counts at -30 °C	5 cps
Active area	4 mm × 10 mm

Table 2.3: Specifications of the RCA C31034A PMT.

of magnetic field. The long length of the fiber bundle allows us to locate the PMT sufficiently far from the magnet. The PMT is housed in a Products for Research Model TE-104-RF cooler running at -30 °C. The bias on the cathode is supplied by a Bertan Model 315 high voltage power supply. The pulses from the anode are fed into a Modern Instrument Technology (MIT) Model F-100T amp-discriminator whose TTL output goes to counters.

2.4.2 Electric Field Plates

To apply an electric field, we use a pair of 1 1/2″ diameter field plates as shown in Fig. 2-5. The plates have 0.125″ holes in the middle for the atomic beam to pass through. The uniformity of the field at the interaction point depends on the size of the holes, the plate diameter, and the plates' separation. The separation should be much less than the plate diameter. On the other hand, it should be much greater than the diameter of the holes. We found the optimum separation to be about 0.75″, which is calculated to yield an rms field nonuniformity of 0.3% over a 1 mm^3 volume. Biasing the field plates symmetrically with respect to ground improves the field uniformity. To detect photoionized Rydberg atoms, obviously the polarity of the bias is important. For example, ion detection requires the field plate closer to the detector be biased negative. A dual +/- 150 V amplifier built by Robert Lutwak is used to bias both plates. It consists of inverting and noninverting amplifiers. The input is controlled by a D/A converter which outputs a voltage between 0 and 10 V. The difference in magnitudes between the two channels can be made less than 1 in 10^5.

2.4.3 Stray Electric Field

Rydberg atoms are greatly affected by electric fields (see Eqn. 1.7). In particular, a stray electric field has the undesirable effects of causing both parity states to be excited, shifting the atomic levels, and otherwise complicating the spectrum. As a result, a major requirement for the interaction region is to provide an environment with a very small stray electric field.

Any contaminant, especially water, carried in by the atomic beam tends to form an insulating layer on the surfaces of the interaction region. This layer holds charge which in turn induces a stray electric field. One obvious remedy is to have all the surfaces of the interaction region far away from the laser-atomic beam intersection point.

Without the field plates, all the surfaces of the interaction chamber are at least 1″ away from the interaction point. In addition, the Aqua-dag coating is conductive and hence reduces stray electric field. We also found that baking the interaction region significantly reduces stray electric fields. A 20 Ω heater is installed on one of the end plates of the interaction region cylinder along with a type T thermocouple. We usually bake the interaction region around 90 °C for several days. This end plate also holds the Hall probe mentioned in Sec. 2.3.2.

We can estimate the magnitude of this stray electric field by observing one particular n manifold of the lithium spectrum in the absence of the magnetic field. In the presence of a stray electric field, we no longer excite just the P state but the entire n Stark manifold. Because of the linear Stark effect, the width of this manifold, $\Delta\nu_S$,

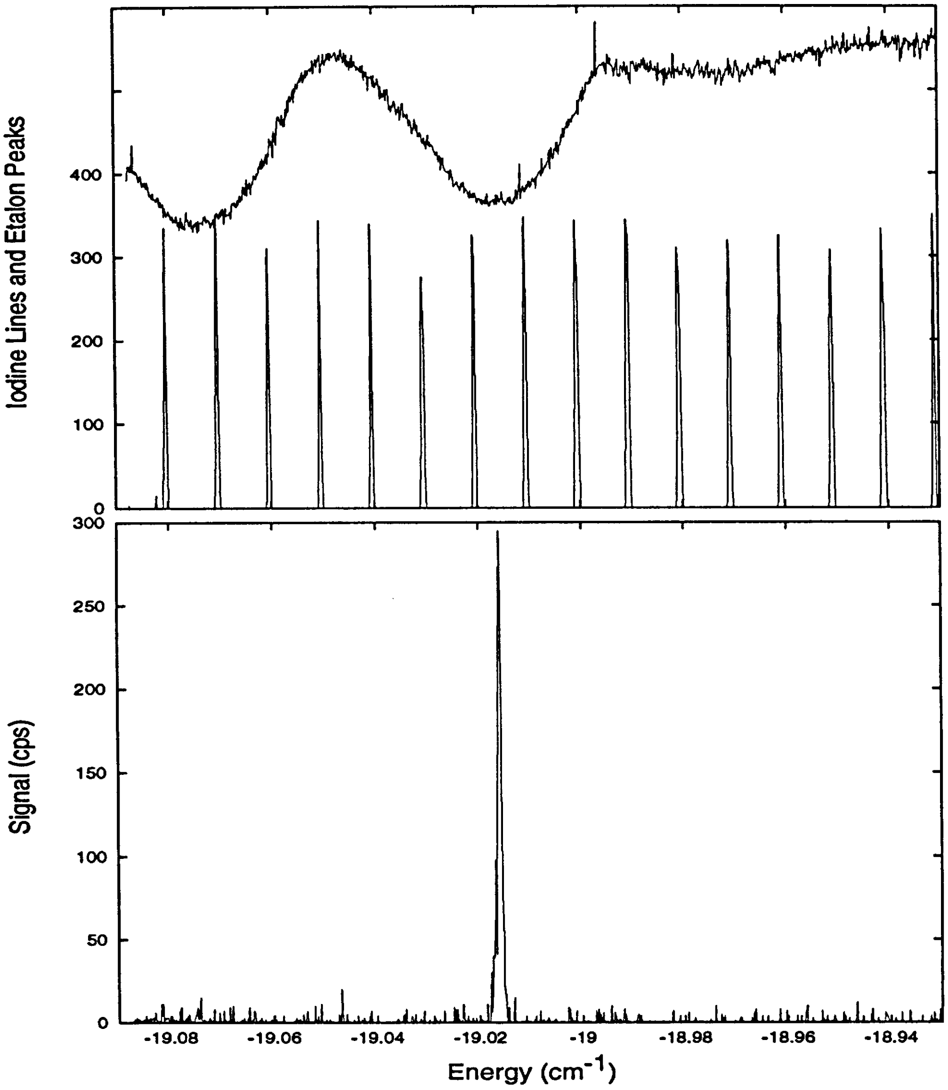

Figure 2-6: Experimental measurement of the stray electric field with lithium $n = 76$ manifold. The stray field is about 5 mV/cm. The iodine absorption lines and the transmission peaks of the 300 MHz etalon are shown above.

is proportional to the magnitude of the stray electric field [Kas88],

$$\Delta\nu_S \approx \frac{1.28 \times 10^{-4}\mathrm{cm}^{-1}}{\mathrm{V\,cm}} n^2 F. \tag{2.4}$$

Figure 2-6 shows the result of such a measurement for $n = 76$. The effect of the stray electric field on this particular day is hardly discernible compared to its experimental linewidth. The field is about 5 mV/cm. However, the field does not remain constant. It builds up as the atomic beam passes through. Smaller atomic beam flux helps somewhat (i.e. running the oven at a lower temperature), but the stray electric field strength may reach as high as 50 mV/cm. When the field plates are installed, their surfaces are only 0.325″ away from the laser-atom intersection point, and the stray electric field can increase to about 100 mV/cm.

2.5 Detection of Rydberg Atoms

The Rydberg atoms are detected by ionizing them and collecting the ions with a charged particle detector, to be described in Sec. 2.5.2. For Rydberg atoms that are photoionized, the photo-ions are swept out of the interaction region and accelerated to the detector. For Rydberg states that are not photoionized, the atoms drift out of the interaction region and into a large electric field region, where they are field ionized.

2.5.1 Field Ionization

The process of electric field ionization has been reviewed by Gallagher [Gal94]. However, for lithium it is known that the threshold for ionization is given by a simple classical consideration [LKK78]. The potential due to the Coulomb and external electric field is

$$V(\rho, z) = -\frac{1}{(\rho^2 + z^2)^{1/2}} + Fz. \tag{2.5}$$

It has a local maximum at $z = -1/F^{1/2}$ and $V_{max} = -2F^{1/2}$. If the electron energy is greater than V_{max}, the electron can escape classically, a process that rapidly leads to ionization. This critical field can be found by equating the energy with V_{max},

$$F_c = \frac{1}{16} n^{-4}. \tag{2.6}$$

The n^{-4} dependence implies that the high n Rydberg states can ionize in a relatively small electric field. The magnetic field along z direction has no effect on the motion in the z direction.

The ionizing field in our system is created by the potential between the detector and the interaction region as described in the next section. Typically, the field strength is about 80 V/cm which, according to Eqn. 2.6, will ionize any Rydberg state higher than $n = 38$. However, we also detect Rydberg states lower than $n = 38$, in particular the $n = 21$ states that are used for field calibration (see Sec. 2.6.1). We believe this latter detection is due to collisional ionization. The idea here is that Rydberg atoms have large radii ($\approx n^2$) and thus the cross sections are rather large. This poses the possibility that not all Rydberg atoms excited are detected. Indeed we actually detect more Rydberg states at $n = 76$ than $n = 21$. Fortunately, the oscillator strength for 21P is rather strong, and we only do spectroscopy on $n = 21$ for field calibration. Consequently, we are only concerned with location of the peak, not the height of the peak.

2.5.2 The Detector

Detecting Rydberg signals in a strong magnetic field is a formidable task. Field ionization requires a high gain charged particle detector that is relatively insensitive to magnetic fields. The conventional charged particle detectors, such as dynode electron multipliers or channeltrons, rely on cascading charge multiplication, in which electrons bounce from surface to surface, creating a cascade of secondary electrons. This process, however, is seriously impaired by a magnetic field. For example, the diameter of a typical channeltron is about 1 mm. The cyclotron radius of a 2 keV electron at 1 T is about 150 μm. The electrons tightly spiral about the magnetic field lines, and this action inhibits the charge multiplication process. In a channeltron, we have observed that the gain drops quickly to zero at only few hundred gauss.

Early Efforts

All detectors that are immune to magnetic field share one serious drawback: They require very high energy thresholds for detection. A surface barrier diode has a threshold energy of 20 keV for electrons and even higher for ions. High gain scintillators like NaI require at least 100 keV threshold energy. Achieving this energy requires either the detector or the interaction region to be floated to least 20 kV. Our predecessors used a surface barrier diode. They floated the interaction region to 20 kV and detected electrons. However, high voltage breakdown was a constant problem.

We spent a great deal of time developing a more efficient detection scheme. Initially, we tried a scintillator that has a relatively low threshold energy, about 12 keV. It consists of a thin-film of a strontium alloy on a sapphire substrate, made by Quantex. While not affected by high magnetic field, it exhibited a long afterglow after a strong signal. That is, it kept scintillating (even in the absence of charged particles) for several seconds. Attenuating the signals to avoid this afterglow resulted in the

Number of channel plates	3
Maximum bias per plate	1000 V
Channel diameter	12 μm
Gain	10^8
Pulse height at full gain	50 mV
Diameter of the active area	2 cm

Table 2.4: Specifications of the microchannel plate (MCP).

loss of small signals. We also found that the quantum efficiency was much lower than specified. Consequently, we could only detect a tiny fraction of the excited Rydberg atoms.

Present Detector

We finally chose to detect ions using a microchannel plate assembly (MCP) made by Galileo Electro-Optics Corporation. The charge multiplication process is similar to that of a channeltron, but each channel of a MCP has only a 12 μm diameter, which is significantly smaller than the cyclotron radius mentioned above. We expect the multiplication process to be relatively unaffected by a moderate magnetic field. The parameters of the MCP are given in Table 2.4.

We determine the gain by measuring the average output pulse height at different magnetic fields. The pulses from the anode are enhanced by an MIT Model F-100T amp-discriminator [2], whose TTL output goes to counters. We set the discriminator level just slightly above the noise level of the discriminator, which has been carefully calibrated with a Wavetek pulse generator to be about 0.5 mV. That is, only pulses with pulse heights of at least 0.5 mV will be registered. Figure 2-7 displays the gain of the MCP as a function of the magnetic field. As can be seen, the gain drops by roughly one order of magnitude in a 0.6 T magnetic field. The average height of the

---

[2] Care should be taken here since the magnetic field induces a slight noise in the amplifier

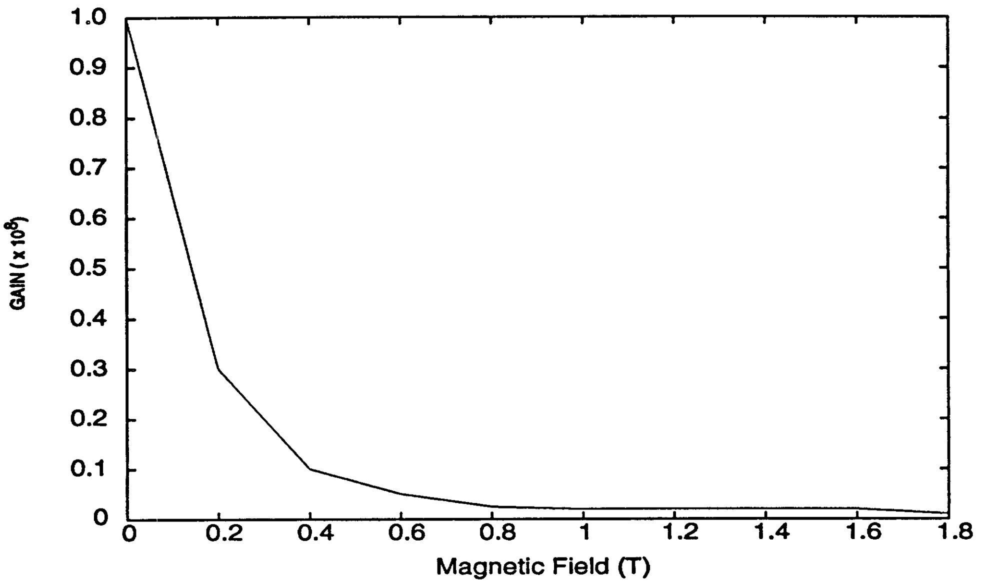

Figure 2-7: The gain of the MCP in a magnetic field.

corresponding output pulses is about 2 mV, which fortunately is well above the noise level. Consequently, the drop in gain does not affect the signal counts greatly.

Figure 2-3 shows that to ensure a field of 0.6 T or less at the MCP for a 6 T field at the center of the magnet, the MCP must be placed at least 30 cm away from the center of the magnet. To convince ourselves that the MCP can actually collect all the ions at 30 cm, we did a numerical computation of the trajectory of a lithium ion travelling in the fringing field of the magnet and the guiding electric field. The magnetic field is assumed to be about 6 T at the center of the magnet. The spatial field configuration is found as described in Sec. 2.3.2. The electric field is assumed to be 80 V/cm (the actual electric field in our system) constant in the z direction. The initial conditions are taken to be those of a most divergent particle, namely $\rho =$ 0.5 mm, $v_\rho = 2.0 \times 10^3$ cm/sec, $z = 0$, and $v_z = 2.0 \times 10^5$ cm/sec. Physically these parameters correspond to a particle at 0.5 mm off the axis with a divergence angle of 0.02 radian. Figure 2-8 shows the result. At small z, the magnetic field confines

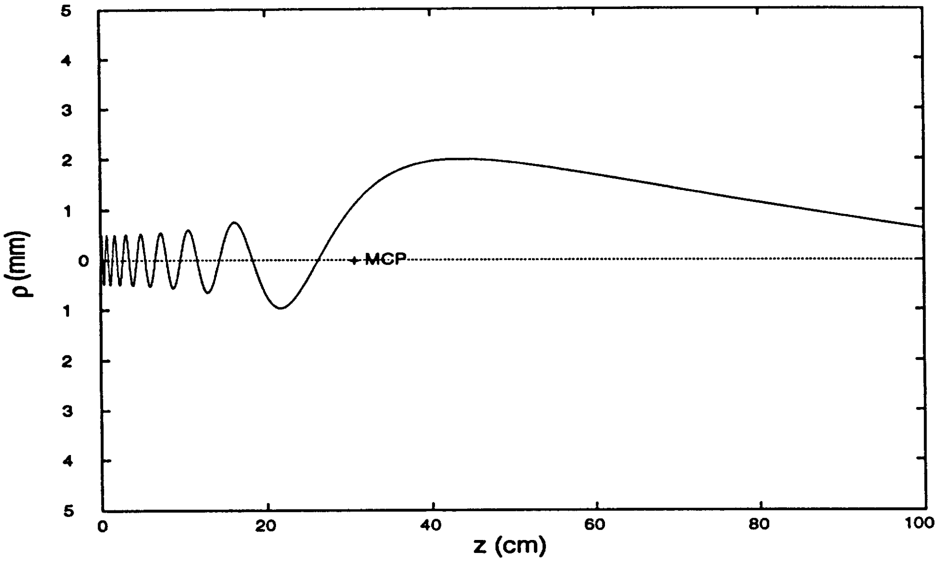

Figure 2-8: The trajectory of a lithium ion in the fringing field of the magnet from the interaction region to the MCP; the horizontal axis is z and vertical axis is ρ; the cross marks the location of the MCP; and the field parameters and initial conditions are discussed in the text.

the ion in the ρ direction. The ion spirals around the field line and at the same time accelerates in the z direction. Farther from the center of the magnet at z = 50 cm, the ion begins to lose its confinement in the ρ direction. At still larger z, it completely loses its confinement in the ρ direction and accelerates in the z direction. The calculation clearly shows that at z = 30 cm, the ion has only diverged about 2 mm in the ρ direction. The active diameter of the MCP is about 2 cm (see Table 2.4). As a result, the MCP located at 30 cm easily intercepts all the oncoming ions.

We detect lithium ions rather than electrons because the background noise is lower. Also, ions can be conveniently collected on a negative biased cathode, allowing the output anode to be at ground potential. To detect electrons, the input plate must be biased at a reasonably high voltage to ionize the Rydberg atoms and to accelerate the resulting electrons. The multiplier output needs to be at an even higher voltage in order to accelerate the secondary electrons. As a result, the anode must be floated at 5 kV. The signals must then be coupled out capacitively. Figure 2-9 shows such a biasing circuit.

Though the MCP can be biased up to -3 kV ($V_{input} - V_{output}$), we typically use -2.4 kV. At larger voltage, the signal counts do not increase appreciably. This is important because the lifetime of a MCP is seriously reduced with increasing bias. The bias voltages come from Bertan Model 315 high voltage power supplies. The detector assembly is mounted on a conflat flange on the axis of the atomic beam. To avoid noise induced by the atomic beam and possible destruction of the detector, a thin carbon foil, made by the Arizona Carbon Foil, Inc. and mounted on a copper mesh, is used to stop the atomic beam. We apply a -2.3 kV bias on the carbon foil to create the electric field needed to ionize the Rydberg atoms and provide the ions with enough energy to penetrate the carbon foil and proceed to the MCP. We notice appreciable decrease in ion counts if the thickness of the carbon foil is more than 5 μm. To shield the laser-atom interaction point from such an electric field and yet not block the atomic beam, the atoms leave the interaction region through a $0.1''$ diameter hole in the middle of a $3/8''$ thick disk. The external field does not penetrate very significantly because of the small diameter to length ratio. The carbon foil assembly is mounted on an aluminum disk, located about 1.5 cm in front of the MCP.

We found that the magnetic field can induce significant noise on the MCP. The magnitude increases rapidly as a function of magnetic field strength. Enclosing the MCP and the carbon foil in an insulating tube eliminates the problem. The only direct path to the MCP is through the carbon foil. As a result, we suspect the noise is induced by stray charged particles. The whole detector arrangement is shown schematically in Fig. 2-10.

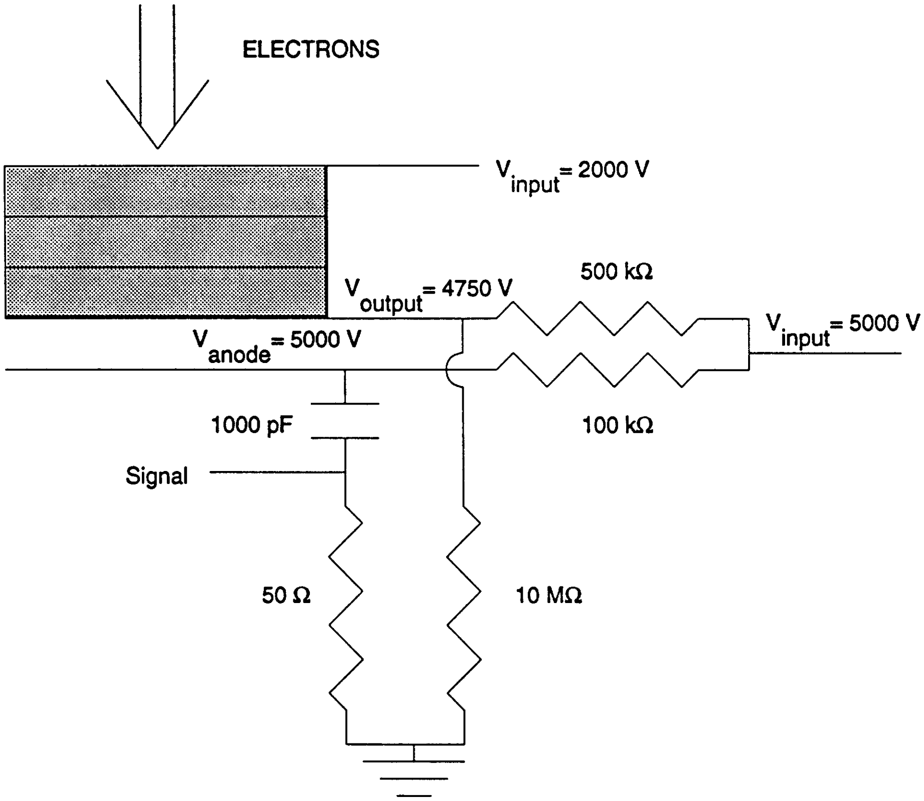

Figure 2-9: The biasing circuit for electron detection. The shaded regions represent the three channel plates of the MCP.

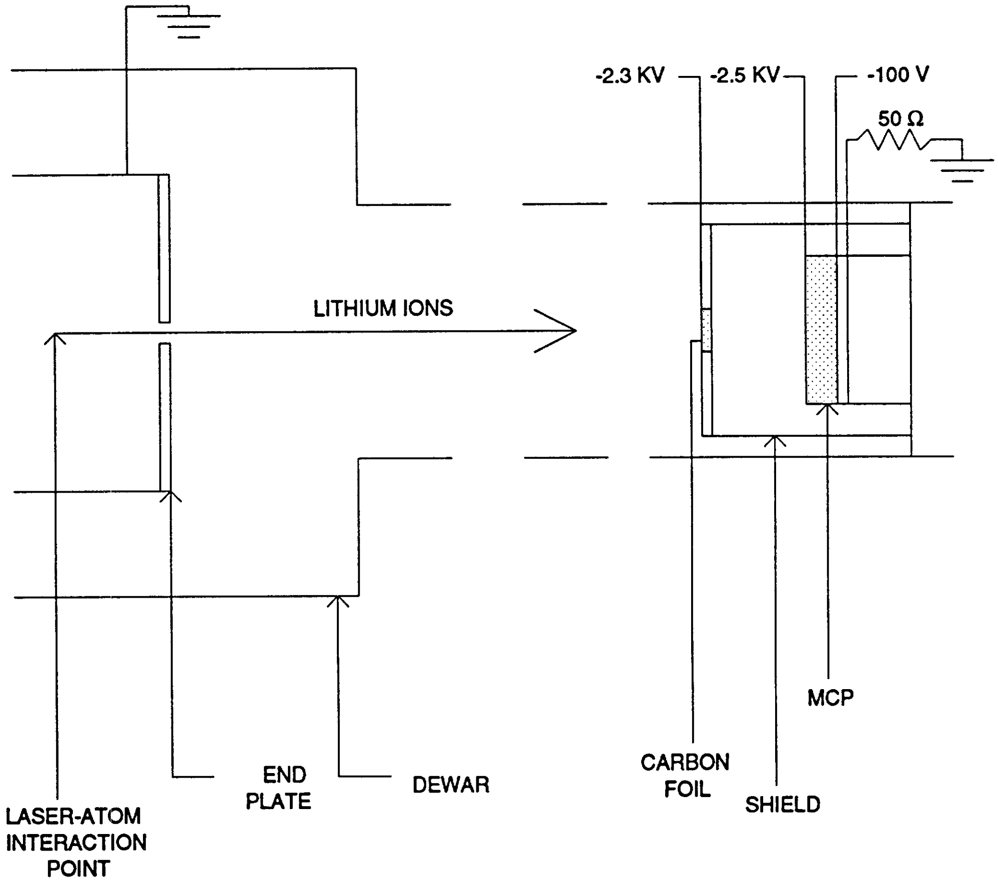

Figure 2-10: Schematic of the detector arrangement.

2.6 High-Resolution Spectroscopy

This concluding section describes the calibration procedures for the electric and magnetic fields using lithium atoms (Sec. 2.6.1) and the procedures for conducting conventional high-resolution spectroscopy (Sec. 2.6.2) and scaled-energy spectroscopy (Sec. 2.6.3).

2.6.1 Field Calibration

Precision spectroscopy of atoms in fields requires accurate determination of the fields. As always, the atoms themselves are the best calibrators. Our approach is to carry out spectroscopy on low-level Rydberg states where quantum computations are uncomplicated and reliable. A careful comparison between computations and experimental measurements yields accurate values for the applied fields.

Magnetic Field

The method for determining the magnetic field was developed by our predecessors. We give only a brief overview here. Details can be found in [Kas88]. The field is calibrated by measuring the energy difference between the lowest lying states of $m = +1$ and $m = -1$ of the $n = 21$ manifold. From Eqn. 1.1, this energy difference,

$$\Delta E_B = B \approx \frac{1\,\mathrm{cm}^{-1}}{\mathrm{T}} B, \tag{2.7}$$

is entirely due to the paramagnetic interaction. (The diamagnetic term is the same for both m states.) Figure 2-11 shows the quantum computations of the energy levels of odd-parity lithium $n = 21$ in a magnetic field.

To measure the magnetic field, the laser polarization is oriented perpendicular to the field so that only $m = +1$ and $m = -1$ states are excited. Figure 2-12 shows

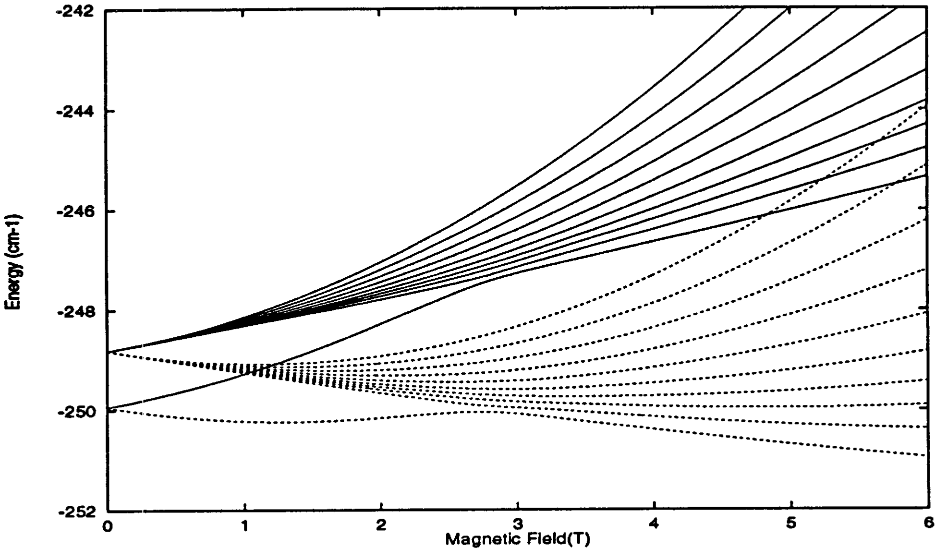

Figure 2-11: Quantum computations of the energy levels of odd-parity lithium at $n = 21$ in a magnetic field. The solid lines are the $m = +1$ states, and the dash lines are the $m = -1$ states.

the spectrum observed in such a measurement. (The state in the middle is $m = 0$, due to imperfect polarization.) Comparison of the energy separation between the two peaks with the quantum computation in Fig. 2-11 gives the desired field value. In this case the magnetic field was determined to be 0.542 T. In larger fields, the states of $m = +1$ and $m = -1$ move so far apart that the laser must be mode-hopped to the appropriate places. A separate scan is required for each state. The uncertainty in the field measured in this way is about ±20 gauss, primarily limited by the determination of the location of the iodine absorption peak. The fractional uncertainty $\Delta B/B$ gets smaller as the field increases. However, we usually ramp the magnet between 0.5 T and 3 T as described in Sec. 2.6.3, corresponding to $\Delta B/B = 4 \times 10^{-3}$ and $\Delta B/B = 6.7 \times 10^{-4}$. By measuring the field for a few different current values, we can determine the field to current ratio to roughly 1 in 10^3. Similarly by measuring the Zeeman splittings for the beginning and the end of a small field interval, the Hall

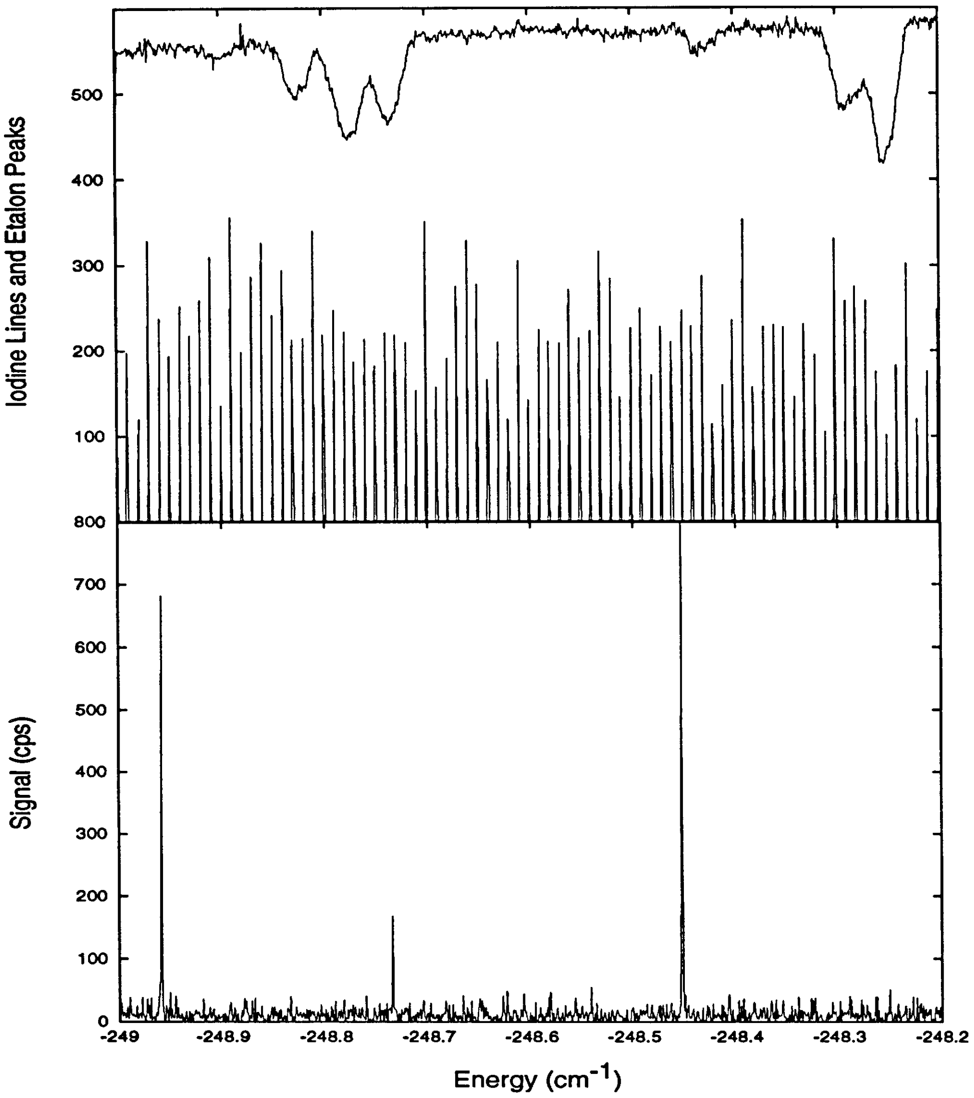

Figure 2-12: Experimental measurement of the magnetic field with odd-parity lithium at $n = 21$. The one on the left is $m = -1$, the one on the right is $m = +1$, and the one in the middle is $m = 0$. The iodine absorption lines and the transmission peaks of the 300 MHz etalon are also shown.

probe can be calibrated (see Sec. 2.3.2).

Parallel Electric Field

We use the lowest lying states of odd and even parities of $m = -1$ at $n = 31$ to measure the electric field parallel to the magnetic field. The $m = 0$ states cannot be used here due to the huge quantum defect of the S state (≈ 0.4). Figure 2-13 shows the quantum computation of the energy levels of $m = -1$ lithium states of both parities as a function of the magnetic field in the absence of an electric field. As can be seen, the lowest lying states of odd and even parities are nearly degenerate. An electric field parallel to the magnetic field mixes these two states and results in a linear Stark effect. Figure 2-14 diplays this splitting in a 3 T magnetic field. The bottom figure shows that the energy difference between these two states,

$$\Delta E_F \approx \frac{0.1\,\mathrm{cm}^{-1}}{\mathrm{V\,cm}} F, \tag{2.8}$$

can provide a sensitive probe of the parallel electric field. Experimentally, as in the case of measuring the magnetic field, we polarize the laser beam perpendicular to the magnetic field, thus exciting only $m = \pm 1$ states.

By using the measurements for several applied voltages, we can obtain a field to voltage ratio for a particular set of field plates. The result of one such calibration is shown in Fig. 2-15. The diamonds are the measured points and the solid line is a linear fit. The slope is the field to voltage ratio and the y-intercept is a stray electric field in the system. For this particular set of field plates, the ratio is 1.782(2) V/cm/V. The stray field is about 0.09 V/cm. The electric field thus determined has an uncertainty of 1 in 10^3.

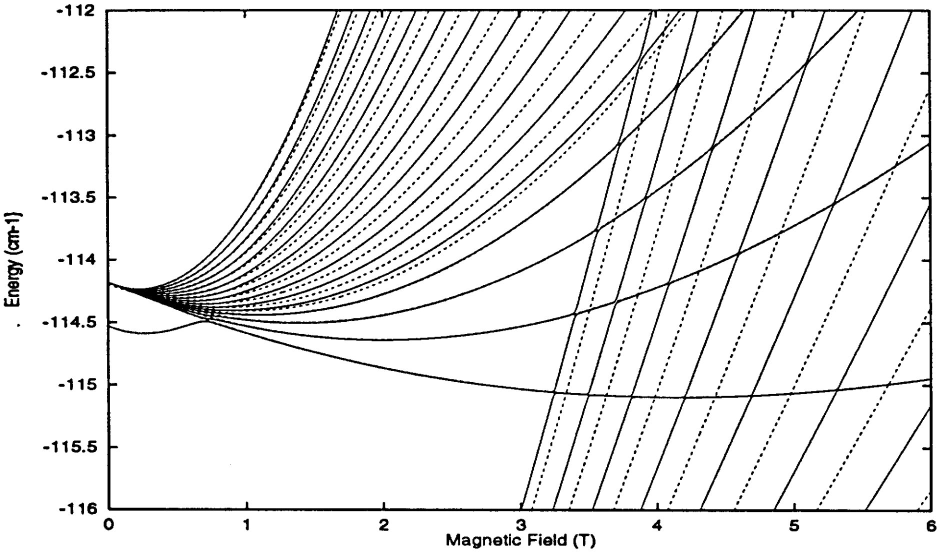

Figure 2-13: Quantum computation of the energy levels of $m = -1$ lithium at $n = 31$ in a magnetic field in the absence of an electric field. The solid lines represent odd-parity states and the dashed lines represent even-parity states.

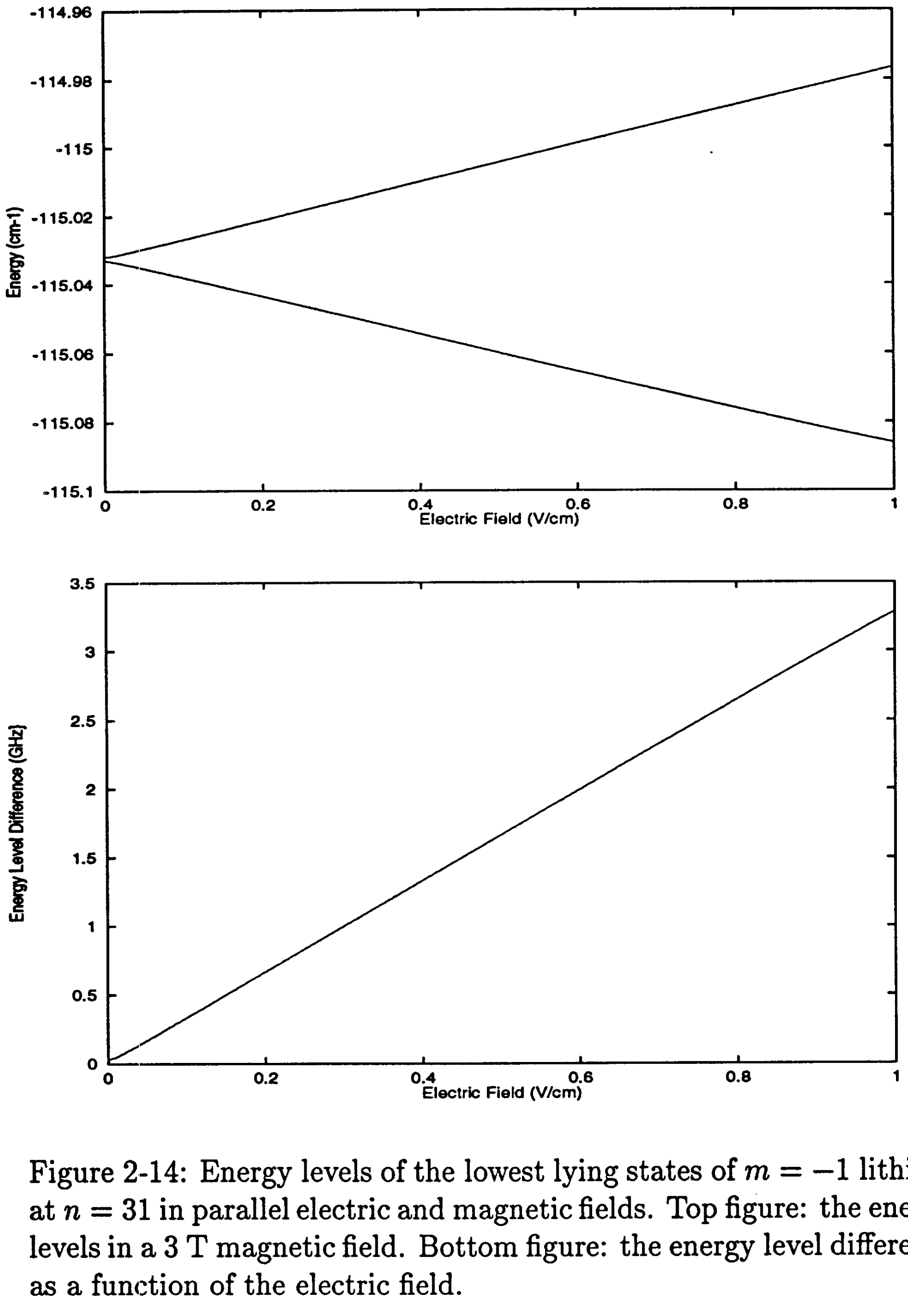

Figure 2-14: Energy levels of the lowest lying states of $m = -1$ lithium at $n = 31$ in parallel electric and magnetic fields. Top figure: the energy levels in a 3 T magnetic field. Bottom figure: the energy level difference as a function of the electric field.

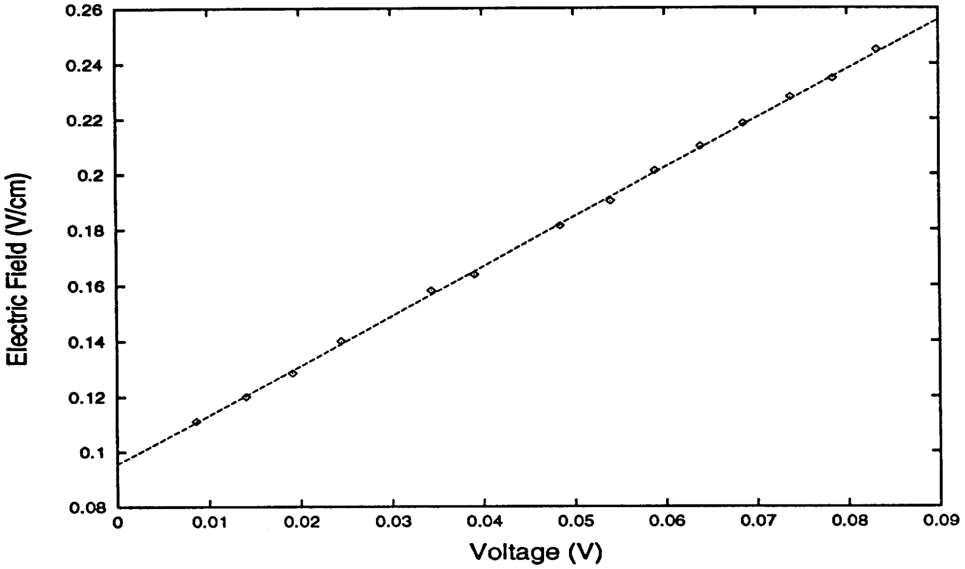

Figure 2-15: Electric field to voltage ratio calibration: The diamonds are the measured points, and the solid line is a linear fit.

2.6.2 Conventional Lithium Spectrum

One goal of the experiment involves determining the energies of Rydberg levels in strong electric and magnetic fields. As already described, we excite the atoms by locking the red laser to the 2S → 3S two-photon transition and measuring the energy by scanning the yellow laser and detecting either the field or photo ionization signal. To take into account the variation in the power of the lasers, the computer records the signals of the 2P → 2S fluorescence and the power of the yellow laser. To monitor the frequency, the transmission signals of the iodine cell and the 300 MHz spectrum analyzer are measured. The Rydberg and fluorescent signals are read by counters while the rest are recorded by A/D's.

To generate a conventional energy spectrum of lithium in parallel fields, we scan the yellow laser at fixed electric and magnetic fields. The yellow laser can be scanned continuously for about 30 GHz. Then we must manually mode-hop the laser by changing the thick etalon in its ring cavity. Consequently we find it more practical to scan the laser in the same frequency range for a few different field values and then mode-hop the laser to the next frequency range and repeat the process. The scans corresponding to each set of field values are later overlapped using iodine absorptions which are common to the data of the two consecutive scans. Obviously, carrying out high-resolution spectroscopy (0.001 cm^{-1}) over a wide frequency spectrum (60 cm^{-1}) is a very time consuming process, over 10 hours. The magnetic field at the interaction region is determined from the Hall probe voltage and the magnet current as described in Sec. 2.6.1. We usually switch the magnet to the persistence mode at the desired field. In this mode and at 2 T, the field of the magnet is stable to at least 1 in 10^3 over the course of one day. We believe the magnet to be much more stable than this, but we are limited by the uncertainty of the magnetic field determination as described in Sec. 2.6.1. In any case, the value of the magnetic field does not need to be measured very often. Before each laser scan, we apply a voltage to the field plates with a D/A drive. At the beginning and the end of each scan (about 1 cm^{-1}), a GPIB interface reads this voltage from the Keithley 197 DMM. The electric field at the interaction region is obtained from the field to voltage ratio as described in Sec. 2.6.1.

2.6.3 Scaled-Energy Spectroscopy

To perform scaled-energy spectroscopy, we vary the magnetic field, the electric field, and the yellow laser frequency such that the classical parameters $\epsilon = EB^{-2/3}$ and $f = FB^{-4/3}$ remain constant. Ideally we would scan the laser and vary the magnetic field and the electric field simultaneously. This procedure relies on our ability to quickly set the field values. The electric field can be set almost instantaneously by applying a voltage to a pair of field plates. However, the magnet has a huge inductance (112 H), and hence changing the current requires an enormous voltage drop across the magnet. The maximum slew rate with our magnet power supply is only 0.045 A/sec, corresponding to 0.0051 T/sec. As a result, in practice we ramp the magnet and vary the electric field and the yellow laser frequency while keeping ϵ and f constant.

Procedure

The red laser remains locked to the 2S → 3S two-photon transition. We measure the magnetic field by measuring the voltage across the calibrated shunt in series with the magnet as described in Sec. 2.3.2. The value of the electric field needed for a given f is obtained from

$$F = fB^{4/3}. \tag{2.9}$$

This desired electric field is conveniently set by applying a voltage to a pair of field plates using the known field to voltage ratio described in Sec. 2.6.1.

The energy of the electron (or the yellow laser frequency plus the binding energy of the 3S state) for a give ϵ is determined according to

$$E = \epsilon B^{2/3}. \tag{2.10}$$

Unlike setting the electric field, it is tricky to set the laser frequency. As mentioned, the yellow laser can be scanned continuously for only 30 GHz maximum. To set the laser frequency, the laser must first be manually mode-hopped to the correct frequency range. Next, the frequency of the laser at each point in the scan is determined by a quick scan of the laser over the desired frequency interval while recording the iodine absorption and etalon transmission. These data are then used to compute the laser frequency at each point in the scan. Each laser scan covers about 25 GHz with 1024 data points. Each point corresponds to a voltage from the D/A of the computer. As the magnet is ramped , the A/D of the computer records the shunt voltage. For a given ϵ, the correct value of the output voltage of the D/A of the computer (corresponding to the desired laser frequency) is calculated according to Eqn. 2.10. This voltage is then sent to the external scan input of the yellow laser. When a laser scan completes, we manually mode-hop the laser in a manner such that there is some overlap between two consecutive scans. This means the magnet has to be ramped back a little every time we mode-hop the laser. For each set of scaled parameters f and ϵ, the magnet is typically ramped between 0.5 T and 3 T. Depending on the value of ϵ, this can be a very time consuming process. In one limit $\epsilon = 0$, the laser is left at one frequency while we ramp the magnet. For larger absolute values of ϵ, for example $\epsilon = -0.4$, we need to mode-hop about 40 times for the same magnetic field range. We usually spend several hours producing scaled-energy spectrum for just *one* set of f and ϵ. Coherent manufactures a ring dye laser, called Autoscan, that would produce a continuous scan over 100 cm^{-1} automatically. Such a ring laser will greatly speed up our data acquisition process.

Error Analysis

For each scaled-energy spectrum obtained, the fractional error in ϵ is

$$\begin{aligned}\frac{\Delta\epsilon}{\epsilon} &= \sqrt{(\frac{\Delta E}{E})^2 + (\frac{2}{3}\frac{\Delta B}{B})^2} \\ &= \sqrt{(10^{-7})^2 + (\frac{2}{3}10^{-3})^2} \\ &= 6 \times 10^{-4},\end{aligned} \tag{2.11}$$

and the fractional error in f is

$$\begin{aligned}\frac{\Delta f}{f} &= \sqrt{(\frac{\Delta F}{F})^2 + (\frac{4}{3}\frac{\Delta B}{B})^2} \\ &= \sqrt{(10^{-3})^2 + (\frac{4}{3}10^{-3})^2} \\ &= 1.7 \times 10^{-3}.\end{aligned} \tag{2.12}$$

The fractional error in ϵ is limited by the uncertainty in the magnetic field determination, and the fractional error in f is limited by the uncertainties in both the electric and the magnetic field determinations.

Figures 2-16 and 2-17 show two scaled-energy spectra and their Fourier transforms, the recurrence spectra of diamagnetic lithium ($f = 0$) at $\epsilon = -0.2$ and $\epsilon = -0.1$, respectively. In the scaled-energy spectroscopy, the scan is taken as a function of $w = B^{-1/3}$, and its Fourier transform is in the scaled action domain (see Sec. 5.3.2 for more detail).

Limitations

We conclude this chapter by considering the intrinsic limitations of a recurrence spectrum. In particular, we are interested in the resolution of peaks associated with individual orbits and the largest-action orbit that is observable.

The width of each peak in the recurrence spectrum is given by

$$\delta\tilde{S} \approx \frac{1}{\Delta w}, \tag{2.13}$$

where Δw is the range of $w = B^{-1/3}$ over which the spectrum is taken. We typically scan the magnet from 0.5 T to 3 T, corresponding to $\Delta w \approx 35.46$ in atomic units. This implies that the intrinsic width of each peak is $\delta\tilde{S} = 0.03$.

Finally, the orbit with the maximum action observable experimentally is given by

$$\tilde{S}_{max} = \frac{\pi}{\delta w}, \tag{2.14}$$

where δw is the step size taken in w during a scan. However, in the actual experiment our step size is smaller than the uncertainty in w and is limited by uncertainty in the magnetic field determination. Therefore the uncertainty in the magnetic field

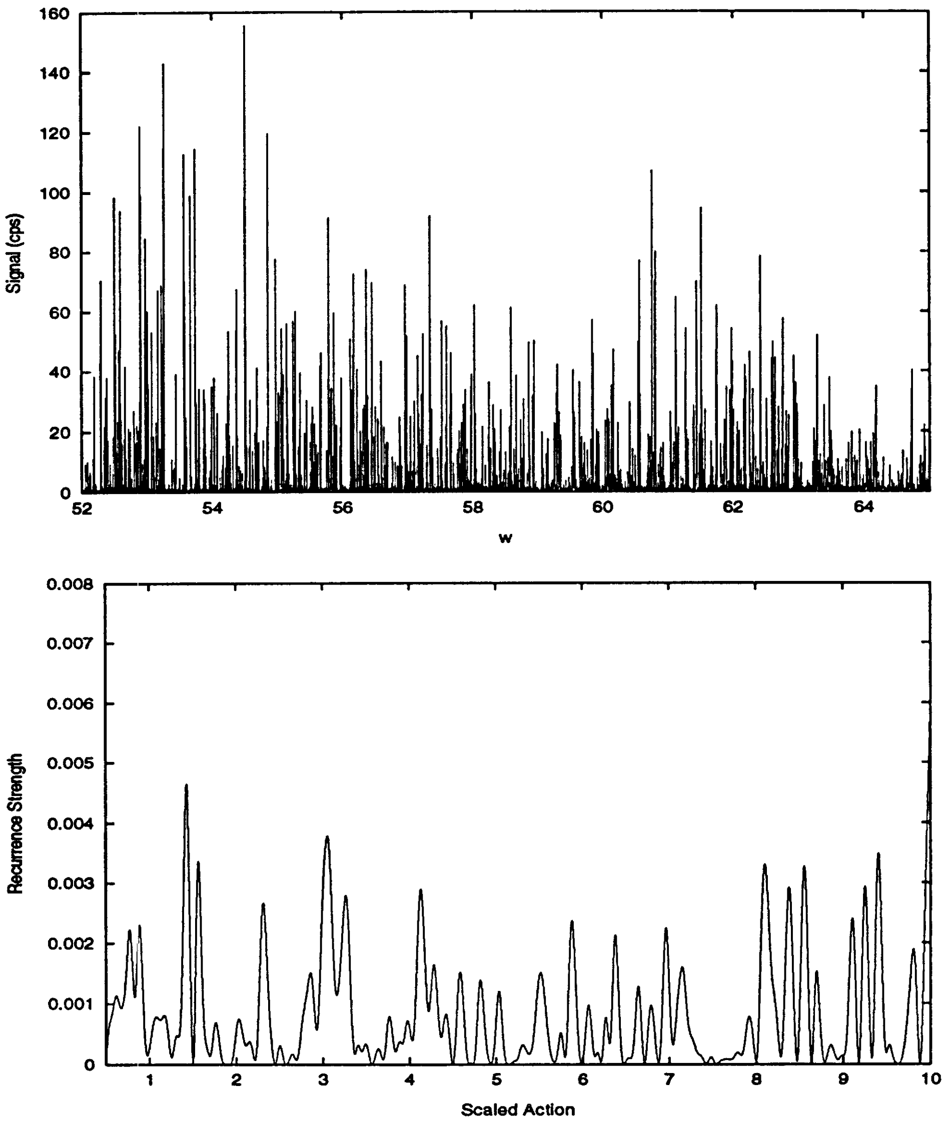

Figure 2-16: Diamagnetic lithium at $\epsilon = -0.2$. Top: the scaled-energy spectrum, $w = B^{-1/3}$. Bottom: the recurrence spectrum.

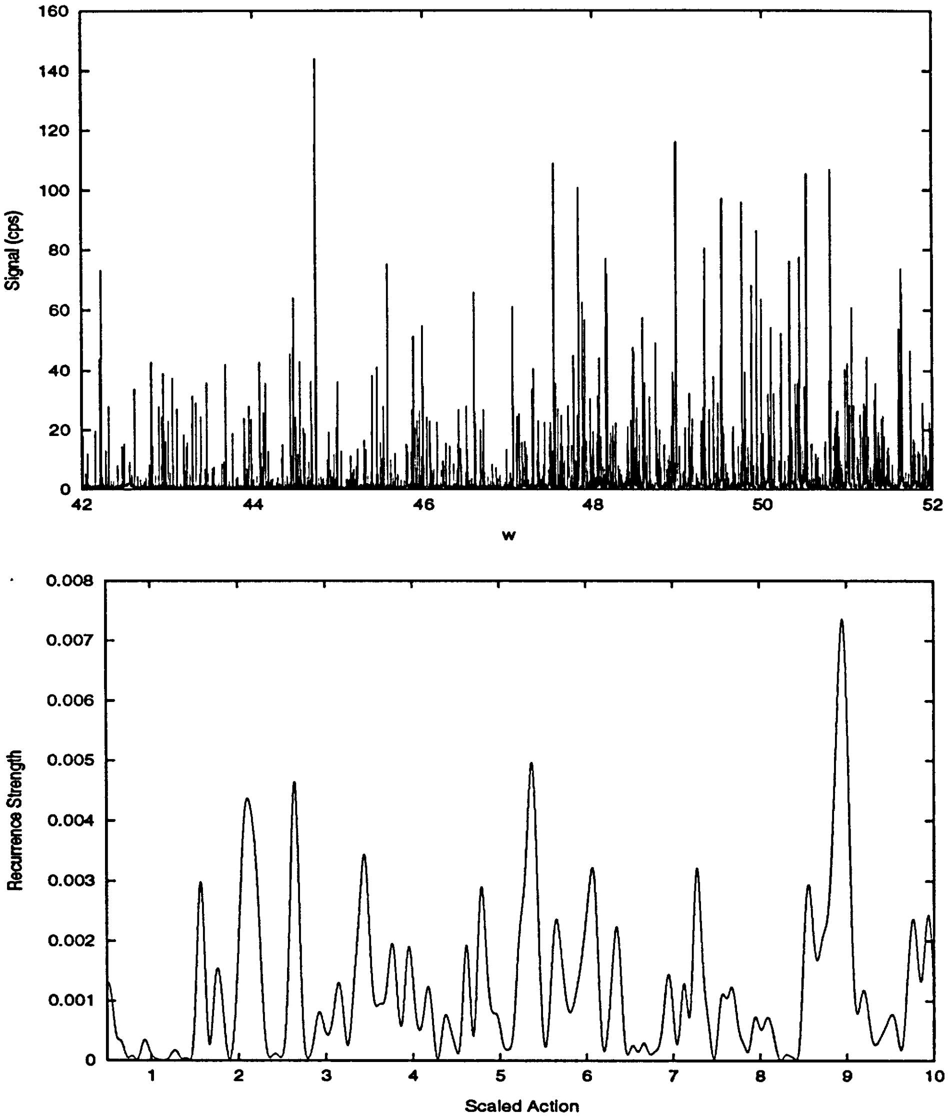

Figure 2-17: Diamagnetic lithium at $\epsilon = -0.1$. Top: the scaled-energy spectrum, $w = B^{-1/3}$. Bottom: the recurrence spectrum.

determination actually limits the accuracy of the large action orbits. Our fractional error in the field determination is about 10^{-3}, which corresponds to $\delta w = 0.04$ at $w \approx 60$. Substituting this value into Eqn. 2.14 yields $\tilde{S}_{max} \approx 85$.

Chapter 3

Stepwise Excitation Scheme

Notwithstanding the advantages of the excitation scheme in the previous chapter, the 2S → 3S two-photon transition is very inefficient. The red laser has to be driven at the limit of its power capability (≈ 1 W), and the beam has to be focused to a small waist size ($\approx 50\ \mu$m). Due to the large detuning from the 2P intermediate state, the intensity is still about one order of magnitude below the saturation intensity.

In this chapter, we describe a stepwise excitation scheme that was developed over the last six months. Figure 3-1 shows the excitation scheme. As we will show, the first two transitions, 2S → 2P and 2P → 3S, are easy to drive and can be easily saturated. The excitation source consists of a tunable diode laser, and two tunable dye lasers pumped by one large frame argon ion laser. Among other advantages, this eliminates the use of the krypton ion laser, whose tube needs to be replaced every four years or so at a cost of \$35,000. However, because a real intermediate state is populated, the structure of that state must be analyzed in detail. Furthermore, the shift in its energy levels in the applied magnetic field is a potential complication. In this alternative method, the first two transitions are monitored by their respective fluorescent signals, and the Rydberg signals continue to be detected through field ionization. Experimentally, we discuss only the relevant features, the lasers (Sec. 3.4.1),

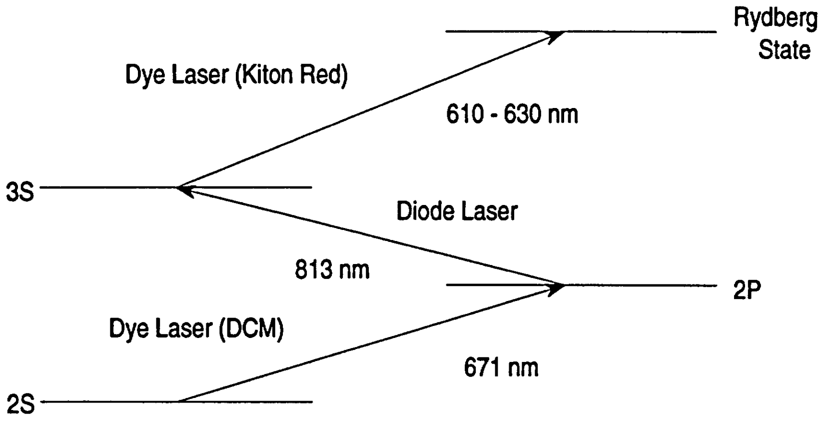

Figure 3-1: New excitation scheme. Lithium atoms are excited from 2S to 2P by a dye laser and 2P to 3S by a diode laser. Finally, another dye laser drives the transition to Rydberg states. (Dye names are enclosed in the parentheses.)

optics (Sec. 3.4.2), and the detection scheme (Sec. 3.4.3), since the rest of the apparatus (i.e. the atomic beam, the magnet, and the interaction region) remains the same. Again our multi-step excitation scheme allows the laser selection of the desired isotope. We excite ^{7}Li. The discussion in the entire chapter is limited to this isotope with the exception of Sec. 3.2.3.

3.1 Two-Photon Transition vs. Stepwise Excitation

The transition rate between two atomic levels is given by

$$R = \frac{\gamma(\omega_R/2)^2}{\delta^2 + \omega_R^2/2 + (\gamma/2)^2} \tag{3.1}$$

where γ is the spontaneous decay rate of the upper level, ω_R is the Rabi frequency, and δ is the detuning. For a resonant interaction ($\delta = 0$), the transition is saturated when $\omega_R \approx \gamma$.

We consider the two-photon transition 2S → 3S. The two-photon Rabi frequency ω_R is approximately [Pri92]

$$\omega_R = \frac{1}{2\hbar^2}\frac{e^2 < 2S|x|2P >< 2P|x|3S >}{2\pi\Delta}\frac{2I}{c\epsilon_0} \tag{3.2}$$

where $\Delta = 1302 \text{ cm}^{-1}$ is the detuning from the 2P intermediate state and I is the laser intensity. γ_{3S} is $3.42 \times 10^7 \text{ sec}^{-1}$, and the matrix elements are given in Table 3.1. The saturation intensity I_{sat} is calculated to be 98 kW/cm^2. The maximum intensity I we can achieve in the laboratory is about 1 W focused to 50 μm waist, I = 10 kW/cm^2. Thus we are one order of magnitude from saturating the transition.

We can estimate the total signal counts (number of 3S atoms per unit time):

$$S_{3S} = n_A(2r\pi w^2)\frac{\omega_R^2}{\gamma_{3S}} \tag{3.3}$$

where n_A is the atomic density, r is atomic beam radius, and w is the waist size of the laser beam. Table 2.1 gives $n_A = 4.2 \times 10^8$ atoms/cm^3 and r = 1 mm. ω_R can be found from Eqn. 3.2, (I = 10 kW/cm^2). Substituting these values along with w = 50 μm and $\gamma_{3S} = 3.42 \times 10^7 \text{ sec}^{-1}$ yields

$$S_{3S} = 5.3 \times 10^9 \,\text{sec}^{-1}. \tag{3.4}$$

Next we consider a stepwise excitation scheme 2S → 2P and 2P → 3S. The Rabi frequencies are

$$\omega_R(2S \to 2P) = \frac{e < 2S|x|2P >}{\hbar}\left(\frac{2I}{c\epsilon_0}\right)^{1/2} \tag{3.5}$$

and

$$\omega_R(2P \to 3S) = \frac{e < 2P|x|3S >}{\hbar}\left(\frac{2I}{c\epsilon_0}\right)^{1/2}. \tag{3.6}$$

γ_{2P} is 3.8×10^7 sec^{-1} and γ_{3S} is 3.42×10^7 sec^{-1}. The saturation intensities are 0.006 W/cm^2 and 0.009 W/cm^2 for 2S → 2P and 2P → 3S, respectively. Clearly both transitions can be easily saturated.

We can also estimate the total signal counts of the saturated 2S → 2P transition (number of 2P atoms per unit time):

$$S_{2P} = n_A(2r\pi w^2)\frac{\gamma_{2P}}{2}. \tag{3.7}$$

Substituting the values of $n_A = 4.2 \times 10^8$ atoms/cm^3, $r = 1$ mm, $\gamma_{2P} = 3.8 \times 10^7$ sec^{-1}, and $w = 0.5$ mm [1] gives

$$S_{2P} = 1.2 \times 10^{13}\,\mathrm{sec}^{-1}. \tag{3.8}$$

Similar calculations for the 2P → 3S transition yield

$$S_{3S} = 4.8 \times 10^{12}\,\mathrm{sec}^{-1}. \tag{3.9}$$

A comparison with Eqn. 3.4 reveals that the number of 3S atoms excited should increase by a factor of 900 with the stepwise excitation scheme.

The laser that drives the Rydberg transition remains the same. To compare number of Rydberg atoms excited by the two excitation schemes, we again focus this laser beam to a 0.05 mm waist size. The ratio of the Rydberg signal from the two excitation schemes is

$$\frac{S_R(\mathrm{stepwise})}{S_R(\mathrm{two-photon})} = \frac{S_{3S}(\mathrm{stepwise})\left(\frac{0.05\,\mathrm{mm}}{0.5\,\mathrm{mm}}\right)^2}{S_{3S}(\mathrm{two-photon})} \approx 9. \tag{3.10}$$

---

[1] We have plenty of laser power (≈ 200 mW), and thus there is no need to focus the beam to a small waist size.

Atomic State	Natural Linewidth (MHz)	Transition Wavelength (nm)	Matrix Element (atomic unit)	I_{sat} (W/cm^2)
2S	-	670.8	2.38	0.006
3S	5	812.7	1.74	0.009
3D	12	610.4	2.29	0.025
4S	2	497.2	0.46	0.011
4D	4	460.3	0.82	0.022

Table 3.1: Parameters for transitions between 2P and some of the low lying states of ^{7}Li.

Atomic State	Transition Wavelength (nm)	Detuning from 2P (cm^{-1})	I_{sat} (W/cm^2)
3S	735.1	-1302	98 × 10^3
3D	639.3	735	82 × 10^3
4S	571.2	2599	210 × 10^3
4D	546.1	3404	381 × 10^3

Table 3.2: Parameters for the two-photon transition between 2S and some of the low lying states of ^{7}Li.

Thus our Rydberg signal should improve by about one order of magnitude.

Table 3.1 and Table 3.2 list some useful parameters for other possible stepwise excitations and two-photon transitions, respectively. Appendix D discusses other possible excitation schemes for ^{7}Li.

3.2 Fine and Hyperfine Structure

Performing high resolution spectroscopy on lithium in strong external fields requires a detailed knowledge of the atomic structure in zero fields. As we will show, our experiment can clearly resolve the atomic fine and hyperfine splittings of the low lying states. Consequently, a detailed understanding of these interactions is essential. This section describes the fine structure of 2P, the hyperfine structure of 2S, $2P_{1/2}$, and 3S, and the isotope shift of $2P_{3/2}$. Our measurements are not intended to accomplish as high a precision as achieved by such spectroscopic techniques as atomic beam magnetic resonance. Rather, the measurements are made as a check on our spectroscopic method.

3.2.1 The Hamiltonians

The intrinsic magnetic moment of an electron interacts with the magnetic field due to the motion of the electron through the Coulomb field of the nucleus. The resulting spin-orbit interaction gives rise to the fine structure. The Hamiltonian is of the form

$$H_f = a(n,l)\vec{L}\cdot\vec{S}, \tag{3.11}$$

where n is the principal quantum number and l is the orbital quantum number. For the hydrogen atom, $a(n,l)$ can be obtained exactly from Dirac's equation [Sak84]. For alkali atoms, $a(n,l)$ can be determined approximately using quantum defect theory [Sob72]:

$$a(n,l) = \frac{\alpha^2}{2}\frac{(Z^*)^2}{(n^*)^3 l(l+1)(l+1/2)}, \tag{3.12}$$

where $Z^* \approx 0.94$ for ^{7}Li, n^* is the effective principal quantum number, α is the fine structure constant, and $l > 0$. (S states have no spin-orbit interactions.)

Hyperfine splittings result from the interaction of the nuclear multipole moments with the multipole moments associated with the angular momentum of the electron. Time reversal and parity invariance restrict the possible magnetic moments to dipole, octopole, etc. and the possible electric moments to quadrupole, etc. The hyperfine interaction is usually dominated by magnetic dipole and electric quadrupole interactions.

For the single valence electron of an alkali-metal atom, the hyperfine Hamiltonian is [Wei78]

$$H_{hf} = H_{mag} + H_Q = A(n,l,j)\vec{I}\cdot\vec{J} + B(n,l,j)(2\vec{I}\cdot\vec{J})(2\vec{I}\cdot\vec{J}+1) \tag{3.13}$$

where $I = 3/2$ for ^{7}Li and $I = 1$ for ^{6}Li. $A(n,l,j)$ describes the spin-spin magnetic interaction, which requires $I \geq 1/2$ and $J \geq 1/2$. $B(n,I,J)$ describes the nuclear quadrupole interaction, which requires $I \geq 1$ and $J \geq 1$.

Similar to the fine structure interaction, the hyperfine constants A and B can be approximated with semi-empirical formulas [Sob72]. For S states, A is given by the famous Fermi-Segré formula

$$A(nS_{1/2}) = \frac{8}{3}\frac{\alpha^2 g_I (Z^*)^3}{(n^*)^3}\frac{m_e}{m_n}[1 + |\frac{\partial\delta_s}{\partial n}|]cR, \tag{3.14}$$

where m_n is the mass of the nucleus and δ_s is the quantum defect for the S states. For $l \neq 0$, A is given by

$$A(n,l,j) = \frac{\alpha^2 g_I (Z^*)}{(n^*)^3(l+1/2)j(j+1)}\frac{m_e}{m_n}cR, \tag{3.15}$$

Finally, the parameter of the electric quadrupole interaction B can be approximated by

$$B(n,l,j) = \frac{3}{8}\frac{Q(Z^*)}{(n^*)^3(l+1)(l+1/2)lI(2I-1)j(j+1)}cR, \tag{3.16}$$

where $Q = -0.0366$ is the electric quadrupole moment for ^{7}Li. The expression for the magnetic dipole hyperfine interaction is very similar to the spin-orbit interaction. The ratio is

$$\frac{A}{a} \approx g_I\frac{m_e}{m_n}\frac{1}{Z^*}. \tag{3.17}$$

Typically, the hyperfine interaction is smaller than the fine structure interaction by

ΔE	Magnetic Dipole	Electric Quadrupole	Total
$2P_{3/2}(F=0)-2P_{3/2}(F=1)$	3.055(14)	0.228(30)	3.283
$2P_{3/2}(F=1)-2P_{3/2}(F=2)$	6.110(28)	-0.221(29)	5.889
$2P_{3/2}(F=3)-2P_{3/2}(F=2)$	3.165(42)	0.221(29)	9.387

Table 3.3: Hyperfine splittings of $2P_{3/2}$ of ^{7}Li. $A(2P_{3/2}) = -3.055(14)$ MHz and $B(2P_{3/2}) = -0.221(29)$ MHz [AIV77] and all values are in MHz.

the mass ratio of the nucleus to the electron.

3.2.2 Measured Values

The spin-orbit interaction keeps the total angular momentum of the electron $\vec{J} = \vec{L} + \vec{S}$ constant. The fine structure splitting for a single electron atom is

$$\Delta E_f(n,l) = a(n,l)(<\vec{L}\cdot\vec{S}>_{j=l+1/2} - <\vec{L}\cdot\vec{S}>_{j=l-1/2}) = a(n,l)(l+1/2). \tag{3.18}$$

Similarly, the spin-spin magnetic interaction allows the total angular momentum of the system $\vec{F} = \vec{I} + \vec{J}$ to remain constant. However, the hyperfine interaction splits the atomic states into more than two nondegenerate levels if $J \geq 1$. In particular, the $2P_{3/2}$ states are split into 4 nondegenerate levels. These hyperfine splittings have been measured previously and the results are shown in Table 3.3 [AIV77]. The splittings are below our experimental resolution of 25 MHz. However, as we will show, the hyperfine splittings of 2S, $2P_{1/2}$, and 3S are well resolved. These states have no electric quadrupole interaction. The hyperfine splitting simplifies to

$$\Delta E_{hf}(n,l) = A(n,l)(<\vec{I}\cdot\vec{J}>_{F=I+1/2} - <\vec{I}\cdot\vec{J}>_{F=I-1/2)}) = A(n,l)(I+1/2). \tag{3.19}$$

Both $\Delta E_f(n,l)$ and $\Delta E_{hf}(n,l)$ can be calculated by various methods [BJLS89], but for our purpose their spectroscopic values are more reliable. The goal of our

$a(n,l)$	Theory	Previous Measurement	Reference	Our Measurement
2P	6708.20(15)	6702.16(15)	[AIV77]	6703(3)

$A(n,l,j)$	Theory	Previous Measurement	Reference	Our Measurement
$2S_{1/2}$	402.47(5)	401.7520433(5)	[AIV77]	402(3)
$2P_{1/2}$	45.96(1)	45.914(25)	[AIV77]	46(3)
$3S_{1/2}$	93.24(2)	94.68(22)	[SIW+95]	92(3)

Table 3.4: Fine and hyperfine parameters of ^{7}Li. All values are in MHz.

measurement is not to set any unprecedentedly high precision, but to check our spectroscopic method.

Figure 3-2 shows the possible transitions between the fine and hyperfine states of 2S and 2P of ^{7}Li and ^{6}Li. As noted before, we do not resolve the hyperfine structure of $2P_{3/2}$. To measure the fine and hyperfine splittings, we scan one of the lasers around the principal transition 2S → 2P while monitoring the frequency of the laser with a high resolution calibrated Fabry-Perot etalon. The fluorescent signal is detected by a photomultiplier tube. Such a scan is shown in Fig. 3-3. Each peak corresponds to one of the transitions in Fig. 3-2. Figure 3-4 shows a blowup about the $2S \rightarrow 2P_{3/2}$ transition of ^{7}Li, and Figure 3-5 shows a blowup about the $2S \rightarrow 2P_{1/2}$ transition of ^{7}Li. All transitions are labelled according to Fig. 3-2.

According to Fig. 3-2, the frequency difference between transition (c) and the center of gravity of the transitions (a) and (b) gives the fine structure splitting $\Delta E_f(2P)$; the frequency difference between transitions (a) and (d) (or transitions (b) and (e)) gives the 2S hyperfine splitting $\Delta E_{hf}(2S)$; and the frequency difference between transitions (a) and (b) (or transitions (d) and (e)) gives the $2P_{1/2}$ hyperfine splitting $\Delta E_{hf}(2P)_{1/2}$. The results of all these measurements are summarized in Table 3.4 which also contains previous high precision measurements and the theoretical results. The agreement among the values is reasonable.

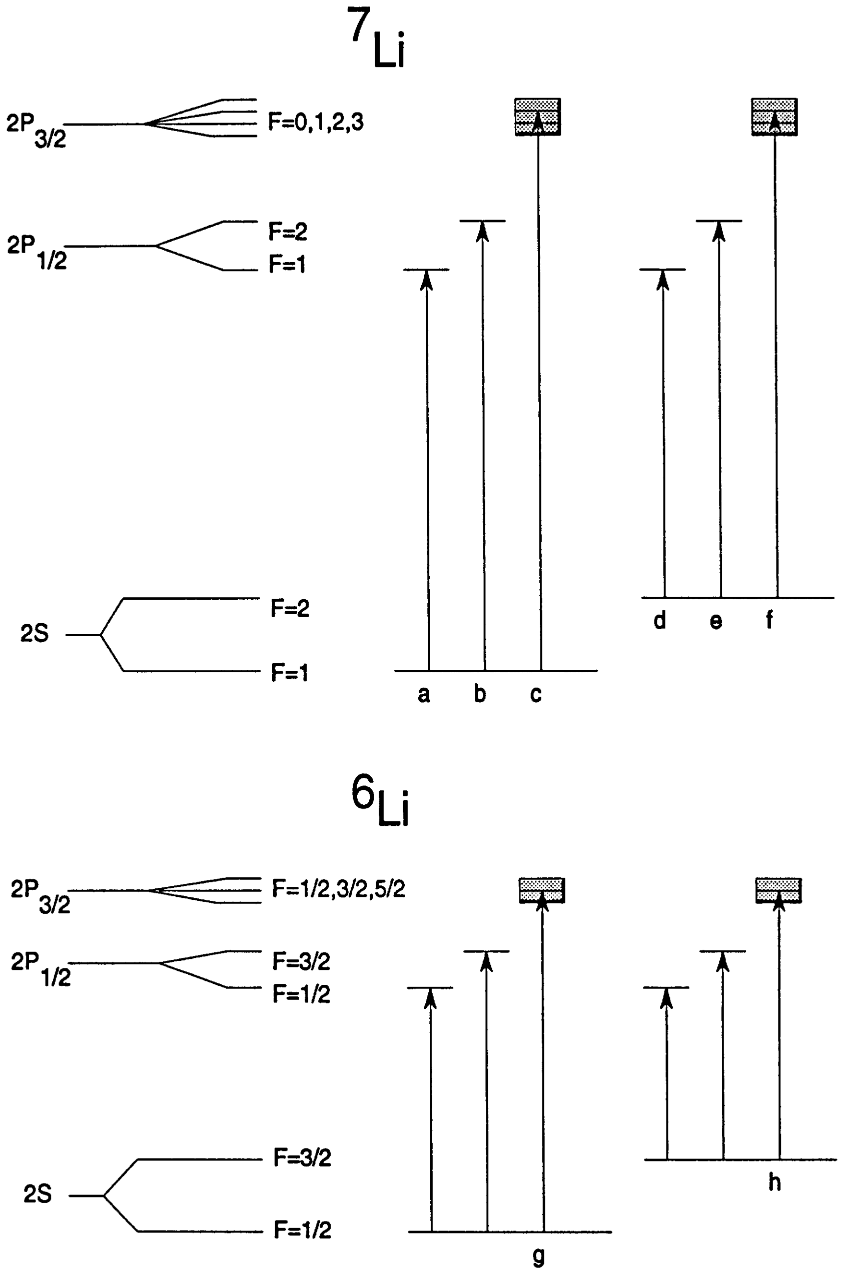

Figure 3-2: Principal transition, 2S → 2P, between different fine and hyperfine states of ^{7}Li and ^{6}Li (not drawn to scale). We do not resolve the hyperfine structure of $2P_{3/2}$.

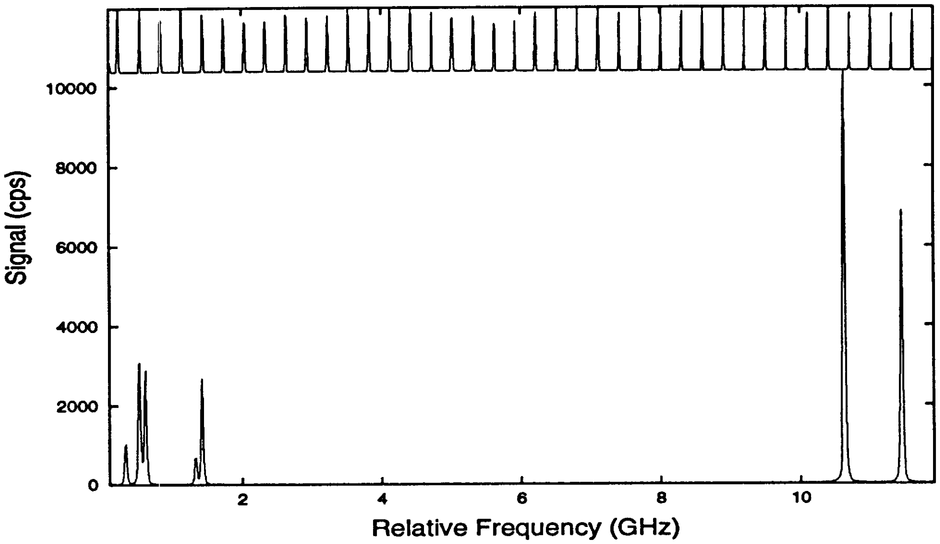

Figure 3-3: Experimental scan of the 2S → 2P transition. The 300 MHz frequency markers are shown on the top.

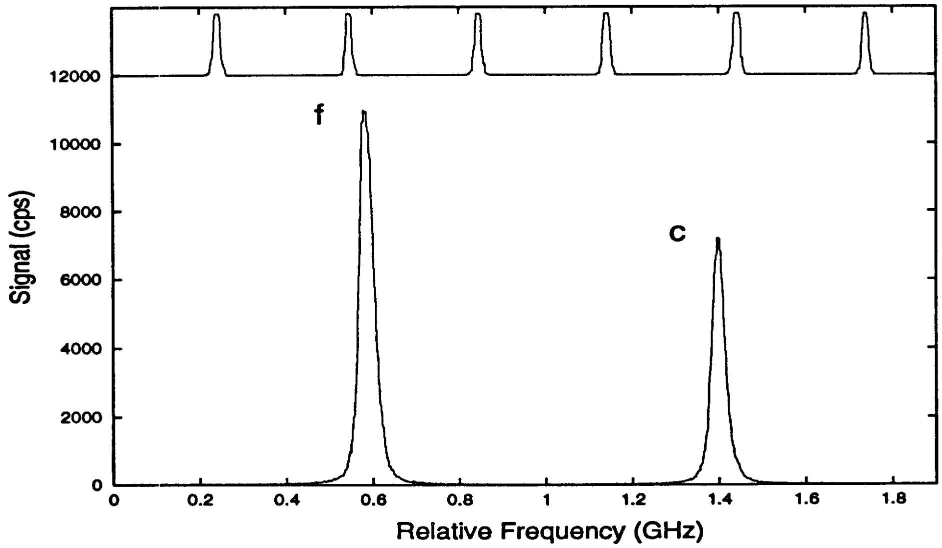

Figure 3-4: 2S → $2P_{3/2}$ transition. The 300 MHz frequency markers are shown on the top.

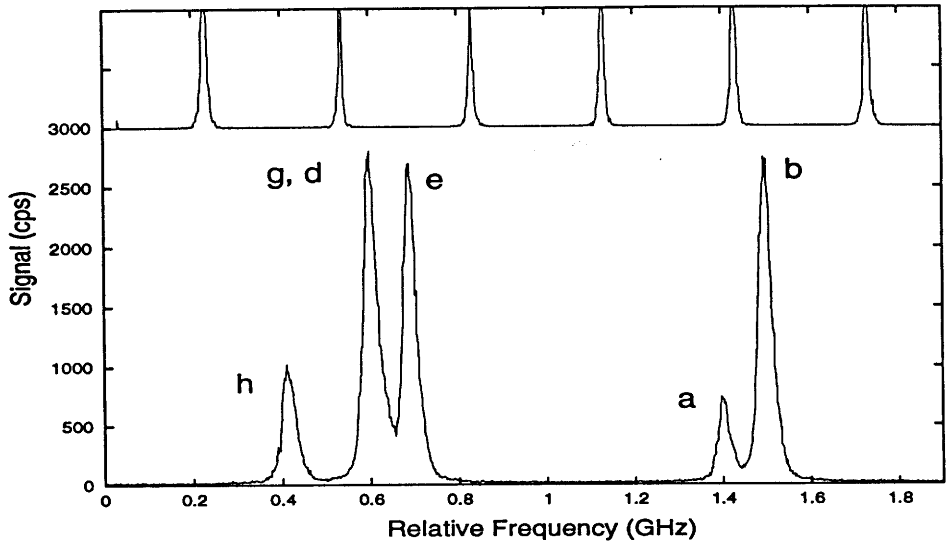

Figure 3-5: 2S → $2P_{1/2}$ transition. The 300 MHz frequency markers are shown on the top.

Unfortunately, the 2P → 3S transition wavelength (813 nm) is beyond the optical range of our 300 MHz Fabry-Perot etalon. While we can excite the 3S state, we have no way of measuring the transition frequency to the desired accuracy [2]. However, the 3S hyperfine splitting has been studied extensively by our predecessors in the two-photon transition [Kas88]. The result is shown in Table 3.4.

Finally, both the fine and hyperfine splittings of the 2S, 2P, and 3S states of ^{7}Li are summarized graphically in Fig. 3-6. The transition wavelengths between these states are shown in Table 3.5.

---

[2] See however [SIW$^+$95] for an ingenious method of measuring this hyperfine splitting using Stark spectroscopy of Rydberg states.

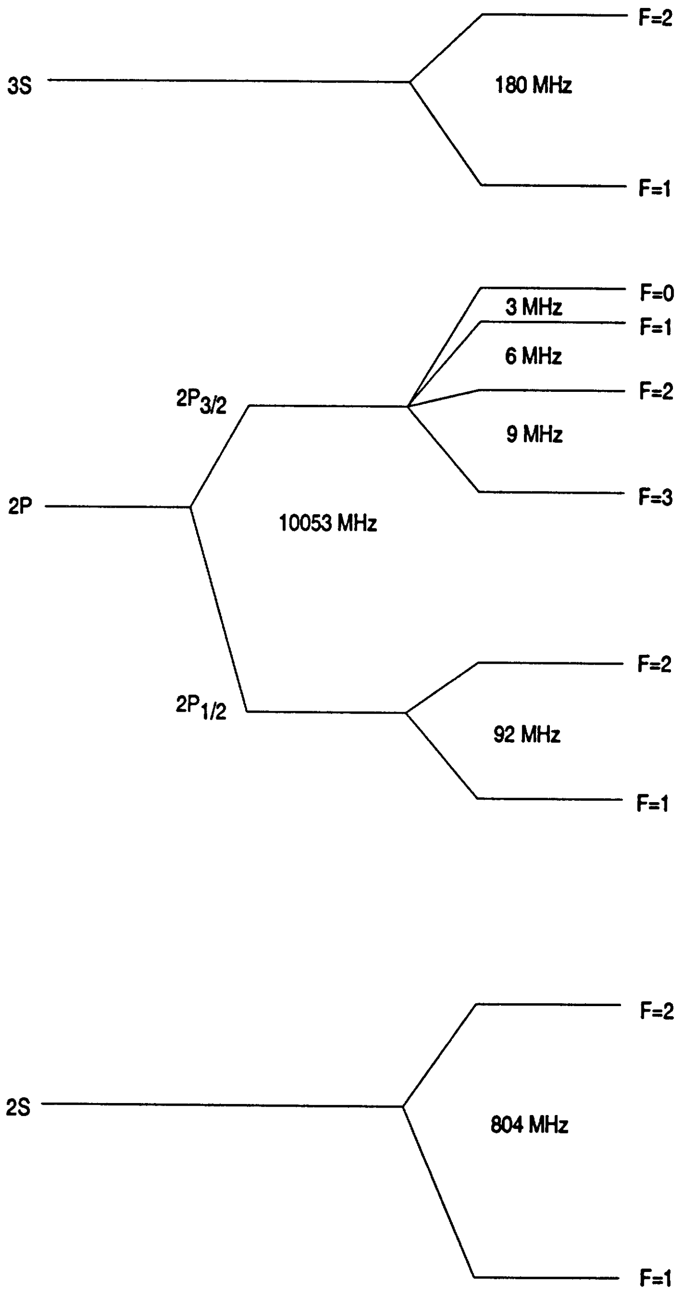

Figure 3-6: Fine and hyperfine splittings of 2S, 2P, and 3S states of ^{7}Li (not drawn to scale).

Transition	Wavelength (nm)
2S → $2P_{1/2}$	670.976
2S → $2P_{3/2}$	670.961
$2P_{1/2}$ → 3S	812.845
$2P_{3/2}$ → 3S	812.868
3S → 21P	623.783
3S → 76P	614.925
3S to the Ionization Limit	614.209
HeNe	632.988

Table 3.5: Useful wavelengths (in vacuum).

3.2.3 Isotope Shift

Figure 3-5 reveals an interesting fact about the lithium isotope shift. As discussed earlier, our atomic beam consists of 94% ^{7}Li and 6% ^{6}Li. We believe the frequencies of transition (g) (2S($F = 1/2$) → $2P_{3/2}$($F = 3/2, 1/2$) of ^{6}Li) and transition (d) (2S($F = 2$) → $2P_{1/2}$($F = 1$) of ^{7}Li) are degenerate. (Again, we do not resolve the hyperfine structure of $2P_{3/2}$ of ^{6} Li.) This accidental degeneracy has potential problem for the laser selection of the desired isotope. Fortunately, the 2P → 3S transitions of the two isotopes are not degenerate. However, a two-step excitation scheme through 2P states, i.e. 2S → 2P → Rydberg states (see Appendix D), will require the use of isotopically pure lithium.

Finally, the isotope shift, ^{7}Li-^{6}Li, of 2S → $2P_{3/2}$ (the frequency difference between transitions (h) and (f)) can be determined from a continuous scan over both transitions such as shown in Fig. 3-3. We find that a careful measurement yields 1033(3) MHz. As far as we know, this has not been published previously. The isotope shifts for other transitions are summarized in Table 3.6.

Transition	Isotope Shift	Reference
2S → $2P_{3/2}$	10.33(3)	[Jia94]
2S → 3S	11.44(3)	[KWI88]
2S → 3D	13.312(4)	[KNS+78]
2S → 4S	14.661(14)	[KNS+78]

Table 3.6: Isotope shift of ^{7}Li and ^{6}Li. All values are in GHz.

3.3 Fine and Hyperfine Structure in a Magnetic Field

The goal of our experiment is to determine the binding energy of the Rydberg states as a function of external fields. We do so by measuring the wavelength of the laser that drives 3S to Rydberg states. This requires a precise value of the binding energy of 3S in a magnetic field as well as its hyperfine structure. Furthermore, the 2S → 2P → 3S excitation scheme requires that the lasers be properly tuned as the magnetic field is varied, which requires the understanding of how the fine and hyperfine structure varies in the magnetic field. We will discuss these issues in this section.

3.3.1 The Hamiltonian

In a uniform magnetic field, the Hamiltonian is

$$H(B) = H_A + H_d + H_b \tag{3.20}$$

where H_A is the unperturbed atomic Hamiltonian, H_d is the diamagnetic contribution in Eqn. 1.1, and

$$H_b = H_f + H_{hf} + \frac{1}{2}(\beta \vec{L} + g_s \vec{S} + g_I \vec{I}) \cdot \vec{B}. \tag{3.21}$$

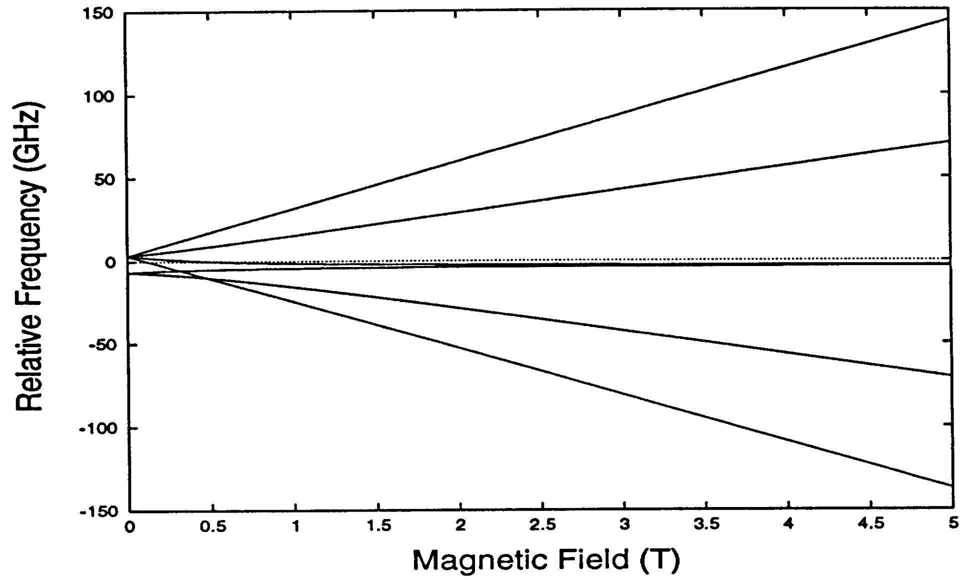

Figure 3-7: Fine and hyperfine states of 2P in a magnetic field, total of 24 states.

Here β is the reduced mass factor [Kas88], $g_I = -1.1822130(6) \times 10^{-3}$ [AIV77] is the nuclear g-factor, and $g_s = 2.002319304386(20)$ [CG87] is the electron g-factor. H_f and H_{hf} are the fine and hyperfine Hamiltonians given by Eqn. 3.11 and Eqn. 3.13, respectively.

3.3.2 2S, 2P, and 3S Energy Levels in a Magnetic Field

The eigenvalues of H_b can be found by solving secular equations. At small fields, F, J, and m are good quantum numbers; at large fields, m_I, m_s, and m are good quantum numbers. Because n and l mixings are negligible for low lying states at laboratory field value, I and L are always good quantum numbers. For all field values, the states can be written in either basis. Appendix E provides the Clebsch-Gordon coefficients for such a superposition of basis states. The resulting Hamiltonian matrix can be diagonalized.

2P contains a total of 24 states. In general, the eigenvalues are found numerically by diagonalizing a 24 by 24 matrix. However, states with different m do not mix, and consequently the matrix can be reduced to 7 matrices with smaller dimensions, each of which corresponds to a distinct m. Each of these matrices is diagonalized separately using, for example, the Jacobi method. The calculations are straightforward but tedious. The behavior of 2P fine and hyperfine states of ^{7}Li in a magnetic field is displayed in Fig. 3-7. (The diamagnetic effects are completely negligible for these states in this field range.) Figure 3-8 and Figure 3-9 show blowups of Fig. 3-7, displaying the hyperfine states of $2P_{1/2}$ and $2P_{3/2}$ in a magnetic field, respectively.

As the magnetic field increases, the total angular momentum of the electron, J, and nuclear spin, I, become decoupled, the Back-Goudsmit effect. We define a critical field

$$B_c^{hf} = |A(n,l,j)|. \tag{3.22}$$

For $B >> B_c^{hf}$, the decoupling is essentially complete (($B_c^{hf}(2P_{1/2}) = 35$ Gauss and $B_c^{hf}(2P_{3/2}) = 5$ Gauss). As the magnetic field increases further, the spin S and the orbital angular momentum L of the electron decouple, the Paschen-Back effect. We define the critical field for the Paschen-Back effect as

$$B_c^f = |a(n,l)|. \tag{3.23}$$

For $B >> B_c^f$, S and L decouple ($B_c^f(2P) = 5000$ Gauss).

Finally, the eigenvalues of 2S and 3S of ^{7}Li in a magnetic field are given by the Breit-Rabi formula. The results are shown in Fig. 3-10 and Fig. 3-11. Details can be found in [Kas88].

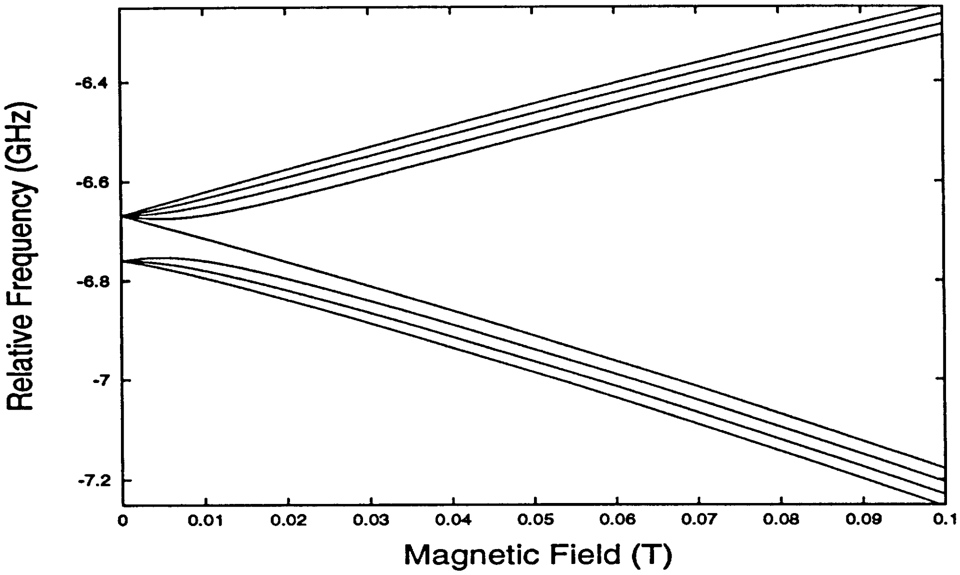

Figure 3-8: Blowup of Fig. 3-7 near hyperfine states of $2P_{1/2}$, total of 8 states.

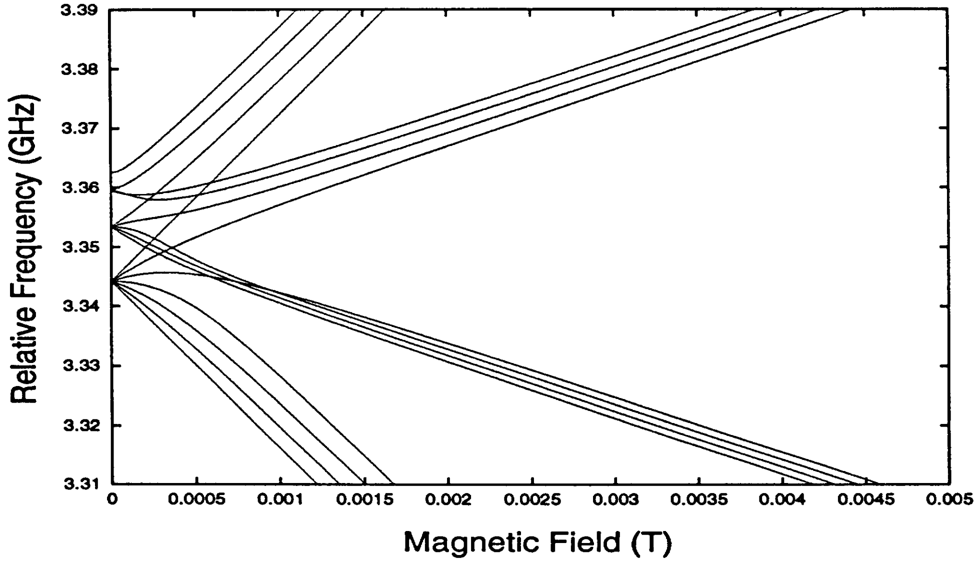

Figure 3-9: Blowup of Fig. 3-7 near hyperfine states of $2P_{3/2}$, total of 16 states.

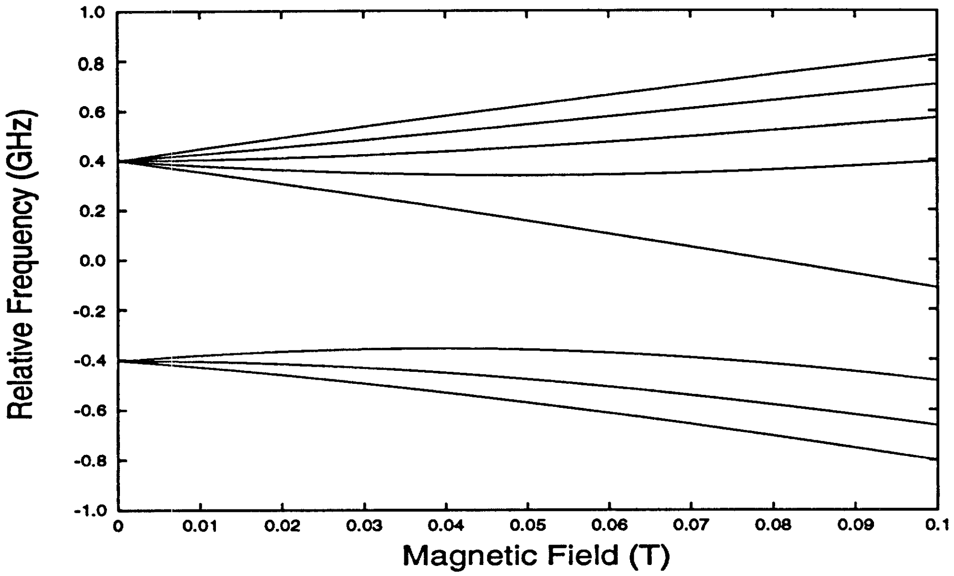

Figure 3-10: Hyperfine states of 2S, total of 8 states.

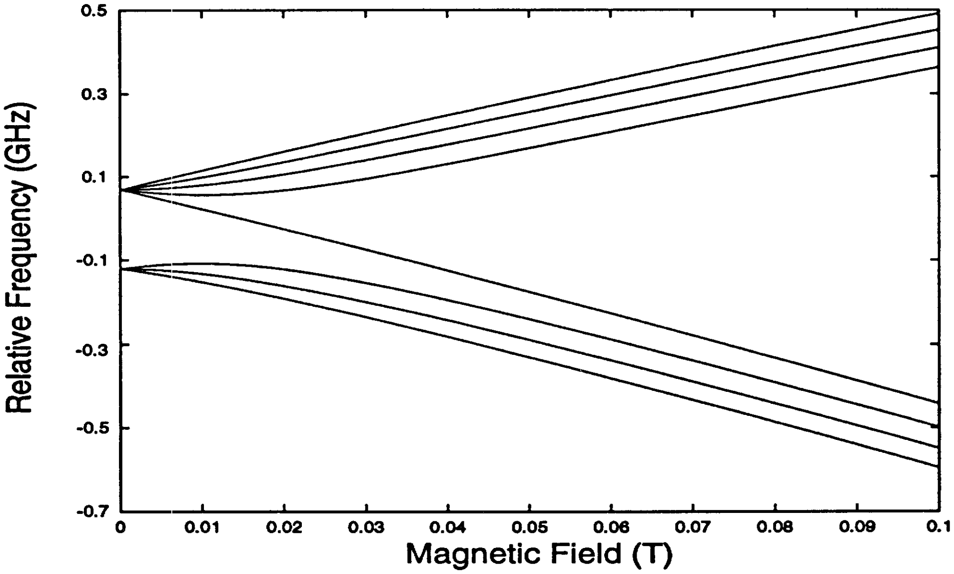

Figure 3-11: Hyperfine states of 3S, total of 8 states.

3.3.3 Electric Dipole Transitions in the High Field Regime

Our excitation scheme consists of electric dipole transitions of 2S → 2P, 2P → 3S, and 3S → Rydberg states. In this section, we will present the corrections to the transition frequencies due to the magnetic field and the fine and hyperfine interactions. We usually operate the magnet at $B > 0.5$ T, where all spins and angular momenta decouple (the Paschen-Back regime). The energy of a given state in Eqn. 3.20 can be expressed in terms of the high field quantum numbers (m_S, m_I, m_L) by using perturbation theory. In this limit, the selection rule for an electric dipole transition is $\Delta m_s = \Delta m_I = 0$ and $\Delta m_L = \pm 1, 0$.

2S → 2P Transition

The energies of the 2S and 2P states in the Paschen-Back regime can be expressed as

$$\begin{aligned} E(2S) &= E_A(2S) + E_d(2S,B) + \frac{1}{2}(g_s m_S + g_I m_I)B \qquad (3.24)\\ &\quad + A(2S) m_S m_I, \\ E(2P) &= E_A(2P) + E_d(2P,B) + \frac{1}{2}(\beta m_L + g_s m_S + g_I m_I)B \qquad (3.25)\\ &\quad + A(2P)(m_L + m_S)(m_I) + a(2P) m_L m_S, \end{aligned}$$

where $E_A + E_d$ are the eigenvalues of $H_A + H_d$ in Eqn. 3.20. 2S → 2P is an electric dipole transition which requires $\Delta m_S = \Delta m_I = 0$. The transition frequency is thus

$$\begin{aligned} \nu &= \{[E_A(2P) + E_d(2P,B)] - [E_A(2S) + E_d(2S,B)]\} \qquad (3.26)\\ &\quad + \frac{1}{2}\beta m_L B + A(2P) m_L m_I + [A(2P) - A(2S)] m_I m_S + a(2P) m_L m_S. \end{aligned}$$

Due to the paramagnetic interaction $\frac{1}{2}\beta m_L B$, the transition frequency is in general a very sensitive function of the magnetic field ($\approx$ (0.47 cm^{-1}/T)$m_L B$). However, by choosing $\Delta m_L = 0$, the transition is only slightly field dependent (solely due to the diamagnetic interaction). In this case, the transition frequency simplifies to

$$\nu = \{[E_A(2P) + E_d(2P, B)] - [E_A(2S) + E_d(2S, B)]\} + [A(2P) - A(2S)]m_I m_S. \quad (3.27)$$

The shift in transition frequency due to the diamagnetic interaction and the hyperfine interaction is given in practical units by

$$\Delta\nu = (0.011\,\mathrm{MHz/T^2})B^2 - (356\,\mathrm{MHz})m_S m_I. \quad (3.28)$$

As can be seen, the diamagnetic contribution is below our experimental resolution, and the transition is nearly field independent. However, the hyperfine interaction makes a noticeable difference. There are eight transitions, but only four are distinct. The observed transition peaks are separated by 178 MHz.

2P → 3S Transition

The energy of the 3S state in the Paschen-Back regime can be expressed as

$$E(3S) = E_A(3S) + E_d(3S, B) + \frac{1}{2}(g_s m_S + g_I m_I)B + A(3S)m_S m_I. \quad (3.29)$$

The 2P → 3S is also an electric dipole transition which requires $\Delta m_S = \Delta m_I = 0$. Again by choosing the $\Delta m_L = 0$ transition, the transition frequency given by

$$\nu = [(E_A(3S) + E_d(3S, B) - (E_A(2P) + E_d(2P, B)] + [A(3S) - A(2P)]m_I m_S \quad (3.30)$$

is independent of the paramagnetic interaction. The shift in transition frequency due to the diamagnetic interaction and the hyperfine interaction is given by

$$\Delta\nu = (0.9\,\mathrm{MHz/T^2})B^2 + (46\,\mathrm{MHz})m_S m_I. \tag{3.31}$$

The diamagnetic effect is again negligible. The hyperfine contribution is roughly at our experimental resolution. Different m_s and m_I make a small shift. However, their values are fixed by the 2S → 2P transition.

3S to Rydberg States

Our goal is to extract the binding energy of a Rydberg state from the wavelength of the yellow laser. The energy of a Rydberg state can be expressed as

$$E(nP) = E(nP, B) + \frac{1}{2}(g_s m_S + g_I m_I)B, \tag{3.32}$$

where $E(nP, B)$ is the binding energy of the Rydberg state in a magnetic field B, which includes the paramagnetic and the diamagnetic interactions. According to Eqn. 3.12 and Eqn. 3.14, the fine and the hyperfine interactions have a $(n^*)^{-3}$ dependence. For instance, the fine structure parameter $a(\mathrm{21P}) \approx 5.6$ MHz is below our experimental resolution. The hyperfine interaction is even smaller. Hence, these interactions are neglected in the Eqn. 3.32.

The transition frequency is given by (3S → nP is again an electric dipole transition, $\Delta m_S = \Delta m_I = 0$)

$$\nu = \{(E(nP, B) - [E_A(3S) + E_d(3S, B)]\} - A(3S)m_I m_S. \tag{3.33}$$

Determination of $E(nP, B)$ thus requires the accurate values of the binding energy of 3S, $E_A(\mathrm{3S})$, the diamagnetic shift $E_d(3S, B)$, and the hyperfine coupling $A(\mathrm{3S})m_I m_S$.

These values have been carefully investigated [Kas88] and are given by

$$\begin{aligned} E_A(3S) = &\quad -16,281.067(5)\mathrm{cm}^{-1} && (3.34) \\ E_d(3S,B) = &\quad (4.0 \times 10^{-5}\,\mathrm{cm}^{-1}/\mathrm{T}^2)B^2. && (3.35) \end{aligned}$$

Finally, the binding energy of the Rydberg state is

$$\begin{aligned} E(nP,B) &= \nu - 16,281.067(5)\,\mathrm{cm}^{-1} - (0.00307\,\mathrm{cm}^{-1})m_I m_S && (3.36) \\ &\quad +(4.0 \times 10^{-5}\,\mathrm{cm}^{-1}/\mathrm{T}^2)B^2. \end{aligned}$$

The diamagnetic shift of $3S$ is negligible in our field range. However, the different values of m_S and m_I make a measurable difference. We usually select $m_I m_S = 3/4$.

3.4 Experimental Realization

The discussions in the previous two sections provide the necessary background for performing high resolution spectroscopy on lithium in strong external fields with the stepwise excitation scheme. In this section, we will present details of the experimental apparatus. In particular, we will discuss the lasers (Sec. 3.4.1), the optics (Sec. 3.4.2), and the detection schemes (Sec. 3.4.3).

3.4.1 Laser Operation

The three transition wavelengths are 671 nm, 813 nm, and 620 nm. The lasers involved are one large frame Coherent Innova 100-10 argon-ion laser pumping two Coherent CR699-21 ring dye lasers with DCM and Kiton Red, driving the 2S → 2P and 3S → Rydberg transitions, respectively, and a New Focus tunable external cavity diode laser driving the 2P → 3S transition.

At full current (50 A), the output power of the argon ion laser is about 20 W multiline. Table 3.7 displays the spectral distribution of the output power. More than half of the output power belongs to the 514.5 nm line. We operate the argon ion laser at 13.5 W multiline (33 A). This power is split between DCM and Kiton Red with a CVI high power argon ion laser beamsplitter. This beamsplitter reflects 45% and transmits 55% of the laser power. One side is AR coated to avoid doubly reflected beams.

The reflected beam (6 W) is used to drive the red laser. A CVI CW argon ion laser dielectric mirror is used to deflect the reflected beam onto the pump mirror in the DCM ring laser. Despite the long travelling distance of the pump beam and the resulting large beam size, we were delighted to find that the DCM dye laser works extremely well. Moreover, we did not observe any long term instability.

The transmitted beam (7.5 W) is used to pump the yellow laser. However, Kiton Red does not absorb the 488 nm photons. When pumped by multiline, the output of the dye laser displays power drop and instability. However, we find that mixing some DCM into the Kiton Red solution eliminates the problem, though the gain curve is slightly red shifted and the overall gain drops by 10% [3]. We should note that this kind of trick does not always work. For example, Rhodamine 6G, a very efficient and friendly dye, is tunable from 560 nm to 600 nm. However, in an attempt to red shift the gain curve we added a small amount of Kiton Red and found the dye completely inoperative.

DCM is adequate for the red laser that drives the transition 2S → 2P (671 nm), though the peak of its gain curve is at about 640 nm (tunable from 630 nm to 680 nm). We actually use Exciton DCM Special, consisting of 25% Kiton Red and 75% DCM, because we find it difficult to dissolve pure DCM in any convenient solvent.

---

[3] See Appendix F for an alternative idea.

Wavelength (nm)	Percent % of Total Multiline Power
514.5	52
488	25
496	13
501	4
others	6

Table 3.7: Spectral distribution of the argon ion laser.

The resulting gain curve is slightly blue shifted but has no drastic effect on the gain at 671 nm [4]. Recall that unlike the two-photon transition, we can easily saturate the principal transition, and thus do not require much power. The dye solution is obtained by dissolving 2 grams of Exciton DCM Special in 400 ml of reagent grade benzyl alcohol, stirring for about 3-4 hours, and adding 600 ml of reagent grade ethylene glycol. Although the lifetime of DCM Special is relatively short (about 400 Watts Hours), the gain is reasonable. With a circulator pressure of 40 psi and the pump power of 6 W, the single-mode output power is about 600 mW at the peak of the gain curve (640 nm) and about 300 mW at 671 nm. The laser optics used are the standard DCM optics. The laser output is rather stable.

A mixture of DCM and Kiton Red is used for the yellow laser that drives the 3S to Rydberg transition. The dye solution is made by dissolving 2 grams of Exciton Kiton Red in 100 ml of reagent methanol, stirring for 2 hours, and adding 850 ml of reagent grade ethylene glycol. Simultaneously we dissolve 0.2 grams of Exciton DCM Special in 50 ml of reagent grade benzyl alcohol in a different beaker and stir for about 3-4 hours. The final dye solution is achieved by mixing the two solutions. Although the lifetime of Kiton Red itself is about 1000 Watts Hours, the lifetime of the mixture is unknown. As mentioned before, the gain drops by 10%. With a circulator pressure

---

[4] DCM Special of Lambda has about 50% Kiton Red and 50% DCM. The gain curve may be too far blue shifted to cover 671 nm.

Laser Dye	Tuning Range (nm)	Peak Wavelength (nm)	Pumping Laser
Rhodamine 6G	560-600	575	Ar multiline or 514.5 nm
Kiton Red	590-640	610	Ar 514.5 nm
Kiton Red Special	590-640	615	Ar multiline
DCM Special	630-680	640	Ar multiline
LD700	710-780	740	Kr multiline red

Table 3.8: Useful laser dye information.

Laser		Dye Recipe	
Dye	Amount	Premix	Solvent
Rhodamine 6G	1.0 g	50 ml methanol	950 ml E.G.
Kiton Red	2.0 g	100 ml methanol	900 ml E.G.
Kiton Red Special	2.0 g of K.R.	K.R in 100 ml methanol	850 ml E.G.
	0.2 g of DCM	DCM in 50 ml benzyl alcohol	
DCM Special	2.0 g	400 ml benzyl alcohol	600 ml E.G.
LD700	1.5 g	100 ml methanol	900 ml E.G.

Table 3.9: Useful laser dye recipes. E.G.=ethylene glycol. All solvents should be reagent grade.

of 55 psi, and the pump power of 7.5 W, the single-mode output power is about 250 mW at the peak of the gain curve (620 nm). The standard Rhodamine 6G optics are used. Some useful laser dye information is summarized in Table 3.8, and the dye recipes are shown in Table 3.9.

Finally, a New Focus Model 6200 external cavity tunable diode laser is used to drive the 2P → 3S transition. The cavity of the laser consists of a high reflection coating on one end of the diode laser and a high reflecting tuning mirror. In addition, a diffraction grating is used as a narrow spectral filter (passband, a few GHz) which forces the laser to operate in single frequency. The beam from the diode passes through a collimating lens and hits the grating at a grazing angle. The beam is then diffracted toward the tuning mirror. The reflected light forms the output beam. A picomotor provides coarse tuning, and a PZT is used for fine tuning (continuous scan range about 60 GHz). The laser head is temperature stabilized to about 10 mK. We usually run the laser at 70 mA and the output power at 813 nm is about 17 mW. Because of the diode lasing medium, the output beam shape is actually elliptical. We use an anamorphic prism pair outside the cavity to correct the beam to a circular shape.

3.4.2 Optics

Figure 3-12 displays the optical layout. In the main path, the goal is to overlap all three laser beams and intersect them with the atomic beam at right angles. The beams of the red laser and the diode laser that drive the 2S → 2P transition and the 2P → 3S transition, respectively, are first merged. These are then merged with the beam of the yellow laser that drives the Rydberg transition. A small amount of the beam from each laser is used to monitor its frequency.

The Red Laser: 2S → 2P

After passing through a thick glass plate, which reflects a small portion of the beam for frequency monitoring, the main beam of the red laser passes through a +5 magnification telescope, formed with -20 mm and +100 mm focal length lens. (The beam is expanded to reduce divergence.) The expanded beam then traverses two linear polarizers. The second polarizer is adjusted so that the polarization is parallel to the magnetic field (exciting $\Delta m = 0$ transition). The first polarizer then functions as an attenuator. After being reflected by a CVI longpass dichroic beamsplitter DBS(a), the beam then passes through another CVI longpass dichroic beamsplitter DBS(b) before being focused into the interaction region by a 40 cm focal length lens (not

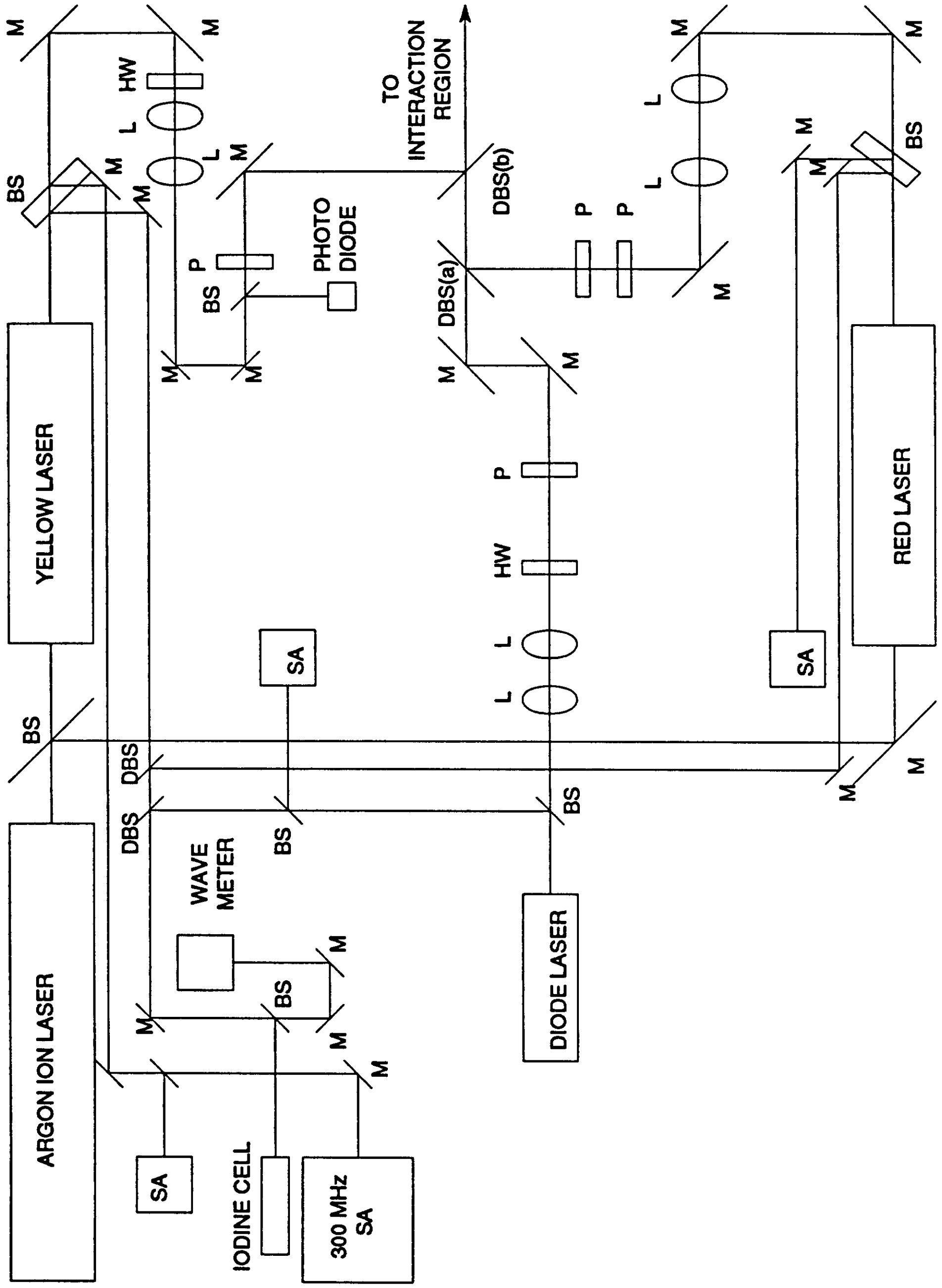

Figure 3-12: The optical layout for the new excitation scheme. M: mirror; L: lens; BS: beamsplitter; DBS: dichroic beamsplitter; SA: spectrum analyzer; P: linear polarizer; HW: halfwave plate.

Dichroic	Transmission			Reflection		
Beamsplitter	620 nm	670 nm	813 nm	620 nm	670 nm	813 nm
DBS(a)	-	2	80	-	98	20
DBS(b)	2 P 0.5 S	60	80	98 P 99.5 S	40	20

Table 3.10: CVI longpass dichroic beamsplitters. All values are in %. P and S represent the parallel and perpendicular polarizations, respectively.

shown). The properties of these two dichroic beamsplitters are shown in Table 3.10. The system is not very efficient: Between the first glass plate and DBS(b), the loss is about 50% [5]. However, this is not important because we usually attenuate the red laser power anyway. All mirrors are New Focus 5101 broadband visible dielectric mirrors.

The two weak beams reflected from the thick glass plate are used to monitor the laser frequency. One beam is deflected by a plane mirror onto a 1.5 GHz FSR spectrum analyzer (640 nm to 780 nm optics with a peak finess of 200), which displays the laser's spectral characteristics. The second beam is deflected by two mirrors onto a dichroic beamsplitter (used to transmit a portion of the yellow laser) which reflects about 50% of the incident laser power. The reflected beam then passes through a second dichroic beamsplitter (used to overlap the beams from all three lasers) onto the wavemeter.

The Diode Laser: 2P → 3S

The main beam of the diode laser passes through a beamsplitter (about 60% transmission) before entering a +5 magnification telescope, formed with -20 mm and +100

---

[5] The reason for such a high loss is due to the fact that the red laser wavelength (671 nm) and the yellow laser wavelength (620 nm) are too close for efficient dichroic beamsplitting.

mm focal length lens. The expanded beam then passes through a halfwave plate and a linear polarizer. The polarizer is positioned such that the output polarization is parallel to the magnetic field, and the halfwave plate is used to maximize the power. A halfwave plate is necessary here because the diode laser power is limited. The beam is then deflected by two mirrors onto DBS(a). The transmitted beam then passes through DBS(b) before being focused into the interaction region by the 40 cm focal length lens. To achieve optimum overlap between beams of the diode laser and the red laser, one of the mirrors is placed in an Aerotech mount with differential screws, which are used to maximize the 3S → 2P fluorescent signal while the red laser is locked on the 2S → 2P transition. It turns out that the optimum overlap is easily achieved because the signal is usually huge. This system is also not very efficient: Between the anamorphic prism and DBS(b), the loss is about 60%. But the intensity in the interaction region is still well above the saturation intensity. All mirrors are New Focus 5102 broadband near infrared dielectric mirrors.

The reflected beam from the first beamsplitter is split again at a second beamsplitter. The reflected beam is directed onto a 1.5 GHz FSR spectrum analyzer (790 nm to 930 nm optics with a peak finess of 200), which displays the laser's spectral characteristics. The transmitted beam is reflected by a dichroic beamsplitter towards the wavemeter.

The Yellow Laser: 3S → Rydberg

After passing through a thick glass plate, which provides weak reflected beams for monitoring purposes, the main beam of the yellow laser traverses a halfwave plate. The beam then enters a -7.5 magnification telescope, formed with +20 mm and +150 mm focal length lens. The expanded beam next traverses a linear polarizer which can be adjusted to excite either the $\Delta m = 0$ or the $\Delta m = \pm 1$ transitions. Again, the halfwave plate needs to be rotated to give optimum output power. After deflection by two more mirrors, the beam passes through a thick wedge beamsplitter. The reflected beam, used for power monitoring, is focused onto a photodiode. The transmitted beam is then reflected by DBS(b) and overlapped with the other two beams before being focused into the interaction region by the 40 cm focal length lens. DBS(b) is positioned on an Aerotech mount with differential screws, and the optimum overlap is achieved by maximizing the Rydberg signal while the other two lasers are locked on their respective transitions. The system is relatively efficient: Between the first glass plate and DBS(b), the loss is about 20%. All mirrors are New Focus 5101 broadband visible dielectric mirrors.

The two weak beams reflected from the thick glass plate are used to monitor the laser frequency. The first beam is deflected by three plane mirrors onto a beamsplitter. The reflected beam from the beamsplitter is directed onto a 1.5 GHz FSR spectrum analyzer (550 nm to 700 nm optics with a peak finess of 200), which displays the laser's spectral characteristics. The transmitted beam is deflected by two more mirrors onto a 300 MHz Fabry-Perot etalon, which sits in a temperature and pressure stabilized box.

The second beam passes through two dichroic beamsplitters which are used to overlap the beams of the red laser and the diode laser. The beam is then deflected by another mirror onto a thick glass beamsplitter. The transmitted beam is directed to the wavemeter, and the two reflected beams are used to monitor transmission through the iodine cell, and to normalize its transmission signals.

Recently, a Burleigh model WA-20VIS wavemeter has replaced our homemade Michelson interferometer. The new wavemeter is reliable, compact and easy to align, though the accuracy remains about the same (1 part in 10^6). Some of the useful transition wavelengths were shown in Table 3.5. All wavelengths were expressed in values in vacuum because the Burleigh wavemeter measures wavelengths in vacuum.

3.4.3 Monitoring the Stepwise Excitation

Figure 3-13 displays our detection scheme. The transitions 2S → 2P and 2P → 3S are monitored through the fluorescent signals. Unlike the two-photon transition, the incident and the fluorescent photons now have exactly the same wavelength. The scattered light is completely depolarized, and it cannnot be easily filtered out. Great care is thus needed in maximizing the fluorescent signal and at the same time minimizing the scattered light. Unfortunately, sometimes this is still a problem. Both fluorescent signals are coupled out of the interaction region with a light pipe and a long fiber bundle as described in Sec. 2.4.1 and shown in Fig. 3-13. The collected light is then split into two signals by a bifurcated fiber bundle from Ealing Optics.

The photons from the 2P → 2S fluorescence pass through an Ealing 670 nm interference filter (bandwidth 10 nm) and are focused onto a Hamamatsu R669 red sensitive PMT. Useful specifications of this PMT are shown in Table 3.11. The focusing optics are two Melles Griot aspherical lenses, the first one with an 18 mm focal length and the second one with a 26.5 mm focal length. The PMT is mounted in a homemade PMT housing with a homemade gate valve and is operated at room temperature. The dark counts are relatively high ($\approx$ 5000 cps) and the gain is low. However, the fluorescent signal from the 2S → 2P principal transition is huge, about 3×10^6 sec^{-1} when the oven is operated at 650°C. The scattered light is often $5-10\%$ of the total signal counts. We usually operate the PMT with 750 V on the cathode, lower than the suggested 1000 V bias.

The collection efficiency, E_{PMT}, is the product of the following factors,

$$\begin{aligned}E_{PMT} &= (\text{fractional solid angle subtended by the light pipe} = 0.05)\\ &\quad\times(\text{coupling into the light pipe} = 0.5)\\ &\quad\times(\text{transmission of the light pipe} = 0.5)\end{aligned}$$

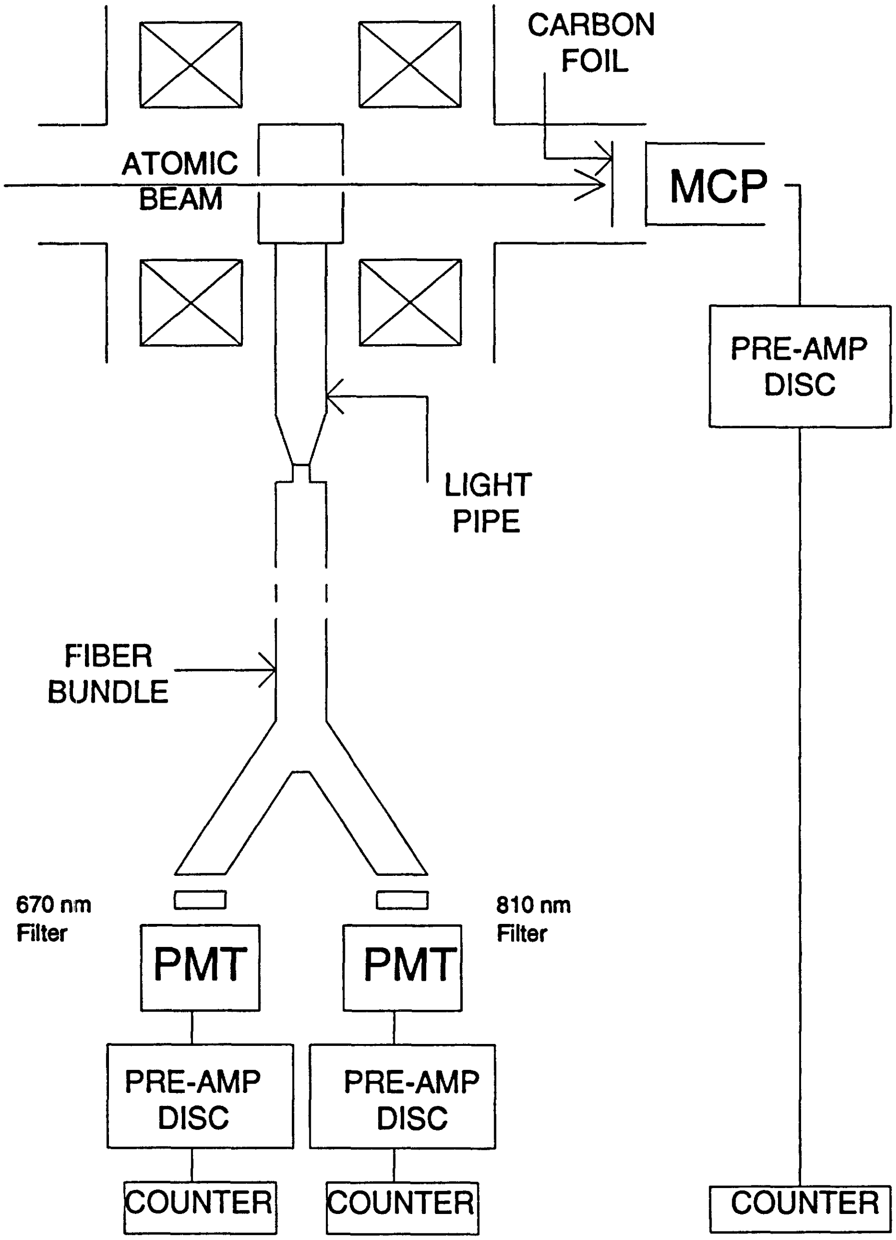

Figure 3-13: New detector arrangements. The fluorescences from the first two transitions are collected by two PMT's and the Rydberg signals are detected by a MCP.

Photocathode material	Extended Red Multialkali
Maximum bias on the cathode	1000 V
Operating bias on the cathode	750 V
Quantum efficiency at 670nm	5%
Quantum efficiency at 813nm	1%
Gain at maximum bias	3.3×10^5
Dark counts at maximum bias	5000 cps (25°C)
Dark counts at operating bias	500 cps (25°C)
Active area	4 mm × 10 mm

Table 3.11: Specifications of the Hamamatsu R669 PMT.

$$\begin{aligned}
& \times(\text{coupling into the fiber bundle} = 0.5) \\
& \times(\text{transmission of the fiber bundle} = 0.25) \\
& \times(\text{coupling into the dual fiber bundle} = 0.25) \\
& \times(\text{transmission of the dual fiber bundle} = 0.5) \\
& \times(\text{filter transmission} = 0.5) \\
& \times(\text{lens transmission} = 0.75) \\
& \times(\text{PMT quantum efficiency} = 0.05) \\
\approx\; & 3.5 \times 10^{-7}. \qquad (3.37)
\end{aligned}$$

With this efficiency, our observed counting rate of 3×10^6 sec^{-1} implies that the lithium atoms are emitting about 8.8×10^{11} photons/sec. Compared with the estimated rate for the emission from a saturated transition given in Eqn. 3.8, this is about a factor of 14 too low. Possibly the collection efficiency is over-estimated, but in any case this is not too far below the calculated value.

The photons from the 3S → 2P fluorescence pass through an Ealing 810 nm inteference filter (bandwidth 10 nm) and are focused onto a RCA C31034A PMT. This is the tube used to monitor the two-photon cascade fluorescence. Its parameters were presented in Fig. 2.3. The focusing optics are two Melles Griot aspherical lenses (HEBBAR coated), the first one with an 18 mm focal length and the second one with a 26.5 mm focal length. We operate the PMT at –30°C. The fluorescent signal from the 2P → 3S transition is about 5×10^4 sec^{-1}, when the oven is operated at 650°C. The scattered light is about 5% of the total signal counts.

The collection efficiency for this detection, E_{PMT}, is given by the product of the following factors,

$$\begin{aligned}
E_{PMT} &= (\text{fractional solid angle subtended by the light pipe} = 0.05) \\
&\quad \times(\text{coupling into the light pipe} = 0.5) \\
&\quad \times(\text{transmission of the light pipe} = 0.5) \\
&\quad \times(\text{coupling into the fiber bundle} = 0.5) \\
&\quad \times(\text{transmission of the fiber bundle} = 0.25) \\
&\quad \times(\text{coupling into the dual fiber bundle} = 0.25) \\
&\quad \times(\text{transmission of the dual fiber bundle} = 0.5) \\
&\quad \times(\text{filter transmission} = 0.5) \\
&\quad \times(\text{lens transmission} = 0.95) \\
&\quad \times(\text{PMT quantum efficiency} = 0.1) \\
&\approx 8.9 \times 10^{-7}. \qquad (3.38)
\end{aligned}$$

With this efficiency, our observed counting rate of 5×10^4 sec^{-1} implies that the lithium atoms are emitting about 5.6×10^{10} photons/sec. Compared with the estimated rate for the emission from a saturated transition given in Eqn. 3.9, this is about a factor of 85 too low. Again maybe the collection efficiency is over-estimated, but this is still not too far below the calculated value.

At one point, we were concerned about angle tuning of our interference filter: The transmission peak shifts blue if the angle of incidence is away from normal. In general, the photons exiting the fiber bundle will not be normal to the filter. Hence, the light bluer than 813 nm will have higher transmission than light redder than 813 nm. In particular, the fluorescent signal from the 2S → 2P transition is much stronger and its transition wavelength 671 nm is bluer than 813 nm. Chun-ho Iu at SUNY-Stonybrook reports that his detector for 813 nm fluorescence is completely overwhelmed by the 671 nm photons. To our delight, the counts due to the fluorescent photons from the 671 nm transition, as well as the scattered light from the lasers, are negligible for our 813 nm fluorescent PMT.

Finally the Rydberg states continue to be field ionized and the ions are detected by the MCP as described in Sec. 2.5.1 and Sec. 2.5.2 and shown in Fig. 3-13. Bertan Model 315 high voltage power supplies are used to bias both PMT's and the MCP. The Modern Instrument Technology Model F-100T amp-discriminators are used to enhance the signals from the anodes of all three detectors, and the output TTL pulses are sent to the counters.

The Rydberg signal from this excitation scheme was found to improve by a factor 2 or 3. This is the same order of magnitude as the estimate in Eqn. 3.10. Data taken with this stepwise excitation scheme will be the subject of a future thesis.

Chapter 4

Classical Chaos

We turn now to the scientific goal of this thesis: to understand the quantum mechanics of a classically chaotic system. Before exploring the world of quantum chaos, some discussion of classical chaos seems appropriate. One of the pioneering works on chaos is the analysis of a nonlinear oscillator by Henon and Heiles in 1964 [HH64]. They demonstrated that there exist simple, nonlinear systems which display chaotic behavior in which the motion cannot be predicted, even in principle, though the laws of motion are known. The evolution in time is described by Hamilton equations of motion, and the solutions are possible for sufficiently short times by numerical integration. Yet for sufficiently long times, the motion can be unpredictable. The reason for such chaotic behavior is the instabilities of orbits. Two such orbits, with slightly different initial conditions, separate *exponentially* in time, whereas regular trajectories separate *linearly*. In other words, the motion displays sensitive dependence on initial conditions. Thus our finite precision in knowing the initial conditions makes useful predictions of long time behavior impossible.

The aim of this chapter is threefold. First is to provide a general introduction to nonintegrable Hamiltonian systems and the origins of chaotic behavior (Sec. 4.1 and Sec. 4.2). Second is to intoduce the diamagnetic hydrogen problem as an archetype

(Sec. 4.3). Finally, we discuss chaos in unbound systems — the so-called open systems (Sec. 4.4). Since we are interested in time-independent Hamiltonian systems, non-autonomous or dissipative systems are not discussed.

4.1 Integrable Hamiltonians

This section reviews the fundamental properties of integrable Hamiltonian systems [Gol81] [Tab89]. It begins with the formulation of the necessary conditions for the integrability of a given Hamiltonian system. Some basic ideas such as canonical transformation and action-angle variables are introduced (Sec. 4.1.1). These ideas are illustrated using an important example of an integrable system in atomic physics, the hydrogen atom in a uniform electric field (Sec. 4.1.2). Finally, a useful numerical method, the surface of section, is introduced (Sec. 4.1.3).

4.1.1 Hamilton Equations of Motion

Consider a time independent Hamiltonian with n degrees of freedom $H(\vec{q},\vec{p})$, where $\vec{q} = (q_1, ..., q_i, ..., q_n)$ are the generalized coordinates and $\vec{p} = (p_1, ..., p_i, ..., p_n)$ are the conjugate momenta. The Hamilton equations of motion are

$$\begin{aligned} \dot{q}_i &= \frac{\partial H}{\partial p_i} \\ \dot{p}_i &= -\frac{\partial H}{\partial q_i}. \end{aligned} \tag{4.1}$$

If we can find a canonical transformation ($q \to Q, p \to P$) so that

$$H(\vec{q},\vec{p}) \Longrightarrow H'(\vec{P}), \tag{4.2}$$

then the Hamilton equations of motion become,

$$\begin{aligned} \dot{P}_i &= 0 \\ \dot{Q}_i &= f_i(\vec{P}), \end{aligned} \tag{4.3}$$

which can be trivially integrated to get:

$$\begin{aligned} P_i &= \text{const} \\ Q_i &= f_i t + \delta_i, \end{aligned} \tag{4.4}$$

where $\delta_i = Q_i(0)$ are determined by initial conditions. Clearly, the P_i are n constants of motion, and the Q_i are known as cyclic coordinates. Thus the key to integrating a time-independent Hamiltonian with n degrees of freedom is to identify n independent constants of motion and express them in the form of n constant conjugate momenta. To be more precise, a Hamiltonian system is completely integrable if there exist n constants of motions $F_1, ..., F_n$ which are in involution, that is, for which all Poisson brackets between them vanish,

$$[F_i, F_j] = 0, \; i = 1, ..., n, j = 1, ..., n. \tag{4.5}$$

In other words, the F_i all commute with each other [Tab89]. If these conditions are satisfied, the Liouville-Arnold theorem [Arn78] states that each n-dimensional surface, which each trajectory is confined to in a 2n-dimensional phase space, must have the topology of an n-dimensional torus, the so-called invariant torus.

The phase space of an integrable system is thus filled with non-intersecting invariant tori. Each classical trajectory is confined on such a torus. The motion on an n-dimensional torus is naturally periodic and can be considered as the direct product of n independent 2π periodicities. Therefore it is convenient to find a canonical transformation, $p \rightarrow I_i$ and $q \rightarrow \theta_i$, such that each θ_i increases by 2π after each complete period of motion. One can show that if I_i are defined as [Tab89]

$$I_i = \frac{1}{2\pi} \oint_{Ci} \vec{p} \cdot d\vec{q}, \tag{4.6}$$

where C_i are n topologically independent closed paths on an n-dimensional torus, then

$$\begin{aligned} \dot{I}_i &= -\frac{\partial H}{\partial \theta_i} = 0 \\ \dot{\theta}_i &= \frac{\partial H}{\partial I_i} = \omega_i. \end{aligned} \tag{4.7}$$

That is, H is only a function of I_i, and the θ_i are cyclic. The I_i and θ_i are known as the action-angle variables.

The conserved classical action variables I_i play an important role in the semiclassical quantization ideas in Sec. 5.1. To summarize, an integrable system of n degrees of freedom has n constants of motion. The trajectories in 2n-dimensional phase space lie on n-dimensional tori. They are called the regular trajectories. It is important to note that for an integrable system, the trajectories are regular for all parameters and initial conditions. Otherwise, energy conservation only guarantees that a given trajectory is confined to a (2n-1)-dimensional energy shell. An obvious consequence of the above discussions is that all Hamiltonians with one degree of freedom are integrable. Conversely, a nonintegrable Hamiltonian system must have at least two degrees of freedom.

4.1.2 Hydrogen Atom in a Uniform Electric Field

As an example of an integrable Hamiltonian, we consider a physical system in atomic physics, a hydrogen atom in a uniform electric field. The Hamiltonian in atomic units is

$$H = \frac{p^2}{2} - \frac{1}{r} + \vec{F} \cdot \vec{r} \tag{4.8}$$

where $\vec{F}$ is the electric field. According to Sec. 4.1.1, this Hamiltonian is integrable if there exist three constants of motion. One can easily show that the total energy E and the component of the angular momentum in the direction of the electric field $(\vec{L} \cdot \vec{F}/F)$ are conserved. To show the existence of the third constant of motion, we consider the Laplace-Runge-Lenz vector,

$$\vec{A} = \frac{\vec{r}}{r} + \vec{L} \times \vec{p}, \tag{4.9}$$

which is a constant of motion in the absence of electric field [Gol81]. In an electric field, $\vec{A}$ is no longer conserved. Its rate of change is

$$\frac{d\vec{A}}{dt} = \vec{L} \times \vec{F} + (\vec{r} \times \vec{F}) \times \vec{p}. \tag{4.10}$$

However, some simple vector manipulations show that

$$\frac{d}{dt}(\vec{A} \cdot \vec{F}) - \frac{d}{dt}\frac{1}{2}[(\vec{r} \times \vec{F}) \times \vec{r}] \cdot \vec{F} = 0. \tag{4.11}$$

This implies that $\{\vec{A} - [(\vec{r} \times \vec{F}) \times \vec{r}]/2\} \cdot \vec{F}$ is a new constant of motion [Red64]. The vector

$$\vec{C} = \vec{A} - \frac{(\vec{r} \times \vec{F}) \times \vec{r}}{2} \tag{4.12}$$

is sometimes known as the generalized Laplace-Runge-Lenz vector. The third constant of motion is the component of $\vec{C}$ in the direction of the electric field. In the absence of an electric field, $\vec{C}$ reduces to the Laplace-Runge-Lenz vector.

It is evident that the third constant of motion is a direct result of the conservation of the Laplace-Runge-Lenz vector in the absence of an electric field. This symmetry is the result of the special nature of the Coulomb potential. The Coulomb potential is supersymmetric in the sense that it has more constants of motion than necessary for an integrable system. One would not expect this symmetry to hold for a general central potential. In fact, a third constant of motion does not exist for an arbitrary central potential in the presence of a uniform electric field. An example is an alkali atom in a uniform electric field. Courtney offers a detailed description of this problem [Cou95]. We will examine this system more closely in Sec. 4.4 in the context of chaos in an open system.

4.1.3 Surface of Section

In the example in the last section, we managed to find all three constants of motion analytically. However, except for some special cases, there are no systematic methods for finding constants of motion for a given Hamiltonian. In other words, there are no analytic methods to determine whether a given Hamiltonian is integrable. One has to investigate the motion using numerical means. One technique for analyzing the motion is the surface of section, developed by Poincaré [Poi92]. This technique is especially suited for studying Hamiltonians with two degrees of freedom, and the discussion in this section is restricted to such Hamiltonians. Some methods for generalizing this method to systems with three degrees of freedom will be described in Sec. 8.2.

Consider a two-dimensional Hamiltonian

$$H = \frac{p_x^2 + p_y^2}{2} + V(x,y). \tag{4.13}$$

The phase space is four-dimensional, composed of p_x, p_y, x, and y. However, energy conservation confines the trajectories to a three-dimensional energy surface, and there are only three independent variables. For example, for a given energy, p_y is determined within a sign by p_x, x, and y. The key idea of a surface of section is to inspect the behavior on a slice of the phase space, for example $y = 0$. One records the values of p_x and x every time the trajectory intercepts this slice. This way every point on the slice defines the state of the system within a sign. Clearly, this is only suitable for a bound system. Section 4.4 will present methods for characterizing unbound systems. For the rest of the discussion, we will restrict ourselves to bound trajectories. These trajectories are obtained through integrating Hamilton equations of motion numerically. From the discussion in Sec. 4.1.1, we learn that if the Hamitonian is integrable, the trajectories are confined on two-dimensional tori. The interception of one of the tori with the surface of section is a one-dimensional manifold, a smooth curve. Otherwise the trajectories can migrate on the whole three-dimensional energy surface. This is manifest on the surface of section as points on a two-dimensional manifold.

We now return to our example of the hydrogen atom in a uniform electric field. We take $\vec{F} = F\hat{z}$. Conservation of L_z effectively reduces the system to two-dimensional. The Hamiltonian for $L_z = 0$ in cylindrical coordinates is

$$H = \frac{p_\rho^2 + p_z^2}{2} - \frac{1}{(\rho^2 + z^2)^{1/2}} + Fz. \tag{4.14}$$

Before examining the surface of section, we can further simplify the problem by taking advantage of a classical scaling rule,

$$\begin{aligned} \vec{r} &\rightarrow F^{1/2}\vec{r} \\ \vec{p} &\rightarrow F^{1/4}\vec{p} \\ \epsilon_F &= B^{-1/2}H. \end{aligned} \tag{4.15}$$

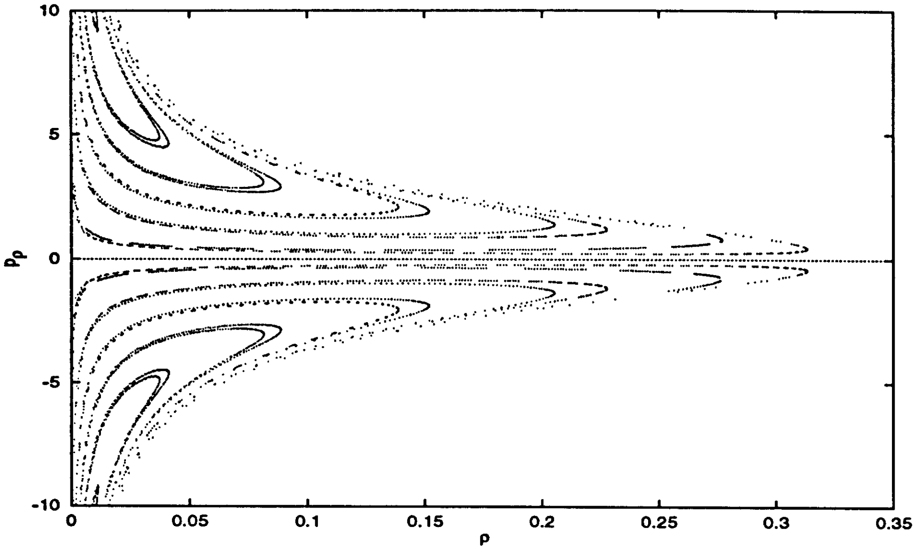

Figure 4-1: Surface of section at z=0 of a hydrogen atom in a uniform electric field at $\epsilon_F = -3.0$.

The scaled Hamiltonian is

$$\epsilon_F = \frac{p_\rho^2 + p_z^2}{2} - \frac{1}{(\rho^2 + z^2)^{1/2}} + z, \tag{4.16}$$

which only depends on one parameter ϵ_F, not on E and F separately.

As our surface of section, we take a slice of the phase space at $z = 0$ and record the points at ρ and p_ρ. Figure 4-1 shows such a surface of section for $\epsilon_F = -3.0$. It is clear that all points lie on smooth curves. Each smooth curve corresponds to a unique trajectory defined by a particular set of initial conditions. We conclude that the motion is indeed regular for the given ϵ_F. One can actually show that this is true for all values of ϵ_F, which agrees with the existence of the third constant of motion in Sec. 4.1.2.

4.2 Canonical Perturbation Theory and Classical Chaos

In this section, we are concerned with what happens to the tori of an integrable system under a small perturbation. An important example is the atomic system of this thesis, the Rydberg atom in external fields. Although much of the material presented in this section, i.e. the canonical perturbation theory, is not used explicitly in the studies reported in this thesis, it is very helpful in developing our understanding of classical chaos. We summarize some of the major ideas following the treatment by Tabor [Tab89].

We discuss classical canonical perturbation theory for systems with one degree of freedom in Sec. 4.2.1. Then we address the difficulties of this method for systems with more than one degree of freedom in Sec. 4.2.2. Finally, we state the celebrated KAM theorem and its consequences in Sec. 4.2.3.

4.2.1 One Degree of Freedom

In order to apply canonical perturbation theory, we represent a given Hamiltonian system in the form of an integrable part H_0 plus some nonintegrable part H'. In terms of action-angle variables (I, θ) of the integrable part, we have

$$H(I,\theta) = H_0(I) + H'(I,\theta). \tag{4.17}$$

The Hamilton equations of motion for this system are

$$\dot{I} = -\frac{\partial}{\partial\theta}H(I,\theta) \tag{4.18}$$

$$\dot{\theta} = \frac{\partial}{\partial I}H(I,\theta). \tag{4.19}$$

Due to the dependence on θ in H', I is no longer a constant of motion. The basic idea of canonical perturbation theory is to find a new pair of action-angle variables (J,φ) for the system such that there is a canonical transformation to a new Hamiltonian in which φ is cyclic (ignorable), that is, $H(I,\theta) \to K(J)$. If this is possible, then the new Hamiltonian becomes integrable and can be trivially integrated.

We start by expressing the nonintegrable part H' in a power series of ϵ ($\epsilon \ll 1$),

$$H(I,\theta) = H_0(I) + \epsilon H_1(I,\theta) + \epsilon^2 H_2(I,\theta) + O(\epsilon^3). \tag{4.20}$$

Equations 4.18 and 4.19 become

$$\dot{I} = -\epsilon \frac{\partial H_1}{\partial \theta} - \epsilon^2 \frac{\partial H_2}{\partial \theta} + O(\epsilon^3) \tag{4.21}$$

$$\dot{\theta} = \omega_0(I) + \epsilon \frac{\partial H_1}{\partial I} + \epsilon^2 \frac{\partial H_2}{\partial I} + O(\epsilon^3), \tag{4.22}$$

where $\omega_0(I) \equiv \partial H_0(I)/\partial I$ is the frequency of an unperturbed trajectory around a torus. In order to generate a new pair of action-angle variables (J,φ), we need to find the generating function S = S(θ,J). (For a review of generating functions and the Hamilton-Jacobi equation, see for example Goldstein [Gol81].) The relations between the new and old action-angle variables are

$$\begin{aligned} I &= \frac{\partial}{\partial \theta} S(\theta, J) \\ \varphi &= \frac{\partial}{\partial J} S(\theta, J). \end{aligned} \tag{4.23}$$

Through these relations and Eqn. 4.20, we obtain the time-independent Hamilton-Jacobi equation

$$H_0(\frac{\partial S}{\partial \theta}) + \epsilon H_1(\frac{\partial S}{\partial \theta}, \theta) + \epsilon^2 H_2(\frac{\partial S}{\partial \theta}, \theta) + O(\epsilon^3) = K(J). \tag{4.24}$$

We expand S and K in power series of ϵ,

$$\begin{aligned} S &= S_0 + \epsilon S_1 + \epsilon^2 S_2 + O(\epsilon^3) \\ K &= K_0 + \epsilon K_1 + \epsilon^2 K_2 + O(\epsilon^3). \end{aligned} \tag{4.25}$$

By using these series expansions in Eqn. 4.24 and expanding the right hand side in a Taylor series, we get

$$\begin{aligned} &H_0(J) + \epsilon\,[\frac{\partial S_1}{\partial \theta}\frac{\partial H_0}{\partial J} + H_1] + \epsilon^2\,[\frac{1}{2}(\frac{\partial S_1}{\partial \theta})^2\frac{\partial^2 H_0}{\partial J^2} + \frac{\partial S_2}{\partial \theta}\frac{\partial H_0}{\partial J} + \frac{\partial S_1}{\partial \theta}\frac{\partial H_1}{\partial J} + H_2] \\ &+O(\epsilon^3) = K_0(J) + \epsilon K_1(J) + \epsilon^2 K_2(J) + O(\epsilon^3). \end{aligned} \tag{4.26}$$

Equating powers of ϵ, we have

$$O(\epsilon^0): \quad H_0(J) = K_0(J) \tag{4.27}$$

$$O(\epsilon^1): \quad \frac{\partial S_1}{\partial \theta}\frac{\partial H_0}{\partial J} + H_1(J,\theta) = K_1(J) \tag{4.28}$$

$$O(\epsilon^2): \quad \frac{1}{2}(\frac{\partial S_1}{\partial \theta})^2\frac{\partial^2 H_0}{\partial J^2} + \frac{\partial S_2}{\partial \theta}\frac{\partial H_0}{\partial J} + H_2(J,\theta) = K_2(J). \tag{4.29}$$

These equations show that in zeroth order, K_0 is found by replacing I by J in H_0,

$$\begin{aligned} O(\epsilon^0): \quad J &= I \\ \varphi &= \theta. \end{aligned} \tag{4.30}$$

To find corrections to first order, we need to solve Eqn. 4.28 for S_1. Let

$$\tilde{H}_1(J,\theta) = K_1(J) - H_1(J,\theta), \tag{4.31}$$

and together with Eqn. 4.7, we can write Eqn. 4.28 as

$$\frac{\partial}{\partial\theta}S_1(\theta,J)=\frac{1}{\omega_0(J)}\tilde{H}_1(J,\theta). \tag{4.32}$$

An unperturbed trajectory is confined on a torus with frequency ω_0. It is reasonable to expand both S_1 and $\tilde{H}_1$ as Fourier series in the unperturbed angle variable θ,

$$\tilde{H}_1(J,\theta)=\sum_{k=0}^{\infty}A_k(J)e^{ik\theta}, \tag{4.33}$$

$$S_1(J,\theta)=\sum_{k=0}^{\infty}B_k(J)e^{ik\theta}. \tag{4.34}$$

The first order correction to the generating function is

$$S_1(J,\theta)=\sum_{k}\frac{iA_k(J)}{k\omega_0(J)}e^{ik\theta}. \tag{4.35}$$

Equations 4.23 can now be used to find the new action-angle variables to first order in ϵ,

$$\begin{aligned}\varphi &= \theta+\epsilon\frac{\partial}{\partial J}S_1(J,\theta)\\ J &= I-\epsilon\frac{\partial}{\partial\theta}S_1(J,\theta).\end{aligned} \tag{4.36}$$

This process can be generalized to higher orders in ϵ. However, from Sec. 4.1.1 we know that all Hamiltonians with one degree of freedom are integrable. Thus the canonical perturbation theory here confirms something we already know: The new action-angle variables, J and φ (φ is cyclic), can always be found for a one-dimensional Hamiltonian system.

4.2.2 Many Degrees of Freedom

We now attempt to generalize canonical perturbation theory to Hamiltonian systems with more than one degree of freedom. It will soon be obvious that serious difficulties arise. These difficulties and the subsequent failure of classical canonical perturbation theory are the roots of classical chaos. We proceed as in the one-dimensional case,

$$H(\vec{I},\vec{\theta}) = H_0(\vec{I}) + H'(\vec{I},\vec{\theta}), \tag{4.37}$$

where $\vec{I} = (I_1, ..., I_n)$ and $\vec{\theta} = (\theta_1, ..., \theta_n)$ are now the n-dimensional vectors of the action-angle variables. We again attempt to find a new set of angle-action variables $(\vec{J}, \vec{\varphi})$ such that $\vec{\varphi}$ are cyclic. Proceeding as in the one-dimensional case, the equations for the generating function are

$$O(\epsilon^0): \quad H_0(\vec{J}) = K_0(\vec{J}) \tag{4.38}$$

$$O(\epsilon^1): \quad \nabla_\theta S_1(\vec{J},\vec{\theta}) \cdot \nabla_I H_0(\vec{J}) + H_1(\vec{J},\vec{\theta}) = K_1(\vec{J}). \tag{4.39}$$

Let

$$\tilde{H}_1(\vec{J},\vec{\theta}) = K_1(\vec{J}) - H_1(\vec{J},\vec{\theta}), \tag{4.40}$$

and the n-dimensional frequency vector

$$\vec{\omega}_0(\vec{I}) = \nabla_I H_0(\vec{I}). \tag{4.41}$$

Equation 4.39 can be written as

$$\vec{\omega}_0(\vec{J}) \cdot \nabla_\theta S_1(\vec{\theta}, \vec{J}) = \tilde{H}_1(\vec{J},\vec{\theta}). \tag{4.42}$$

Expanding both S_1 and $\tilde{H}_1$ in Fourier series as before, we find

$$S_1(\vec{J},\vec{\theta}) = i\sum_m \frac{A_m(\vec{J})}{\vec{m}\cdot\vec{\omega}_0(\vec{J})}e^{i\vec{m}\cdot\vec{\theta}}. \tag{4.43}$$

Unlike the one-dimensional case, Eqn. 4.43 may not converge. In fact, when the denominator $\vec{m}\cdot\vec{\omega}_0(\vec{J}) = 0$, the sum blows up! Physically, the components of $\vec{\omega}_0(\vec{J})$ correspond to the frequencies around an unperturbed torus. The physical situation of $\vec{m}\cdot\vec{\omega}_0(\vec{J}) = 0$ thus corresponds to commensurable fundamental frequencies around an unperturbed torus. Such a torus is sometimes called a rational torus. A torus with incommensurable fundamental frequencies is called an irrational torus. Classical canonical perturbation theory breaks down for rational tori. This is sometimes known as the problem of the small divisors. As we will see later, this is essentially the source of classical chaos.

4.2.3 KAM Theorem

The solution to the problem of the small divisors came in the form of the famous KAM theorem. Qualitatively, the theorem states that all irrational tori of an unperturbed system outside a region centered around each rational torus survive when perturbed, though they may be distorted. The region centered around each rational torus is known as a resonant gap, the width of which vanishes as the perturbation goes to zero. The proof turns out to be highly complicated [Arn63]. What happens to the tori inside the resonant gaps and the rational tori themselves? Tabor gives a detailed analysis of the motion inside the resonant gaps around rational tori [Tab89]. Roughly speaking, a perturbation destroys these tori. The motion inside the resonant gaps is no longer confined on any tori and becomes chaotic.

We are now ready to describe the behavior of a typical integrable system under a perturbation. For a small perturbation, the system displays essentially all the features

Degrees of Freedom	1	2	3	4	n
Dimensions of phase space	2	4	6	8	2n
Dimensions of energy shell	1	3	5	7	2n-1
Dimensions of tori	1	2	3	4	n
Dimensions of surface of section	-	2	4	6	2n-2

Table 4.1: Dimensions of various classical spaces vs. degrees of freedom in the system.

of an integrable system. Almost all tori are preserved. As the perturbation increases, more tori are destroyed. The so-called stochastic motion occurs in the vicinities of these destroyed tori. At a certain value of the perturbation parameter, almost all tori are destroyed. The motion becomes chaotic almost everywhere on the energy surface in phase space. There are two critical perturbation parameters. One determines the onset of destruction of tori and one determines the onset of global chaos. These values cannot be predicted analytically, and must be determined numerically for individual cases. We will give examples in Sec. 4.3 and Sec. 8.2. Since the existence of a torus is associated with a constant of motion, i.e. a symmetry of the system, the destruction of tori can be interpreted as symmetry breaking. The onset of classical chaos can therefore also be characterized as the destruction of certain symmetries.

Finally, the ideas in this section are summarized in Table 4.1. First we note for a one-dimensional system, the dimension of the energy shell and the dimension of the tori are the same. This simply reiterates the fact that all one-dimensional Hamiltonian systems are integrable. Secondly, the KAM theorem guarantees the existence of irrational tori in a perturbed system. These tori are sometimes called the KAM tori. For a two-dimensional system, these tori are two-dimensional and are embedded on a three-dimensional energy shell. This means they set up boundaries for chaotic trajectories. In other words, the chaotic trajectories in one region are separated from chaotic trajectories in another region by a KAM torus. We recall that a two-dimensional surface can divide a three-dimensional space into two distinct regions. For systems with more than two degrees of freedom, this is no longer true. For example, a three-dimensional system has three-dimensional tori embedded on a a five-dimensional energy surface [1]. In this case, the KAM tori do not confine the chaotic trajectories. The chaotic trajectories can intersect every finite region of the energy surface in phase space. This remarkable phenomenon will be demonstrated in Sec. 8.2.3.

4.3 The Diamagnetic Hydrogen Atom

In this section, we will discuss a classically chaotic system: a hydrogen atom in a uniform magnetic field, the so-called diamagnetic hydrogen atom. This problem has been studied by a number of authors and has been shown to be nonintegrable [Rob81] [DKN84] [HH83]. Excellent review articles are given in references [HRW89] and [FW89]. In the literature, much of the discussion is restricted to the case where the angular momentum along the magnetic field vanishes, a situation particularly convenient experimentally. Here we will study the general situation and emphasize the significance of the angular momentum barrier on the system.

The Hamiltonian in atomic units is

$$H = \frac{p^2}{2} - \frac{1}{r} + \frac{1}{2}\vec{L}\cdot\vec{B} + \frac{1}{8}(\vec{B}\times\vec{r})^2 \tag{4.44}$$

where $\vec{B} = B\hat{z}$ is the magnetic field and $\vec{L}$ is the angular momentum. As in the case of hydrogen in an electric field, the energy and L_z are conserved. The system is effectively two-dimensional, and the Hamiltonian obeys a scaling rule. In cylindrical

---

[1] Three-dimensional surfaces do not divide five-dimensional space into bound regions for the same reason that lines cannot divide three-dimensional space into bound regions.

coordinates the Hamiltonian is

$$H = \frac{p_\rho^2 + p_z^2}{2} + \frac{L_z^2}{2\rho^2} - \frac{1}{(\rho^2 + z^2)^{1/2}} + \frac{1}{2}L_z B + \frac{1}{8}B^2\rho^2. \tag{4.45}$$

The scaling rules are

$$\begin{aligned} \vec{r} &\rightarrow B^{2/3}\vec{r} \\ \vec{p} &\rightarrow B^{-1/3}\vec{p} \\ l_z &= B^{1/3}L_z \\ \epsilon &= HB^{-2/3}. \end{aligned} \tag{4.46}$$

The scaled Hamiltonian is

$$\epsilon = \frac{p_\rho^2 + p_z^2}{2} + \frac{l_z^2}{2\rho^2} - \frac{1}{(\rho^2 + z^2)^{1/2}} + \frac{1}{2}l_z + \frac{1}{8}\rho^2. \tag{4.47}$$

The system only depends on two parameters, ϵ and l_z, not on B, E, and L_z separately. At $B = 6$ T, for example, $\epsilon = -0.5$ corresponds to $E = -95\ \mathrm{cm}^{-1}$ and $\epsilon = -0.1$ corresponds to $E = -20\ \mathrm{cm}^{-1}$. We should emphasize here that l_z is the scaled angular momentum, not the actual angular momentum itself. Because l_z is a constant of motion, the classical dynamics in the cases of $+l_z$ and $-l_z$ differ only by the trivial paramagnetic interaction. For the rest of this chapter, we will only consider $-l_z$. Unlike hydrogen in a uniform electric field, this system does not have a third constant of motion. As we will see shortly, the system is indeed nonintegrable.

One can define an effective static potential for the Hamiltonian in Eqn. 4.47 by setting the kinetic energy to zero,

$$V = \frac{l_z^2}{2\rho^2} - \frac{1}{(\rho^2 + z^2)^{1/2}} + \frac{1}{2}l_z + \frac{1}{8}\rho^2. \tag{4.48}$$

This potential has a minimum which defines the boundary between the classically allowed and forbidden regions. The angular momentum barrier prevents the electron from getting close to the nucleus. This barrier vanishes in the limit that l_z goes to zero. The potential has a local maximum, above which the electron can ionize along the z-axis. In this section, we are primarily interested in the classical dynamics between the minimum and the local maximum.

4.3.1 Surface of Section

We shall examine behavior for z=0. The surface of section is then defined by (p_ρ, ρ), with p_z determined by conservation of energy within a sign. The Hamilton equations of motion are integrated numerically. Appendix G describes the procedures.

Figures 4-2 through 4-7 show surfaces of section for $l_z = 0$ to $l_z = -5$. Each figure shows surfaces of section for three values of ϵ. For all l_z, at large negative ϵ (Figs. a), the whole phase space is filled with tori, implying the motion is regular everywhere. As ϵ increases (Figs. b), some tori are destroyed. Part of phase space is filled with chaotic trajectories. These regions are bound by KAM tori, in agreement with the KAM theorem. At still larger ϵ (Figs. c), motion is chaotic almost everywhere. Note that the angular momentum barrier excludes the trajectories from the origin for large l_z. The angular momentum barrier tends to prevent the system from becoming chaotic. The explanation is straightfoward. Chaos in the diamagnetic hydrogen atom is a result of the competition between the spherical symmetry of the Coulomb potential and the cylindrical symmetry of the magnetic field. For large l_z, the electron is being kept away from the nucleus by the angular momentum barrier, and thus experiences a smaller Coulomb potential than an electron with small l_z. Figure 4-8 shows this transition from regular motion to chaotic motion in the l_z and ϵ space. For all l_z, the systems undergo a transition from orderly to disorderly motion as ϵ increases.

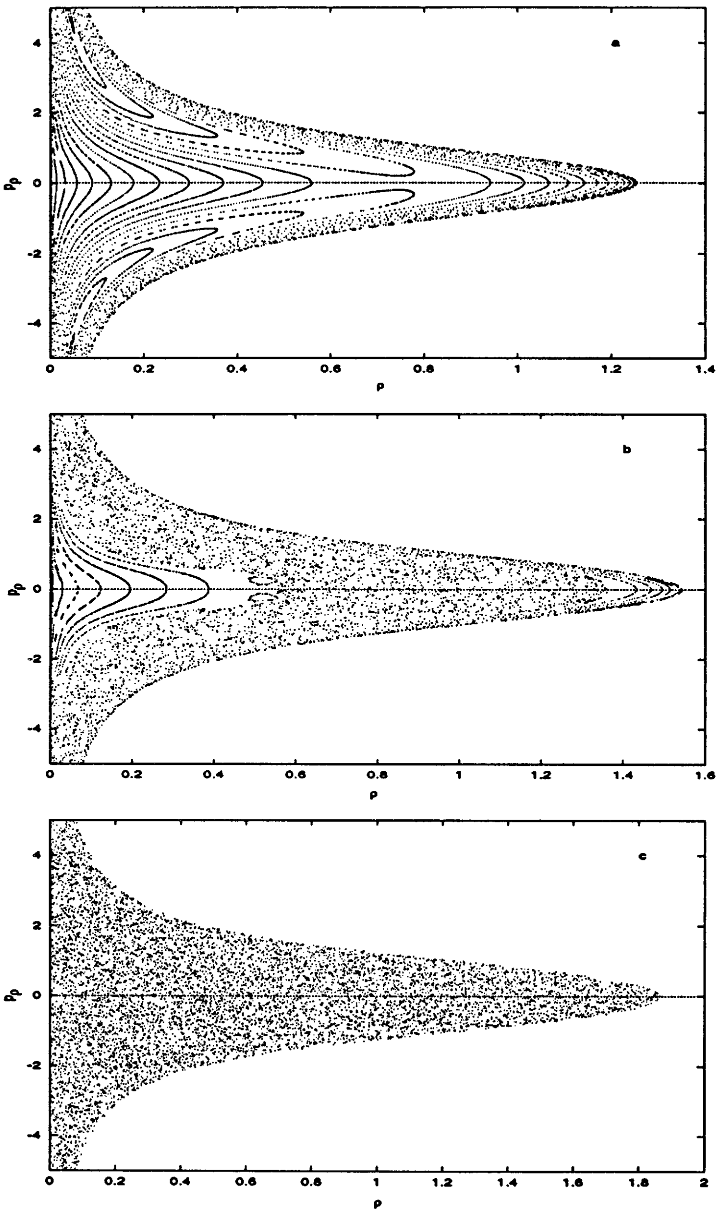

Figure 4-2: Surface of section for hydrogen in a uniform magnetic field for $l_z = 0$, a) $\epsilon = -0.6$, b) $\epsilon = -0.35$, c) $\epsilon = -0.1$.

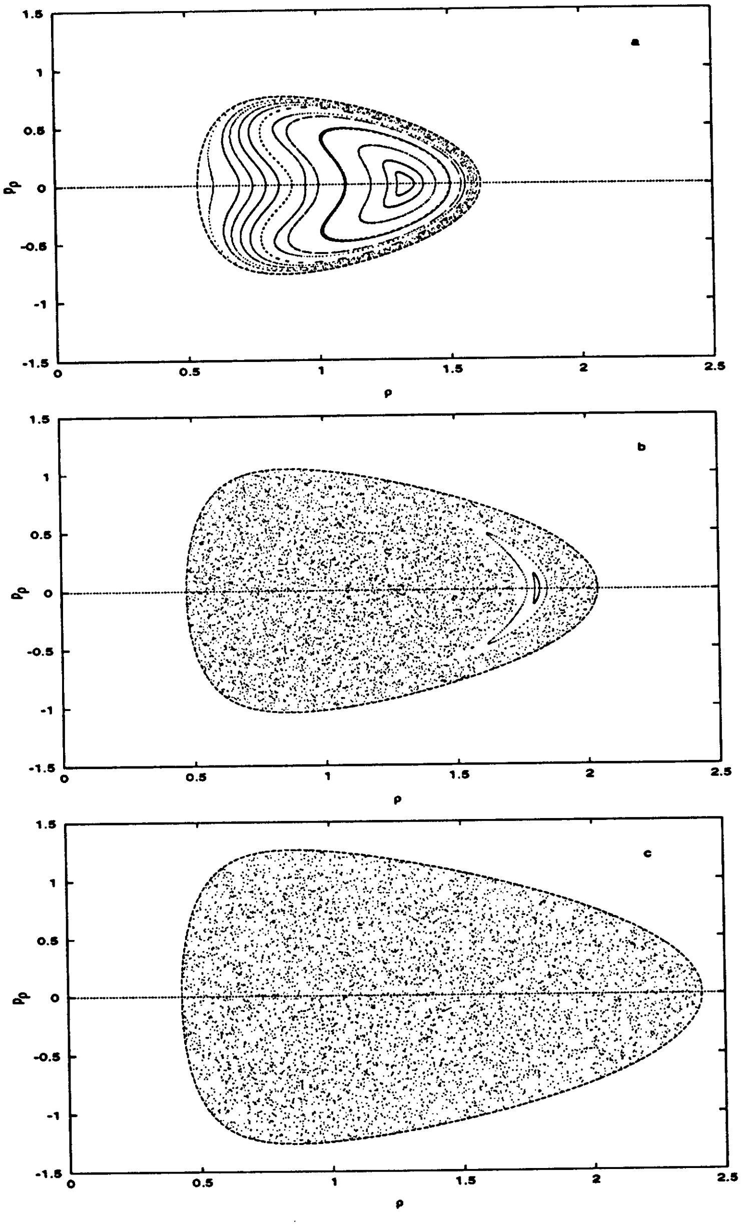

Figure 4-3: Surface of section for hydrogen in a uniform magnetic field for $l_z = -1$, a) $\epsilon = -0.6$, b) $\epsilon = -0.35$, c) $\epsilon = -0.1$.

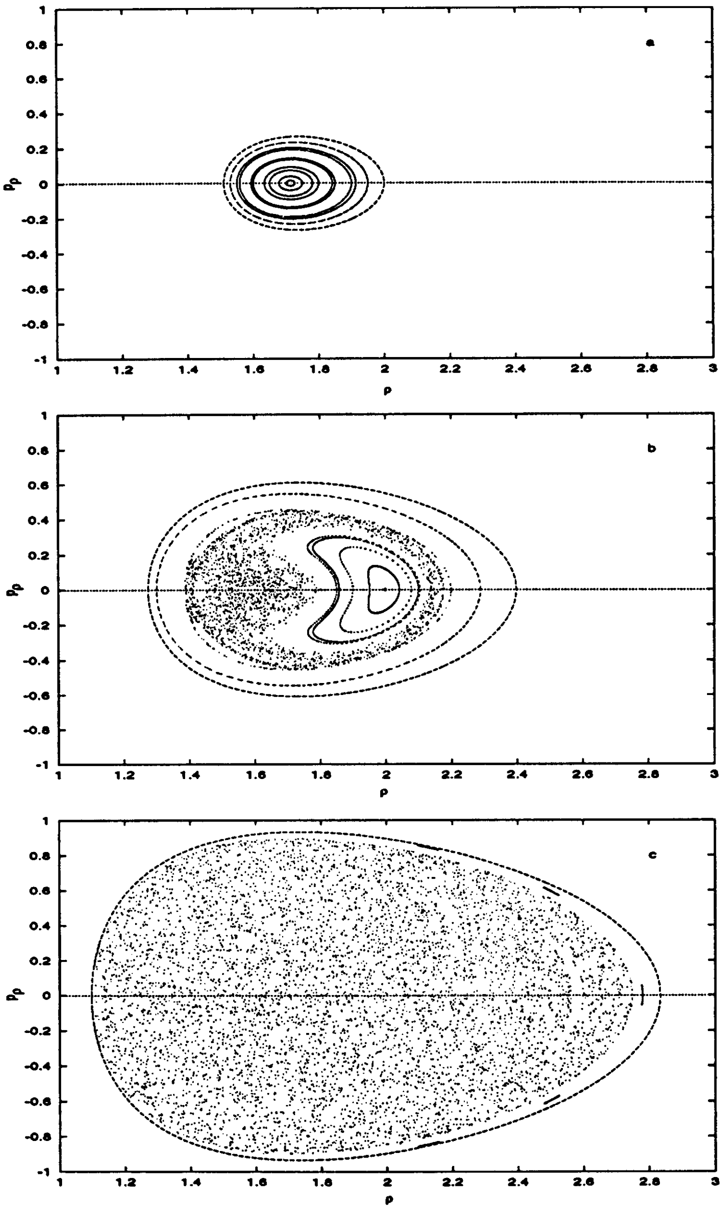

Figure 4-4: Surface of section for hydrogen in a uniform magnetic field for $l_z = -2$, a) $\epsilon = -0.5$, b) $\epsilon = -0.35$, c) $\epsilon = -0.1$.

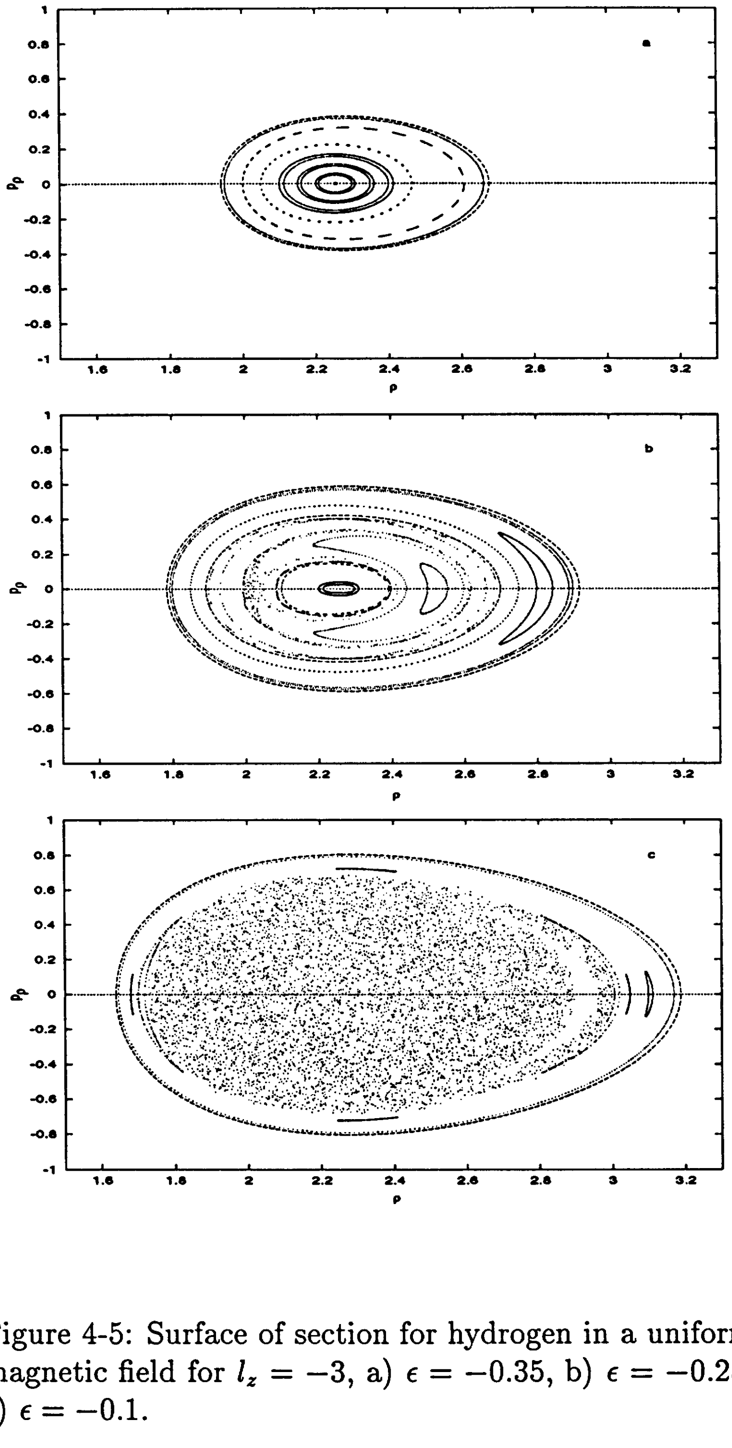

Figure 4-5: Surface of section for hydrogen in a uniform magnetic field for $l_z = -3$, a) $\epsilon = -0.35$, b) $\epsilon = -0.25$, c) $\epsilon = -0.1$.

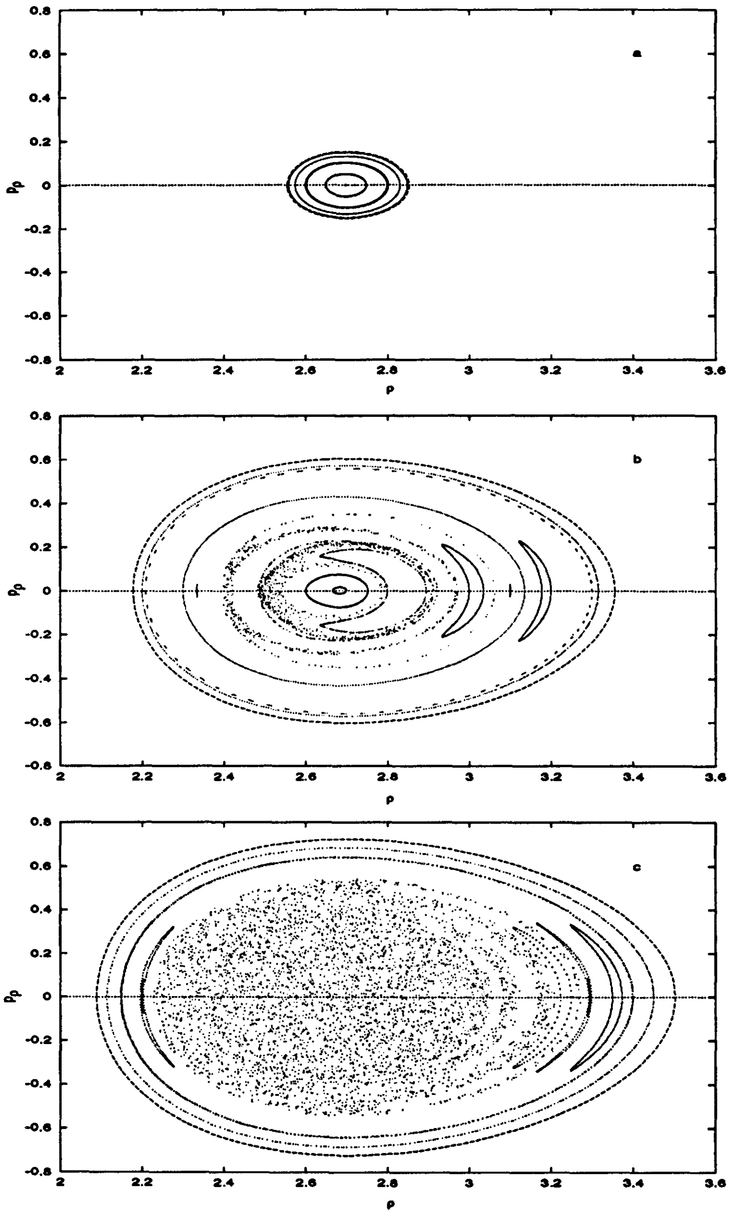

Figure 4-6: Surface of section for hydrogen in a uniform magnetic field for $l_z = -4$, a) $\epsilon = -0.35$, b) $\epsilon = -0.18$, c) $\epsilon = -0.1$.

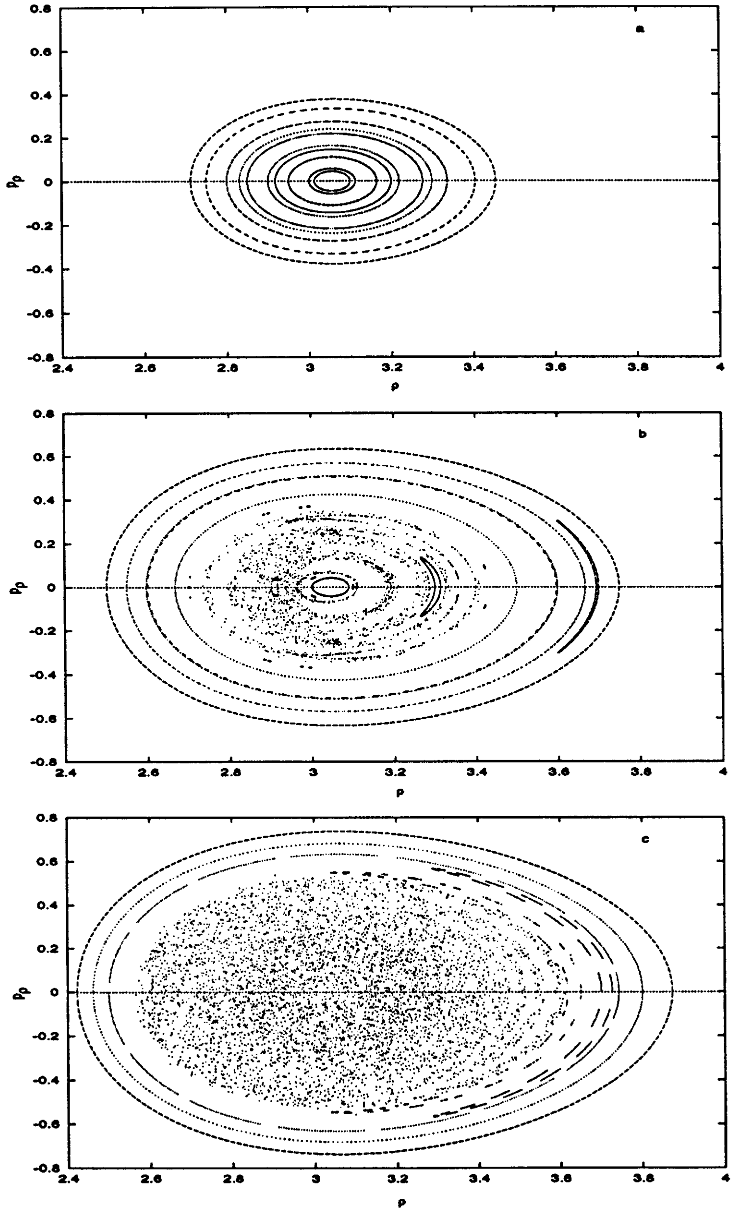

Figure 4-7: Surface of section for hydrogen in a uniform magnetic field for $l_z = -5$, a) $\epsilon = -0.25$, b) $\epsilon = -0.12$, c) $\epsilon = -0.05$.

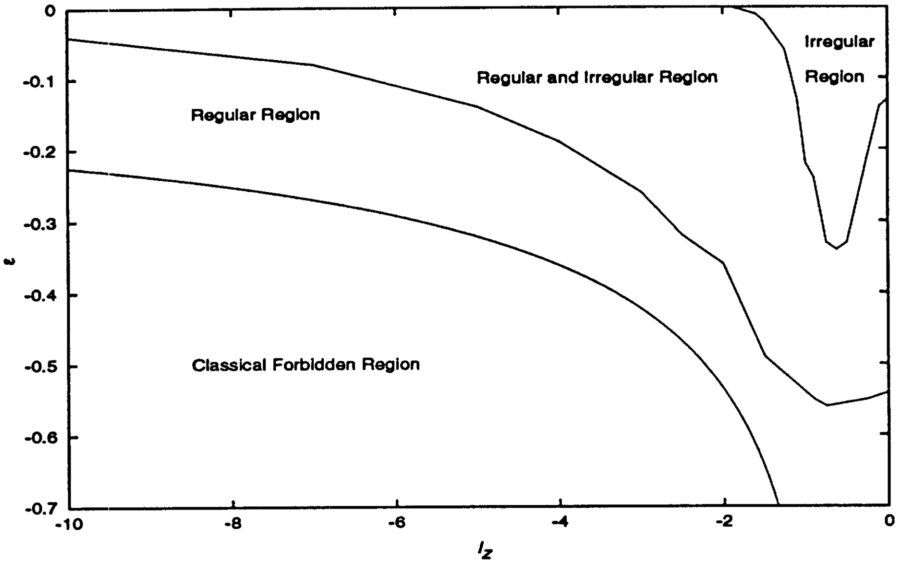

Figure 4-8: Onset of classical chaos in the l_z and ϵ space.

However, for a given ϵ, a system with large magnitude of l_z is less chaotic than a system with a small l_z.

4.3.2 An Approximate Constant of Motion

As mentioned in Sec. 4.2.3, we can correlate the onset of chaos with the destruction of symmetries. The disappearance of tori with increasing magnetic field guarantees the lack of an *exact* third constant of motion. However, the presence of tori everywhere in phase space at small magnetic fields suggests the possible existence of an *approximate* symmetry. Solov'ev indeed found such an approximate constant of motion [Sol81]. He divided the electron motion into the motion along an unperturbed elliptical trajectory and a slow variation of this ellipse due to a small magnetic field. The elliptical parameters are chosen to be $\vec{L}$ and $\vec{A}$, the angular momentum and the Laplace-Runge-Lenz vector (see Eqn. 4.9), respectively. In addition to the exact constants of motion E and L_z, he found a third approximate constant of motion Λ, within an accuracy of B^4:

$$\Lambda = 4A^2 - 5A_z^2. \tag{4.49}$$

One can describe the system in terms of the motion of $\vec{A}$, which is directed along the major axis of the ellipse. $\vec{A}$ rotates around the magnetic field if Λ is positive and vibrates along the magnetic field if Λ is negative. In Fig. 4-2a, the tori that cross the $p_\rho = 0$ axis are the rotators ($\Lambda > 0$) and the tori that do not cross the $p_\rho = 0$ axis are the vibrators ($\Lambda < 0$). Onset of chaos can be interpreted as a gradual destruction of Λ as an approximate constant of motion.

4.3.3 A Brief Remark

As mentioned in the introduction of this chapter, a fundamental characteristic of chaotic motion is great sensitivity of the motion to small changes in initial conditions. Closely neighboring trajectories diverge exponentially. A quantitative measure for such exponential instability is provided by the Lyapunov exponent, which, roughly speaking, measures the mean rate of exponential separation of neighboring trajectories. A number of authors have studied Lyapunov exponents for the diamagnetic hydrogen atom [SNF$^+$88] [Win87]. We will not discuss the Lyapunov exponent for the diamagnetic hydrogen atom here, but we will return to the consideration of the Lyapunov exponent in Chapter 8.

4.4 Chaos in Open Systems

Throughout this chapter we have limited our discussions to trajectories that are bound. Through a judicious choice of a slice in phase space, one can describe the motion with a surface of section. For an unbound system — the so-called open system — this luxury is lost. Positive energy behavior of an initally bound system is related to the process of scattering. Several authors have studied the classical dynamics of nuclear scattering systems with model potentials [Eck87] [BS88]. Eckhardt and Jung discovered that certain scattering systems exhibit sensitive dependence on initial conditions [EJ86]. More precisely, they studied the time delay, the time the incoming particle spends near the scattering center, as a function of the impact parameter. They found that this time delay has a sensitive dependence on the impact parameter. In particular, they showed that this dependence displays fractal properties. They called this behavior irregular or chaotic scattering. Main and Wunner have reported its connection to fluctuations in *quantum* cross sections, the so-called Ericson fluctuations [MW92] [MW94].

In this concluding section, we will apply these ideas to the unbound region of Rydberg atoms in strong fields. We find that the classical dynamics of Rydberg atoms in strong fields in the continuum can be conveniently characterized by considering how the atoms ionize. Our atomic system is not a generic scattering system with an asymptotically incoming and outgoing particle. Rather, the electron is initially localized to the nucleus. This corresponds to the fact that in a real experiment, the electron is excited from a low-lying state confined close to the nucleus. A trajectory does not depend on an impact parameter but on its initial angle with respect to the external fields. We will define the classical ionization time T_{ion} as the time a given trajectory spends near the nucleus before it escapes to infinity. We will study T_{ion} as a function of this initial angle for two systems: one that displays regular behavior and another one that displays chaos.

To illustrate a regular unbound system, we will use the example in Sec. 4.1.2, hydrogen in a uniform electric field. Recall that the integrability of this system is guaranteed by its three constants of motion. The trajectories are launched from the origin. If the electron has enough energy to surmount the saddle point potential that

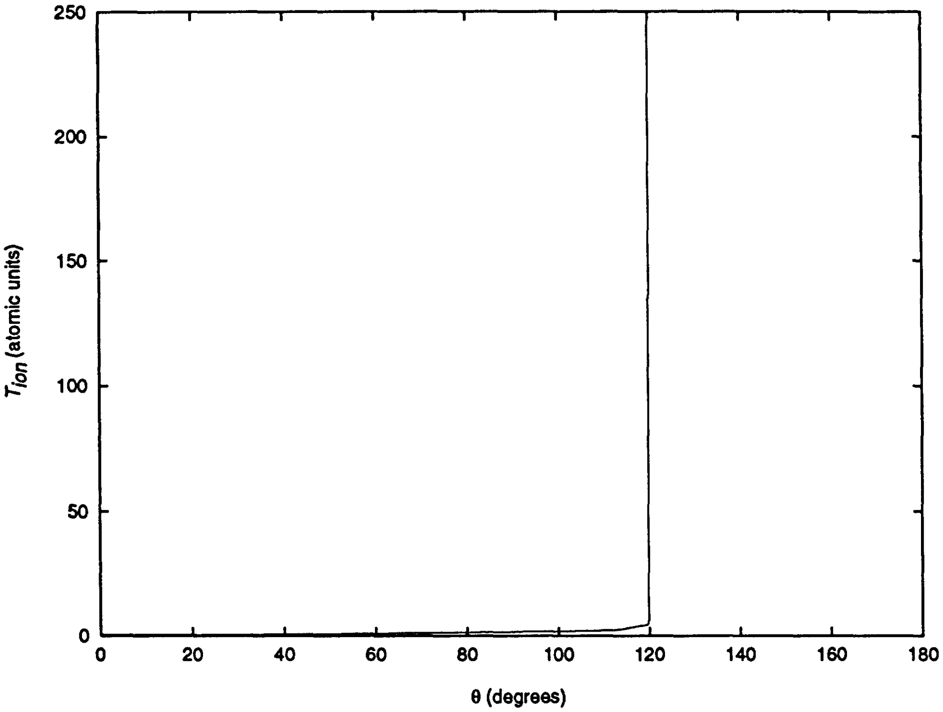

Figure 4-9: T_{ion} of a hydrogen atom in a uniform electric field as a function of θ. $E = -50$ cm^{-1} and $F = 300$ V/cm, and the cutoff on T_{ion} is set at 250.

resulted from the competition between the nuclear and the applied electric field, it will generally ionize. Once the electron has passed the saddle point, it cannot return. Following Main and Wunner [MW92], we define the ionization time T_{ion} to be the time required for an electron near the nucleus to reach the saddle point.

We study T_{ion} as a function of launching angle θ with respect to the electric field axis. Figure 4-9 shows T_{ion} versus θ for an energy below the zero-field ionization limit, but above the saddle point energy. The trajectories ionize very quickly from $\theta = 0°$ to $\theta = 120°$. At $\theta = 120°$, the classical ionzation time rises sharply. Actually, above 120°, T_{ion} is infinite, so we arbitrarily set the cutoff at $T_{ion} = 250$ in atomic units. Since the system is integrable, these trajectories lie on tori and are bound forever. That is, the motion is quasi-periodic. We note that T_{ion} is a smooth function of θ, except for the sharp rise at $\theta = 120°$. This is not surprising because regular trajectories have a smooth dependence on initial conditions. We conclude that a trajectory either escapes quickly through the saddle point or stays on a torus forever. As we will see shortly, this is not the case at all for a chaotic open system.

Michael Courtney has shown that the lithium atom in a uniform electric field displays core-induced chaos in the bound region. The surfaces of section indeed confirm this chaotic behavior [CJSK94]. We will examine this problem above the saddle point, i.e. in the continuum. The following model Hamiltonian can be used for a lithium atom in a uniform electric field:

$$H = \frac{p^2}{2} - \frac{1}{r} + \vec{F} \cdot \vec{r} + V_c(r), \tag{4.50}$$

where $V_c(r)$ describes the deviation from the pure Coulomb potential due to the core at short distances from the nucleus. We find that the generic classical behavior does not depend strongly on the details of the core but only on the sizes of the quantum

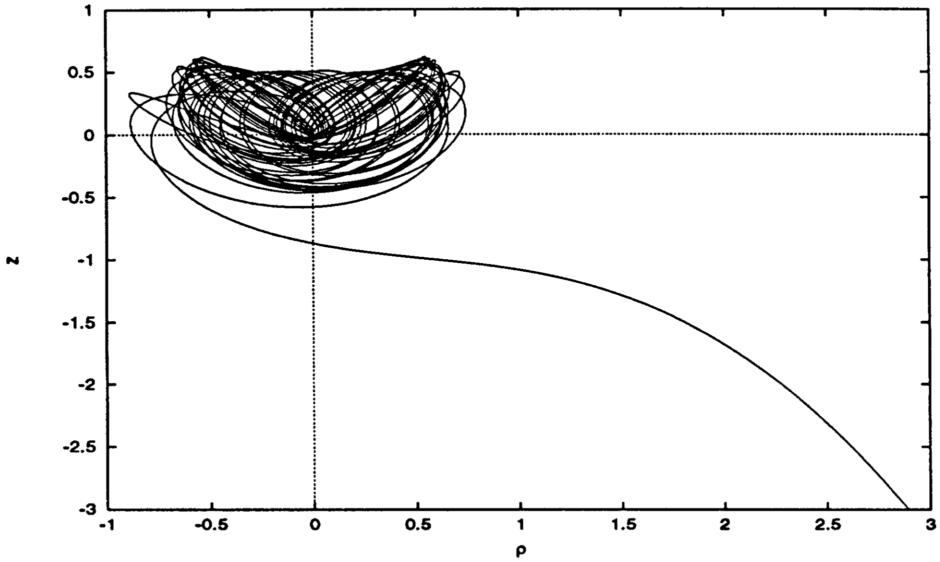

Figure 4-10: Classical trajectory of the valence electron of lithium in a uniform electric field. Horizontal axis is ρ and vertical axis is z. $E = -50$ cm^{-1}, $F = 300$ V/cm, and $\theta = 108.5°$.

defects [CSJK95]. We employ the core potential

$$V_c(r) = -\frac{(Z-1)e^{-ar}}{r}, \tag{4.51}$$

where $Z = 3$ for lithium and $a = 2.13$ is chosen to agree with the measured quantum defects [Cou95].

Figure 4-10 shows a typical trajectory of an electron launched from the origin. In contrast to a hydrogen atom trajectory, this trajectory undergoes very complicated motion near the nucleus for some time before it ionizes through the saddle point. Figures 4-11 show T_{ion} as a function of θ. In contrast to Fig. 4-9, Fig. 4-11a shows wild oscillations of T_{ion} about certain values of θ. Figures 4-11b, 4-11c, and 4-11d show magnifications of 100, 1000 and 10000, respectively, of a region near $\theta = 108.58°$. T_{ion} displays very complicated structure even at a magnification of 10000. These structures

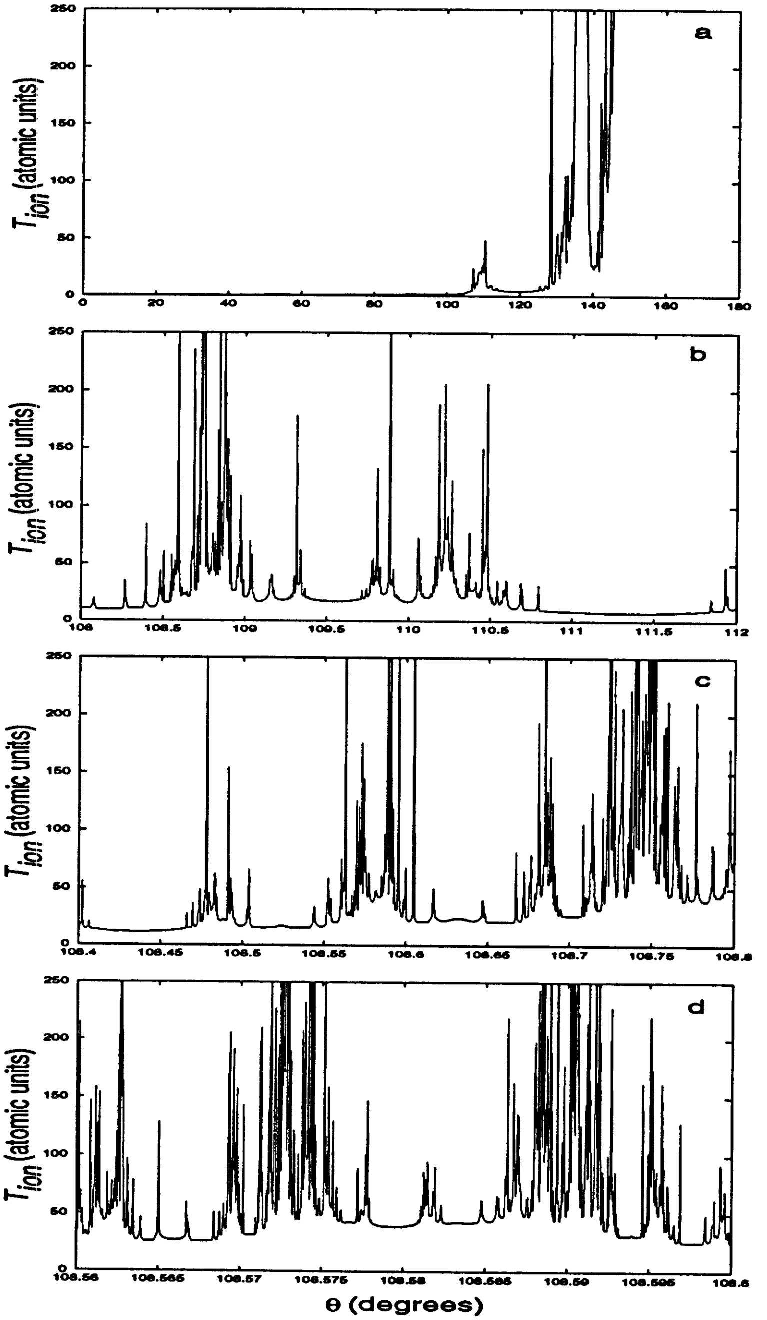

Figure 4-11: T_{ion} of a lithium atom in a uniform electric field, $E = -50$ cm^{-1}, $F = 300$ V/cm, and the cutoff of T_{ion} is set at 250 atomic units. Magnifications about $\theta = 108.58°$, a)×1, b)×100, c)×1000, d) ×10000.

actually persist to ever finer scales: The fractal behavior is evident. The physical explanation lies in the great sensitivity of these trajectories to initial conditions. A small change in initial condition, i.e. the launching angle θ, results in a huge change in the classical ionization time. This is reminiscent of chaos in a bound system, where the neighboring trajectories diverge exponentially. Following Main and Wunner [MW92], we adopt the term *chaotic ionization* to describe the ionization process.

In summary, the fractal structure in the classical ionization time of an open chaotic system is a consequence of the sensitive dependence on initial conditions, just as in a bound chaotic system. The classical ionization time appears to provide a useful way to characterize classical chaos for such a system.

Chapter 5

A Semiclassical Method

The relationship between a classically integrable system and its quantum counterpart is rather well understood. As we recall from Sec. 4.1.1, an integrable system with N degrees of freedom has a set of N conserved action variables. The quantum energy eigenvalues and the corresponding wavefunctions can be readily obtained semiclassically through the appropriate quantization of these action variables. This semiclassical quantization method will be discussed in detail in Sec. 5.1.

Such a quantization method fails for a chaotic system because a chaotic trajectory does not lie on any torus and thus does not have any well defined conserved action variables. The goal of quantum chaos is to correlate quantum structure with classically chaotic behavior in a nonintegrable system. In this thesis, we focus on two issues that are more relevant to quantum spectra: the manifestation of classical chaos in quantum spectra and the possible prediction of quantum spectra from classical dynamics. The semiclassical periodic-orbit theory and the closely related closed-orbit theory were developed to address these issues. They relate large scale spectral structure to classical trajectories. In particular, periodic-orbit theory asserts that every periodic orbit leads to a modulation of the spectral density of states. Closed-orbit theory asserts that every closed orbit, a periodic orbit that is closed at the nucleus, modulates the photoexcitation spectrum. These will be the subjects of Sec. 5.2 and Sec. 5.3.

5.1 Semiclassical Quantization

In this section we will review the semiclassical quantization conditions for an integrable system. The familiar WKB expansion for bound systems with one degree of freedom will be introduced (Sec. 5.1.1). This will be generalized to systems with N degrees of freedom, the EBK quantization (Sec. 5.1.2). The difficulty of semiclassical quantization for a chaotic system will be pointed out.

5.1.1 WKB Expansion and Bohr-Sommerfeld Quantization

We consider a one-dimensional time-independent Schroedinger equation

$$\frac{\hbar^2}{2m}\frac{\partial^2\psi}{\partial x^2} + (E - V(x))\psi = 0. \tag{5.1}$$

The wavefunction can be written as

$$\psi(x) = Ae^{iS(x)/\hbar}, \tag{5.2}$$

where S(x) can be expanded in powers of $\hbar$

$$S(x) = S_0 + \hbar S_1 + \frac{\hbar^2}{2}S_2 + \cdots. \tag{5.3}$$

Substituting into Eqn. 5.1 and equating powers of $\hbar$ lead to

$$O(\hbar^0) : (\frac{\partial S_0}{\partial x})^2 = p^2 \tag{5.4}$$

$$O(\hbar^1) : \frac{\partial S_0}{\partial x}\frac{\partial S_1}{\partial x} = \frac{i}{2}\frac{\partial^2 S_0}{\partial x^2}, \tag{5.5}$$

where $p^2 = 2m[E - V(x)]$. The bound solutions are

$$S_0(x) = \pm \int_{x_0}^{x} p(x)dx, \tag{5.6}$$

and

$$S_1(x) = \frac{i}{2}\ln p(x). \tag{5.7}$$

The wavefunction to first order in $\hbar$ is

$$\begin{aligned} \psi(x) &= \frac{A}{\sqrt{p}}\exp(+\frac{i}{\hbar}\int_{x_0}^{x} p(x)dx) + \frac{B}{\sqrt{p}}\exp(-\frac{i}{\hbar}\int_{x_0}^{x} p(x)dx) \\ &= \frac{A}{\sqrt{p}}\sin(\frac{1}{\hbar}\int_{x_0}^{x} p(x)dx + \alpha). \end{aligned} \tag{5.8}$$

This is the semiclassical WKB approximation to a true bound state quantum wavefunction in the limit $\hbar \to 0$. In a region $E > V(x)$ (classically allowed region), $p(x)$ is positive and the wavefunctions are oscillatory. For $E < V(x)$ (classically forbidden region), $p(x)$ is negative and the wavefunctions are exponentially decaying. Careful use of the connecting formulas in both regions (see any quantum mechanics book, for example Liboff [Lib80]) and imposing single valuedness on the wavefunction give the famous Bohr-Sommerfeld quantization rule for the quantum eigenvalues,

$$\oint p(x)dx = 2\pi\hbar(n + \frac{1}{2}), \tag{5.9}$$

where $\oint$ represents the integral around a closed path.

5.1.2 EBK Quantization

The above discussions can be readily generalized to a system with N degrees of freedom. We define the action as

$$S(\vec{q}) = \int_{q_0}^{q} \vec{p}(\vec{q}) \cdot d\vec{q}, \tag{5.10}$$

where the integral runs over each topologically independent trajectory on a torus. Together with a density function $\rho(\vec{q})$ (the density of the classical trajectories in phase space, assuming a uniform distribution of initial conditions), the above equation can be used to construct a wave function

$$\psi(\vec{q}) = \sum_r |\rho_r(\vec{q})|^{1/2} \exp(\frac{i}{\hbar} S_r(\vec{q})), \tag{5.11}$$

where the sum runs over all topologically independent trajectories on a torus. This wavefunction satisfies the Schroedinger equation in the limit $\hbar \to 0$. As in the case of one degree of freedom, the connecting formulas and single-valuedness of the wavefunction give the quantization conditions. However, here we have more than one closed path. As mentioned in Sec. 4.1.1, an N-dimensional torus has N topologically distinct closed circuits. As a result one should quantize the action variables as defined in Eqn. 4.6,

$$\oint_{C_k} \vec{p} \cdot d\vec{q} = 2\pi\hbar(n_k + \frac{\alpha_k}{4}), \tag{5.12}$$

where C_k is over each topologically distinct closed path on a given torus and α_k is the Maslov index which keeps track of the number of caustics traversed [1]. The quantum spectrum (the set of eigenvalues) can thus be extracted from this semiclassical quantization method, the so-called EBK quantization rule. This quantization condition

---

[1] In optics, caustics correspond to the coalescence of rays which leads to points of high intensity such as those observed in the focusing of light.

assumes the existence of a torus. Einstein was the first one to realize that if C_k is not well defined, as in the case of a chaotic trajectory, this quantization rule and thus the construction of a wavefunction from the classical trajectories will not be possible [Ein17].

5.2 Periodic-Orbit Theory

In 1970, Gutzwiller develped periodic-orbit theory to help answer the key question in quantum chaos: How can classical dynamics be used to predict the quantum energy spectrum when the classical system is chaotic? [Gut90] In contrast to the EBK quantization for an integrable system where the goal is to obtain the eigenvalue of each individual state, period-orbit theory deals with the fluctuations in the spectral *density of states.*

5.2.1 Background

The starting point of the theory is the quantum mechanical propagator $K(\vec{q}\,'', \vec{q}\,', t)$ which gives the transition amplitude for a particle to arrive at $\vec{q}\,''$ when its initial location is at $\vec{q}\,'$. That is,

$$\psi(\vec{q}\,'', t) = \int d^3\vec{q}\,' K(\vec{q}\,'', \vec{q}\,', t)\psi(\vec{q}\,', t_0). \tag{5.13}$$

Clearly, the time evolution of the wave function and hence the eigenvalues are completely determined if $K(\vec{q}\,'', \vec{q}\,', t)$ and $\psi(\vec{q}\,', t_0)$ are known. The explicit formula for the propagator is given by Feynman's path integral [Sak85]:

$$K(\vec{q}\,'', \vec{q}\,', t) = \int_{\vec{q}\,'}^{\vec{q}\,''} D[\vec{q}, t] e^{iS(\vec{q},t)/\hbar} \tag{5.14}$$

where $S(\vec{q})$ is the action function defined in Eqn. 5.10. $\int_{\vec{q}'}^{\vec{q}''} D[\vec{q}]$ is the path integral summing over *all* possible paths, given by [Sak85]

$$\int_{\vec{q}_1}^{\vec{q}_n} D[\vec{q},t] \equiv \lim_{n\to\infty} \left(\frac{1}{2\pi i\hbar\Delta t}\right)^{(n-1)/2} \int dx_{n-1} \int dx_{n-2} \cdots \int dx_2. \tag{5.15}$$

In the semiclassical limit ($\hbar \to 0$), the propagator is given by a sum over *classical* trajectories only. The contributions from other paths interfere destructively due to the smallness of $\hbar$. The explicit semiclassical approximation to Feynman's path integral can be written as [Gut82]

$$K(\vec{q}\,'',\vec{q}\,',t) = (\frac{1}{2\pi i\hbar})^{N/2} \sum_r \det \left|\frac{\partial^2 S_r}{\partial q'\partial q''}\right|^{1/2} e^{i(S_r/\hbar-\mu_r\pi/2)}, \tag{5.16}$$

where N is the dimensionality of the system, S_r is the classical action over one trajectory, μ_r is the same Maslov index as described in Sec. 5.1.2, and the sum is over all *classical* trajectories. The determinant is the classical amplitude. It gives a semiclassical approximation to the probability density. This semiclassical equation for the propagator has a striking resemblence to the wave function constructed from the EBK quantization in Eqn. 5.11. Indeed, for an integrable system where all trajectories are confined on tori, this sum can be readily evaluated and the results are identical to those achieved using separations of variables and the application of the EBK quantization [Gut90]. For a chaotic system, where the trajectories do not lie on any torus, evaluating such a sum is a formidable task. As of now, no general methods are available.

5.2.2 The Trace Formula

The problem becomes more tractable if one is interested only in the energy level density of states. This is given by [Gut82],

$$\rho(E) = -\frac{1}{\pi} \int \mathrm{Im}\,[G(q,q,E)]dq \tag{5.17}$$

where

$$G(q,q,E) = -\frac{i}{\hbar} \int_0^\infty e^{iEt/\hbar} K(q,q,t)dt \tag{5.18}$$

is the Fourier transform of the propagator, known as the Green's function. $\rho(E)$ is also known as the trace of $G(q'',q',E)$ because one can think of $G(q'',q',E)$ as a matrix with rows numbered by q'' and columns numbered by q'. $\rho(E)$ is essentially the sum of the diagonal elements. The diagonal elements $G(q,q,E)$ can be evaluated using Eqn. 5.18 and Eqn. 5.16. Since the propagator of each diagonal element $K(q,q,t)$ starts and ends at the same position, we no longer need to sum over all possible classical trajectories, but only those that start and end at the same position. Gutzwiller also proves that the trajectories with different initial and final momenta have negligible contributions [Gut90]. Trajectories with the same initial and final positions and momenta are called *periodic orbits.* Thus the calculation of the spectral density of state reduces to a summation over all periodic orbits. After many manipulations using Eqn. 5.16, Eqn. 5.17, and Eqn. 5.18, the trace formula can be written more explicitly as

$$\rho(E) = \frac{1}{i\hbar} \sum_r \frac{T_r}{2\sinh(\chi_r/2)} e^{i(S_r/\hbar - \mu_r\pi/2)}, \tag{5.19}$$

where T_r and S_r are the period and the action of a given orbit, respectively, and the sum is over all periodic orbits. The amplitude $1/2\sinh(\chi_r/2)$ is proportional to the density of neighboring trajectories. χ_r, proportional to the Lyapunov exponent, determines the relative instability of an orbit. The situation is different for a stable orbit, where the neighboring trajectories wind around it. In this case $1/2\ \sinh(\chi_r/2)$ becomes $1/2\ \sin(\chi_r/2)$, where $\chi_r = 2\pi m$ is the winding number. This presents a singularity at $\sin(\chi_r/2) = 0$. As we will see in Sec. 6.3.2, this breakdown in the trace formula corresponds to a classical bifurcation of periodic orbits.

It is worth emphasizing that periodic-orbit theory does not claim any relationship between individual classical orbits and individual quantum states. It merely asserts that every classical periodic orbit contributes a sinusoidal oscillation to the density of states. A large number of periodic orbits (including very long period orbits) is required to obtain an approximation to individual eigenvalues. The periodic orbits proliferate and become increasingly unstable as the system becomes chaotic. Consequently, hunting down all periodic orbits in a chaotic system poses a formidable task. It is not yet known whether periodic-orbit theory converges. Nevertheless, a finite set of short period orbits gives a semiclassical approximation to the finite resolution density of states.

5.3 Closed-Orbit Theory

In a typical spectroscopic experiment, one measures either well resolved oscillator strengths or the average oscillator strength density, but not a density of states. In 1987, Delos and co-workers extended the ideas of periodic-orbit theory to oscillator strength density and developed closed-orbit theory.

5.3.1 Basic Formulation

For an atomic transition between initial state ψ_i and final state ψ_f, the oscillator strength is given by

$$f_{fi} = \frac{2m_e(E_f - E_i)}{\hbar^2} | < \psi_f | D | \psi_i > |^2, \tag{5.20}$$

where D is the electric dipole operator. The transition rate to an excited state is directly proportional to this oscillator strength.

If the final states are not resolved in the experiment, then the total transition rate is proportional to the average oscillator strength density given by

$$D\bar{f}(E_f) = \int f_{fi}\rho(E_f)g(E - E_f)dE_f, \tag{5.21}$$

where $\rho(E_f)$ is the density of final states given by Eqn. 5.17, and $g(E - E_f)$ is the experimental resolution function. Using the Green's function of Eqn. 5.18 in Eqn. 5.17, the average oscillator strength can be written as

$$D\bar{f}(E) = -\frac{2m_e(E - E_i)}{\pi\hbar^2} \operatorname{Im} < D\psi_i | G(E) | D\psi_f > . \tag{5.22}$$

Using the semiclassical approximation of Eqn. 5.16, Delos and co-workers obtained an expression similar to Eqn. 5.19 for the average oscillator strength density [DD88a] [DD88b],

$$D\bar{f}(E) = Df_0(E) + \sum_k \sum_{n=1}^{\infty} D_{nk} \sin(T_{nk}E + \phi_{nk}), \tag{5.23}$$

where $Df_0(E)$ is a smooth background term. Because the initial state is usually the ground state localized near the nucleus, the sum runs only over all periodic orbits that are closed at the nucleus, the so-called closed orbits. In the above equation, k goes over all primitive closed orbits and n runs over their repetitions. T_{nk} is the period of a given orbit. D_{nk} is the strength of the modulation, known as the recurrence amplitude of each closed orbit. It contains information about the short-time stability of the orbit, its initial and final angles, and the polarization of the incident photons. ϕ_{nk} is a phase that is computed from the Maslov index and other geometrical considerations. More explicit expressions for D_{nk} and ϕ_{nk} can be found in [DD88b].

Equation 5.23 has a simple physical interpretation. When an atom absorbs a photon, the electron goes into an outgoing Coulomb wave. This wave propagates away from the nucleus to large distances. At these distances, the outgoing wave fronts can be approximated semiclassically, and they are basically correlated with classical trajectories. Eventually, the trajectories and the wave fronts are turned back by the external fields; some of the orbits return to the nucleus, and the associated waves interfere with the outgoing waves to produce the sinusoidal oscillations. This is the essence of closed-orbit theory.

Finally, using closed-orbit theory to compute an experimental spectrum with resolution δE requires summing over all closed orbits with periods up to $2\pi\hbar/\delta E$. The theory has enjoyed considerable success for low resolution spectra [MWW+94]. But, as with periodic-orbit theory, its applicability to high resolution spectra is still an open question.

5.3.2 Technique of Scaled-Energy Spectroscopy

If the oscillator strength density is modulated by each closed orbit, then the Fourier transform of the experimental spectrum will give signatures (known as the recurrences) corresponding to individual closed orbits. A typical photoexcitation spectrum is taken at a fixed external field value while the laser frequency (corresponding to the excitation energy E) is varied. This limits the useful energy range over which the Fourier transform can be taken for two reasons. First, the period of each closed orbit changes with excitation energy. Secondly, the recurrence amplitude also changes rapidly as a function of energy. For these reasons, the Fourier transform of a regular photoexcitation spectrum gives only recurrences of closed orbits that have relatively constant periods over the given energy range, generally only very short period orbits. To observe the recurrences of all closed orbits, the spectrum has to be limited to a very small energy range. This has the implication that long period orbits may not be observable.

To circumvent this difficulty, Welge and co-workers developed the technique of scaled-energy spectroscopy. They originally applied the technique to diamagnetic hydrogen, but it can be readily extended to other systems. The key idea is to exploit a classical scaling law such as the one shown in Eqn. 4.46. The scaled Hamiltonian of Eqn. 4.47 depends on $\epsilon = E/B^{2/3}$. Thus a spectrum generated under conditions of constant ϵ corresponds to the classical dynamics of an invariant Hamiltonian. In such a scaled-energy experiment, the magnetic field and the laser frequency are varied so that ϵ remains constant. The Fourier transform of the resulting spectrum bears clear signatures of the closed classical orbits.

We now turn to a more quantitative analysis. Equation 5.23 for a scaled spectrum recorded as a function of $B^{-1/3}$ yields

$$D\bar{f}(B^{-1/3}) = Df_0(B^{-1/3}) + B^{1/6}\sum_k \sum_{n=1}^{\infty} D_{nk}\sin(B^{-1/3}\tilde{S}_{nk} + \phi_{nk}). \qquad (5.24)$$

The recurrence amplitude D_{nk} and scaled action $\tilde{S}_{nk}$ of each closed orbit are kept constant during the scaled-energy scan. The only dependence of the modulation strength on B is via $B^{1/6}$ which is proportional to $E^{1/4}$, a very weak dependence. (This weak dependence on B is negligible for a typical scaled-energy spectrum. However, it needs to be taken into account for a spectrum covering a large range of magnetic field.) The actions of the modulating orbits can be clearly identified in the Fourier transform of a scaled-energy spectrum, using $B^{-1/3}$ as the Fourier transform variable.

Chapter 6

Rydberg Atoms in Parallel Fields

Our understanding of physics in the semiclassical regime — particularly the quantum behavior of a disorderly system — has been deepened by theoretical and experimental studies of Rydberg atoms in applied static fields [HRW89]. For a variety of reasons, up to now these studies have focused on the bound state: Quantum solutions are more tractable in the bound states than for the continuum; classical motion can be portrayed by surfaces of section, a powerful method that is convenient for bound systems only; and experimental studies are much easier to carry out and interpret for bound states than for the continuum. Nevertheless, an understanding of unbound systems is essential for establishing the connections between quantum and classical descriptions of irregular systems. As a step toward this goal, we report in this chapter a study of the behavior of a Rydberg atom in parallel electric and magnetic fields at energies where the system is unbound.

The work described in this chapter builds on a foundation of experimental and theoretical studies by a number of groups. The technique of scaled-energy spectroscopy, pioneered by Welge and his associates [HMW+88], is here extended to the two-field system [1]. We interpret some of the essential features using the closed-orbit theory of Delos and co-workers [DD87], which was developed from the periodic-orbit theory of Gutzwiller [Gut90]. An early study of barium in parallel fields by Rinneberg and co-workers [KNV$^+$88] revealed some of the features one might expect, including a transition from "Quasi-Landau" behavior [GT69] to electric field induced oscillations [FEBL78]. However, the classical interpretation was limited to short period orbits because the spectra were not taken at scaled energies [MRBF$^+$93].

6.1 Qualitative Features

The Hamiltonian of hydrogen in parallel electric field F and magnetic field B (both fields taken to lie along the z-axis) is

$$H = \frac{p^2}{2} - \frac{1}{r} + \frac{1}{8}B^2\rho^2 - Fz. \tag{6.1}$$

In the limit of vanishing magnetic field, the system becomes the hydrogen atom in a uniform electric field, which has an exact quantum solution and its classical motion is regular everywhere. This system has provided a touchstone for closed-orbit theory [GD94] and has served as a testing ground for our understanding of the generation of closed orbits by bifurcations [CJSK95]. However, such a system is obviously not suited to studies of irregular motion. In contrast, in the limit of vanishing electric field, the system evolves into hydrogen in a pure magnetic field, the so-called diamagnetic hydrogen atom, which is known to become strongly chaotic while in the bound regime.

From the above discussion, we expect a transition to disorder as the system evolves from an electric field to a magnetic field dominated region. This is very nicely illus-

---

[1] Scaled energy spectroscopy has previously been employed in a study of Rydberg atoms in crossed electric and magnetic fields in the bound regime [RFW91].

trated by the surfaces of section of the parallel field system in the bound regime as shown in Fig. 6-1. (See Appendix G for a discussion on the semiparabolic uv representation.) The top figure (B = 0.0 T) displays tori everywhere in phase space, signifying regular motion everywhere. Some broken tori appear to be islands-like, but in fact they are rational tori. The middle figure (B = 1.0 T) shows the destruction of some tori, hinting the onset of chaos. The bottom figure (B = 6.0 T) exhibits disorder everywhere.

As mentioned in Sec. 5.3, closed-orbit theory provides a useful connection between the classical and quantum descriptions of a disorderly system. In particular, it asserts that every closed orbit modulates the quantum spectrum with its period. Figures 6-2 show an experimental spectrum from $E = -48$ cm^{-1} to $= -31$ cm^{-1} at $B = 1$ T and $F = 87$ V/cm and its Fourier transform. Although this is not a scaled-energy spectrum, the periodic structure is clearly visible in the spectrum. The oscillations correspond to the closed orbit parallel to the external fields and extending from the nucleus to the classical turning point. This parallel orbit is sometimes known as the "uphill" orbit. The Fourier transform reveals the periods of the primitive orbit and its first repetition. The recurrences due to higher repetitions as well as other closed orbits are not discernible because their periods change rapidly as a function of excitation energy as already discussed in Sec. 5.3.2. To observe these recurrences, we need to employ the technique of scaled-energy spectroscopy described in Sec. 5.3.2.

6.2 Classical Ionization

Before carrying out scaled-energy spectroscopy in the continuum, it is first necessary to characterize the classical motion in this region. As we have discussed in Sec. 4.4, in search for a substitute to the surface of section, we have found that the concept of ionization time T_{ion} provides a useful signature for the transition from orderly to

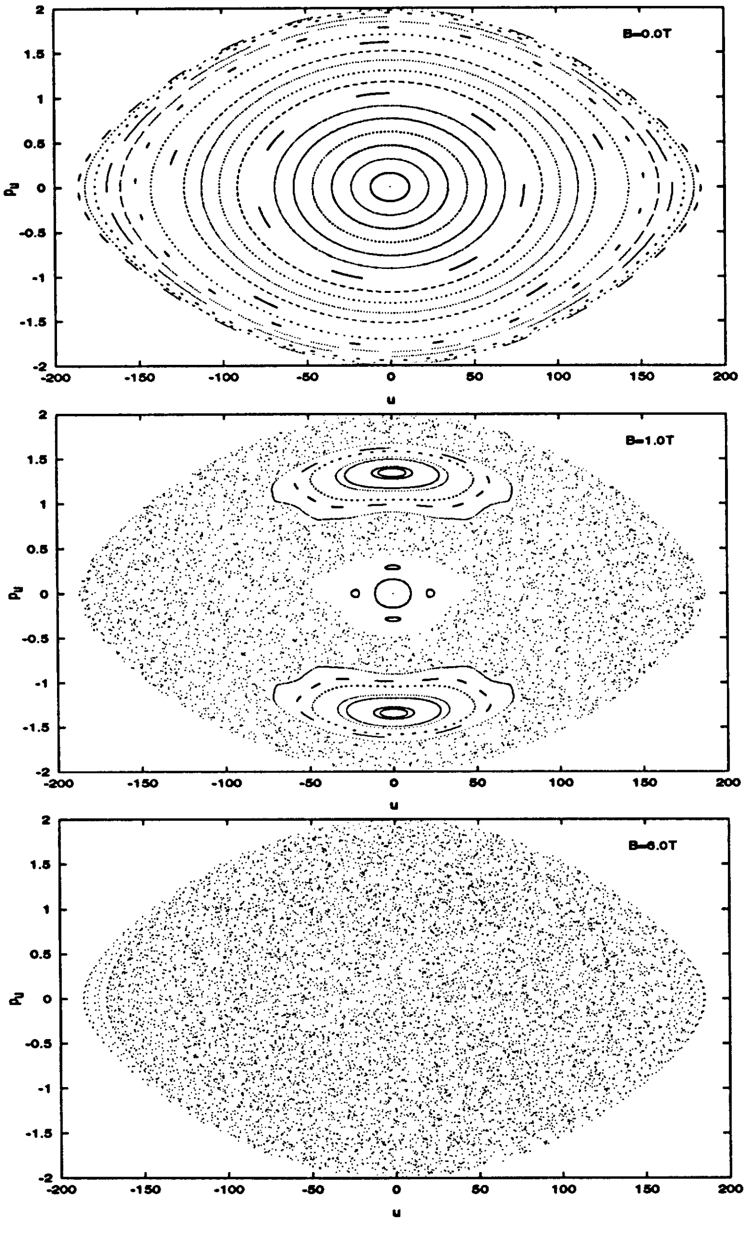

Figure 6-1: Surfaces of section of hydrogen in parallel electric and magnetic fields in uv representation. $E = -20$ cm^{-1} and $F = 15$ V/cm, a) B=0.0 T, b) B=1.0 T, c) B=6.0 T.

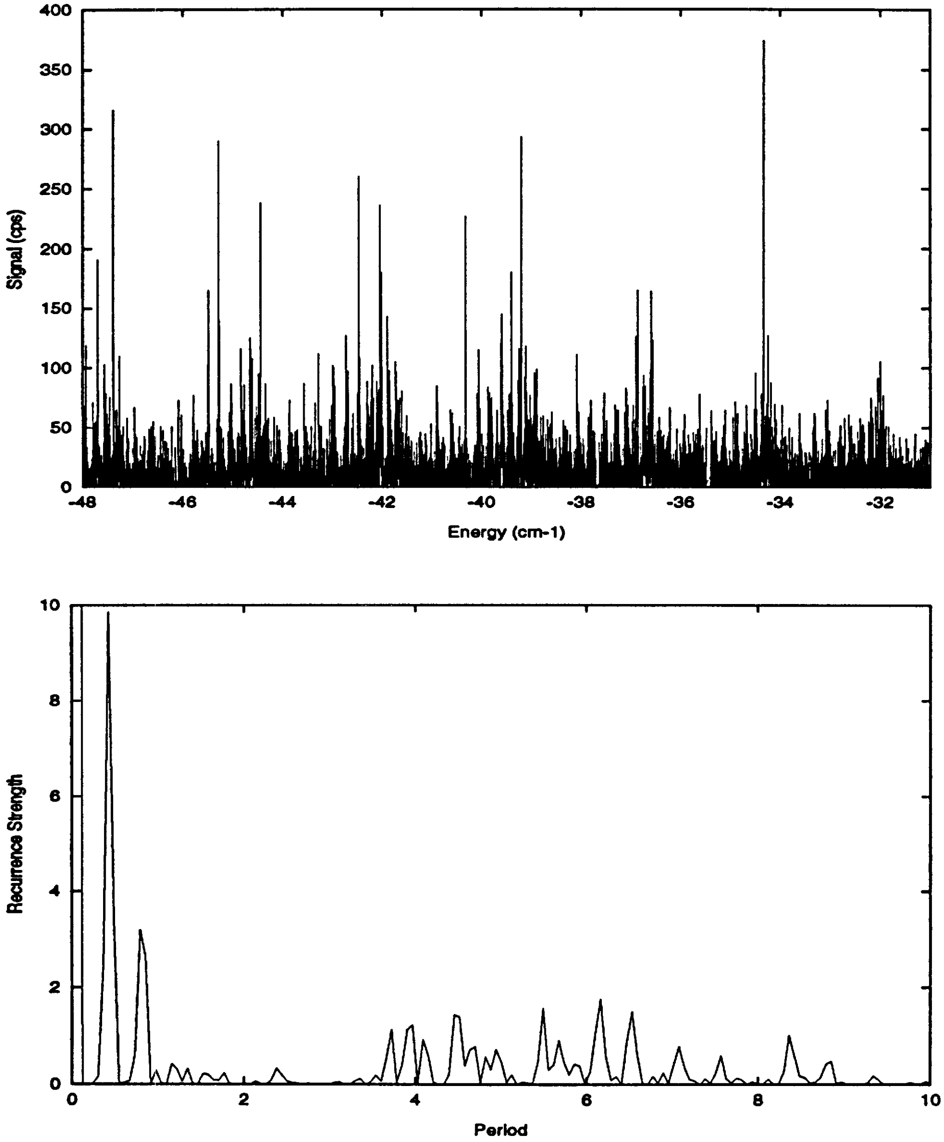

Figure 6-2: Photoexcitation and Fourier transform spectra at $F = 87$ V/cm and $B = 1$ T. Top: photoexcitation spectrum. Bottom: Fourier transform spectrum.

disorderly behavior in an unbound system. Consider a bound atom in parallel electric and magnetic fields, which we take to lie along the z-axis. As we shall show, similar to the lithium atom in an electric field (Sec. 4.4), T_{ion} here displays generic behavior that reveals the nature of the classical motion.

6.2.1 Classical Ionization Time

Turning now to a quantitative description, the classical dynamics of this problem is most conveniently described using scaled variables. Denoting the magnetic field and electric field by B and F, respectively, the Hamiltonian can be rescaled using the substitutions

$$\begin{aligned} r &\rightarrow B^{2/3} r \\ p &\rightarrow B^{-1/3} p \\ f &= B^{-4/3} F. \end{aligned} \tag{6.2}$$

The scaled Hamiltonian $H \rightarrow B^{-2/3} H$ can be written

$$H = \frac{p^2}{2} - \frac{1}{r} + \frac{1}{8}\rho^2 - fz. \tag{6.3}$$

The classical dynamics depends only on the scaled energy $\epsilon = EB^{-2/3}$ and scaled field $f = FB^{-4/3}$, not on E, F, and B separately. In particular, spectra generated under conditions of constant ϵ and f correspond to classical dynamics of an invariant Hamiltonian.

As $f \rightarrow 0$, the system evolves into the diamagnetic hydrogen system which is known to be strongly chaotic for $\epsilon > -0.1$ [HH83]. As $f \rightarrow \infty$, the system evolves into the hydrogen Stark system for which the motion is regular everywhere. At energy $\epsilon > -2\sqrt{f}$ (the saddle point energy), the system lies in the continuum and the motion is unbound.

To investigate the evolution of orderly into disorderly motion, we have studied the behavior of the ionization time at a fixed value of ϵ as f is varied. An electron is launched from the origin at an initial angle θ with respect to the z-axis, and T_{ion} is calculated. ($\theta = 0°$ corresponds to initial motion directly toward the saddle point.) We have chosen to calculate T_{ion} at $\epsilon = 0$ because this energy is particularly convenient for experiment. Figure 6-3 shows how T_{ion} varies with θ for $f = 1.0, 0.4$, 0.25 and 0.05.

In the pure Stark problem, the only periodic orbit is the "uphill" orbit, along the axis with $\theta = 180°$. At other angles, the electron leaves essentially immediately. Consequently, for very large f the ionization time would display almost a delta function dependence on θ. For $f = 1$, (Fig. 6-3a), the system behaves very much like this except T_{ion} remains large for angles down to about 170° due to the stabilizing effect of the magnetic field. At $f = 0.5$ (Fig. 6-3b), the stable region extends to 140°, but below this angle T_{ion} varies erratically for about 15°. At $f = 0.04$ (Fig. 6-3d), the erratic behavior extends to below 60°, with the system displaying wild and random fluctuations. Successive magnifications of a region near 100° at $f = 0.04$ (Figs. 6-4) show the randomly varying pattern similar to the lithium atom in an electric field discussed in Sec. 4.4.

6.2.2 Relationship to Closed Orbits

To investigate the origin of chaotic ionization, we have examined numerically the closed orbits — periodic orbits that are closed at the nucleus. Figure 6-5 shows locations of these periodic orbits with scaled action up to $\tilde{S} = 10$, and T_{ion} as functions of θ. Each needle represents one periodic orbit, and its height indicates the relative short-time stability of each orbit. These orbits themselves never ionize. Stable closed

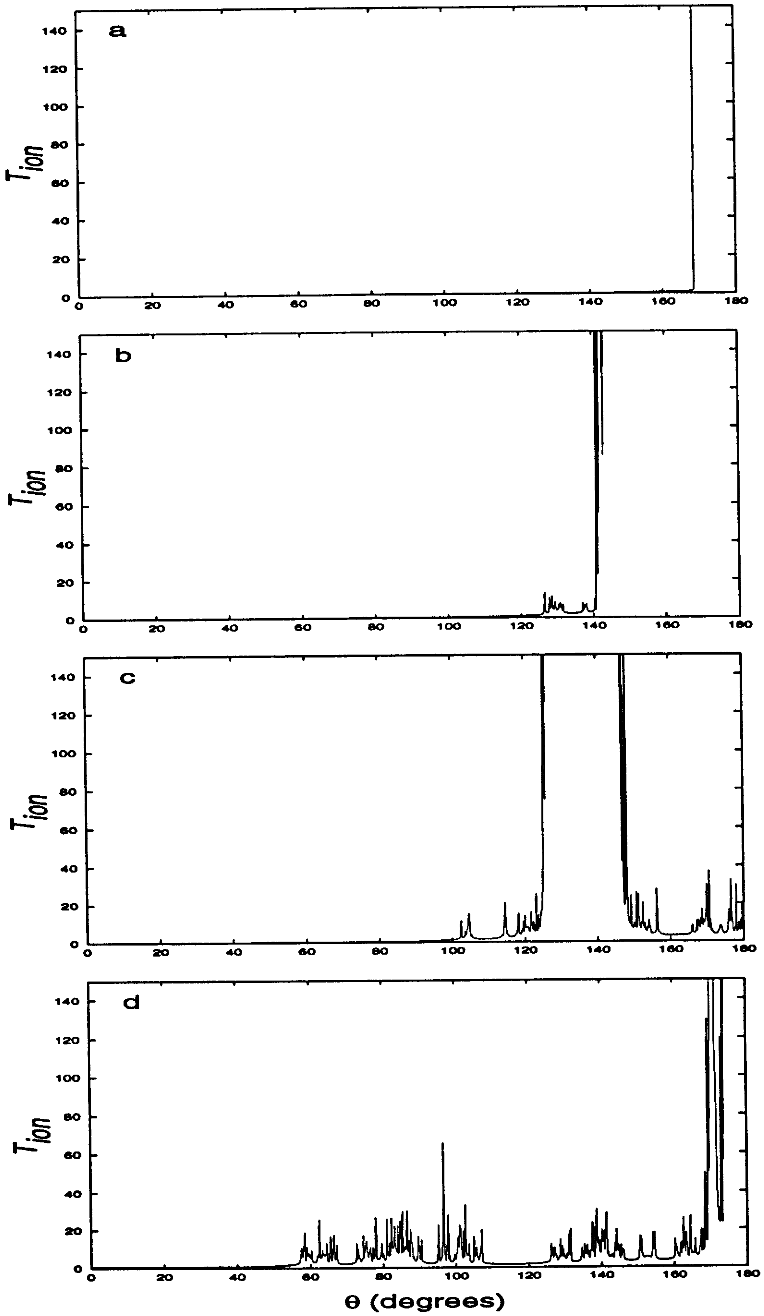

Figure 6-3: T_{ion} (atomic units) as a function of θ at $\epsilon = 0$, cutoff of T_{ion} is set at 150. a) $f = 1.0$, b) $f = 0.4$, c) $f = 0.25$, d) $f = 0.05$.

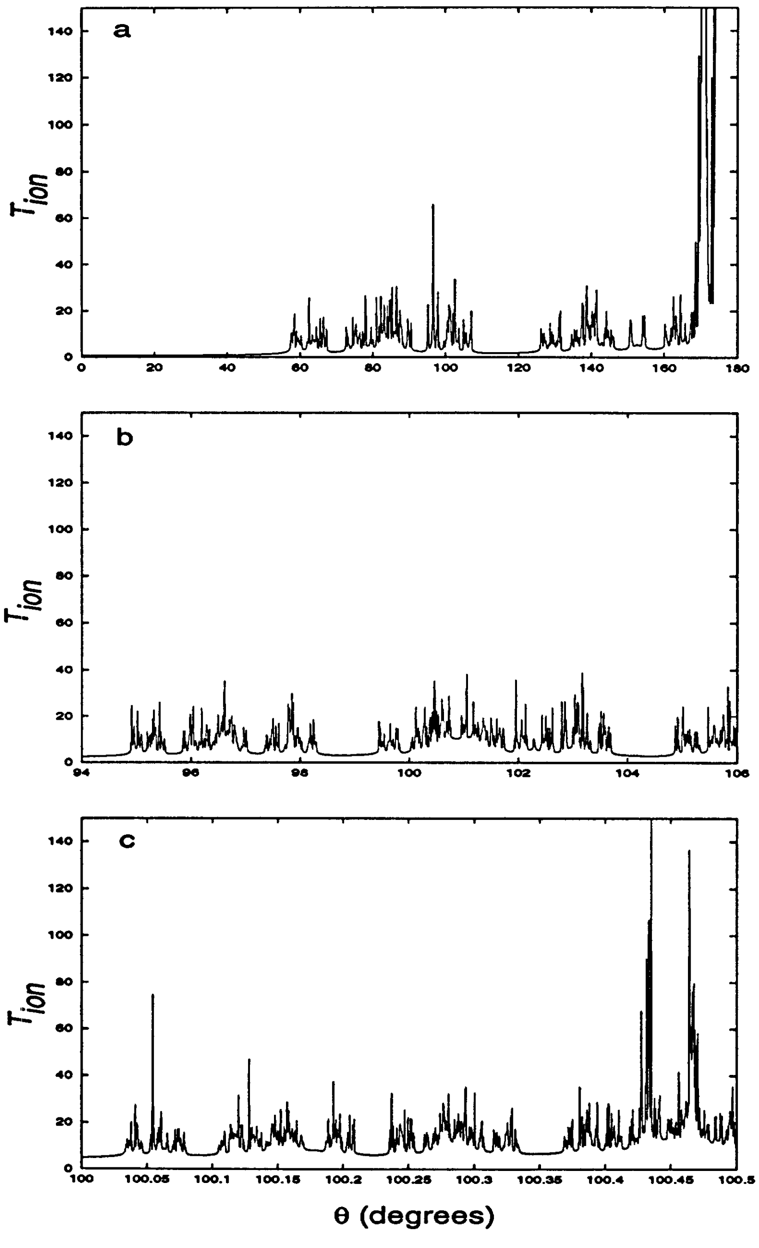

Figure 6-4: Enlargements of a region near $\theta = 100°$ at $\epsilon = 0$ and $f = 0.05$. Magnification of a) 1, b) 15, c) 360.

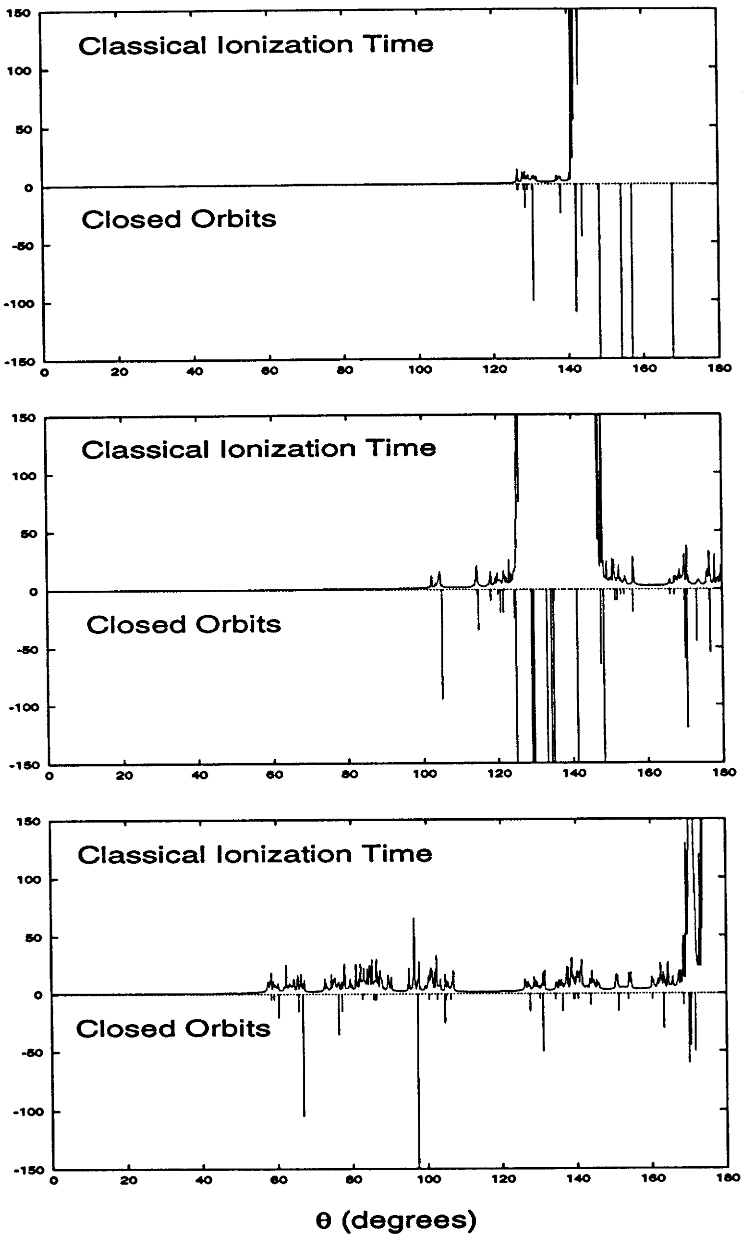

Figure 6-5: Classical ionization time and closed orbits as a function of θ. Each needle represents one closed orbit, and its height indicates the relative stablity of the orbit, $\epsilon = 0$. Top: $f = 0.4$. Middle: $f = 0.25$. Bottom: $f = 0.05$.

orbits tend to confine the neighboring trajectories for a very long time. An example is given in the middle figure of Fig. 6-5 where the trajectories near stable closed orbits tend to have a very long ionization time. The fractal structures appear to be localized in the vicinity of unstable closed orbits. For unstable orbits the time their neighbors spend near the vicinity before escaping to infinity depends sensitively on the initial conditions. These orbits seem to exert a "trapping" effect on nearby trajectories: The sensitivity of these trajectories to θ is the source of the fractal behavior in T_{ion} [KB92]. Analogous behavior occurs in bound systems, where successive enlargements of typical chaotic regions in a surface of section reveal a proliferation of islands and hyperbolic points which correspond to periodic orbits.

6.3 Experimental Results

Closed orbits leave an imprint on the photoexcitation spectrum which can be interpreted using scaled-energy spectroscopy and closed-orbit theory [DD87]. Every closed orbit leads to a modulation of the spectrum with a period corresponding to its scaled action. The Fourier transform of the spectrum, known as the recurrence spectrum, reveals the action of each orbit. Repetitions of a primary orbit generate successive recurrences at multiples of its action. The intensity of a recurrence is related to the stability of the orbit.

6.3.1 Recurrence Spectroscopy

We have performed scaled-energy spectroscopy on $m = 0$ states of lithium at scaled energy $\epsilon = 0$ and scaled fields between $f = 1.0$ and $f = 0.05$. As mentioned before, alkali-metal atoms in external fields are fundamentally different from hydrogen because they can exhibit core-induced chaos [CJSK94]. However, the recurrence spectra are nearly identical for the short-period orbits studied here [ERWS88]. Consequently, the lithium spectra can be interpreted in terms of the classical dynamics of hydrogen.

Figures 6-6 show the photoionization spectrum and its recurrence spectrum of lithium at $\epsilon = 0$ and $f = 0.35$. The periodic structures are evident in the photoionization spectrum. They are more quantitatively characterized by the recurrence spectrum. The heights of the peaks there correspond to recurrence strengths. These peaks are actually the recurrences due to the "uphill" orbit and its repetitions. In contrast to the unscaled spectrum of Fig. 6-2, higher repetitions are clearly visible here. In fact, as we will see shortly, the big peaks here correspond to the approximate locations of the bifurcations of classical periodic orbits.

6.3.2 Bifurcations

For large f, there is but one closed orbit, the "uphill" orbit. This orbit has been extensively investigated for the pure Stark problem and was found to be unstable at $\epsilon \geq 0$ [GD94]. As a result, none of its neighboring trajectories returns to the nucleus. The spectrum contains a fundamental Fourier component from this orbit plus harmonics from its repetitions. The amplitude of the harmonics decreases roughly exponentially.

To investigate more general behavior, we have measured a series of recurrence spectra for values of f between 1.0 and 0.05. Results are shown in Fig. 6-7. For $f = 0.9$, a number of recurrences due to the repetitions of the primary parallel orbit are visible, though the primary recurrence is not. As f is reduced, new recurrences become visible. As we shall explain, these are due to new orbits created by bifurcations of the parallel orbit and its repetitions. Most of these orbits are unstable and their recurrence strengths are so small that experimental identification is not possible. Near bifurcation points, however, orbits often generate large recurrences. A number of these are evident in Fig. 6-7.

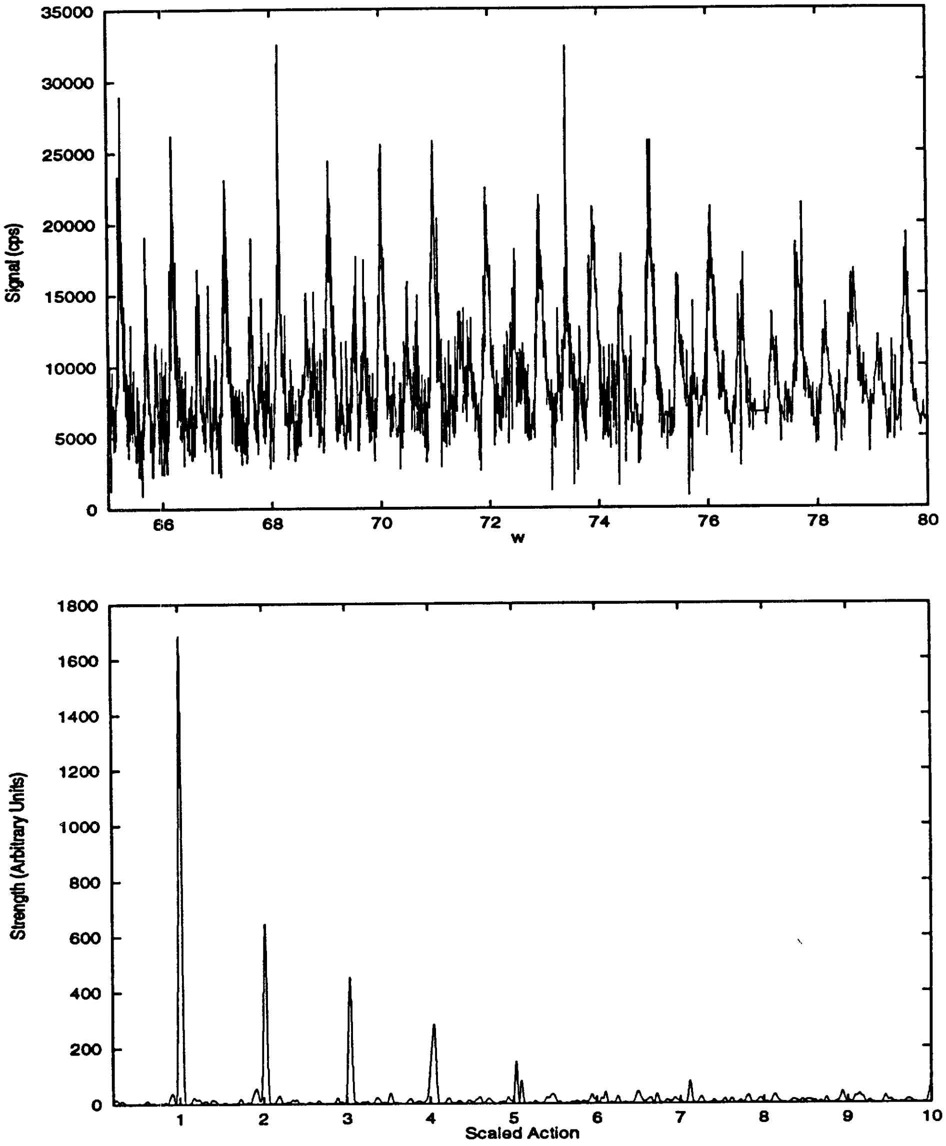

Figure 6-6: Photoionization and recurrence spectra at $\epsilon = 0$ and $f = 0.35$. Top: Photoioniztion spectrum as a function of $w = B^{-1/3}$. Bottom: Fourier transform or the recurrence spectrum.

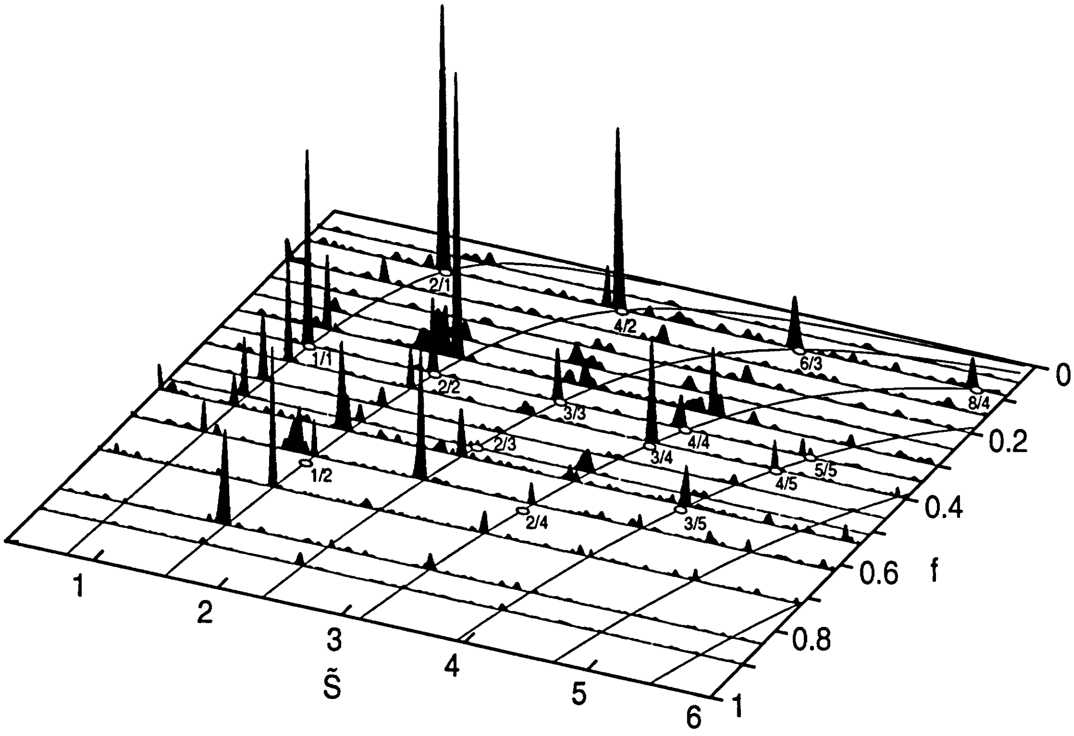

Figure 6-7: Experimental recurrence spectra at $\epsilon = 0$ for scaled fields ranging from $f = 0.05$ to $f = 1$. The curve lines are the calculated scaled actions of the parallel orbit and its repetitions. The bifurcation points are marked with small ovals.

The large increase in recurrence strength near a bifurcation is the result of the focusing of the incoming wave nearly to a point. In its originally formulation, closed-orbit theory actually predicts infinite classical amplitude. The physical reason for this divergence is connected with the singularity of the trace formula discussed in Sec. 5.2.2. At the bifurcation, the neighbors of a closed orbit oscillate about it with a period that is rationally related to the period of the orbit. After precisely n repetitions the neighbors all come back together and are focused at the nucleus [GD94]. Such divergences are familiar in geometical optics with predicts infinite intensity if a plane wave is focused to a point. This can be quantitatively repaired by incorporating diffraction effects in the closed-orbit theory [CJSK95].

A Map of Recurrence Spectra

We consider the motion in semiparabolic coordinates $(u = (r+z)^{1/2}, v = (r-z)^{1/2})$. For the pure Stark system, the u and v motions are independent, but here they are coupled. Consequently, one cannot define independent periods for the two motions. However, an orbit is closed whenever it contains m cycles of motion along v and l cycles of motion along u, where l and m are integers. We define the period ratio of a closed orbit as l/m. Short period orbits correspond to ratios of small integers. Many of these periodic orbits do not touch the nucleus. However, within each family of periodic orbits with period ratio, m/l, there is one closed orbit. In Fig. 6-7, the first bifurcation (the 1/2 bifurcation) and its repetition 2/4 occur at $f = 0.65$. The recurrence at the classical bifurcation point is relatively small, but there is a major enhancement at nearby values of f. This behavior is reminiscent of the pure Stark system as the electrically scaled energy ϵ_F is reduced from positive energy into quasi-discrete region [CJSK95]. For scaled fields between $f = 0.6$ and $f = 0.4$, the bifurcations 3/5, 2/3, 3/4, and 4/5 are visible. At $f = 0.35$, the 1/1 bifurcation and its first few repetitions take place, and at $f = 0.1$, the 2/1 bifurcation and its first

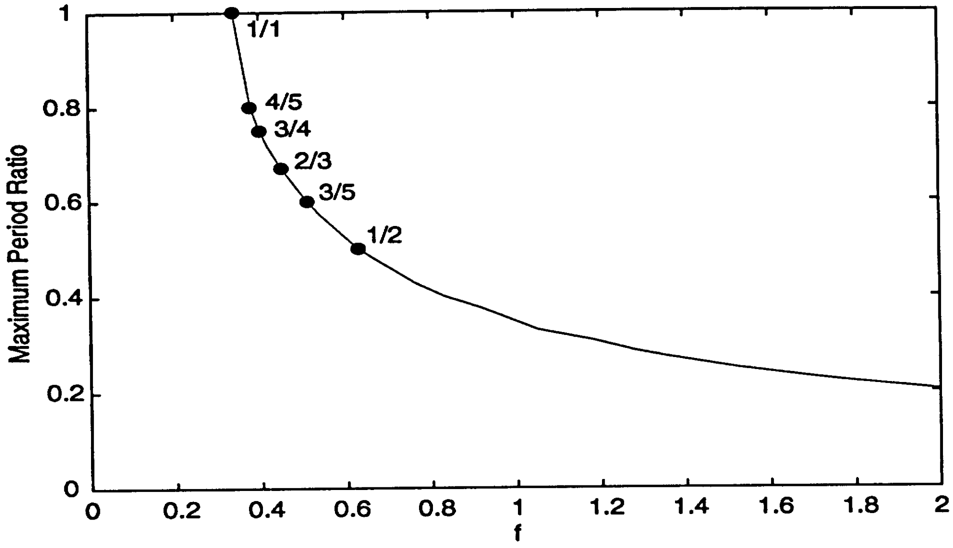

Figure 6-8: The calculated maximum period ratio as a function of f. Dark circles are experimentally observed bifurcation points.

three repetitions can be seen. It is noteworthy that we observed these bifurcations experimentally before we could identify them numerically.

Proliferation of Closed Orbits

Closed orbits are believed to proliferate rapidly as a system becomes chaotic. A graph of the maximum period ratio as f is reduced is shown in Fig. 6-8. Short period orbits correspond to ratios of small integers. As the scaled field is lowered, a bifurcation produces a new closed orbit every time the maximum ratio is a rational number. Some of the experimentally observed bifurcation points are shown as dark circles in Fig. 6-8. At a given f, a closed orbit exists for every rational period ratio between zero and this maximum. A proliferation of possible closed orbits is evident as f is reduced and the system becomes increasingly chaotic. This is contrary to a hydrogen atom in an electric field, where the system is integrable. The maximum period ratio there increases slowly and approaches a finite number asymptotically as the scaled energy is lowered from zero field ionizaton limit into the quasi-discrete region [CJSK95]. The contrast is generic: A regular system possesses a limited number of closed orbits while a chaotic one exhibits a proliferation of closed orbits.

6.3.3 Numerical Results

To check the experimental results, we have also conducted a thorough numerical search of closed orbits. As the system becomes more chaotic, the long period orbits tend to proliferate and become increasingly unstable. Numerical calculations for these orbits tend to be unreliable. For this reason, our numerical efforts are limited to short period orbits. For each orbit, its classical action and classical amplitude are computed. Furthermore, bifurcation process of closed orbits is carefully monitored. A map of such a calculation at $\epsilon = 0$ and scaled fields between $f = 0$ and $f = 1$ is shown in Fig. 6-9. Some of the bifurcation points are marked. However, the peaks shown are not at the exact bifurcation locations since the classical amplitudes diverge there. A quick comparison with Fig. 6-7 shows reasonable agreement. Figure 6-10 displays pictures of some short period orbits in the (ρ, z) space. Each orbit is labelled by its period ratio as discussed in the previous section. We note that each primitive orbit is denoted by an irreducible fraction. For example, orbit $1/2$ is a primitive orbit and orbit $2/4$ is its first repetition. Table 6.1 lists some properties of these orbits at bifurcation points.

6.4 Summary

In summary, we have shown that one can characterize classical chaos in the continuum through the concept of chaotic ionization, and we have demonstrated the validity of the closed-orbit theory for interpreting the continuum spectra of a disorderly system.

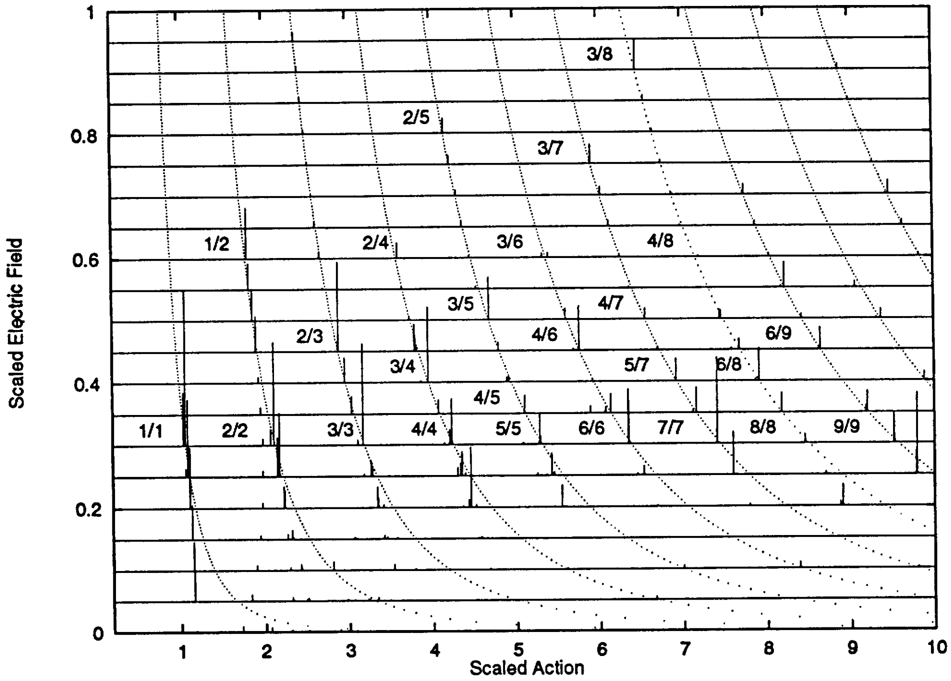

Figure 6-9: Classical computation of closed orbits at $\epsilon = 0$. Each needle represents a closed orbit and the height is the classical amplitude, indicating the stability of a given orbit. The dash lines are the parallel orbit and its repetitions and the bifurcation points of some short period orbits are marked.

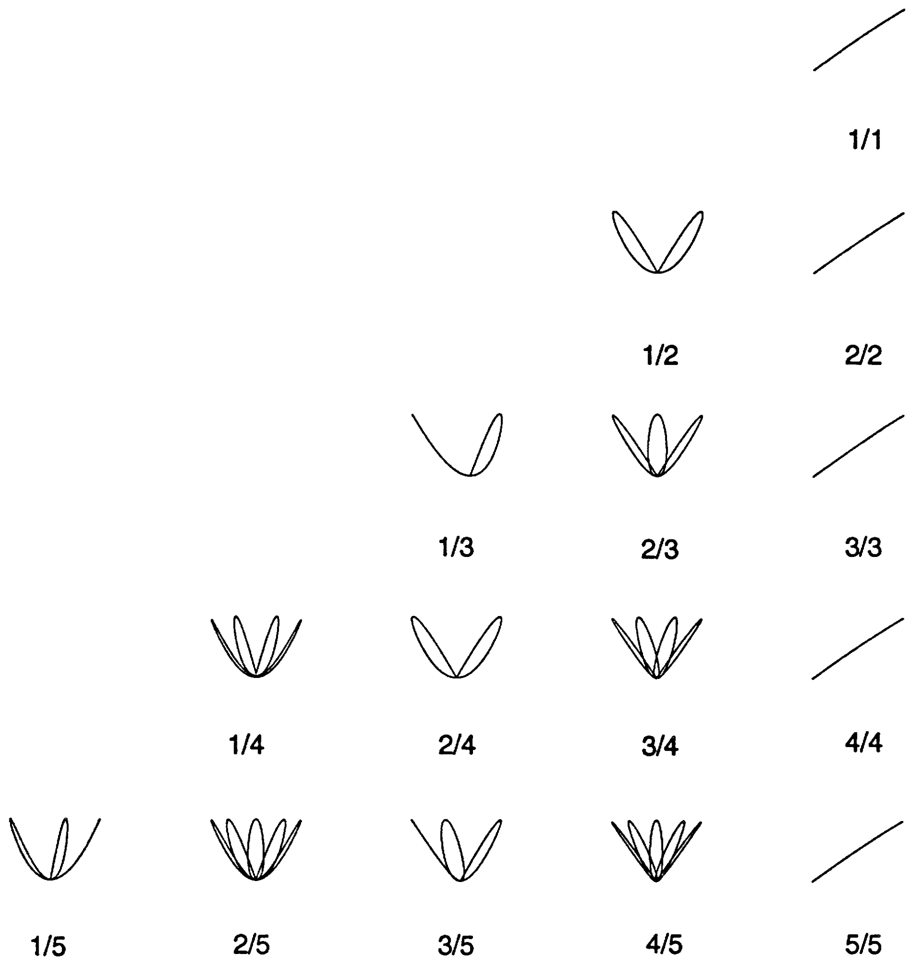

Figure 6-10: Pictures of some short period orbits. The labelling of each orbit is discussed in the text. ρ is horizontal and z is vertical.

Orbit	Initial Angle (in degree)	f_{bif}	$\tilde{S}$
1/5	179.524966	2.04	3.291621
1/4	179.159996	1.52	2.834189
1/3	179.180260	1.05	2.331519
2/5	173.273118	0.80	4.160135
1/2	176.932876	0.63	1.765822
3/5	177.537908	0.51	4.655172
2/3	170.278623	0.45	2.881700
3/4	167.798490	0.40	3.957121
4/5	168.412112	0.38	5.010431
1/1	165.595461	0.34	1.029909
2/1	143.881599	0.09	1.436545

Table 6.1: Properties of some short period orbits at bifurcation points at $\epsilon = 0$. f_{bif} is the scaled field at which a given orbit bifurcates and $\tilde{S}$ is the corresponding scaled action.

In particular, bifurcations of closed orbits provide a natural way to interpret the spectra as the system evolves from an electric field to a magnetic field dominated region in the continuum. These results help establish a useful connection between classical and quantum descriptions of an unbound chaotic system.

Chapter 7

Diamagnetic Rydberg Atoms

There has been considerable theoretical and experimental progress on diamagnetic Rydberg atoms since the discovery of the quasi-Landau oscillation by Garton and Tomkins many years ago [GT69], but nearly all of them have been limited to the bound (i.e.the negative energy) region. Consequently, relatively little is known about behavior above the classical ionization limit. High resolution spectroscopy in this region has revealed unexpected phenomena such as narrow resonances and orderly structures [WKI$^+$89b][IWK$^+$89]. Statistical ideas from random matrix theory were consequently used to explain some of the findings [GDG93]. In addition, methods accurate for numerical computations were developed and the results were found to be in good agreement with experimental results [IWK$^+$91]. However, a clear physical understanding of the system in this region is still lacking. The classical dynamics is left largely unexplored, and the extent of classical chaos is for the most part unknown. In this chapter, we undertake a study of this problem in two parts. In Sec. 7.1, the classical dynamics in the positive energy region is investigated, including the ionization process and its connection to closed orbits. In Sec. 7.2, a semiclassical connection to quantum spectra is presented.

7.1 Classical Description

The classical dynamics of diamagnetic hydrogen atom can be scaled as described in Sec. 4.3, and the resulting scaled Hamiltonian is given by

$$H = \frac{p^2}{2} - \frac{1}{2} + \frac{1}{2}l_z + \frac{1}{8}\rho^2. \tag{7.1}$$

The classical dynamics depends only on $\epsilon = EB^{-2/3}$ and $l_z = B^{1/3}L_z$, not on E, L_z, and B separately (see Sec. 4.3). l_z, a constant of motion, is usually negligible for laboratory fields. Hence, the dynamics depends only on ϵ and the initial conditions.

In the bound region, the surfaces of section reveal that the system is regular for $\epsilon < -0.54$. It starts to demonstrate irregular behavior at $\epsilon \approx -0.54$, and becomes completely chaotic at $\epsilon \approx -0.13$ [HH83]. This transition to chaos also manifests itself as a proliferation of classical closed orbits [MWW+94]. Physically, large negative scaled energy ($\epsilon << 0$) corresponds to large electron binding energy and small magnetic field. As the scaled energy becomes less negative, chaos develops when the strength of the magnetic interaction becomes comparable to the binding energy.

Characterization of classical chaos in the positive energy region is difficult because the trajectories are not bound. The phase space is open and a "slice" cannot be chosen conveniently. Consequently, the conventional description by surfaces of section method is not useful. For value of ϵ close to zero, the system appears to be extremely chaotic due to the comparable strengths of the magnetic field and electron binding energy. On the other hand, large positive scaled energy ($\epsilon >> 0$) corresponds to large electron energy for a given magnetic field, or equivalently a small magnetic field for a given energy. In either case, the electron behaves very much like a free particle. In this limit we expect the dynamics to be regular. Consequently, we expect the system to undergo a transition from chaos back to order as the scaled energy increases positively.

To explore this unbound region, we turn to its classical ionization properties as in the discussion of behavior in parallel fields (Sec. 6.2). The electron is initially localized near the nucleus. Its subsequent motion depends on the initial angle θ with respect to the magnetic field. The motion of its trajectory is bounded in the x-y plane, and ionization can occur only in the z direction. We define the classical ionization time as the time a given trajectory spends near the nucleus before it escapes to infinity along the z-axis. However, unlike the situation in parallel fields or a pure electric field where escaping across the saddle point gives an unambiguous signature of ionization, here the ionization process is not clearly defined. In our calculation, we consider a trajectory to have ionized if it reaches a certain cutoff distance along z-axis. The choice of the cutoff distance affects the actual value of the ionization time, but not the general characteristics of the ionization behavior.

A map of the classical ionization time as a function of θ for scaled energies between $\epsilon = 0$ and $\epsilon = 10$ is shown in Fig. 7-1. The dependence is smooth for angles between 0 and some critical angle θ_c. In this range, the ionization time is essentially zero. These trajectories have significant initial momenta along the magnetic field. They escape through the potential "hole" along the z-axis before being deflected appreciably by the magnetic field. Beyond θ_c, the ionization time shows wild and random fluctuations. Magnifications of these regions (similar to Figs. 6-4) reveal the same complicated structures persisting to ever finer scales. Again, the structures appear to be fractal so that the ionization can be characterized as chaotic.

In Fig. 7-2 we quantitatively characterize the degree of chaos of the system by displaying as a function of scaled energy ϵ the fraction of initial angles θ whose ionization trajectories are regular (i.e. their ionization time shows nonfractal behavior). (The Lyapunov exponent of these trajecties was also found to vanish.) This fraction increases rather rapidly. For example, at $\epsilon = +5$, almost 90% of the trajectories are regular. In fact, in the limit of large scaled energy, all trajectories are regular except

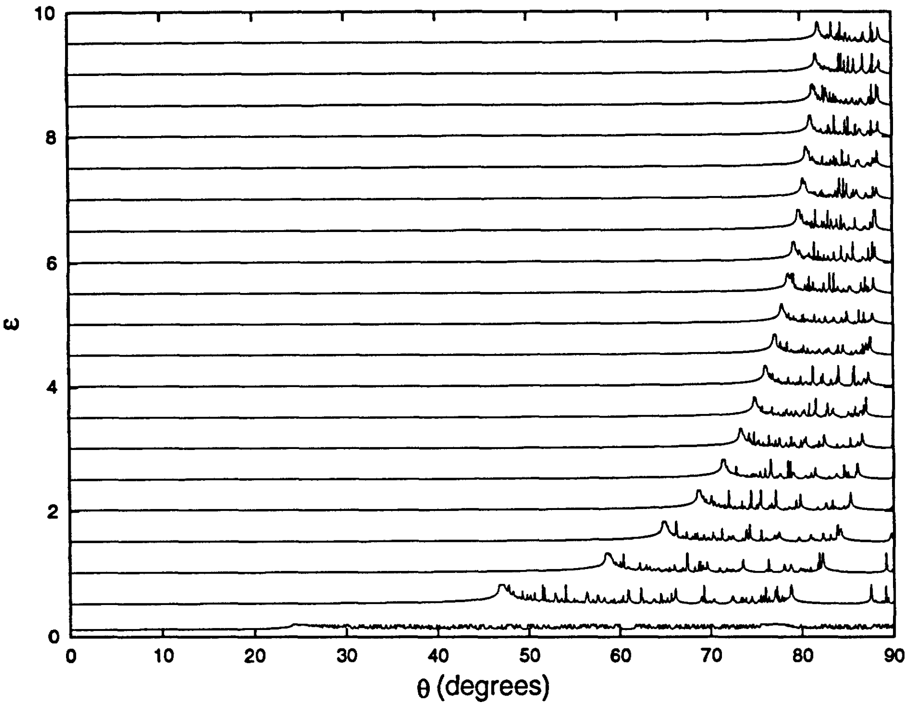

Figure 7-1: Classical ionization time as a function of the initial angle relative to the magnetic field for scaled energy between $\epsilon = 0$ and $\epsilon = 10$. The trajectories ionize quickly from $\theta = 0$ to $\theta = \theta_c$, beyond which the fractal structures develop. As scaled energy increases, the fractal structures rapidly converge onto $\theta = 90°$.

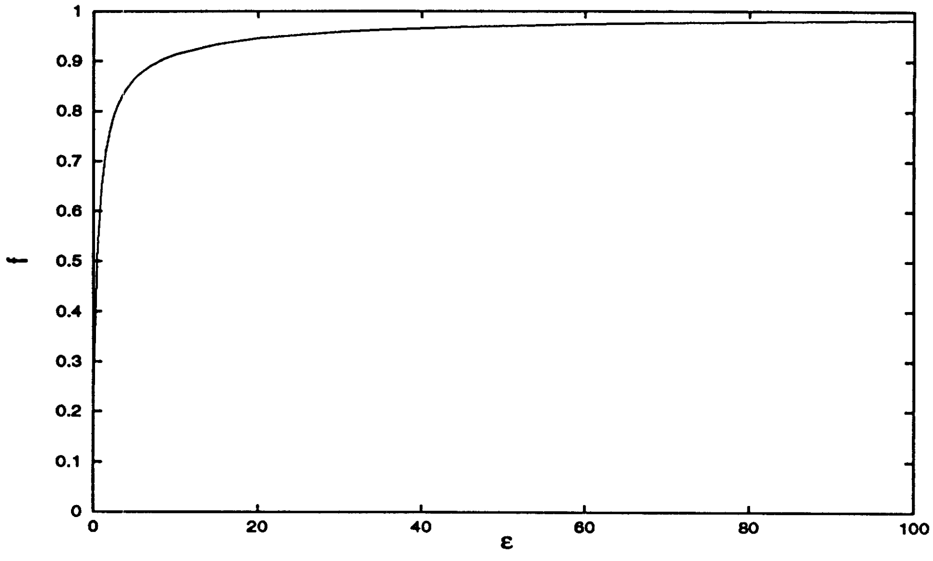

Figure 7-2: Fraction f of ionization trajectories that are regular as a function of scaled energy ϵ.

for a small region near the plane perpendicular to the magnetic field.

We again seek to correlate chaotic ionization with periodic orbits. Due to numerical limitations, we examine short period orbits that are closed at the nucleus (scaled action less than 10). Figure 7-3 shows the locations of these orbits and the classical ionization time at scaled energy $\epsilon = 0.1$. The horizontal axis is the initial angle θ. Each needle corresponds to a closed orbit and the height is proportional to its relative short-time stability. Figure 7-4 displays the pictures of some of these orbits. Almost all of them are found to be unstable. As expected, the fractal structures are most pronounced in the vicinity of unstable closed orbits.

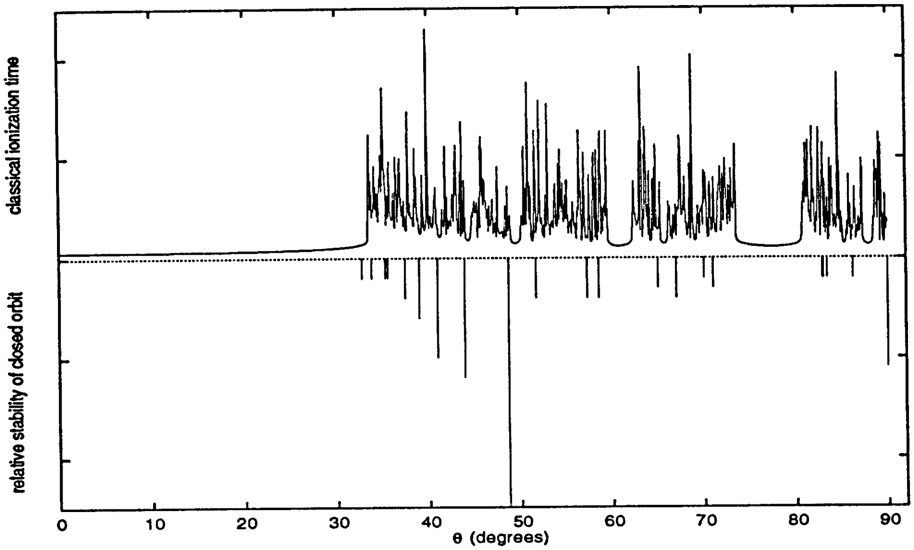

Figure 7-3: The classical ionization time and closed orbits as a function of the initial angle θ at scaled energy $\epsilon = 0.1$. Every needle represents a closed orbit and its height indicates the relative stability of the orbit. The fractal structures are visible in regions where closed orbits exist.

Figure 7-4: Some of the closed orbits at $\epsilon = 0.1$. ρ is the horizontal axis and z is the vertical axis. From left to right, the initial angle $\theta = 90.00°, 43.91°, 48.69°, 40.97°$, and $38.94°$, respectively.

7.2 Semiclassical Recurrence Spectra

As we have seen in Sec. 6.3, closed-orbit theory provides a powerful tool for understanding the semiclassical behavior of Rydberg atoms in parallel fields. According to closed-orbit theory, the inverse Fourier transform of a recurrence spectrum gives the photoexcitation spectrum (Sec. 5.3). In the positive energy regime, the photoionization spectrum is modulated by classical closed orbits. The strength of the modulations depends on the relative stabilities of the orbits.

Figure 7-5 shows such a map of classically computed recurrence spectra. The horizontal axis is the classical action of each orbit. Each needle corresponds to a closed orbit or one of its repetitions. The height is the classical amplitude which reflects the relative stability of each orbit. At $\epsilon \approx 0$, we see a proliferation of closed orbits, indicating a great degree of chaos. As the scaled energy is raised, closed orbits rapidly disappear. For $\epsilon > 3$, the only survivor is the perpendicular orbit which becomes unstable logarithmically as a function of ϵ at large scaled energy [FW89]. Consequently, a quantum signature of the classical transition to orderly motion as the scaled energy becomes large is the disappearance of modulations of closed orbits in the photoionization cross section. In this limit, the quantum spectrum is expected to be weakly modulated by a very unstable perpendicular orbit and its repetitions.

We see that hydrogen is regular in the limits of both large positive and negative scaled energy. In between these limits, chaos develops due to the mixed effects of the spherical Coulomb symmetry and the cylindrical symmetry of the magnetic field, reaching a maximum near $\epsilon = 0$. However, an important distinction needs to be made between these two limits. At large negative scaled energy, the system is bound and is characterized by the existence of stable parallel and perpendicular closed orbits which in turn bifurcate and result in a proliferation of closed orbits as the system turns chaotic; at large positive scaled energy, the system is unbound, the parallel orbit is no

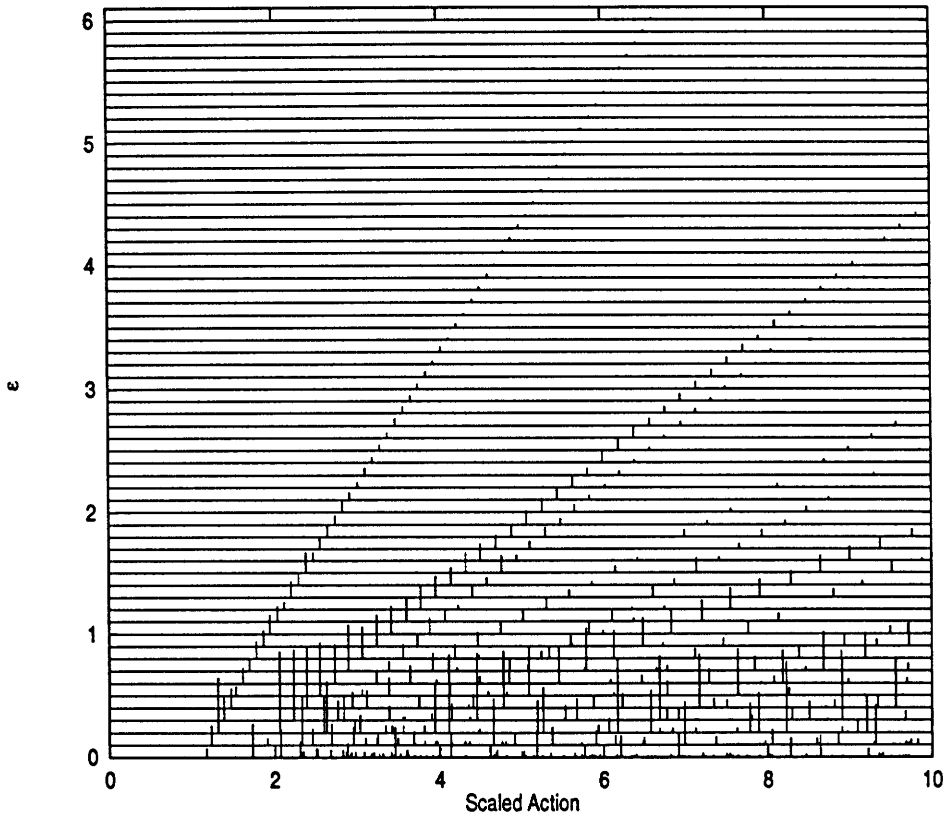

Figure 7-5: A map of the classically computed recurrence spectra between scaled energy $\epsilon = 0$ and $\epsilon = 6$. Horizontal axis is the classical action. Each needle corresponds to a closed orbit and the relative stability is given by the height. The spectra are dominated by a rapid disappearance of closed orbits as ϵ increases.

longer closed, and the perpendicular orbit becomes unstable. Detailed calculations have shown that the Lyapunov exponent of the perpendicular orbit never vanishes in the positive energy region [FW89]. According to basic bifurcation theory, an unstable orbit cannot bifurcate [MD92]. Consequently, the onset of chaos as ϵ decreases in the positive energy region cannot be characterized by any bifurcation process.

We have carried out scaled-energy spectroscopy in this region. Figures 7-6 show the experimental scaled spectrum and its recurrence spectrum at $\epsilon = 0$. Many weak peaks are visible in the recurrence spectrum. However, the recurrences due to the perpendicular orbit and its repetitions are absent. Since we excite $m = 0$ final states of odd parity, all final states must have an angular distribution with a node in the x-y plane. Hence this important contribution of the perpendicular orbit is absent in our spectrum [1]. As ϵ increases positively, we expect the recurrences of the perpendicular orbit and its repetitions to dominate the recurrence spectrum. Unfortunately, our current excitation scheme is not suited for investigating such recurrences. An excitation scheme that is capable of exciting even parity final states is needed to observe the signature of the perpendicular orbit, see Appendix D for such excitation schemes for lithium.

7.3 Summary and Discussion

Classical trajectory calculations for the positive energy diamagnetic Rydberg atoms reveal the fractal nature of the ionization process, which characterizes the chaotic ionization. In addition, this chaotic behavior is found to be confined near closed orbits. Except for a small region close to the perpendicular plane, at large positive scaled energy, corresponding to large electron energy and small magnetic field, the

---

[1] Our predecessors have also reported such absence of the "Quasi-Landau" behavior in their spectrum [Wel89].

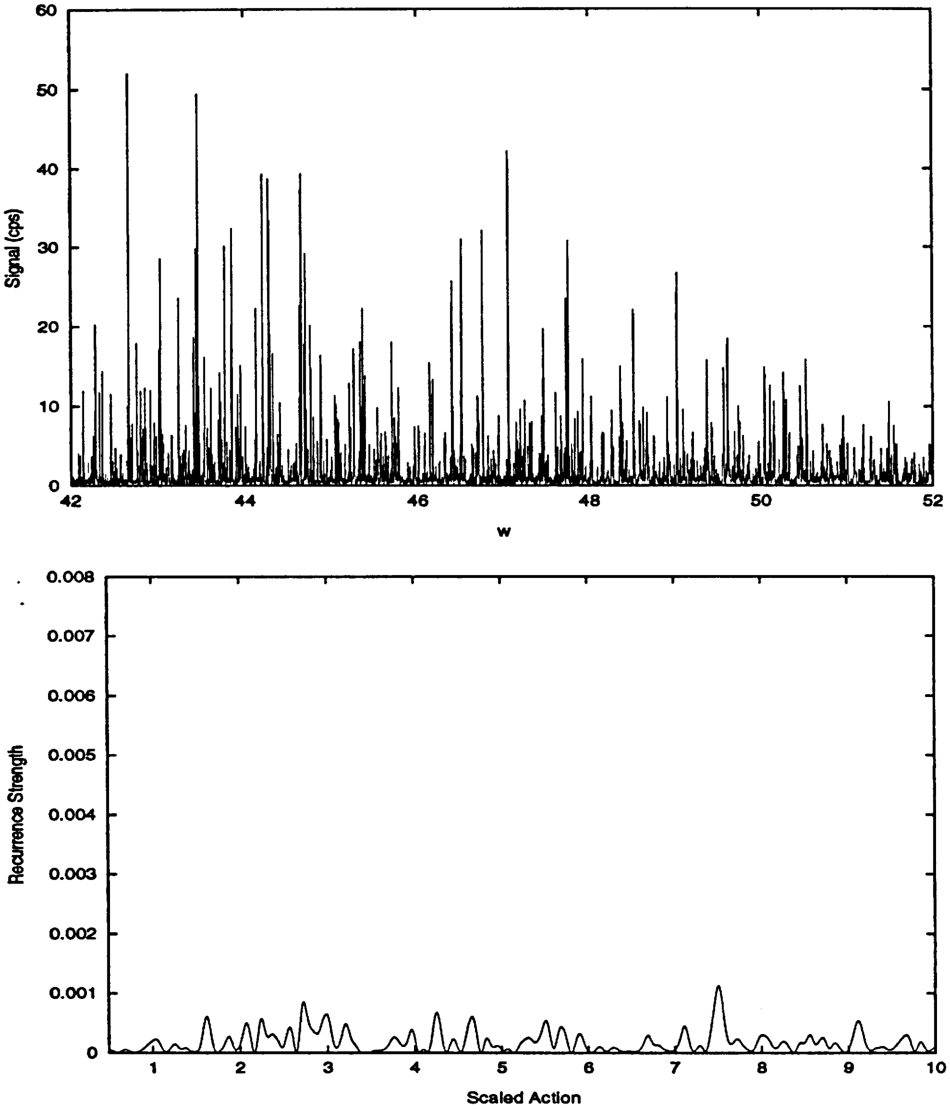

Figure 7-6: Diamagnetic lithium at $\epsilon = 0$. Top: the scaled-energy spectrum. Bottom: the recurrence spectrum.

system displays a regular ionization process. This transition from chaos to order is accompanied by a rapid disappearance of closed orbits.

Quantum manifestations of chaos can also be described by statistical methods [DG86] [WF86b]. Gay and coworkers have used random matrix theory to explain the existence of ultranarrow resonances observed experimentally [GDG93]. This use of the random matrix model was justified by the classically chaotic nature of the system. However, we expect this approach to break down as the system becomes more regular at large positive scaled energy. For example, the nearest-neighbor-spacing distribution (NNS) of the resonances of a regular unbound system obeys a Poisson distribution [MW94]. The observation of such a Poisson distribution of NNS will be another quantum signature of the transition to order classically. The physical energy of the electron at which the system turns orderly is extremely high. For example, at $B = 6$ T, $\epsilon = +5$ corresponds to $E \approx +865$ cm^{-1}. At such a field the highest energy currently achieved by experiments and by reliable quantum computations is only $E \approx +30$ cm^{-1} [IWK^{+}91]. Nevertheless, a rigorous quantum mechanical study in this energy range will be invaluable in providing insights into the quantum manifestation of this transition from classical chaos to order.

Chapter 8

Rydberg Atoms in Crossed Fields

As we have seen in the last two chapters, a Rydberg atom in applied static fields is well suited for the study of quantum chaos. Its classical behavior displays a transition to chaos, and it can be investigated experimentally with great clarity and detail. Thus far, however, we have only discussed systems that preserve rotational symmetry about the field axis. The conservation of angular momentum along the field axis effectively reduces these to two-dimensional systems, greatly simplifing the problem. As we have seen in Sec. 4.1.3 and Sec. 4.3.1, the surface of section, being two-dimensional, can be conveniently used to portray classical motion. Moreover, the quantum solutions are reasonably tractable.

A system with three degrees of freedom is far less tractable. An immediate difficulty is visualizing a surface of section that is now four-dimensional (see Table 4.1). Furthermore, as mentioned at the end of Sec. 4.2.3, chaotic trajectories are no longer confined by KAM tori but are free to explore all of the available phase space. Finally, the number of basis states required to achieve accurate quantum solution can be enormous. Nevertheless, understanding the chaotic behavior in such a system is essential for connecting the quantum and classical descriptions of irregular systems. In this chapter, we report a study of such a system: a hydrogen atom in crossed electric and magnetic fields.

Experiments have been performed on this system both below [RFW93] and above [WMK+89] the classical ionization limit (the saddle point). In addition, numerical methods have been developed to perform accurate quantum computations in certain field-energy regime [MW92]. However, a quantitative comparison with classical mechanics was limited due to lack of a useful characterization of its behavior under conditions of classical chaos. We undertake here a theoretical study of the classical dynamics and a statistical analysis of its quantum spectra in the bound region (below the classical saddle point). These results serve as a first step towards the goal of establishing the connection between the quantum and classical descriptions of this system.

The crossed electric and magnetic fields destroy the rotational symmetry about either field axis, and the system remains three-dimensional. Furthermore, as in Sec. 6.2.1, in introducing scaled variable, the crossed field system requires a second parameter $f = FB^{-4/3}$, where F is the electric field. As $f \to \infty$, the system becomes the hydrogen Stark problem which has an exact quantum solution and its classical motion is regular everywhere. As $f \to 0$, the system evolves into the familiar diamagnetic hydrogen system. Though nonintegrable, this system remains regular for $\epsilon \leq -0.55$. As we shall show, an intermediate electric field can cause chaos in this region.

In Sec. 8.1, we describe the Hamiltonian of the system and derive an approximate one-body Hamiltonian from an exact two-body Hamiltonian. A detailed classical description, including surfaces of section, Lyapunov exponents, and Arnold diffusion, is presented in Sec. 8.2. In Sec. 8.3, we will give a brief review of energy level statistics. In particular, we will discuss the nearest-neighbor spacings distribution (NNS). This is followed by a discussion on the numerical techniques for computing quantum spectra in Sec. 8.4. Finally. the NNS statistics are investigated for the crossed field system, and the results are compared with the Brody distribution as the classical counterpart undergoes a transition to chaos (Sec. 8.5).

8.1 The Hamiltonian

The two-body Hamiltonian of a hydrogen atom in a uniform electric field $\vec{F}$ and magnetic field $\vec{B}$, with magnetic vector potential $\vec{A}$ is

$$H = \frac{[\vec{p}_e + \frac{e}{c}\vec{A}(\vec{r}_e)]^2}{2m_e} + \frac{[\vec{p}_n - \frac{e}{c}\vec{A}(\vec{r}_n)]^2}{2m_n} + e\vec{F}\cdot(\vec{r}_e - \vec{r}_n) - \frac{e^2}{|\vec{r}_e - \vec{r}_n|} \tag{8.1}$$

where e and n denote electron and nucleus, respectively. (As usual for such problems, spin and relativistic terms are omitted.) For a uniform magnetic field, it is convenient to use the symmetric gauge, $\vec{A} = \frac{1}{2}(\vec{B}\times\vec{r})$. Introducing $\vec{R} = (m_e\vec{r}_e + m_n\vec{r}_n)/(m_e + m_n)$ and $\vec{P} = \vec{p}_e + \vec{p}_n$, $\vec{r} = \vec{r}_e - \vec{r}_n$ and $\vec{p} = (m_n\vec{p}_e - m_e\vec{p}_n)/(m_n - m_e)$, the center-of-mass and relative coordinates and conjugate momenta, respectively, the Hamiltonian can be written [JHY83]

$$H = \frac{1}{2M}(\vec{K} + \frac{e}{c}\vec{B}\times\vec{r})^2 + \frac{1}{2\mu}(\vec{p} + \frac{(m_n - m_e)e}{2Mc}\vec{B}\times\vec{r})^2 + e\vec{F}\cdot\vec{r} - \frac{e^2}{|\vec{r}|} \tag{8.2}$$

where $M = m_n + m_e$ and $\mu = \frac{m_n m_e}{m_n + m_e}$ are the total and reduced masses, respectively, and $\vec{K} = \vec{P} - \frac{1}{2}(\frac{e}{c})(\vec{B}\times\vec{r})$ is a conserved generalized momentum (sometimes called pseudomomentum). The cross term $\frac{e}{Mc}\vec{K}\cdot(\vec{B}\times\vec{r})$ couples the relative motion to the center-of-mass motion. In particular, the electron experiences an additional electric field induced by the center-of-mass motion of the atom. An example is the motional electric field "seen" by the atom moving perpendicular to the external magnetic field. Schmelcher and Cederbaum have demonstrated that $\frac{1}{2M}(\vec{K} + \frac{e}{c}\vec{B}\times\vec{r})^2$, the kinetic energy of the center-of-mass motion, can be treated as part of the potential energy for the relative motion [SC93b] [SC93a]. This coupling between the center-of-mass and the relative motion gives rise to unusual ionization properties as well as possible existence of localized states of almost macroscopic dimension [SC93b]. However, in this thesis we are concerned with the dynamics below the ionization limit. In this regime, Walther and co-workers showed that the motion of the nucleus is negligible [RFW93]. In this limit, $m_n \to \infty$, Eqn. 8.2 reduces to the familiar one-body Hamiltonian given in atomic units by

$$H = \frac{1}{2}p^2 - \frac{1}{r} + \frac{1}{2}\vec{L} \cdot \vec{B} + \frac{1}{8}(\vec{B} \times \vec{r})^2 + \vec{F} \cdot \vec{r}. \tag{8.3}$$

The first two terms are the usual unperturbed Hamiltonian with the Coulomb potential. The third term is the paramagnetic term, giving rise to the familiar Zeeman effect. The fourth term is the diamagnetic term, the source of classical chaos in diamagnetic hydrogen atom mentioned in Sec.4.3. The last term $\vec{F} \cdot \vec{r}$, responsible for the Stark effect, maintains the integrabilty of the system in the absence of a magnetic field as we saw in Sec. 4.1.2. As we shall show in the next section, if $\vec{B}$ and $\vec{F}$ are perpendicular, this term can give rise to additional chaos.

8.2 Classical Dynamics

For the crossed fields system $\vec{B} = B\hat{z}$ and $\vec{F} = F\hat{y}$, classical dynamics obeys the same scaling law as for the parallel fields,

$$\begin{aligned} \vec{r} &\to B^{2/3}\vec{r} \\ \vec{p} &\to B^{-1/3}\vec{p} \\ F &\to B^{4/3}F \\ H &\to B^{2/3}H. \end{aligned} \tag{8.4}$$

The scaled Hamiltonian can be written in cylindrical coordinates

$$H = \frac{1}{2}p_\rho^2 + \frac{1}{2}p_z^2 + \frac{1}{2\rho^2}p_\theta^2 + \frac{1}{2}p_\theta + \frac{1}{8}\rho^2 - \frac{1}{(\rho^2 + z^2)^{1/2}} + f\rho\sin\theta. \tag{8.5}$$

Once again, the dynamics depends on two parameters $f = B^{-4/3}F$ and $\epsilon = B^{-2/3}H$ not on B, F, and H separately. Unlike the parallel fields system, however, θ is no longer ignorable. Consequently p_θ is not a constant of motion and the term $\frac{1}{2}p_\theta$ cannot be trivially transformed away. The system remains three-dimensional. Furthermore, p_θ, being the canonical momentum of θ, makes the potential energy effectively momentum dependent, putting any simple static potential description out of reach.

The evolution of a classical trajectory is found by numerical integration of the Hamilton equations of motion (see Appendix G for details). Conservation of energy constrains the trajectories on a five-dimensional surface in a six-dimensional phase space $(\rho, z, \theta, p_\rho, p_z, p_\theta)$. A regular trajectory is confined on a three-dimensional torus (see Sec. 4.1.1), but a chaotic one is free to wander over the entire five-dimensional energy surface.

8.2.1 Surface of Section

In analogy to our approach to a system with two degrees of freedom, we choose for the surface of section the plane at $z = 0$. We view the intersection of a classical trajectory with the surface of section by noting a point in the $(p_\rho, \rho, p_\theta, \theta)$ space whenever the given orbit passes through the $z = 0$ plane. With p_z determined within a sign by energy conservation, a point on the surface of section completely determines the state of the given classical trajectory. The surface of section is four-dimensional. Successive intersections of a regular trajectory with the surface of section, being confined on a three-dimensional torus, will trace out a structure that is topologically two-dimensional — a two-dimensional manifold. Those of a chaotic trajectory will fill a four-dimensional manifold. Determining whether or not a given classical trajectory is chaotic reduces to determining the dimensionality of the manifold on which it lies. Unlike the situation for a system with two degrees of freedom whose surface of section is two-dimensional, finding the dimensionality of manifolds in a four-dimensional space is not trivial.

To characterize such a four-dimensional space, we use a a method originally suggested by Froeschle in his study of three-body problems in astrophysics [Fro70]. The idea is to retain only three coordinates and plot the points in a three-dimensional space. These points are the projection of the four-dimensional space along one of its coordinates. We shall take that coordinate to be θ. A regular trajectory, confined on a two-dimensional manifold in a four-dimensional space, also lies on a two-dimensional manifold in a three-dimensional subspace. (A two-dimensional manifold in a three-demensional space is just an ordinary surface.) A chaotic trajectory filling a four-dimensional space will also fill the three-dimensional subspace. Thus the dimensionality of the manifold on which a given trajectory lies in the three-dimensional subspace determines whether such a trajectory is chaotic.

Froeschle suggested visualizing the three-dimensinal space with the help of stereoscopic viewings. Here we take a different approach. The three-dimensional space is divided into many slices along one of the coordinates. The intersection of a two-dimensional manifold (regular trajectories) with one of these slices is a smooth curve. The intersection of a three-dimensional manifold (chaotic trajectories) with this slice is a two-dimensional manifold.

We choose to view the slices along the p_θ axis. In practice, these slices must have some finite thickness in order to contain any points. The thickness needs to be small to give a good approximation to an ideal slice, this is usually limited by numerical efforts. We choose the thickness to be 0.1% of the maximum allowed p_θ. Figure 8-1

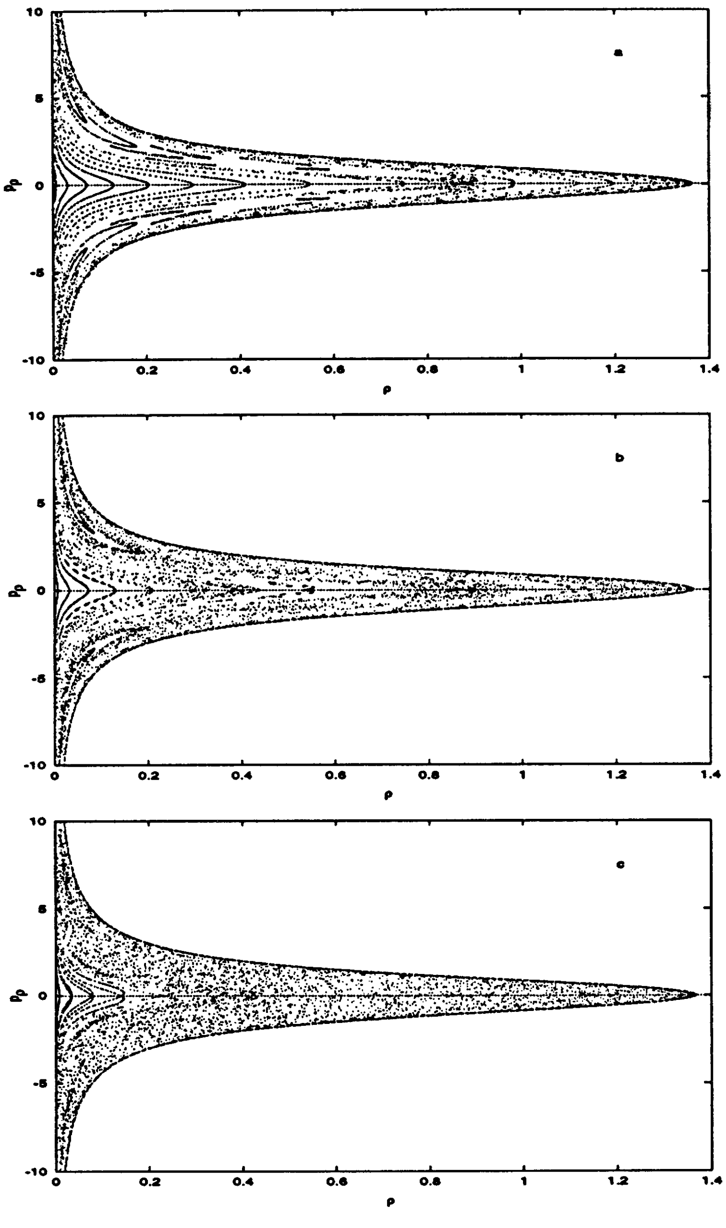

Figure 8-1: Surface of section at z=0 of a hydrogen atom in crossed electric and magnetic fields, slice at $p_\theta = 0.0$, $\epsilon = -0.5$, a) $f = 0.0$, b) $f = 0.01$, c) $f = 0.05$.

shows such a slice at $p_\theta = 0.0$. Surfaces of section are computed for increasing values of f.

To investigate electric field induced chaos, we choose the scaled energy $\epsilon = -0.55$, an energy for which the system is regular in the absence of the electric field $f = 0$. This regular motion is shown graphically in Fig. 8-1a, where all tori are intact. As f increases, the destruction of tori indicates the development of chaos. At $f = 0.01$ (Fig. 8-1b), many of the tori in Fig. 8-1a have vanished. At $f = 0.05$ (Fig. 8-1c), most of the surface of section is chaotic though a few tori are still visible. Further increasing f pushes the system over the saddle point, where the trajectories are unbound and the method of surface of section is no longer useful. Furthermore, the exact two-body Hamiltonian is required in this region. The nature of the motion in this unbound region lies outside the scope of this discussion.

The surfaces of section clearly show that, as expected, a crossed electric field induces chaos in the bound region that is regular otherwise. To completely characterize the state of a classical trajectory, we have examined the surface of section at many different slices along p_θ. The result reveals the same generic behavior. One may note the topological difference between the tori in Fig. 8-1a and the surviving ones in Fig. 8-1c. In the absence of the crossed electric field, the system is two-dimensional. Each curve in Fig. 8-1a corresponds topologically to a slice of a two-dimensional torus in a three-dimensional space, i.e. a simple curve. In a crossed electric field, the tori become three-dimensional. Each curve in Fig. 8-1c corresponds topologically to a cross section of a three-dimensional torus in a five-dimensional space. Each curve actually consists of two simple curves crossing each other. A more mathematical discussion of the topology of a multi-dimensional torus has been given by Arnold [Arn78].

8.2.2 Lyapunov Exponents

Computing surfaces of section of many slices along the p_θ axis requires enormous numerical efforts. Consequently we have investigated an alternative approach to characterize quantitatively the electric field induced chaos in ϵ and f space. The idea was first used by Meyer in his study of a Hamiltonian with two degrees of freedom [Mey86]. Here we generalize it to systems with three degrees of freedom.

The goal is to calculate q, the fraction of the surface of section that is chaotic as a function of ϵ and f. We divide the four-dimensional surface of section into many four-dimensional cells, c_{ijkl}. Trajectories are launched and their evolution is calculated by integrating Hamilton equations of motion. For each trajectory we compute the Lyapunov exponent and store the indices $ijlk$ of all the cells touched by the given trajectory. If the Lyapunov exponent vanishes, then the motion is regular. Otherwise the motion is chaotic. This way we keep track of n^r_{ijkl} the number of times a given cell has been touched by regular trajectories, and n^c_{ijkl} the number of times touched by chaotic trajectories. We keep running the trajectories until every cell has been visited. The numerical approximation to the fraction of the surface of section that is chaotic is given by

$$q = \sum_{ijkl} \frac{n^c_{ijkl}}{(n^c_{ijkl} + n^r_{ijkl})}. \tag{8.6}$$

In order to minimize the error involved in calculating Lyapunov exponent, we usually run each trajectory for a long time, more than 500 intersections with the surface of section. At the end of the calculation, the average number of points in each cell is about 100. The accuracy of computing q is limited by the size of the cell. To check convergence, we reduce the the cell size until q changes by less than 1% when the cell size is reduced by 50%. In our calculation, the widths of these cells are initially set

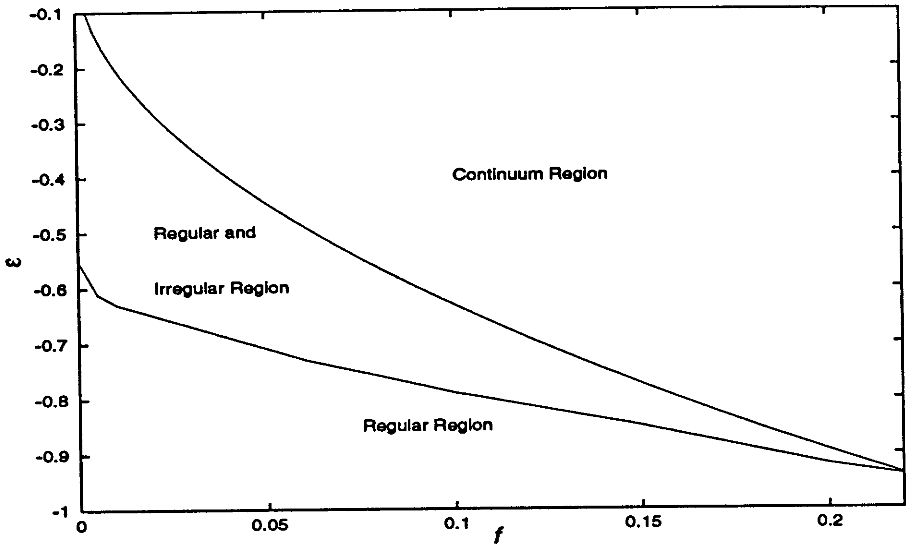

Figure 8-2: Onset of electric field induced chaos in the f and ϵ space.

to be

$$\Delta\rho = 0.01\rho_{max}, \quad \Delta p_\rho = 0.01 p_{\rho max},$$
$$\Delta\theta = 0.01\theta_{max}, \quad \Delta p_\theta = 0.01 p_{\theta max}, \tag{8.7}$$

where the subscript "max" indicates the maximum value that variable can take on a given surface of section, i.e. the boundary between the classically allowed and forbidden regions. Smaller cell size however involves much longer computing time as well as larger computer memory. A detailed description of the method for computing Lyapunov exponents numerically is given in Appendix H.

By computing q for numerous values of ϵ and f, we are able to map out the electric field induced transition to chaos in the ϵ and f space. The results are shown graphically in Fig. 8-2. We arbitrarily define the onset of chaos at $q = 0.05$. The electric field induced chaos is evident. In the absence of the electric field, chaos develops at $\epsilon \approx -0.55$. As f increases, ϵ at the onset of chaos is lowered gradually. At $f \approx 0.22$, the onset of chaos occurs at $\epsilon \approx -0.95$. This also corresponds to the saddle point beyond which the system is unbound. For large f ($f \rightarrow \infty$), the magnetic field is negligible and the electric field dominates. In that limit, the system becomes hydrogen in a uniform electric field which is integrable. Consequently, we expect the system to eventually undergo a transition to regularity as f becomes very large. However, we find that such a transition does not occur below the saddle point.

8.2.3 Arnold Diffusion

The KAM theorem guarantees the survival of sufficiently irrational tori in a perturbed system (the KAM tori). For a Hamiltonian system with two degrees of freedom, these are two-dimensional manifolds embedded on a three-dimensional energy shell. They set up boundaries for the chaotic trajectories. That is, the chaotic trajectories are separated into distinct regions. For a Hamiltonian system with three degrees of freedom, this is no longer true. The KAM tori here are three-dimensional manifolds embedded in a five-dimensional energy shell. The KAM tori are not able to isolate the chaotic trajectories (see Sec. 4.2.3). Consequently, the chaotic trajectories can intersect every part of the energy surface and are thus connected into a single complex web (the Arnold web). This phenomenon is known as Arnold diffusion [LL83]. It was first proven by Arnold for a specific nonlinear Hamiltonian [Arn64]. The time for a given chaotic trajectory to explore the whole phase space is difficult to calculate, but is typically very long. Although there have been a number of numerical investigations [Fro72] [Chi79], a rigorous proof of Arnold diffusion has not been given. We demonstrate Arnold diffusion in the crossed fields system by giving a qualitative example. A more quantitative discussion on this subject has been given by Chirikov [Chi79].

To ilustrate Arnold diffusion, we select a trajectory in one of the stochastic layers

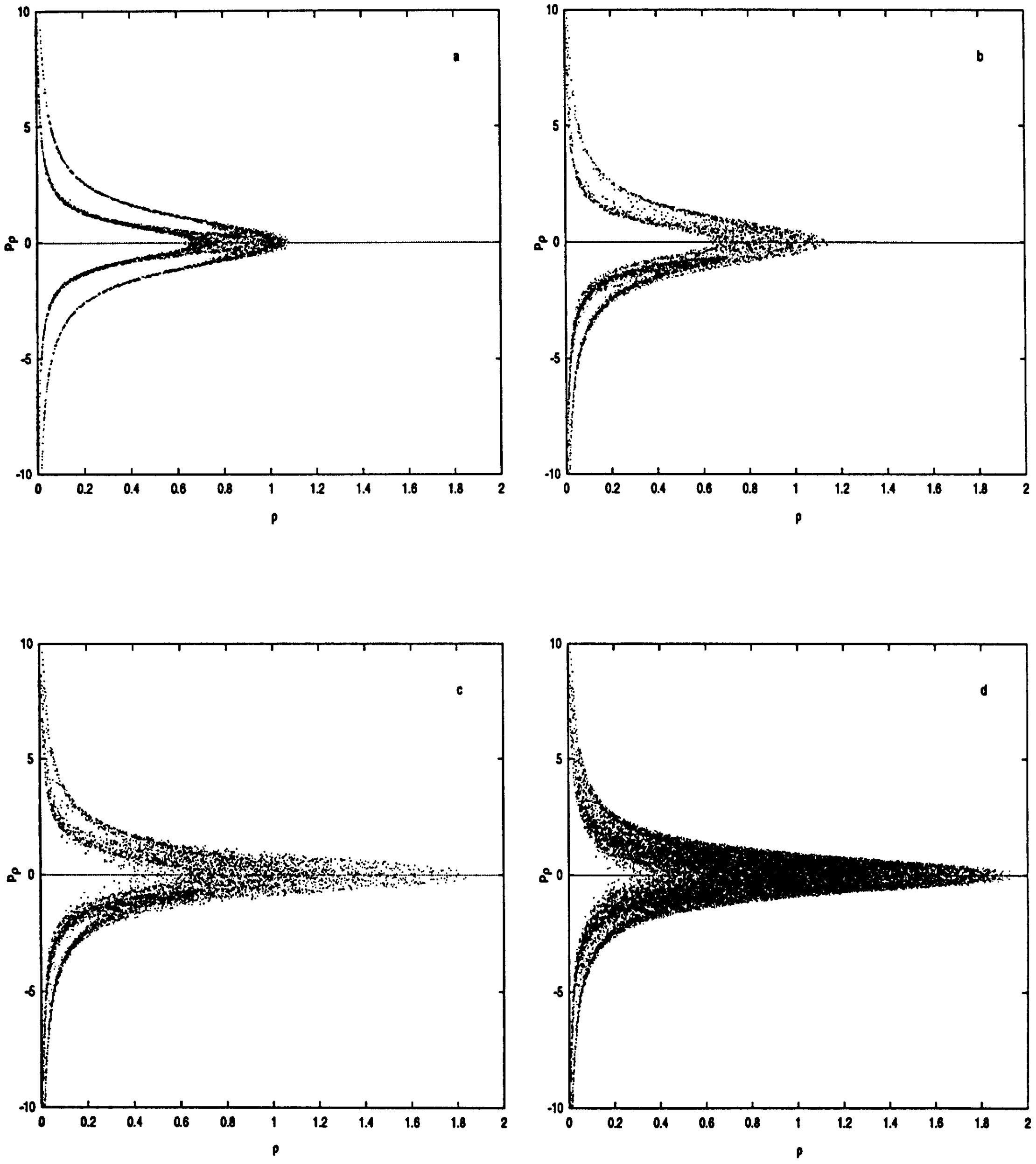

Figure 8-3: Arnold diffusion of a hydrogen atom in crossed field, $\epsilon = -0.5$, $f = 0.01$, slice at $p_\theta = 0.0$, n = number of successive intersections, a) $n = 5 \times 10^3$, b) $n = 5 \times 10^4$, c) $n = 1.5 \times 10^5$, d) $n = 6.5 \times 10^5$.

at $\epsilon = -0.55$ and $f = 0.01$ as shown in Fig. 8-1b. Figures 8-3 show the evolution of this trajectory as a function of n number of times it intersects the slice of the surface of section at $p_\theta = 0.0$. Figure 8-3a shows that for $n = 5 \times 10^3$, this trajectory appears to be isolated by KAM tori. If this were a system with two degrees of freedom, the trajectory will be confined by KAM tori forever. However, as n increases, it slowly diffuses through the phase space. Figure 8-3d shows that at $n = 6.5 \times 10^5$, it has covered most of the available region. We have examined other slices along p_θ to verify that this chaotic trajectory does indeed diffuse throughout the whole phase space. This diffusion process is universal in that there is no critical perturbation strength. That is, Arnold diffusion is present for arbitrarily small crossed electric field (although the diffusion rate may be vanishingly small). This, we believe, is the first observation of Arnold diffusion in this system.

8.3 Nearest-Neighbor Spacings Distribution

Turning now to the quantum description of the crossed field system. From the discussions in Chapter 5, it is reasonable to divide the quantum spectra into two parts, a regular spectrum that can be quantized according to EBK and an irregular one for which EBK is not applicable. Percival made this hypothesis in 1977 and conjectured that these two classes of spectra have very different properties, reflecting the differences in corresponding classical motion [Per77].

One of the earliest successes of quantifying these quantum spectra as the classical counterparts undergo regular to chaotic transition was through the study of the energy level statistics [BG84] [Haa91]. It emphasizes small scale spectral correlations and has been used successfully to determine whether or not a classical system is chaotic from the statistics of quantum spectrum. The most commonly used quantity is the nearest-neighbor spacings distribution (NNS), which displays information about the interaction of adjacent events in a series. Let E_i be an energy eigenvalue of a given Hamiltonian. For each E_i, $i = 1, 2, ..., n-1$, let $s_i = E_{i+1} - E_i$, where s_i is the i^{th} energy level spacing. Then a histogram is made of the number of occurences versus spacing. As more and more events are considered, the historgram approaches a smooth curve $P(s)$. The choice of bin size for the histogram is based on the total number of events. A smaller bin size gives more resolution of the shape of the spacing distribution, but the bin size must be large enough to contain a statistically significant number of levels.

8.3.1 Regular Region

When the classical motion is completely regular, the normalized distribution of NNS is Poissonian [BT77],

$$P(s) = e^{-s}. \tag{8.8}$$

where s is the normalized spacing between two energy levels. This Poisson-type distribution has been observed experimentally by Kleppner and co-workers [WKI$^+$89a]. In particular, they undertook an experimental study of NNS distributions of odd-parity diamagnetic lithium Rydberg spectrum in a regime of regular classical motion. The results are shown to be Poissonian.

8.3.2 Chaotic Region

When the classical motion of a system invariant under time reversal becomes completely chaotic, the energy level statistics are surmised to obey the Gaussian orthogonal ensemble (GOE) of the random matrix eigenvalues. Its NNS is well described by the Wigner distribution

$$P(s) = \frac{\pi}{2} s e^{\frac{\pi}{4} s^2}. \tag{8.9}$$

The level repulsions exhibited by a nonseparable system are signified by $P(0) = 0$. It has been conjectured that this phenomenon is generic for all chaotic systems with the same time reversal symmetry [BGS84]. This transition of NNS from Poisson-like to Wigner-like distributions has been well investigated numerically [WF86b] [DG86] [WWZ+86]. In addition, Michael Courtney has also examined diamagnetic lithium [Cou95]. The classical system displays core-induced chaos in a region where the diamagnetic hydrogen is still regular. While the odd-parity quantum states behave very hydrogenically, the even-parity states, due to the large quantum defect of the S state (≈ 0.4), have very pronounced effects of the core-induced chaos. In particular, the NNS of an even parity spectrum reveals Wigner-type distribution while its odd parity cousin behaves very much Poissonian.

8.3.3 Transition Region

In the transition region, a semiclassical formula which interpolates between the regular and chaotic regions has been given by Berry and Robnik [BR84]. However, there was evidence that the formula is not accurate near the regular limit [WF87]. In particular, the formula does not predict level repulsion due to small residual interaction in a not exactly integrable system. This was eventually repaired by Hasegawa and co-workers through a stochastic formulation of energy level statistics [HMF88].

In this section, we use a heuristic formulation first introduced by Brody [Bro73]. The Brody distribution which interpolates between Poisson and Wigner distributions is

$$P(s) = As^{q_b} exp(-\alpha s^{q_b+1}) \tag{8.10}$$

with

$$\alpha = [\Gamma(\frac{q_b+2}{q_b+1})]^{q_b+1}$$

$$A = (q_b + 1)\alpha.$$

For $q_b = 0$, this becomes the Poisson distribution of Eqn. 8.8; for $q_b = 1$, this reduces to the Wigner distribution of Eqn. 8.9. Thus q_b gives a degree of irregularity of the system. Though introduced phenomenologically, the Brody distribution has been shown to accurately describe the NNS of the diamagnetic hydrogen atom [WF87]. In particular, it predicts level repulsion for a not completely regular system, in agreement with physical intuition that any small interaction in a not exactly integrable system will cause a small level repulsion and make the probabilities for exact level degeneracies strictly zero. The Brody distribution has been found to work extremely well for diamagnetic hydrogen when the classical regular and irregular trajectories coexist [WF87].

8.4 Quantum Computations

We have numerically computed the quantum spectra for the crossed field problem. The energy eigenvalues below the ionization limit are found by diagonalizing a Hamiltonian matrix. We compute the matrix in the basis of field-free eigenstates. The unperturbed Hamiltonian H_0 is diagonal in this basis, and the matrix elements of H_0 are just the unperturbed energies. The matrix elements of the perturbed Hamiltonian are computed by numerical integrations. The resulting matrix is then diagonalized numerically using Given-Household method. Similar to the classical counterpart, the crossed electric field destroys the rotational symmetry around the z-axis. The quantum number m, corresponding to the z component of the angular momentum, is no longer a good quantum number. Consequently, the number of basis states needed to achieve a desired accuracy may become astronomical. Computing quantum spectrum of a crossed fields system thus requires a large numerical effort.

In addition to the total energy, the Hamiltonian does possess a discrete symmetry, the z-parity. That is, the system is invariant with respect to the z-axis. This symmetry splits the basis into two nonmixing parts. For a given n, there are $n(n+1)/2$ even z-parity states and $n(n-1)/2$ odd z-parity states. The total number of basis states from $n=1$ up to $n=n_f$ for a given z-parity is given by,

$$\begin{aligned} N_{odd} &= \sum_{n=1}^{n_f} \frac{1}{2}(n(n-1)) = \frac{1}{6}(n_f^3 - n_f) \\ N_{even} &= \sum_{n=1}^{n_f} \frac{1}{2}(n(n+1)) = \frac{1}{6}(n_f^3 + 3n_f^2 + 2n_f). \end{aligned} \tag{8.11}$$

For our computation, we use the odd z-parity basis with states up to n=26. This is about 2925 basis states. Due to numerical limitations, only eigenvalues are computed.

8.5 Results

The energy level statistics for this sytem have been investigated previously by Hegerfeldt and Henneberg as a function of its *quantum* field parameters [HH94]. However, in order to make quantitative connections between classical and quantum descriptions, we analyze the energy level statistics at scaled classical parameters ϵ and f. That is, the classical dynamics is kept constant. To compute the spectra at constant ϵ and f, the Hamiltonian matrix is diagonalized at a number of closely spaced values of electric field and magnetic field. The energy levels at a given ϵ and f are then found by interpolation.

Figure 8-4 shows the NNS distributions obtained for $\epsilon = -0.55$ and $f = 0.0$, 0.01, and 0.05. In each case, the bin size is 0.1 and the number of levels analyzed is about 500. The classical dynamics is displayed in the surfaces of section at $p_\theta = 0.0$ of Figs. 8-1. At $f = 0$ (top figure), the distribution is purely Poissonian corresponding to regular classical motion. As f increases (middle and bottom figures), a minimum

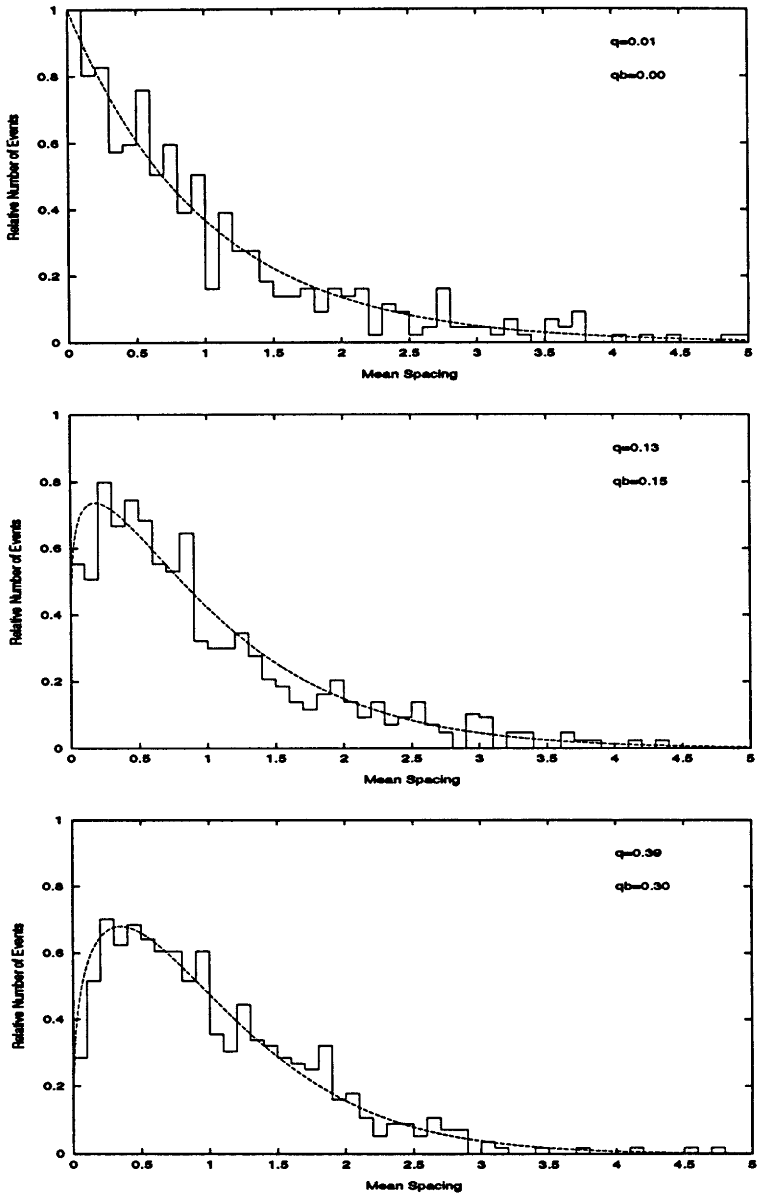

Figure 8-4: Distribution of the nearest-neighbor spacings of energy levels calculated at $\epsilon = -0.55$ and different values of f. The solid lines show the fits obtained with the Brody distribution. q is the fraction of phase space that is chaotic and q_b is the corresponding Brody parameter. Top: $f = 0.0$. Middle: $f = 0.01$. Bottom: $f = 0.05$.

at vanishing level spacings becomes more pronounced, indicating the onset of chaos of its classical counterpart. For a more quantitative description we have fitted to the histograms in Fig. 8-4 the Brody distribution. The results clearly show the transition from Poisson distribution at $f = 0$ to almost Wigner-like distribution at $f = 0.05$. Also shown in Fig. 4 are the fraction q of phase space that is chaotic and the Brody parameter q_b. Though not derived on any physical connection to classical phase space, q_b gives reasonable agreement with q, the fraction of phase space that is chaotic. Consequently, q_b can be used to approximate the extent of classical chaos. In the limit $q_b \to 1$ (the Brody distribution is Wigner-like), the corresponding classical system becomes completely chaotic ($q \to 1$).

8.6 Summary

In this chapter, we have characterized the classical chaos in hydrogen atom in crossed electric and magnetic fields, a system with three degrees of freedom. We have found that the electric field can induce chao in a system that is regular otherwise. Furthermore, this system exhibits Arnold diffusion. The classical behavior was compared with the results of a statistical analysis of quantum spectra. In particular, the NNS distributions of the quantum eigenvalues were found to be Wigner-like as the classical counterpart undergoes a transition to chaos. Finally, the quantitative connection between the classical and the quantum descriptons is well described by the Brody distribution.

Chapter 9

Conclusion

This thesis has presented a series of experimental and theoretical studies of Rydberg atoms in strong fields. We have investigated the connection between classical and quantum behavior of a Rydberg atom in a magnetic field and in parallel electric and magnetic fields in the unbound region, and a Rydberg atom in crossed electric and magnetic fields. Here is a brief summary:

- We have studied the continuum behavior of a Rydberg atom in parallel electric and magnetic fields. Calculations revealed that the classical ionization time displays fractal behavior as the system is moved into a disorderly region, indicating the development of chaotic ionization. Experimental recurrence spectra obtained from scaled-energy spectroscopy of lithium revealed that the spectral features can be naturally interpreted in terms of closed orbits in the continuum. These orbits bifurcate rapidly, producing a proliferation of orbits as the system becomes chaotic.

- We have investigated the classical dynamics of a diamagnetic hydrogen atom in the positive energy region. The system exhibits classically chaotic ionization. This chaotic behavior was found to be correlated with the existence of unstable closed orbits. Except for a small region close to the plane perpendicular to the magnetic field, the ionization process becomes regular as the scaled energy becomes large and positive. This transition from chaos to order is accompanied simultaneously by a rapid disapperance of the corresponding closed orbits.

- We have conducted a numerical investigation of the relationships between classical and quantum dynamics of a hydrogen atom in crossed electric and magnetic fields, a system with three degrees of freedom. Classical chaos was characterized by examing surfaces of section and by calculating the Lyapunov exponent. The system was shown to exhibit Arnold diffusion. The quantum manifestation of this classical chaotic behavior was investigated through energy level statistics. In particular, the nearest-neighbor-spacings distribution was found to be in good agreement with the Brody distribution in the region where regular and chaotic trajectories coexist.

Appendix A

Magnet Power Supply

We summarize in this appendix the operating procedures for the IPS 100A power supply for the superconducting magnet:

1. Set the output current limit. The field to current ratio mentioned in Sec. 2.3.2 can be used to determine the current corresponding to the desired field. For example, about 51 A of current is needed for 6 T of magnetic field.

2. Set the output voltage limit to protect the magnet from excessive voltage drop. The output voltage is the sum of the voltage drops across the cables from the power supply to the current leads, the current leads themselves and the magnet. Figure A-1 shows these voltage drops as a function of the magnet current. The diamonds are the measured voltage values across the cables and the crosses are the measured values across the current leads. The lines are the linear fits from which we get 8.01(.05) mV/A for the cables and 1.48(.05) mV/A for the current leads. Table 2.2 gives the optimum magnet voltage. We usually set the voltage limit at 5 V. If everything goes well, the output voltage should always be below this value.

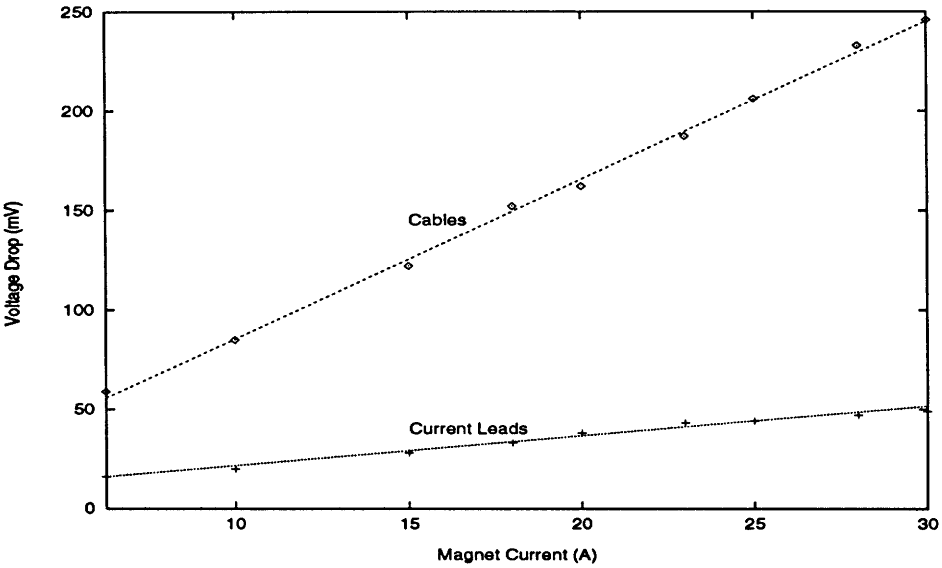

Figure A-1: Voltage drops as a function of magnet current. The diamonds and crosses are the measured values across the cables and the current leads, repectively, and the lines are the linear fits.

3. Set the ramping rate. The rate can be set between 1 A/sec and 0.016 A/sec [1]. The actual rate should be calculated from

$$V = L\frac{dI}{dt}. \tag{A.1}$$

The inductance L is 112 H. For a magnet voltage of 2.5 V, the rate should be set at 22 mA/sec.

4. Turn on the power supply to the persistent switch heater. It delivers about 45 mA. The magnet can now be charged up. Once it has achieved the current limit, one can switch to persistent mode by turning off the persistent switch power supply if desired.

---

[1] Recently, we have replaced the 10K potentiometer with a 100K potentiometer in the ramp generator. Now the rate can go as low as 2 mA/sec. The corresponding magnet voltage is about 0.25 V.

Appendix B

Cryogenic Considerations

This appendix provides details concerning cryogenics. The vacuum jacket of the cryostat is evacuated by a Varian V-60 turbo pump. At room temperature, the pressure, monitored by an ion gauge, is typically about $1 - 2 \times 10^{-6}$ Torr. Mylar, a material used for thermal insulation of the magnet, is a poor vacuum material. When the dewar is pumped down from atmospheric pressure, it can take several days before the mylar stops outgasing. However, we later found by purging the dewar with dry nitrogen and/or baking the system at 50 °C while the dewar is at air, pump down can be shortened to 24 hours. The key is to minimize water condensation on the mylar. Once the desired pressure is reached, we follow the guidelines below to transfer liquid helium to the LHe dewar:

1. While the LHe dewar is at the room temperature, pump on the dewar to eliminate any water condensation. This process usually takes about 20 minutes. The temperature is monitored by a Model 210 Cryothermometer made by American Magnetics. We then back fill the LHe dewar with dry nitrogen.

2. Pump out the LHe transfer tube to $< 5 \times 10^{-4}$ Torr. A Welch Duo-Seal Model 1402 mechanical pump is used to pump out both the LHe dewar and LHe

transfer tube.

3. Pre-cool the LHe dewar with LN_2 while monitoring the temperature. Ideally, we want to stop the flow when it reaches 77 K, LN_2 temperature. This is sometimes difficult. We usually stop at 80 K to 90 K.

4. Close all ports and pump on the dewar while monitoring the temperature. The temperature will initially drop due to evaporative cooling. When all the liquid has been pumped out, the temperature will stabilize or rise sightly. However, solid nitrogen forms if the temperature reaches 63 K, the freezing temperature of nitrogen. Due to its relatively large heat capacity, the frozen nitrogen will boil away large amounts of LHe until it finally cools to 4.2 K if there is any LHe left. Thus, the system needs to be warmed up. *Under no circumstances should one transfer LHe before all the* LN_2 *has been evacuated.*

5. Back fill with dry helium gas and close all ports. The system is now cold, and care should be taken not to admit water or air. Simultaneously, the 50-liter LN_2 dewar can now be filled with LN_2. We usually consume about 180 liters of LN_2 in the whole process. The pressure in the dewar drops quickly to 10^{-7} to 10^{-8}.

6. Now we are ready to transfer LHe. An extension tip is needed to reach the bottom of a 100-liter storage LHe dewar. The whole storage dewar sits on "Little Dickie", the hydraulic lift. We usually use 20 to 30 oz/in^2 of He gas to assist the transfer. All ports on the LHe dewar should be open to release the pressure. The flow through the two vapor-cooled current leads should be checked on a regular basis. Any blockage by air or water can damage the leads when the magnet is being energized. One achieves the most efficient transfer rate when the exit gas forms a light and soft flow of vapor.

7. If everything goes well, it takes about 1 hour to reach 4.2 K and another 1 1/2 hours to accumulate about 35 liters of LHe. The LHe level is monitored by Model 110 Liquid Helium Level Meter made by American Magnetics. The level should only be checked quickly but not too frequently as the operation of the sensor tends to boil away LHe.

We usually need about 100 liters of LHe to cool down the magnet and leave 35 liters of accumulation. The LHe serves as an excellent cryo-pump. We usually close the gate valve and turn off the turbo pump. Recently, however, we noticed that the pressure starts to rise slowly when the turbo pump is off. We suspect the background helium gas in the room may be leaking into our system. Since the performance of a turbo pump is seriously impaired by a magnetic field, Neal Spellmeyer has recently installed a 16.5″ long nipple extension between the dewar and the turbo pump. The field at the pump is now a few hundred gauss, and the pump appears to operate very well. Furthermore, we do not notice any decrease in pumping speed.

The magnet must be fully immersed in LHe when it is operated. We do not know the exact amount of LHe needed to cover the magnet. We have operated the magnet with as little as 15 liters of LHe. However, we usually either transfer more LHe or terminate the experiment when the level indicates 20 liters or less. The thermal insulation of the LHe dewar is excellent: We lose about 5 liters a day when the magnet is off or in persistent mode. However, the LHe storage dewars are even better, losing only 1 liter a day. So the LHe dewar of the magnet should not be used as a storage dewar. After finishing a run, we usually warm up the system quickly to avoid water condensation. To speed up the warming process, we usually blow the LN_2 out of the LN_2 dewar. Then we admit *a little* dry nitrogen. Again, care should be taken to avoid water condensation. The whole system can be warmed up in 24 hours.

Appendix C

Magnetic Field of a Finite Solenoid

In Chapter 2, the magnetic field distribution generated by our superconducting magnet was presented. It was calculated by the following procedure.

The magnetic potential, $\vec{A}$, in SI units is [Jac75]

$$\vec{A}(\vec{x}) = \frac{\mu_0}{4\pi}\int \frac{\vec{J}(\vec{x'})}{|\vec{x}-\vec{x'}|} d^3x', \tag{C.1}$$

where $\vec{J}$ is the current density. A solenoid is azimuthally symmetric. In cylindrical coordinates, $\vec{J}$ lies essentially in the ϕ direction and can be written

$$J_\phi = IN\delta(\rho - a), \tag{C.2}$$

where I is the current, N is the number of turns per unit length, and a is the radius of the winding. Like $\vec{J}$, $\vec{A}$ also has ϕ component only. In the x-y plane $\vec{J}$ can be written as

$$\vec{J} = -J_\phi \sin\phi'\hat{x} + J_\phi \cos\phi'\hat{y}. \tag{C.3}$$

To exploit the symmetry, we choose an observation point in the x-z plane ($\phi = 0$). Integration of Eqn. C.1 vanishes for the x component of the current. The final result for A_ϕ is

$$A_\phi(\rho, z) = \frac{IN\mu_0}{4\pi} \int\int \frac{\cos\phi' dz' d\phi'}{((z - z')^2 + a^2 + \rho^2 - 2a\rho\cos\phi')^{1/2}}, \tag{C.4}$$

where z' is integrated over the length of the solenoid and ϕ' is integrated over 2π. The magnetic field $\vec{B}$ is then found from $\vec{B} = \nabla \times \vec{A}$,

$$B_z = \frac{1}{\rho}\frac{\partial}{\partial\rho}(\rho A_\phi), \tag{C.5}$$

$$B_\rho = -\frac{\partial A_\phi}{\partial z}. \tag{C.6}$$

Except for some special cases, for example on the axis of the solenoid, Eqn. C.4 needs to be integrated numerically.

We calculated the magnetic field of our split-coil magnet by computing the field due to each solenoid separately and combining the results through the superposition principle. Some of the numerical results are shown in Fig. 2-2. The double integral in Eqn. C.4 was solved numerically by applying Simpson's Rule twice [PFTV88].

Appendix D

Other Excitation Schemes for Lithium

The physics that one probes in this experiment depends critically on the excitation scheme. Both excitation schemes mentioned in this thesis prepare the same 3S initial state. This means we can excite only $m = 0, \pm 1$ odd-parity states. The small quantum defect of P states makes odd-parity lithium much like hydrogen, which is an advantage for many purposes. On the other hand, these excitation schemes are not suited to study core-induced chaos or high angular momentum states ($m \geq 1$). Figure D-1 displays the allowed electric dipole transitions among some of the low lying states of ^{7}Li. In addition to using the transitions (2S → 2P → 3S → Rydberg) and (2S → 3S → Rydberg) that were employed in this thesis, there are several other attractive possibilities.

D.1 2S → 3D → Rydberg

The 2S → 3D two-photon transition wavelength (639 nm, see Table. 3.2) is conveniently located near the peak of the DCM gain curve. With 8 W of pumping power,

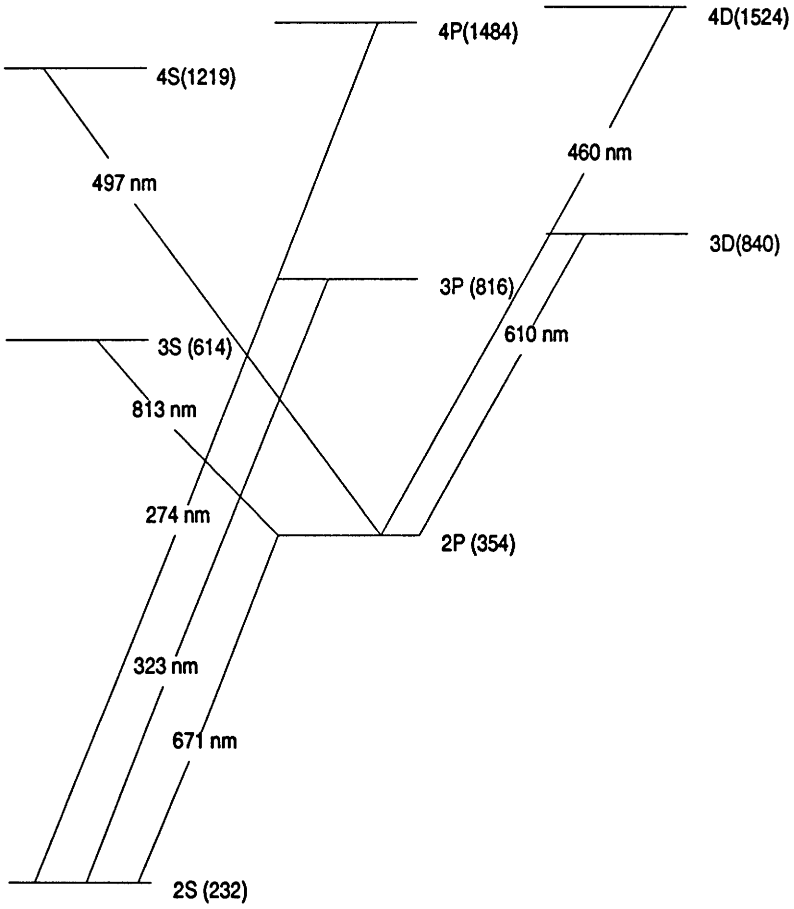

Figure D-1: Some low lying states of ^{7}Li and some important transitions among them. The transition wavelengths are specified, and the number in the parenthesis after a given state is the ionization wavelength of that state (in nm).

we have achieved more than 800 mW of output power from one of our Coherent CR699 ring lasers. We believe that a better jet nozzle, higher jet pressure with sufficient cooling, and higher pumping power can result in even higher output power. Because of the large matrix element between 2P and 3D and small detuning from the intermediate 2P state (Table 3.1 and Table 3.2), this two-photon transition is easier to drive than, for example, the 2S → 3S. In fact, one of the earliest measurements of the fine structure splittings of 3D employed this two-photon Doppler-free transition [KNS+78]. A Ti:Sapphire laser can be used to drive the 3D to Rydberg transition at 840 nm. (Coherent claims that with 10 W of pump power, its 899 Ti:Sapphire can achieve 2 W of output power [Coh93].) Both DCM and Ti:Sapphire lasers can be pumped multiline with an argon ion laser. If we ever acquire a Ti:Sappire laser, this excitation scheme can be implemented easily [1]. Both lasers could be pumped by the argon laser in the same manner as our current excitation scheme.

This alternative excitation scheme also has the advantage of being able to excite P and F states. If the 2S → 3D transition is performed with $\Delta m = \pm 2$, one could excite Rydberg states of $m = \pm 1, \pm 2, \pm 3$. However still only odd-parity final states can be excited.

D.2 2S → 2P → 3D → Rydberg

This excitation scheme prepares lithium atoms in the same inital states (3D) as the previous one, but through a stepwise excitation. This scheme saturates the first two transitions and thus provides a much higher Rydberg signal. The cost of this scheme is a third laser, but it could be a diode laser. A diode laser and a dye laser with Kiton

---

[1] Recently, SDL Inc. announced that they have achieved an output power of 0.5 W for some of their single frequency tunable diode lasers tunable in the wavelength range of 700 nm and 850 nm. This could be a cheaper substitute to a Ti:Sappire laser.

$a(n,l)$	Theory	Previous Measurement	Reference	Our Measurement
3D	1081.4	1083.7(2.0)	[KNS+78]	1074(8)

Table D.1: Fine structure parameter of 3D. All values are in MHz.

Red Special [2] (see Table 3.9) could be used to drive the 2S → 2P (671 nm) and the 2P → 3D (610 nm) transitions, repectively. A Ti:Sapphire laser could be employed to make the Rydberg transition. Again, a single argon laser can be used to pump both the Ti:Sapphire laser and the dye laser.

Fine Structure of 3D

In order to investigate this excitation scheme, we have studied the fine structure of 3D. We observe the fine structure splitting $\Delta E_f(3D)$ by locking one laser to the $2S(F = 2) \rightarrow 2P_{3/2}$ transition and scanning a second laser around the 2P → 3D transition. The frequency of the scanning laser was monitored with the 300 MHz spectrum analyzer similar to the discussion in Sec. 3.2.2. The fluorescent light from 3D → 2P passed through a 610 nm interference filter and was detected by a PMT. The result of such a scan is shown in Fig. D-2. The peak on the right corresponds to $2P_{3/2} \rightarrow 3D_{5/2}$, and the smaller one on the left corresponds to $2P_{3/2} \rightarrow 3D_{3/2}$. (We do not resolve the 3D hyperfine structure.) The stepwise excitation employed here selects the initial state ($2P_{3/2}$) and eliminates the complication due to the hyperfine levels of the ground state. Our result is shown in Table D.1, which also displays the previous two-photon measurement and the theoretical result.

---

[2] Kiton Red is not always a friendly dye to use. If desired, one can also use Rhodamine 6G. Although 610 nm is on the edge of the gain curve, R6G is an extremely efficient dye and should provide enough power to saturate this transition.

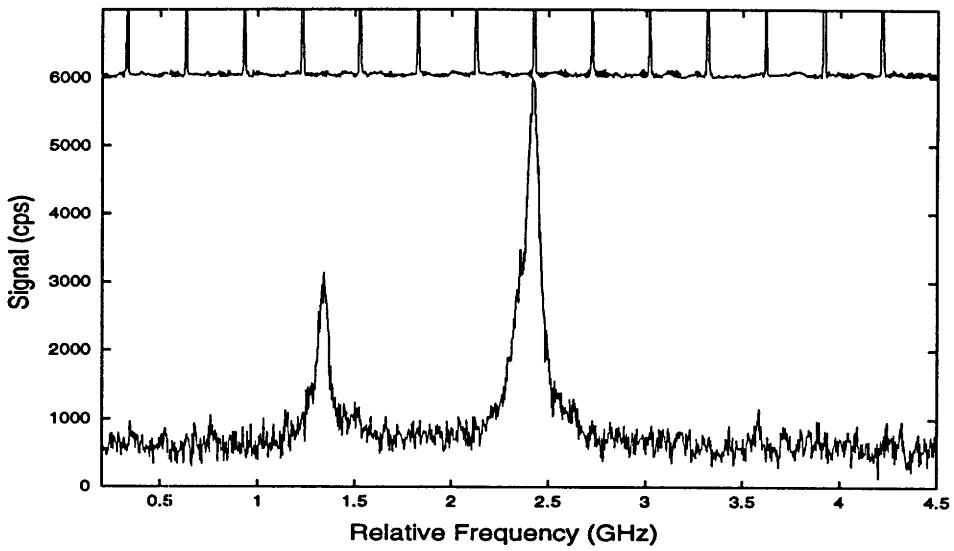

Figure D-2: 3D fine structure splitting of ^{7}Li. The 300 MHz frequency markers are shown on the top.

D.3 2S → 2P → Rydberg

The principal transition 2S → 2P can be driven by a diode laser or a dye laser with DCM dye. The transition to Rydberg states (354 nm) can be achieved with frequency doubling a dye laser with Pyridine 2 dye. Although the peak of the gain curve is around 720 nm, the gain curve is relatively flat, and hence the gain is still reasonably strong at 708 nm [Coh93]. According to Coherent, this dye can only be pumped efficiently with an argon laser at 514.5 nm. If there is need to pump two dye lasers with one argon laser multiline, some dye mixing may be necessary [3]. *Warning:* due to the accidental degeneracy in the principal transition frequencies of the two isotopes (Sec. 3.2.3), an isotopically pure lithium atomic beam must be used in this excitation scheme.

---

[3] Or use the method described in Appendix F.

This excitation scheme has the advantage of exciting even-parity Rydberg states, but the disadvantage of requiring UV radiation for the second step. This path can be used to investigate core-induced chaos and to conduct scaled-energy spectroscopy in the positive energy region (see Sec. 7.2).

D.4 2S → 3P → Rydberg

The above excitation scheme may not be very efficient because the UV output from frequency doubling may not have sufficient power to generate a strong Rydberg signal. (Recall, the oscillator strength between a Rydberg state and the ground state scales as n^{-3}.) Thus, it is more efficient to avoid driving the Rydberg transition with a UV laser. Such a scheme of exciting even-parity Rydberg states involves a stepwise excitation through 3P. The transition 2S → 3P has a wavelength of 323 nm and can be achieved by frequency doubling a dye laser with DCM dye. (646 is near the peak of the DCM gain curve.) The matrix element between 2S and 3P is reasonable large, so the transition can be easily saturated. The transition from 3P to Rydberg states (816 nm) can be driven by a Ti:Sapphire laser.

Appendix E

Clebsch-Gordon Coefficients for the 2P States

In Sec. 3.3, we sought the eigenvalues of

$$H_b = a(n,l)\vec{L}\cdot\vec{S} + A(n,l,j)\vec{I}\cdot\vec{J} + \frac{1}{2}(\vec{L} + g_s\vec{S} + g_I\vec{I})\cdot\vec{B}, \tag{E.1}$$

for the 2P states. At small B, F and J are good quantum numbers; at large B, m_I and m_s are good quantum numbers; L, I, and $m = m_I + m_s + m_l$ are always good quantum numbers. At any field value, the states can be written as linear superpositions of either basis states. For convenience, we have tabulated in Table E.1 the Clebsch-Gordan coefficients for such a linear combination. The horizontal states are in the basis of $|F, J>$, and the vertical states are in the basis of $|m_I, m_s, m_l>$. There are a total of 24 states. States with different m do not mix, and consequently they are divided into 7 nonmixing sets corresponding to 7 different m. The values for $m = -1, -2, -3$ are similar to those of $m = 1, 2, 3$, repectively, and thus are not shown here.

$m = 0$	$\vert 3,3/2 >$	$\vert 2,3/2 >$	$\vert 1,3/2 >$	$\vert 0,3/2 >$	$\vert 2,1/2 >$	$\vert 1,1/2 >$
$\vert 3/2,-1/2,-1 >$	1/20	1/4	9/20	1/4	0	0
$\vert 1/2,1/2,-1 >$	3/20	1/12	-1/60	-1/12	-1/3	-1/3
$\vert 1/2,-1/2,0 >$	3/10	1/6	-1/30	-1/6	1/6	1/6
$\vert -1/2,-1/2,1 >$	3/20	-1/12	-1/60	1/12	1/3	-1/3
$\vert -1/2,1/2,0 >$	3/10	-1/6	-1/30	1/6	-1/6	1/6
$\vert -3/2,1/2,1 >$	1/20	-1/4	9/20	-1/4	0	0

$m = 1$	$\vert 3,3/2 >$	$\vert 2,3/2 >$	$\vert 1,3/2 >$	$\vert 2,1/2 >$	$\vert 1,1/2 >$
$\vert 3/2,1/2,-1 >$	1/15	1/6	1/10	-1/6	-1/2
$\vert 3/2,-1/2,0 >$	2/15	1/3	1/5	1/12	1/4
$\vert 1/2,1/2,0 >$	2/5	0	-4/15	-1/4	1/12
$\vert 1/2,-1/2,1 >$	1/5	0	-2/15	1/2	-1/6
$\vert -1/2,1/2,1 >$	1/5	-1/2	3/10	0	0

$m = 2$	$\vert 3,3/2 >$	$\vert 2,3/2 >$	$\vert 2,1/2 >$
$\vert 3/2,1/2,0 >$	1/3	1/3	-1/3
$\vert 3/2,-1/2,1 >$	1/6	1/6	2/3
$\vert 1/2,1/2,0 >$	1/2	1/2	0

$m = 3$	$\vert 3,3/2 >$
$\vert 3/2,1/2,1 >$	1

Table E.1: Clebsch-Gordon coefficients for ^{7}Li 2P $m = 0, 1, 2, 3$ states. A square root operation applies to each and every coefficient, for example $-1/6$ is understood to be $-\sqrt{1/6}$.

Appendix F

An Alternative Pumping Scheme

In Sec. 3.4.1, we described how we split the argon laser beam to pump the yellow and red lasers using a high power beamsplitter. Although this method works satisfactorily, the output power of the yellow laser is bit low. Furthermore, the lifetime of the dye mixture (Kiton Red and DCM) of the yellow laser is unknown. In this appendix, we suggest an alternative approach to the preparation of 3S atoms.

As described in Sec. 3.4.1, the multiline output of the argon laser consists mainly of 514.5 nm and 488 nm. The Kiton Red dye (yellow laser) strongly absorbs 514.5 nm light and DCM (red laser) absorbs primarily 488 nm light. The only additional hardwares required for a new scheme are a halfwave plate at 488 nm and a cubic polarization beamsplitter. (Both the halfwave plate and the cubic beamsplitter are manufactured by CVI and are AR coated for the appropriate wavelengths.) The schematic of such a pumping scheme is shown in Fig. F-1. The halfwave plate is installed at the output end of the argon ion laser. The cubic polarizing beamsplitter is placed between the halfwave plate and the two dye lasers. The polarization beamsplitter transmits the light polarized parallel to the plane of incidence (P polarization) and reflect the light with perpendicular polarization (S polarization). The beamsplitter is positioned such that the plane of incidence is perpendicular to the optical table.

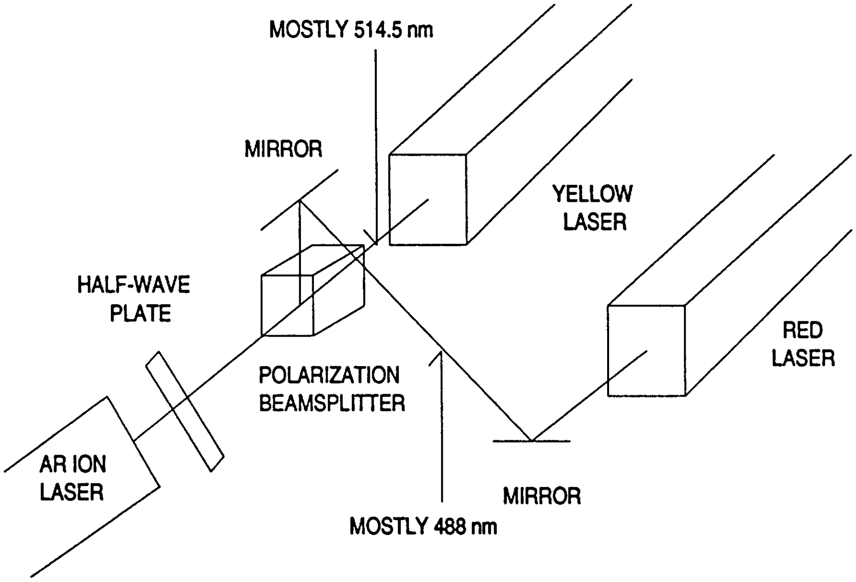

Figure F-1: Schematic of an alternative pumping scheme.

The halfwave plate rotates the 488 nm light by about 90° (S polarization) while the 514.5 nm light is relatively unaffected (remaining P polarization). (The polarization of the original argon laser is vertical with respect to the optical table.) Consequently, the beamsplitter transmits most of 514 nm light onto the pumping mirror of the yellow laser (Kiton Red dye). Most of 488 nm light is reflected vertically with respect to the optical table. It is then deflected by two high power argon mirrors onto the pumping mirror of the red laser (DCM dye). The pump power distribution between the two dye lasers can be adjusted simply by rotating the halfwave plate.

We have attempted to implement this approach. The reflected argon beam pumps DCM rather well. The output power of the red laser is reasonably stable. However, the output power of the yellow laser fluctuates greatly. We find that the shape of the transmitted laser beam is severely distorted. We suspect that 20W ($\approx$ 300 W/cm^2) of CW argon laser power is heating up the coating/epoxy in the center which holds the two halves of the cubic beamsplitter together. Our CVI cubic beamsplitter cannot handle this much CW power. We have attempted unsuccessfully to acquire a cubic beamsplitter with a higher damage threshold. As a result, we had to implement our current pumping scheme as described in Sec. 3.4.1. However, recently Lambda Research Optics announced that it had successfully manufactured a polarization beamsplitter suitable for a high power CW argon laser. The main feature of this new beamplitter is the air gap between the two halves of the cube instead of the usual fragile coating.

Appendix G

Hamilton Equations of Motion

In this appendix, we present some of the numerical details involved in integrating Hamilton equations of motion for a hydrogen atom in strong electric and magnetic fields. The Hamiltonian for such a system in cylindrical coordinates is

$$\begin{aligned} H = \frac{p_\rho^2}{2} + \frac{p_z^2}{2} + \frac{p_\theta^2}{2\rho^2} + \frac{1}{2}Bp_\theta + \frac{1}{8}B^2\rho^2 \\ -\frac{1}{(\rho^2+z^2)^{1/2}} + F_y\rho\sin\theta + F_z z, \end{aligned} \tag{G.1}$$

where $\vec{B} = B\hat{z}$, $\vec{F} = F_y\hat{y} + F_z\hat{z}$. Due to the singular nature of the Coulomb potential at the origin, numerical methods of integration of the equations of motion break down there. To remove this singularity, we use the semiparabolic coordinates originally introduced by Schrufer and Robnik [RS85]

$$\begin{aligned} \rho &= uv \\ p_\rho &= \frac{vp_u + up_v}{u^2+v^2} \\ z &= \frac{1}{2}(v^2 - u^2) \\ p_z &= \frac{-up_u + vp_v}{u^2+v^2} \end{aligned}$$

$$dt \;=\; (u^2+v^2)d\tau. \tag{G.2}$$

These variables are used to generate the "regularized" Hamiltonian

$$\begin{aligned} 2 = \;& \tfrac{1}{2}(p_u^2+p_v^2) - E(u^2+v^2) + \tfrac{1}{2}p_\theta^2(\tfrac{1}{v^2}+\tfrac{1}{u^2}) + \tfrac{1}{2}Bp_\theta(u^2+v^2) \\ & + \tfrac{1}{8}B^2u^2v^2(u^2+v^2) + F_y uv(u^2+v^2)\sin\theta + \tfrac{1}{2}F_z(v^4-u^4). \end{aligned} \tag{G.3}$$

Note that the regularized energy is always equal to 2, and the real energy E enters the regularized Hamiltonian as a parameter. The resulting Hamilton equations of motion are

$$\begin{aligned} \dot{u} &= p_u \\ \dot{p}_u &= 2Eu - \frac{1}{2}B^2u^3v^2 - \frac{1}{4}B^2uv^4 - p_\theta Bu + \frac{p_\theta^2}{u^3} - F_y\sin\theta(3u^2v+v^3) + 2F_zu^3 \\ \dot{v} &= p_v \\ \dot{p}_v &= 2Ev - \frac{1}{2}B^2v^3u^2 - \frac{1}{4}B^2u^4v - p_\theta Bv + \frac{p_\theta^2}{v^3} - F_y\sin\theta(3v^2u+u^3) - 2F_zv^3 \\ \dot{\theta} &= \frac{1}{2}B(u^2+v^2) + p_\theta(\frac{1}{v^2}+\frac{1}{u^2}) \\ \dot{p}_\theta &= -F_y uv(u^2+v^2)\cos\theta. \end{aligned} \tag{G.4}$$

These equations are integrated numerically using a variable step size fourth order Runge-Kutta method. The integration subroutine is described in [PFTV88]. The accuracy of the integration has been tested by calculating the value of E at every integration step. The energy conservation is held to at least 1 in 10^8.

In the course of the integration, the values of the cylindrical coordinates are also calculated by inverting Eqns. G.2. The trajectories can thus be displayed in either representation. Likewise, surfaces of section can be generated in either representation. In the cylindrical representation, we take a slice at $z=0$. In the uv representations, we take a slice at $v=0$. At every integration step, the program holds the current values as well as those from the previous step. When a trajectory crosses the plane of the given slice, these sets of values are used to extrapolate the values on the surface of section. In the case of crossed fields, a close examination of Eqns G.2 reveals that a surface of section at either $u = 0$ or $v = 0$ is impossible. The reason is that either case corresponds to $\rho = 0$ which is forbidden by the angular momentum barrier necessarily developed by the perpendicular electric field. Thus we are restricted to the cylindrical coordinates. As we recall the surface of section is four dimensional. In addition to a trajectory crossing the $z = 0$ plane, the orbit must also fall within the thickness of a slice on the surface of section, typically $p_\theta = 0$ with thickness of 0.01. A typical surface of section consists of about 20 randomly picked initial conditions with 500 points for each initial condition. The computation time for a given surface of section is usually ten times longer for the crossed field system than for the parallel field system.

Appendix H

Lyapunov Exponent

This appendix offers a detailed numerical method for computing the Lyapunov exponent. The Lyapunov exponent is defined to be the mean rate of exponential separation of neighboring trajectories. The Hamilton equations of motion in Eqn. G.4 can be written

$$\frac{dx_i}{dt} = L_i(x_1, ..., x_n), i = 1, ..., 6, \tag{H.1}$$

where $x_1 = u$, $x_2 = p_u$, $x_3 = v$, $x_4 = p_v$, $x_5 = \theta$, and $x_6 = p_\theta$. The Lyapunov exponent can be defined as

$$\sigma = \lim_{t\to\infty} \frac{1}{t} \ln\,(\frac{d(t)}{d(0)}) \tag{H.2}$$

where

$$d(t) = \sqrt{\sum_{i=1}^{n} \delta x_i^2(t)} \tag{H.3}$$

is the separation of two neighboring trajectories. Clearly, we need to obtain equations of motion for δx_i.

In the limit δx_i goes to zero, we can linearize Eqn. G.4,

$$\frac{d\delta x_i}{dt} = \sum_{j=1}^{n} \delta x_j (\frac{\partial L_i}{\partial x_j}). \tag{H.4}$$

The matrix $A_{ij} \equiv \frac{\partial L_i}{\partial x_j}$ is

$$\begin{pmatrix}
0 & 1 & 0 & 0 & 0 & 0 \\
2E - \frac{3}{2}B^2u^2v^2 & 0 & -Bu^3v - Buv^3 & 0 & -3F_yu^2v\cos\theta & -Bu + \frac{2p_\theta}{u^3} \\
-\frac{1}{4}B^2v^4 & & -3F_yv^2\sin\theta & & -F_yv^3\cos\theta & \\
-p_\theta B - \frac{3p_\theta^2}{u^4} & & -3F_yv^2\sin\theta & & & \\
-6F_yuv\sin\theta + 6F_zu^2 & & & & & \\
0 & 0 & 0 & 1 & 0 & 0 \\
-Bv^3u - Bvu^3 & 0 & 2E - \frac{3}{2}B^2v^2u^2 & 0 & -3F_yv^2u\cos\theta & -Bv + \frac{2p_\theta}{v^3} \\
-3F_yv^2\sin\theta & & -\frac{1}{4}B^2u^4 & & -F_yu^3\cos\theta & \\
-3F_yu^2\sin\theta & & -p_\theta B - \frac{3p_\theta^2}{v^4} & & & \\
 & & -6F_yuv\sin\theta - 6F_zu^2 & & & \\
uB - \frac{2p_\theta}{u^3} & 0 & vB - \frac{2p_\theta}{v^3} & 0 & 0 & \frac{1}{v^2} + \frac{1}{u^2} \\
-3F_yu^2v\cos\theta & 0 & -F_yu^3\cos\theta & 0 & F_yu^3v\sin\theta & 0 \\
-F_yv^3\cos\theta & & -3F_yuv^2\cos\theta & & +F_yuv^3\sin\theta &
\end{pmatrix} \tag{H.5}$$

This matrix is used in Eqn. H.4, and δx_i is found by integrating Eqns. H.4 and Eqns. G.4 simultaneously. Eqns H.3 and H.2 are then used to compute the Lyapunov exponent. However, in the actual numerical calculation, $d(t)$ tends to diverge exponentially. The related computation errors are likely to increase as well.

An ingenious scheme has been suggested by Benettin [BGS76]. Numerically, Eqn. H.2 can be written as

$$\sigma = \lim_{N\to\infty} \frac{1}{N\tau} \ln \left(\prod_{j=1}^{N} \frac{d_{j+1}}{d_j}\right), \tag{H.6}$$

where τ is the integration step and N is total number of steps. The trick here is to

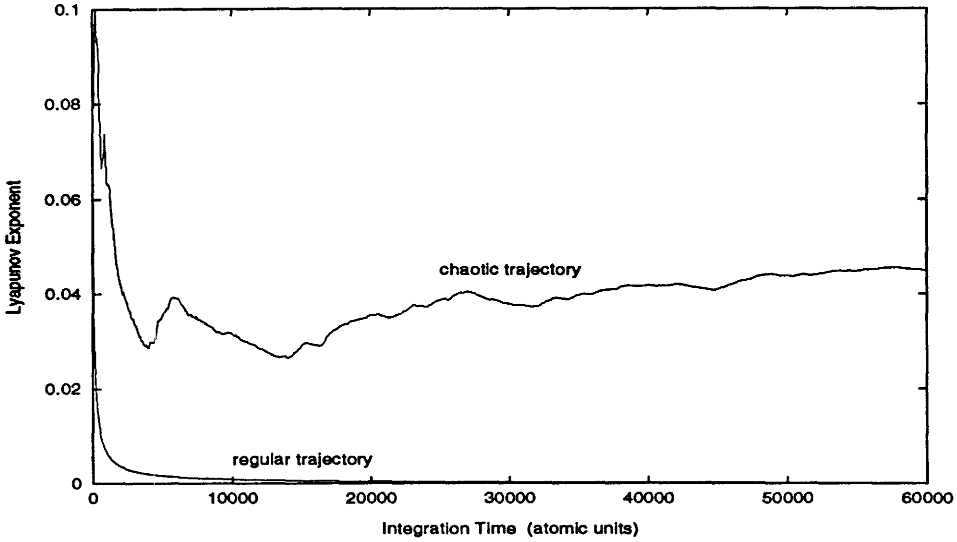

Figure H-1: Numerical calculation of the Lyapunov exponents for regular and chaotic trajectories as a function of the integration time.

rescale d_{j+1} back to d_j [1] at every integration step, such as

$$\tilde{d}_j = 1, \tilde{d}_{j+1} = \frac{d_{j+1}}{d_j}. \tag{H.7}$$

Equation H.6 then becomes

$$\sigma = \lim_{N \to \infty} \frac{1}{N\tau} \sum_{j=1}^{N} \ln \tilde{d}_{j+1}. \tag{H.8}$$

This way the numerical errors are not likely to grow. The typical Lyapunov exponents for a regular trajectory and a chaotic trajetory as a function of the integration time $N\tau$ are shown in Fig. H-1. The Lyapunov exponent of a regular trajectory converges quickly to zero. However the Lyapunov exponent of a chaotic trajectory oscillates

---

[1] d_1 is normalized to 1.

around some nonzero value. To get a precise value, one needs to integrate for a very long time. Except for special cases of periodic orbits [SNF$^+$88], this is usually very difficult. However, for the application in Sec. 8.2.2 where we are only interested in whether the Lyapunov exponents vanish or not, this numerical method is quite adequate.

Bibliography

[AIV77] E. Arimondo, M. Inguscio, and P. Violino. Experimental determinations of the hyperfine structrure in the alkali atoms. *Rev. Mod. Phys.*, 49(1), 1977.

[Arn63] V.I. Arnold. Small denominators and the problem of stability of motion in classical and celestial mechanics. *Russ. Math. Surv.*, 18, 1963.

[Arn64] V.I. Arnold. Instability of dynamical systems with several degrees of freedom. *Dokl. Akad. Nauk. SSSR*, 156(9), 1964.

[Arn78] V.I. Arnold. *Mathematical Methods of Classical Mechanics.* Springer-Verlag, 1978.

[BG84] O. Bohigas and M.J. Giannoni. Lecture notes in physics 209. In J.S. DeHesa, J.M.G. Gomez, and A. Polls, editors, *Mathematical and Computational Methods in Nuclear Physics.* Springer-Verlag, 1984.

[BGS76] G. Benettin, L. Galgani, and J.M. Strelcyn. Kolmogorov entropy and numerical experiments. *Phys. Rev. A*, 14, 1976.

[BGS84] O. Bohigas, M.J. Giannoni, and C. Schmit. Characterization of chaotic quantum spectra and universality of level fluctuation laws. *Phys. Rev. Lett.*, 52(1), 1984.

[BJLS89] S.A. Blundell, W.R. Johnson, Z.W. Liu, and J. Sapirstein. Relativistic all-order calculations of energies and matrix elements for Li and Be. *Phys. Rev. A*, 40(5), 1989.

[BK74] J. Bayfield and P. Koch. Multiphoton ionization of highly excited hydrogen atoms. *Phys. Rev. Lett.*, 33(5), 1974.

[BK87] J. Bayfield and P. Koch. Studies of the sinusoidally driven weakly bound atomic electron in the threshold region for classically stochastic behavior. In E.R. Pike and S. Sarben, editors, *Quantum Measurement and Chaos*. Plenum, 1987.

[BR84] M.V. Berry and M. Robnik. Semiclassical level spacings when regular and chaotic orbits coexist. *J. Phys. A*, 17(1), 1984.

[Bro73] T.A. Brody. A statistical measure for the repulsion of energy levels. *Lett. Al Nuovo Cimento*, 7(12), 1973.

[BS57] H.A. Bethe and E.E. Salpeter. *Quantum Mechanics of One- and Two-Electron Atoms.* Springer-Verlag, 1957.

[BS88] R. Blumel and U. Smilansky. Classical irregular scattering and its quantum-mechanical implications. *Phys. Rev. Lett.*, 60(6), 1988.

[BT77] M.V. Berry and M. Tabor. Level clustering in the regular spectrum. *Proc. R. Soc. Lond. A*, 356(1), 1977.

[Cas85] G. Casati. *Chaotic Behavior in Quantum Systems: Theory and Applications.* Plenum, 1985.

[CG87] E.R. Cohen and P. Giacomo. Symbols, units, nomenclature and fundamental constants in physics. *Physica*, 146(A), 1987.

[Chi79] B.V. Chirikov. A universal instability of many-dimensional oscillator systems. *Phys. Rep.*, 52(5), 1979.

[CJSK94] M. Courtney, H. Jiao, N. Spellmeyer, and D. Kleppner. Long-period orbits in the Stark spectrum of lithium. *Phys. Rev. Lett.*, 73(10), 1994.

[CJSK95] M. Courtney, H. Jiao, N. Spellmeyer, and D. Kleppner. Closed orbit bifurcation in continuum Stark spectra. *Phys. Rev. Lett.*, 74(9), 1995.

[CLKP$^+$86a] P. Cacciani, E. Luc-Koenig, J. Pinard, C. Thomas, and S. Liberman. Anticrossing effects in odd Rydberg states of Li in the presence of a magnetic field. *J. Phys. B*, 19, 1986.

[CLKP$^+$86b] P. Cacciani, E. Luc-Koenig, J. Pinard, C. Thomas, and S. Liberman. Experimental studies of a diamagnetic multiplet in odd Rydberg states of lithium. *Phys. Rev. Lett.*, 56(11), 1986.

[CLLK$^+$89] P. Cacciani, S. Liberman, E. Luc-Koenig, J. Pinard, and C. Thomas. Anticrossing effects in Rydberg states of lithium in the presence of parallel magnetic and electric fields. *Phys. Rev. A*, 40(6), 1989.

[Coh93] Coherent. *899 Ring Laser Series.* Coherent Inc., 1993.

[Cou95] M. Courtney. *Rydberg Atoms in Strong Fields: a Testing Ground for Quantum Chaos.* PhD thesis, Mass. Inst. Tech., 1995.

[CSJK95] M. Courtney, N. Spellmeyer, H. Jiao, and D. Kleppner. Classical, semiclassical, and quantum dynamics in the lithium Stark system. *Phys. Rev. A*, 51(5), 1995.

[CT82] C.W. Clark and K.T. Taylor. The quadratic Zeeman effect in hydrogen Rydberg series: application of sturmian functions. *J. Phys. B*, 15, 1982.

[DD87] M.L. Du and J.B. Delos. Effect of closed classical orbits on quantum spectra: ionization of atoms in a magnetic field. *Phys. Rev. Lett.*, 58(17), 1987.

[DD88a] M.L. Du and J.B. Delos. Effect of closed classical orbits on quantum spectra: ionization of atoms in a magnetic field. I. Physical picture and calculations. *Phys. Rev. A*, 38(4), 1988.

[DD88b] M.L. Du and J.B. Delos. Effect of closed classical orbits on quantum spectra: ionization of atoms in a magnetic field. II. Derivation of formulas. *Phys. Rev. A*, 38(4), 1988.

[DG86] D. Delande and J.C. Gay. Quantum chaos and statistical properties of energy levels: numerical study of the hydrogen atom in a magnetic field. *Phys. Rev. Lett.*, 57(16), 1986.

[DKN84] J.B. Delos, S.K. Knudson, and D.W. Noid. Trajectories of an atomic electron in a magnetic field. *Phys. Rev. A*, 30(3), 1984.

[Eck87] B. Eckhardt. Fractal properties of scattering singularities. *J. Phys. A*, 20, 1987.

[Edm70] A.R. Edmonds. The theory of quadratic Zeeman effect. *J. Phys. (Paris) Colloq.*, 31, 1970.

[Ein17] A. Einstein. Zum quantensatz von sommerfeld und epstein. *Verh. Deutsch. Phys. Ges.*, 19, 1917.

[EJ86] B. Eckhardt and C. Jung. Regular and irregular potential scattering. *J. Phys. A*, 19, 1986.

[ERWS88] U. Eichmann, K. Richter, D. Wintgen, and W. Sandner. Scaled-energy spectroscopy and its relation with periodic orbits. *Phys. Rev. Lett.*, 61(1), 1988.

[FEBL78] R.R. Freeman, N.P. Economu, G.C. Bjorkland, and K.T. Lu. Observation of electric-field-induced resonances above the ionization limit in a one-electron atom. *Phys. Rev. Lett.*, 41(21), 1978.

[Fro70] C. Froeschle. Numerical study of dynamical systems with three degrees of freedom. *Astron. Astrophys.*, 4(1), 1970.

[Fro72] C. Froeshle. Numerical study of a four-dimensional mapping. *Astron. Astrophys.*, 16(2), 1972.

[FW89] H. Friedrich and D. Wintgen. The hydrogen atom in a uniform magnetic field-an example of chaos. *Phys. Rep.*, 183(2), 1989.

[Gal94] T. Gallagher. *Rydberg Atoms.* Cambridge University Press, 1994.

[GD94] J. Gao and J.B. Delos. Resonances and recurrences in the absorption spectrum of an atom in an electric field. *Phys. Rev. A*, 49(2), 1994.

[GDG93] B. Gremaud, D. Delande, and J.C. Gay. Origin of narrow resonances in the diamagntic Rydberg spectrum. *Phys. Rev. Lett.*, 70(11), 1993.

[Gle87] J. Gleick. *Chaos.* Viking, 1987.

[Gol81] H. Goldstein. *Classical Mechanics.* Addison Wesley, 2nd edition, 1981.

[GT69] W.R.S. Garton and F.S. Tomkins. Diamagnetic Zeeman effect and magnetic configuration mixing in long spectral series of Ba_I. *Astrophys. J.*, 158, 1969.

[Gut82] M.C. Gutzwiller. The quantization of a classically ergodic system. *Physica*, 5, 1982.

[Gut90] M.C. Gutzwiller. *Chaos in Classical and Quantum Mechanics.* Springer-Verlag, 1990.

[Haa91] F. Haake. *Quantum Signatures of Chaos.* Springer-Verlag, 1991.

[Her82] D.R. Herrick. Symmetry of the quadratic Zeeman effect for hydrogen. *Phys. Rev. A*, 26(1), 1982.

[HH64] M. Henon and C. Heiles. The applicability of the third integral of motion: some numerical experiments. *Astron. J.*, 69, 1964.

[HH83] A. Harada and H. Hasegawa. Correspondence between classical and quantum chaos for hydrogen in a uniform magnetic field. *J. Phys. A*, 16, 1983.

[HH94] G.C. Hegerfeldt and R. Henneberg. Level statistics for continuous energy spectra with application to the hydrogen atom in crossed electric and magnetic fields. *Phys. Rev. A*, 49(5), 1994.

[HMF88] H. Hasegawa, H.J. Mikeska, and H. Frahm. Stochastic formulation of energy-level statistics. *Phys. Rev. A*, 38(1), 1988.

[HMW$^+$88] A. Holle, J. Main, G. Wiebusch, H. Rottke, and K.H. Welge. Quasi-Landau spectrum of the chaotic diamagnetic hydrogen atom. *Phys. Rev. Lett.*, 61(2), 1988.

[HRW81] H. Herold, M. Ruder, and G. Wunner. The two-body problem in the presence of a homogeneous magnetic field. *J. Phys. B*, 14, 1981.

[HRW89] H. Hasegawa, M. Robnik, and G. Wunner. Classical and quantal chaos in the diamagnetic Kepler problem. *Prog. Theor. Phys. Suppl.*, 98, 1989.

[HWM+86] A. Holle, G. Wiebusch, J. Main, B. Hager, H. Rottke, and K.H. Welge. Diamagnetism of the hydrogen atom in the quasi-Landau regime. *Phys. Rev. Lett.*, 56(24), 1986.

[Iu91] C. Iu. *Energy Levl Structure of Atoms in Magnetic Fields.* PhD thesis, Mass. Inst. Tech., 1991.

[IWK+89] C. Iu, G. Welch, M. Kash, L. Hsu, and D. Kleppner. Orderly structure in the positive-energy spectrum of a diamagnetic Rydberg atom. *Phys. Rev. Lett.*, 63(11), 1989.

[IWK+91] C. Iu, G. Welch, M. Kash, D. Kleppner, D. Delande, and J.C. Gay. Diamagnetic Rydberg atom: confrontation of calculated and observed spectra. *Phys. Rev. Lett.*, 66(2), 1991.

[Jac75] J.D. Jackson. *Classical Electrodynamics.* John Wiley and Sons Inc., 2nd edition, 1975.

[JHY83] B.R. Johnson, J.O. Hirschfelder, and K.H. Yang. Interaction of atoms, molecules, and ions with constant electric and magnetic fields. *Rev. Mod. Phys.*, 55(4), 1983.

[Jia94] H. Jiao. *Data files 1994: aug31.6.* unpublished, 1994.

[JS39] F.A. Jenkins and E. Segré. The quadratic Zeeman effect. *Phys. Rev.*, 55, 1939.

[Kas88] M.M. Kash. *Rydberg Atom Diamagnetism.* PhD thesis, Mass. Inst. Tech., 1988.

[KB92] B.P. Koch and B. Bruhn. Chaotic scattering in a near-integrable system. *J. Phys. A*, 25, 1992.

[Kit86] C. Kittel. *Introduction to Solid State Physics.* John Wiley and Sons Inc., 6th edition, 1986.

[KNS+78] J. Kowalski, R. Neumann, H. Suhr, K. Winkler, and G. zu Putlitz. Two-photon intracavity dye laser spectroscopy of the 4s and 3d term in ^{6,7}Li. *Z. Physik A*, 287(1), 1978.

[KNV+88] A. Konig, J. Neukammer, K. Vietzke, M. Kohl, H.J. Grabka, H. Hieronymus, and H. Rinneberg. Transition from magnetic to electric-field ($F \parallel B$) dominated spectra of barium at threshold. *Phys. Rev. A*, 38(1), 1988.

[KvL95] P.M. Koch and K.A.H. van Leeuwen. The importance of resonances in microwave ionization of excited hydrogen atoms. *Phys. Rep.*, 255(5), 1995.

[KWI88] M.M. Kash, G.R. Welch, and C. Iu. *Data files 1988: apr19.6-10.* unpublished, 1988.

[Lib80] R.L. Liboff. *Introductory Quantum Mechanics.* Holden-Day Inc, 1980.

[LKK78] M.G. Littman, M.M. Kash, and D. Kleppner. Field-ionization processes in excited atoms. *Phys. Rev. Lett.*, 41(103), 1978.

[LL83] A.J. Lichtenberg and M.A. Lieberman. *Regular and Stochastic Motion.* Springer-Verlag, 1983.

[MD92] J.M. Mao and J.B. Delos. Hamiltonian bifurcation theory of closed orbits in the diamagnetic Kepler problem. *Phys. Rev. A*, 45(3), 1992.

[Mey86] H. Meyer. Theory of the Liapunov exponents of Hamiltonian system and a numerical study on the transition from regular to irregular motion. *J. Chem. Phys.*, 84(6), 1986.

[MRB+95] F.L. Moore, J.C. Robinson, C. Bharucha, P.E. Williams, and M.G. Raizen. Observation of dynamical localization in atomic momentum transfer: a new testing ground for quantum chaos. *Phys. Rev. Lett.*, 73(22), 1995.

[MRBF+93] J.M. Mao, K.A. Rapelje, S.J. Blodgett-Ford, J.B. Delos, A. Konig, and H. Rinneberg. Photoabsorption spectra of atoms in parallel electric and magnetic fields. *Phys. Rev. A*, 48(3), 1993.

[MW92] J. Main and G. Wunner. Ericson fluctuations in the chaotic ionization of the hydrogen atom in crossed magnetic and electric fields. *Phys. Rev. Lett.*, 69(4), 1992.

[MW94] J. Main and G. Wunner. Rydberg atoms in external fields as an example of open quantum systems with classical chaos. *J. Phys. B*, 27, 1994.

[MWHW86] J. Main, G. Wiebusch, A. Holle, and K.H. Welge. New quasi-Landau structures of highly excited atoms: the hydrogen atom. *Phys. Rev. Lett.*, 57(22), 1986.

[MWW+94] J. Main, G. Wiebusch, K.H. Welge, J. Shaw, and J.B. Delos. Recurrence spectroscopy: Observation and interpretation of large-scale structure in the absorption spectra of atoms in magnetic fields. *Phys. Rev. A*, 49(2), 1994.

[OT86] P.F. O'Mahony and K.T. Taylor. Quadratic Zeeman effect for nonhydrogenic systems: application to the Sr and Ba atoms. *Phys. Rev. Lett.*, 57(23), 1986.

[Per77] I.C. Percival. Semiclassical theory of bound states. *Adv. Chem. Phys.*, 36, 1977.

[PFTV88] W.H. Press, B.P. Flannery, S.A. Teukolsky, and W.T. Vetterling. *Numerical Recipes in C.* Cambridge University Press, 1988.

[Poi92] H. Poincaré. *Les Methods Nouvelles de la Mechanique Celeste.* Gauthier-Villars, 1892.

[Pri92] D. Pritchard. *Lecture Notes of MIT Course 8.421.* unpublished, 1992.

[Ram56] N. Ramsey. *Molecular Beams.* Oxford University, 1956.

[RBM+95] J.C. Robinson, C. Bharucha, F.L. Moore, R. Jahnke, G.A. Georgakis, Q. Niu, M.G. Raizen, and B. Sundaram. Study of quantum dynamics in the transition from classical stability to chaos. *Phys. Rev. Lett.*, 74(20), 1995.

[Red64] P.J. Redmond. Generalization of the Runge-Lenz vector in the presence of an electric field. *Phys. Rev.*, 133(5), 1964.

[Rei83] W.P. Reinhardt. A time-dependent approach to the magnetic-field-induced redistribution of oscillator strength in atomic photoabsorption. *J. Phys. B*, 16, 1983.

[RFW91] G. Raithel, M. Fauth, and H. Walther. Quasi-Landau resonances in the spectra of rubidium Rydberg atoms in crossed electric and magnetic fields. *Phys. Rev. A*, 44(3), 1991.

[RFW93] G. Raithel, M. Fauth, and H. Walther. Atoms in strong crossed electric and magnetic fields: evidence for states with large electric-dipole moments. *Phys. Rev. A*, 47(1), 1993.

[Rob81] M. Robnik. Hydrogen atom in a strong magnetic field: on the existence of the third integral of motion. *J. Phys. A*, 14, 1981.

[RS85] M. Robnik and E. Schrufer. Hydrogen atom in a strong magnetic field: calculation of the energy levels by quantizing the normal form of the regularized Kepler Hamiltonian. *J. Phys. A*, 18, 1985.

[Sak84] J.J. Sakurai. *Advanced Quantum Mechanics.* Benjamin Cummings, 1984.

[Sak85] J.J. Sakurai. *Modern Quantum Mechanics.* Addison Wesley, 1985.

[SC93a] P. Schmelcher and L.S. Cederbaum. Intermittent chaos in Hamiltonian systems: the three-dimensional hydrogen atom in magnetic field. *Phys. Rev. A*, 47(4), 1993.

[SC93b] P. Schmelcher and L.S. Cederbaum. Two-body effects of the hydrogen atom in crossed electric and magnetic fields. *Chem. Phys. Lett.*, 208(5), 1993.

[Sch84] H.G. Schuster. *Deterministic Chaos.* Physik-Verlag, 1984.

[SIW$^+$95] G.D. Stevens, C. Iu, S. Williams, T. Bergeman, and H. Metcalf. The hyperfine splitting of the 3^2s state of ^{7}Li measured using Stark spectroscopy of Rydberg states. *Phys. Rev. A*, 51(4), 1995.

[SN87] T. Seligman and H. Nishioka. *Quantum Chaos and Statistical Nuclear Physics.* Springer, 1987.

[SNF+88] W. Schweizer, R. Niemier, H. Friedrich, G. Wunner, and H. Ruder. Lyapunov exponents for classical orbits of the hydrogen atom in a magnetic field. *Phys. Rev. A*, 38(4), 1988.

[Sob72] I.I. Sobelman. *Introduction to the Theory of Atomic Spectra.* Pergamon, 1972.

[Sol81] E.A. Solov'ev. Approximate motion integral of a hydrogen atom in a magnetic field. *JETP Lett.*, 34(5), 1981.

[SS39] L.I. Schiff and H. Snyder. Theory of the quadratic Zeeman effect. *Phys. Rev.*, 55, 1939.

[Tab89] M. Tabor. *Chaos and Integrability in Nonlinear Dynamics.* Wiley Inter-Science, 1989.

[vdVVH93] T. van der Veldt, W. Vassen, and W. Hogervorst. Quasi-Landau structure of diamagnetic helium Rydberg atoms. *Europhys. Lett.*, 21(9), 1993.

[Wei78] M. Weissbluth. *Atoms and Molecules.* Academic Press, 1978.

[Wel89] G.R. Welch. *High Resolution Spectroscopy of Rydberg Atoms in a Magnetic Field.* PhD thesis, Mass. Inst. Tech., 1989.

[WF86a] D. Wintgen and H. Friedrich. Photoabsorption calculations for the magnetized hydrogen atom in the quasi-Landau region. *J. Phys. B*, 19, 1986.

[WF86b] D. Wintgen and H. Friedrich. Regularity and irregularity in spectra of the magnetized hydrogen atom. *Phys. Rev. Lett.*, 57(5), 1986.

[WF87] D. Wintgen and H. Friedrich. Classical and quantum-mechanical transition between regularity and irregularity in a Hamiltonian system. *Phys. Rev. A*, 35(3), 1987.

[WHW+86] D. Wintgen, A. Holle, G. Wiebusch, J. Main, H. Friedrich, and K.H. Welge. Precision measurements and exact quantum mechanical calculations for diamagnetic Rydberg states in hydrogen. *J. Phys. B*, 19, 1986.

[Win87] D. Wintgen. Calculation of the Liapunov exponent for periodic orbits of the magnetized hydrogen atom. *J. Phys. B*, 20, 1987.

[WKI+89a] G. Welch, M. Kash, C. Iu, L. Hsu, and D. Kleppner. Experimental study of energy-level statistics in a regime of regular classical motion. *Phys. Rev. Lett.*, 62(8), 1989.

[WKI+89b] G. Welch, M. Kash, C. Iu, L. Hsu, and D. Kleppner. Positive-energy structure of the diamagnetic Rydberg spectrum. *Phys. Rev. Lett.*, 62(17), 1989.

[WMK+89] G. Wiebusch, J. Main, K. Kruger, H. Rottke, A. Holle, and K.H. Welge. Hydrogen atom in crossed electric and magnetic fields. *Phys. Rev. Lett.*, 62(24), 1989.

[WWZ+86] G. Wunner, U. Woelk, I. Zech, G. Zeller, T. Ertl, F. Geyer, W. Schweitzer, and H. Ruder. Rydberg atoms in uniform magnetic fields: uncovering the transition from regularity to irregularity in a quantum system. *Phys. Rev. Lett.*, 57(26), 1986.

[WZW+87] G. Wunner, G. Zeller, U. Woelk, W. Schweizer, R. Niemeier, F. Geyer, H. Friedrich, and H. Ruder. Strongly magnetized atoms - in the laboratory and in the cosmos. In K.T. Taylor, editor, *Physics of Atoms and Molecules*. Plenum, 1987.

[ZKK80] M.L. Zimmerman, M.M. Kash, and D. Kleppner. Evidence of an approximate symmetry for hydrogen in a uniform magnetic field. *Phys. Rev. Lett.*, 45(13), 1980.

ACKNOWLEDGEMENTS

Michael Courtney and I worked together for four years. Together, we survived many mishaps and some frustrating years in the Spec Lab. The experiment profited greatly from his clear understanding of the physics and fine experimental skills.

Neal Spellmeyer joined us about two and half years ago. His carefulness and hardwork significantly helped to speed up the progress in the laboratory. I wish to especially thank Neal for countless hours in the Spec Lab during the data-taking months of January and Frebruary of 1995. Neal proofread chapters 3 and 5.

I benefited greatly from members of the Rydberg experiment. Robert Lutwak has been helpful almost from the day I joined the Kleppner group. Whether it was a vacuum problem or a computer bug, Robert seemed to have ideas for everything. Due to his vast amount of technical knowledge and willingness to help, Robert has become the "consultant" on the AMO floor. Jeff Holley and I have been roommates for over three years. Jeff has good understanding about almost every physics or non-physics related subject. I benefited a lot from our interactions both in and out of the laboratory. Both Jeff and Robert loaned us equipments and offered great help on many occasions. Robert proofread chapters 1 and 7. Jeff proofread chapter 4.

Chun-ho Iu, Peter Chang, Scott Paine, and Tomaz Catunda, former members of the Kleppner group, introduced me to dye lasers, electronics, and vacuum systems.

Ken Davis and Marc-Oliver Mewes loaned us the Burleigh Wavemeter, laser accessories, and liquid nitrogen on numerous occasions.

I am grateful to Professor David Pritchard, Professor Wolfgang Ketterle, and Professor Ted Ducas for many hours of useful discussions which helped in deepening my understanding of physics overall.

I enjoyed many hours of stimulating physics discussions with other members of the AMO groups, including Joel DeVries, Mike Bradley, Fred Palmer, Troy Hammond, Richard Rubenstein, Edward Smith, Michael Andrews, and Claudio Cesar.

I thank James Childs for very helpful suggestions during my early experience with the krypton ion laser power supply.

I thank John Brandenberger for carefully proofreading chapter 2 and the appendices of this manuscript.

I thank Carol Costa and Peggy Berkovitz for invaluable administrative assistance throughout the years.

I also acknowledge all the help I received from other former and present members of the AMO groups.

I thank my thesis committee members Professor June Matthews and Professor Michel Baranger for their helpful suggestions about this manuscript.

Finally, I wish to thank Professor Dan Kleppner for his patience and encouragement, especially during these years when the progress in the Spec Lab was next to nothing. Dan was always very willing to help solving whatever the problem we faced in the laboratory. His careful proofreading of this thesis vastly improved its quality. I always admired his ability to understand a complex problem in a simple and intuitive way. Throughout the years, probably the greatest thing I learned from Dan was how to be independent and develop my own ideas.